



University of Kentucky
UKnowledge

Theses and Dissertations--Physics and
Astronomy

Physics and Astronomy


2020

A THEORETICAL AND EXPERIMENTAL STUDY OF CHARGE TRANSPORT IN ORGANIC THERMOELECTRIC MATERIALS AND CHARGE TRANSFER STATES IN ORGANIC PHOTOVOLTAICS

Ashkan Abtahi

University of Kentucky, a.abtahi@uky.edu

Author ORCID Identifier:

 <https://orcid.org/0000-0002-9599-1745>

Digital Object Identifier: <https://doi.org/10.13023/etd.2020.507>

[Right click to open a feedback form in a new tab to let us know how this document benefits you.](#)

Recommended Citation

Abtahi, Ashkan, "A THEORETICAL AND EXPERIMENTAL STUDY OF CHARGE TRANSPORT IN ORGANIC THERMOELECTRIC MATERIALS AND CHARGE TRANSFER STATES IN ORGANIC PHOTOVOLTAICS" (2020). *Theses and Dissertations--Physics and Astronomy*. 78.
https://uknowledge.uky.edu/physastron_etds/78

This Doctoral Dissertation is brought to you for free and open access by the Physics and Astronomy at UKnowledge. It has been accepted for inclusion in Theses and Dissertations--Physics and Astronomy by an authorized administrator of UKnowledge. For more information, please contact UKnowledge@lsv.uky.edu.

STUDENT AGREEMENT:

I represent that my thesis or dissertation and abstract are my original work. Proper attribution has been given to all outside sources. I understand that I am solely responsible for obtaining any needed copyright permissions. I have obtained needed written permission statement(s) from the owner(s) of each third-party copyrighted matter to be included in my work, allowing electronic distribution (if such use is not permitted by the fair use doctrine) which will be submitted to UKnowledge as Additional File.

I hereby grant to The University of Kentucky and its agents the irrevocable, non-exclusive, and royalty-free license to archive and make accessible my work in whole or in part in all forms of media, now or hereafter known. I agree that the document mentioned above may be made available immediately for worldwide access unless an embargo applies.

I retain all other ownership rights to the copyright of my work. I also retain the right to use in future works (such as articles or books) all or part of my work. I understand that I am free to register the copyright to my work.

REVIEW, APPROVAL AND ACCEPTANCE

The document mentioned above has been reviewed and accepted by the student's advisor, on behalf of the advisory committee, and by the Director of Graduate Studies (DGS), on behalf of the program; we verify that this is the final, approved version of the student's thesis including all changes required by the advisory committee. The undersigned agree to abide by the statements above.

Ashkan Abtahi, Student

Dr. Joseph Brill, Major Professor

Dr. Christopher Crawford, Director of Graduate Studies

A THEORETICAL AND EXPERIMENTAL STUDY OF CHARGE TRANSPORT IN
ORGANIC THERMOELECTRIC MATERIALS AND CHARGE TRANSFER
STATES IN ORGANIC PHOTOVOLTAICS

DISSERTATION

A dissertation submitted in partial fulfillment of the
requirements for the degree of Doctor of Philosophy
in the College of Arts and Sciences
at the University of Kentucky

By

Ashkan Abtahi

Lexington, Kentucky

Co- Directors: Dr. Kenneth Graham, Professor of Chemistry

and Dr. Joseph Brill, Professor of Physics and Astronomy

Lexington, Kentucky

2020

Copyright © Ashkan Abtahi 2020
<https://orcid.org/0000-0002-9599-1745>

ABSTRACT OF DISSERTATION

A THEORETICAL AND EXPERIMENTAL STUDY OF CHARGE TRANSPORT IN ORGANIC THERMOELECTRIC MATERIALS AND CHARGE TRANSFER STATES IN ORGANIC PHOTOVOLTAICS

Applications of organic electronics have increased significantly over the past two decades. Organic semiconductors (OSC) can be used in mechanically flexible devices with potentially lower cost of fabrication than their inorganic counterparts, yet in many cases organic semiconductor-based devices suffer from lower performance and stability. Investigating the doping mechanism, charge transport, and charge transfer in such materials will allow us to address the parameters that limit performance and potentially resolve them. In this dissertation, organic materials are used in three different device structures to investigate charge transport and charge transfer. Chemically doped π -conjugated polymers are promising materials to be used in thermoelectric (TE) devices, yet their application is currently limited by their low performance. Blending two polymers is a simple way to change the TE properties of the film. Here we use an analytical model to calculate the TE properties of polymer blends, which takes into account energetic disorder, energetic offsets between mean energy of states of the two polymers, and localization length. These calculations show that the TE performance of polymer blends can exceed the individual polymers when there is a small (e.g., 0.1-0.2 eV) offset between the mean of the density of states (DOS) distributions of the two polymers, the polymer with the higher energy DOS has a wider DOS distribution and a larger localization length (mobility), and the polymers are homogeneously mixed. We show these improvements are achievable by experimentally testing TE properties of selected polymer blends. These sets of polymers are selected with variations in electrical mobility, ionization energy and degree of crystallinity to cover a range of possibilities explored in the calculations. Further, to investigate the effect of dopant size in polymers, we use organic electrochemical transistors to investigate the effect

of anion size on polaron delocalization and the thermoelectric properties of single polymers. This device structure allows us to control the charge carrier concentration with minimizing the effects on the film morphology. Another application of OSC is in organic photovoltaics (OPVs), where they can potentially provide a cheap and flexible source of solar energy, yet they currently suffer from low performance and stability. In OPVs, fluorination of donor molecules is a proven strategy for increasing the performance of OPV donor materials. Herein, we investigate the charge transfer state energy between the electron donor anthradithiophene (ADT) and the electron acceptor C_{60} upon halogenation of the ADT molecule. Interfacial energetics and charge transfer state energies between donor and acceptor are crucial to the PV performance of these devices. We probe interfacial energetics of donor/acceptor interfaces with ultraviolet photoemission spectroscopy (UPS), charge transfer state energies with sensitive external quantum efficiency (EQE) both in bilayer and bulk heterojunction device structures. These measurements coupled with DFT calculations allow us to explain that in bulk-heterojunction OPVs the halogenated ADT derivatives will likely increase charge recombination due to lower energy CT states present in the mixed phase. Therefore, the less favorable energy landscapes observed upon halogenation suggest that the benefits of fluorination observed in many OPV material systems may be more due to morphological factors.

KEYWORDS: Organic Electronic, Organic Semiconductors, Charge Transport, Organic Thermoelectric, Organic photovoltaics, Organic Electrochemical Transistor

Ashkan Abtahi

(Name of Student)

11/22/2020

Date

A THEORETICAL AND EXPERIMENTAL STUDY OF CHARGE TRANSPORT
IN ORGANIC THERMOELECTRIC MATERIALS AND CHARGE TRANSFER
STATES IN ORGANIC PHOTOVOLTAICS

By
Ashkan Abtahi

Kenneth Graham

Co-Director of Dissertation

Joseph Brill

Co-Director of Dissertation

Christopher Crawford

Director of Graduate Studies

11/22/2020

Date

To my mother and father, Shokouh Ejlali and Mohammad Reza Abtahi, and my sisters Azadeh and Bahareh who have supported me and were always beside me through my entire life during happy or difficult times, to best friend who made it possible for me endeavoring years far from family, to many friends cheering during the path I was walking, and to Dr. Graham and Dr. Brill who taught me to be a great scientist with endless kindness and patience

ACKNOWLEDGMENTS

I would like to express my gratitude to my research advisor Prof. Kenneth Graham who has been supported me patiently through out my whole Ph.D. here at the University of Kentucky. I am grateful the time I have had working together on many projects in his lab and group. I so thankful to my academic advisor, Prof. Joseph Brill who has been closely following my progress in the learning new field of science and helping whenever I faced a problem in both my research and academic courses.

I would like to thank my member of committee, Prof. Yang-Tse Cheng, whose advice and insightful questions has broadened the scope of my research and his guidance has helped me as president of MRS UK Chapter, Prof. Douglas Strachan, whose discussion and collaboration in my projects has been so helpful.

I should thank my group members especially Dr. So Min Park whose assistant and guidance has helped me to go through joining a group working in area new to me, Dr. Alex Boehm, Dr. Maryam Shahi, Tuo Liu and Kyle Baustert whose assistant in our laboratory and collaboration in my projects has been essential. I should thank Prof. Chad Risko for his gaudiness throughout my Ph.D. that has been indispensable for my research. I am grateful to Prof. Jianguo Mei, Prof. Seth Marder and Prof. John Anthony who has been providing new and high-quality chemicals. I should thank many other collaborators whose effort made it possible for me to complete my projects; Dr. Ruipeng Li, Dr. Stephen Johnson, Samuel Mazza, Dr. Joel Bombile, Dr. Zhiming Liang, Dr. Yadong Zhang and Xuyi Luo, Dr. Mohsen Nasser, Dr. Mathias Boland and many other. I should thank teaching assistant coordinator and mentors in our department, Dr. Sumit Das, Dr. Michael Eides, Dr. Ribhu Kaul, Dr. Max Brown, Maxwell Ankrah, Dr. Lauren Falco and Steven

Ellis. I should specially thank Art Sebesta and Steve Maynard for helping build new instruments and help me to learn more about electronics and machinery. I should also thank the funding agencies, the University of Kentucky startup fund for Dr. Kenneth Graham from 2015 to 2018, National Science Foundation grant no. 1262261 awarded to Dr. Joseph Brill for summer of 2015, The American Chemical Society Petroleum Research Fund awarded to Dr. Kenneth Graham from 2018 and 2019 and National Science Foundation grant no. 1905734 awarded to Dr. Kenneth Graham in 2020.

I should thank my new friends in the department who helped to go through hard time during first years of coming to a new country, Dr. Javad Farrokhi, Dr. Armin Ansary, Lakshya Malhotra, Laura Kelton, Danielle Schaper, Dr. Alina Aleksandrova, Dr. Nisheeta Desai.

Finally, I should thank my parents, Mohammadreza and Shokouh, my sisters Azadeh and Bahareh who have been always encouraging and supportive during all these years we far apart from each other.

TABLE OF CONTENTS

ACKNOWLEDGMENTS	iii
LIST OF TABLES	viii
LIST OF FIGURES	ix
CHAPTER 1. INTRODUCTION TO ORGANIC SEMICODUCTOR	1
1.1 Brief History and Recent Applications	1
1.2 General Chemistry and Physics of Organic Semiconductors	3
1.2.1 Materials; sp, sp ² and sp ³ orbitals and conjugation of orbitals	3
1.2.2 Energetics of Organic Semiconductors	8
1.2.3 Charge Carrier Injection	11
1.3 Charge Transport in Organic Semiconductors	13
1.4 Dissertation Structure	15
1.4.1 Chapter 2: Instrumental Setups and Methods of Measurements	15
1.4.2 Chapter 3: Effect of Donor Halogenation on Interfacial Energetics and Charge Transfer State Energies in Model OPVs	16
1.4.3 Chapter 4: Thermoelectric Power Factor Enhancement in Polymer Blend	17
1.4.4 Chapter 5: Effect of Anion Size and Fluorination on Polaron Formation, Polymer Crystallinity, and Thermoelectric Properties in Organic Electrochemical Transistors	18
1.4.5 APPENDIX 1: LabVIEW	18
1.4.6 APPENDIX 2: Calculating Surface coverage using XPS	19
CHAPTER 2. INSTRUMENTAL SETUPS AND METHODS OF MEASUREMENTS	20
2.1 Photoemission Spectroscopy	20
2.1.1 Ultraviolet photoemission Spectroscopy	21
2.1.1.1 Source, Analyzer, sample preparations and other considerations	28
2.1.2 Inverse Photoemission spectroscopy	29
2.1.2.1 IPES instrumental detail	31
2.1.3 X-ray photoemission spectroscopy	31
2.1.3.1 XPS instrumental detail	34
2.2 Photovoltaic device fabrication and characterizing	34
2.2.1 Substrate and substrate cleaning	34
2.2.2 PV Device fabrication process	35
2.2.3 Device characterization	36
2.3 External quantum efficiency (EQE)	36
2.4 UPS fitting procedure to stepwise deposition of C ₆₀ on ADT	38
2.5 Grazing Incidence Wide-Angle X-ray Scattering (GIWAXS)	40

2.6	Density functional theory calculations	40
2.7	Quadrupole calculations	41
2.8	Thermoelectric device fabrication and characterizing.....	41
2.8.1	Substrate and substrate cleaning	41
2.8.2	Thermoelectric Device fabrication process.....	42
2.8.3	Materials.....	43
2.8.4	Device characterizing.....	43
2.9	Photothermal Deflection Spectroscopy (PDS)	44
2.9.1	PDS Device fabrication process.....	44
2.9.2	PDS characterizing.....	44
2.10	Film fabrication for absorbance spectroelectrochemistry.....	46
2.11	UV-Vis-NIR absorption spectroelectrochemistry in liquid electrolyte	46
2.12	UV-Vis-NIR absorption spectroelectrochemistry on solid state	47
2.13	Raman spectroelectrochemistry.....	48
2.14	Temperature dependent thermoelectric measurement on OECT.....	48
2.14.1	Film fabrication and device structure	48
2.14.2	setup for temperature dependent TE properties measurements	52
2.14.3	Calibration and temperature dependent Seebeck coefficient measurement.....	56
CHAPTER 3. EFFECT OF DONOR HALOGENATION ON INTERFACIAL		
ENERGETICS AND CHARGE TRANSFER STATE ENERGIES IN MODEL OPVs		
61		
3.1	Introduction	61
3.1	Interfacial Energetics.....	66
3.2	Blend Energetics.....	78
3.3	Conclusion.....	89
CHAPTER 4. THERMOELECTRIC POWER FACTOR ENHANCEMENT IN POLYMER		
BLEND.....		
90		
4.1	Introduction	90
4.2	Theoretical model.....	94
4.3	Single polymer.....	99
4.4	Polymer blends	105
4.5	Effective localization length.....	117
4.6	Experimental results	123
4.7	Conclusion.....	136
CHAPTER 5. EFFECT OF ANION SIZE AND FLUORINATION ON POLARON		
FORMATION, POLYMER CRYSTALLINITY, AND THERMOELECTRIC PROPERTIES IN		
ORGANIC ELECTROCHEMICAL TRANSISTORS.....		
138		

5.1	Introduction	138
5.2	Materials and device structure	141
5.3	Absorbance spectroelectrochemistry	143
5.4	Conclusion.....	150
APPENDICES		152
APPENDIX 1. LabVIEW		152
APPENDIX 2. Calculating Surface coverage using XPS.....		157
BIBLIOGRAPHY		162
VITA		181

LIST OF TABLES

Table 2.1 Fitting parament for the fits shown in Figure 2.4	27
Table 3.1 Molecular quadrupole principal components for H-ADT, CH3-ADT, F-ADT, and Cl-ADT determined via distributed multipole analysis of the ω B97X-D/6-31G(d,p) density matix. θ_{XX} , θ_{YY} , and θ_{ZZ} correspond to the molecular long axis, short axis, and normal axis, respectively. All data are given in units of Debye-Angstroms.	73
Table 3.2 Summary of experimentally measured CT state energies, λ , f , and IEs.	82
Table 3.3 Calculated E_{CT} and oscillator strengths (f) values of X-ADT:C ₆₀ complexes with varying orientations. Details of calculations are provided in the Methods section of the main document.	88
Table 4.1 fitting parameters for each polymer in each individual blend system	126
Table 4.2 The molecular weight of a polymer repeat unit and the density of polymers (estimated) and dopant. γ is extracted from solution preparation and concentration of dopant and maximum number of states are calculated using equation S15 and S16.	134

LIST OF FIGURES

Figure 1.1 (a) Electron configuration of a C atom. (b) Shape of s and p electronic orbitals. Colors show the phase of the wave function. (c) Electronic configuration of C atom in CH ₄ . (d) shape of 4 sp ³ orbital.	5
Figure 1.2 (a) showing overlap of two sp ³ orbitals forming a σ orbitals and σ bonding and σ* anti-bonding orbitals. (b) showing overlap of two sp ² orbitals forming a π orbitals which form a π bonding and π* anti-bonding.	7
Figure 1.3 Chemical structure and MO of (a) 1,3-Butadiene and (b) benzene. For Benzene only bonding MOs are shown.	8
Figure 1.4. energy diagram of (a) s and p orbitals, (b) sp ³ , (c) sp ² and (d) sp orbitals.	8
Figure 1.5 Energetic diagram of σ, σ*, π and π* orbitals in (a) methane, (b) ethane and (c) ethyne. The accurate energetics can be found elsewhere. ³³	9
Figure 1.6 Shows schematic of energy diagram of an organic semiconductor if (a) gas phase and (b) in solid state	11
Figure 1.7 (a) Schematic of charge injection by photon absorbance. (b) and (c) Show charge injection by chemical doping. (b) is p-doped and (c) is n-doped.....	13
Figure 2.1 Energetic schematics of electrons and photoelectrons in/from a metal at absolute zero. The curve is showing DOS with blue regions indicating occupied states. (a) shows a case with electron as the E _F and (b) the case for electron at states lower than E _F . (c) is showing collected KE spectrum and (d) is showing E _{Bi} spectrum. These spectra doesn't resemble the UPS due to the contribution of inelastically scattered electrons.	22
Figure 2.2 Energetics of sample and detector with respect to each other when they are (a) electrically isolated and (b) when they both grounded.	23
Figure 2.3 UPS spectrum of 50nm gold. Darker blue represents the DOS of gold and light blue represents the scattered electron that show up in spectrum. The DOS of gold shown in dark blue is just a representation for showing the difference between the actual DOS and UPS spectrum.....	25
Figure 2.4 UPS spectrum of 50nm gold showing the region around E _F . Solid lines showing fits to the spectrum using the Equations (2.7),(2.8),(2.9) and (2.10).....	27
Figure 2.5 (a) UPS spectrum of 64 nm C ₆₀ , (b) zoomed in view of the SECO region and (c) HOMO onset region.....	28
Figure 2.6 Energetic schematics of electrons in a metal. The curve is showing DOS with blue regions indicating occupied states. (a) shows a case where the electron falls into a state at the E _F and (b) shows the case for electron absorbs at states higher than E _F	30
Figure 2.7 (a) XPS survey of Regiorandom Poly(3-hexylthiophene) on ITO coated glass. Small area scan for (b) S 2p and (c) C1s region of same film.	34
Figure 2.8 Device fabrication process.	36
Figure 2.9 Sensitive EQE setup schematics.....	37

Figure 2.10 Example of H-ADT/C ₆₀ stepwise deposition with UPS spectra for 2Å (a, b), 20Å (c, d) and 80Å (e, f) C ₆₀ on H-ADT. Plots b, d and f show zoomed in regions of the spectrum where the H-ADT onset appears. In all figures the solid black line is pure H-ADT, solid red line is 160Å C ₆₀ on H-ADT which represents pure C ₆₀ , solid blue line shows spectrum of 2, 20 and 80 Å of C ₆₀ on top of H-ADT, hollow black circles show the shifted and rescaled H-ADT spectrum (H-ADT fit) and hollow red circles show the spectrum of the H-ADT fit subtracted from the 2, 20 and 80 Å C ₆₀ on H-ADT, which represents the contribution of C ₆₀ .	39
Figure 2.11 Device fabrication schematics for Seebeck coefficient measurement.	43
Figure 2.12 Schematic of the PDS setup.	45
Figure 2.13 Schematic of absorption spectroelectrochemistry setup.	47
Figure 2.14 (a) Schematic of device for UV-Vis-NIR absorption spectroelectrochemistry on solid state and (b) absorption spectroelectrochemistry setup.	48
Figure 2.15 Device structure for measuring temperature dependent thermoelectric properties of chemically doped polymers.	50
Figure 2.16 schematics of gold deposition of the first layer for OECT device	50
Figure 2.17 (a-e) Schematics of OECT device fabrication. (f) Cross sectional view of an OECT device.	52
Figure 2.18 (a) Schematics of vacuum chamber for measuring TE properties of OECT. (b) outside view and (c) inside view of vacuum chamber.	54
Figure 2.19 The vacuum chamber and all the measuring instruments connected.	55
Figure 2.20 (a) Peltier module and aluminum stage. (b) and (c) Top view of aluminum stage with substrate on it. (d) and (e) Bottom and top view of the measuring stage	56
Figure 2.21 (a) Schematic of the device structure. (c) Thermoelectric voltage of bismuth as function of time with varying applied heater line power (each step corresponds to a different power input and the applied voltage is shown next to each step). The temperature gradient is calculated based on the voltage of the bismuth film.	57
Figure 2.22 (a) Temperature gradient versus applied voltage to heater line squared at different temperatures. (b) Temperature gradient versus applied voltage to heater line squared for different channel length and position in the active area in the slit.	58
Figure 2.23 (a) Temperature profile of glass substrate for a 1mm thick glass substrate with 9 mm slit for different position of heater line. (b) Temperature profile of glass substrate with 5 mm slit and heater line positioned at -1 mm for different thickness of glass. In both figure the temperature of substrate is at 293 K and temperature heater line at 321 K.	60
Figure 3.1 Chemical structures of C ₆₀ and ADT derivatives used in this work.	66
Figure 3.2 UPS spectra showing the secondary electron cut-off (a, c, e) and HOMO onset (b, d, f) regions for H-ADT/C ₆₀ , F-ADT/C ₆₀ , and Cl-ADT/C ₆₀ bilayers during stepwise C ₆₀ deposition. The UPS measurements were recorded with a H Lyman-α source emitting at 10.2 eV. ⁵⁹	69
Figure 3.3 UPS spectra showing the secondary electron cut-off (a) and HOMO onset (b) regions for a CH ₃ -ADT/C ₆₀ bilayer during stepwise C ₆₀ deposition.	69
Figure 3.4 Resulting energy diagrams for CH ₃ -ADT/C ₆₀ (a), H-ADT/C ₆₀ (b), F-ADT/C ₆₀ (c) and Cl-ADT/C ₆₀ (d) bilayers during stepwise C ₆₀ deposition.	69

Figure 3.5 HOMO onsets vs. Fermi energy of ADT derivatives (a) and C ₆₀ (b), Ionization energies of ADT derivatives (c) and C ₆₀ (d) and work functions (e) as a function of C ₆₀ thickness. Dashed lines show an approximate trend for the points. Solid lines simply have connected the points in the graph.....	70
Figure 3.6 GIWAXS measurements of H-ADT:C ₆₀ (a,c,e,g) and Cl-ADT:C ₆₀ (b,d,f,h) blends with different ratio of C ₆₀ . Pure X-ADT (a,b), 9:1 (c,d), 1:1 (e,f) and 1:9 (g,h)...	71
Figure 3.7 Crystal structures for H-ADT, F-ADT, and Cl-ADT in order from left to right. The crystal structure for H-ADT is taken from Mamada, <i>et al.</i> ¹³⁹ and the structures for F-ADT and Cl-ADT were experimentally determined in our laboratories using single crystal X-ray diffraction.	72
Figure 3.8 a) Sensitive EQE of H-ADT/C ₆₀ , F-ADT/C ₆₀ and Cl-ADT/C ₆₀ bilayer PV devices. The fit to the CT states is shown with dashed lines. b) Current density vs. voltage characteristics in the dark and under AM1.5G illumination.....	76
Figure 3.9 EQE of Cl-ADT/C ₆₀ bilayer PV device. This graph shows fitting with different λ and f values yield similar CT state energies	77
Figure 3.10 EQE of H-ADT/C ₆₀ (a) and Cl-ADT/C ₆₀ (b) bilayers, 9:1, and 1:9 blends with fits to the CT state component indicated by dashed lines.	79
Figure 3.11 EQE spectra of CH ₃ -ADT:C ₆₀ blend and bilayer devices with the fits to the CT band shown with dashed lines.....	80
Figure 3.12 UPS spectra of H-ADT:C ₆₀ (a,b), CH ₃ -ADT:C ₆₀ (c,d) and Cl-ADT:C ₆₀ (e,f) at 1:9 and 9:1 ratios. Plots a,c and e show the SECO regions whereas plots b,d and f show the HOMO onset regions.	81
Figure 3.13 EQE spectra of F-ADT:C ₆₀ bilayer and blend films (a). The 1:49 F-ADT:C ₆₀ blend shows the appearance of a new low-energy CT band. EQE spectra of H-ADT blend films (b).....	82
Figure 3.14 EQE spectra of Cl-ADT:C ₆₀ blend and bilayer PVs with fits to the CT absorbance band shown (a), and UPS spectra of pure C ₆₀ , Cl-ADT:C ₆₀ , and F-ADT:C ₆₀ blends at a 1:19 ratio (b). In the UPS spectra the binding energy is referenced to the vacuum level at 0 eV.	85
Figure 3.15 UPS spectra for pure C ₆₀ , Cl-ADT:C ₆₀ 1:19 and 1:49 blend, and F-ADT:C ₆₀ 1:19 and 1:49 blend. The data are plotted with the vacuum level at 0 eV.....	86
Figure 3.16 Schematic of the intermolecular orientations investigated in the DFT calculations.	88
Figure 4.1 Seebeck coefficient vs. electrical conductivity. Parameters are $NC = 3 \times 10^{19} \text{cm}^{-3}$, $\nu_0 = 10^{12} \text{s}^{-1}$, a has values of 1, 1.18, 1.35, 1.52 and 1.7 nm (corresponding to $Nt = 10, 6.09, 4.06, 2.85$ and $2.06 \times 10^{20} \text{cm}^{-3}$), and Δ has values of ranging from 1 to 6 KBT . α is chosen such that the ratio between a and α is constant for each figure, $a\alpha$ is 10 for (a), 7 for (b), 5 for (c), 3 for (d), 2 for (e) and 1 for (f).	101
Figure 4.2 Power factor vs. electrical conductivity. Parameters are $NC = 3 \times 10^{19} \text{cm}^{-3}$, $\nu_0 = 10^{12} \text{s}^{-1}$, a has values of 1, 1.18, 1.35, 1.52 and 1.7nm (corresponding to $Nt = 10, 6.09, 4.06, 2.85$ and $2.06 \times 10^{20} \text{cm}^{-3}$), Δ has values of 1-6 KBT . α is chosen in such way that the ratio between a and α is constant for each figure, $a\alpha$ is 10 for (a), 7 for (b), 5 for (c), 3 for (d), 2 for (e) and 1 for (f).	102

Figure 4.3 (a) Seebeck coefficient and (b) power factor as a function of electrical conductivity for varying DOS widths (indicated by color) and localization lengths (indicated by symbol). Here $N_C=3\times 10^{19} \text{ cm}^{-3}$, $v_0=10^{12} \text{ s}^{-1}$, α has values of 1, 1.18, 1.35, 1.52 and 1.7 nm (correspondent to $N_t=10, 6.09, 4.06, 2.85$ and $2.06 \times 10^{20} \text{ cm}^{-3}$), Δ has values of 1-6 $K_B T$ and α values of 1, 1.18, 1.35, 1.52, and 1.7 Å. For each point, the intrinsic length is chosen so $\alpha\alpha=10$. (c) Schematic illustration comparing average transport energy of two DOS distributions with the same α but different DOS widths. (d) Schematic illustrating how α affects the average transport energy. 103

Figure 4.4 Fermi energy as a function of polymer concentration for added polymer with the same, narrower and broader DOS width at 0.15 and 0.3 eV offset. The Fermi energy of pure polymer A is set to be zero. Fitting parameters are $N_{t,A}=N_{t,B}= 1\times 10^{21} \text{ cm}^{-3}$, $\Delta_A=2.5 K_B T$, $\Delta_B=1.5, 2.5$ and $6 K_B T$, $\Delta E_0=0.15$ and 0.3 eV , $T=300 \text{ K}$ and $N_C=3\times 10^{19} \text{ cm}^{-3}$ 108

Figure 4.5 DOS of two polymer blends with varying compositions. In (a) the polymer with its DOS centered at higher energies has a broader DOS than the polymer with its DOS centered at lower energies and in (b) the polymer with the higher energy DOS has a narrower DOS. In both cases the DOS distributions of the polymers display a 0.15 eV energy offset..... 109

Figure 4.6 (a) Seebeck coefficient, (b) electrical conductivity and (c) power factor of polymer blend systems. Polymer A has fitting parameters of $\alpha_A=2 \text{ Å}$, $N_{t,A}= 6.1\times 10^{20} \text{ cm}^{-3}$, $\Delta_A=2.5 K_B T$ and $E_{0,A}=0 \text{ eV}$ and polymer B has fit parameters of $\alpha_B=1, 4$ and 5 Å , $N_{t,B}= 6.1\times 10^{20} \text{ cm}^{-3}$, $\Delta_B=1, 2.5$ and $6 K_B T$ and $E_{0,B}=0.15 \text{ eV}$ ($\Delta E_0=0.15 \text{ eV}$). Other fit parameters are $v_0=10^{12} \text{ s}^{-1}$, $T=300 \text{ K}$ and $N_C=3\times 10^{19} \text{ cm}^{-3}$ 110

Figure 4.7 Transport energy in polymer blends with varying compositions. In (a) the polymer with its DOS centered at higher energies has a broader DOS ($\Delta_B=6 K_B T$) than the polymer with its DOS centered at lower energies and in (b) the polymer with the higher energy DOS has a narrower DOS ($\Delta_B=1.5 K_B T$). In both cases the DOS distributions of the polymers display a 0.15 eV energy offset. To calculate transport energy from equation 9, Polymer A parameters are $\alpha_A=2 \text{ Å}$, $N_{t,A}= 6.1\times 10^{20} \text{ cm}^{-3}$, $\Delta_A=2.5 K_B T$ and $E_{0,A}=0 \text{ eV}$ and parameters for Polymer B are $N_{t,B}= 6.1\times 10^{20} \text{ cm}^{-3}$, $\alpha_B=1 \text{ Å}$ (Dashed green line) and 5 Å (Dashed orange line) and $E_{0,B}=0.15 \text{ eV}$ ($\Delta E_0=0.15 \text{ eV}$) and the common parameters are $v_0=10^{12} \text{ s}^{-1}$, $T=300 \text{ K}$ and $N_C=3\times 10^{19} \text{ cm}^{-3}$ 112

Figure 4.8 (a,b) Seebeck coefficient, (c,d) electrical conductivity, and (e,f) power factor calculated for polymer blends. Polymer A fitting parameters are $\alpha_A=2 \text{ Å}$, $N_{t,A}= 6.1\times 10^{20} \text{ cm}^{-3}$, $\Delta_A=2.5 K_B T$ and $E_{0,A}=0 \text{ eV}$. Each column has a different DOS width for polymer B, $\Delta_B=1.5 K_B T$ (a,c,e), and $\Delta_B=6 K_B T$ (c,d,f). The other parameters for polymer B are $N_{t,B}= 6.1\times 10^{20} \text{ cm}^{-3}$ and $E_{0,B}=0.15 \text{ eV}$ ($\Delta E_0=0.15 \text{ eV}$) and the common parameters are $v_0=10^{12} \text{ s}^{-1}$, $T=300 \text{ K}$ and $N_C=3\times 10^{19} \text{ cm}^{-3}$. The results for $\Delta_B=2.5 K_B T$ can be found in Figure 4.9. Dashed lines correspond to the data presented in Figure 3. One data line for $\Delta_B=6 K_B T$ was less than 10^{-3} , which is out of the range shown in the heat map. 115

Figure 4.9 (a) Seebeck coefficient, (b) electrical conductivity, and (c) power factor calculated for polymer blends. Polymer A fitting parameters are $\alpha_A=2 \text{ Å}$, $N_{t,A}= 6.1\times 10^{20} \text{ cm}^{-3}$, $\Delta_A=2.5 K_B T$ and $E_{0,A}=0 \text{ eV}$ and fitting parameters for Polymer B are $N_{t,B}= 6.1\times 10^{20} \text{ cm}^{-3}$, $\Delta_B=2.5 K_B T$ and $E_{0,B}=0.15 \text{ eV}$ ($\Delta E_0=0.15 \text{ eV}$) and the common parameters are $v_0=10^{12} \text{ s}^{-1}$, $T=300 \text{ K}$ and $N_C=3\times 10^{19} \text{ cm}^{-3}$. Dashed lines correspond to calculations from Fig3. One data line was less than 10^{-3} , so it has been cut from the heat map. 116

Figure 4.10 (a,b) Seebeck coefficient, (c,d) electrical conductivity and (e,f) power factor of polymer blend systems calculated as described in the paper (a,c,e) and calculated based on an effective α as described in the SI (b,d,f). Polymer A has fitting parameters of $\alpha_A=2$ Å, $N_{t,A}=6.1 \times 10^{20}$ cm⁻³, $\Delta_A=2.5$ K_BT and $E_{0,A}=0$ eV and polymer B has fitting parameters of $\alpha_A=1,4$ and 5 Å, $N_{t,B}=6.1 \times 10^{20}$ cm⁻³, $\Delta_A=1, 2.5$ and 6 K_BT and $E_{0,B}=0.15$ eV ($\Delta E_0=0.15$ eV). Other fit parameters are $v_0=10^{12}$ s⁻¹, $T=300$ K and $N_C=3 \times 10^{19}$ cm⁻³. 120

Figure 4.11 (a, b, c) Seebeck coefficient, (d, e, f) electrical conductivity and (g, h, i) power factor of polymer blend systems. Each column presents slight variations in parameters where power factor improvements in the blends are expected. In figures a, b, d, e, g and h polymer A has fitting parameters of $\alpha_A=2$ Å, $N_{t,A}=6.1 \times 10^{20}$ cm⁻³, $\Delta_A=2.5$ K_BT and $E_{0,A}=0$ eV and figures c, f and i all parameters for polymer A are same except for localization length which the value is $\alpha_A=3$ Å. Polymer B has fit parameters of $\alpha_A=1,4$ and 5 Å, $N_{t,B}=6.1 \times 10^{20}$ cm⁻³, $\Delta_A=1, 2.5$ and 6 K_BT (6 K_BT for figure a, d and g) and $E_{0,B}=0.15$ eV ($\Delta E_0=0.15$ eV, for figure b, e and h the value is $\Delta E_0=0.1$ eV). Other fit parameters are $v_0=10^{12}$ s⁻¹, $T=300$ K and $N_C=3 \times 10^{19}$ cm⁻³. 122

Figure 4.12 (a) Molecular structure of polymers and dopant, RR-P3HT, RRA-P3HT, PDPP-4T, PDPP-T-TT-T and Mo(tfd)₃. (b) Ionization energy (IE) of polymers and electron affinity (EA) of dopant¹⁷⁷. Normalized (c) secondary cutoff and (d) HOMO onset regions of undoped polymers measured by ultraviolet photoemission spectroscopy (UPS)..... 124

Figure 4.13 (a,c,e) Seebeck coefficient and electrical conductivity and (b,d,f) power factor as a function of PDPP-4T concentration in polymer blend. The blends are PDPP-4T:RR-P3HT (a,b) and PDPP-4T:RRA:P3HT (c,d) and PDPP-4T:PDPP-T-TT-T (e,f). Dashed lines are the fits to the model as calculated with Equations (4.16) and (4.17). The fitting parameters can be found in Table 4.1. 125

Figure 4.14 (a,c,e) Seebeck coefficient and electrical conductivity and (b,d,f) power factor as a function of PDPP-4T concentration in the polymer blend. The blends are PDPP-4T:RR-P3HT (a,b) and PDPP-4T:RRA:P3HT (c,d) and PDPP-4T:PDPP-T-TT-T (e,f). Darker dashed lines with shorter dashes are the fits to the model as calculated with Equations (4.16) and (4.17) and lighter dashed lines with longer dashes are the fits to the model accounting for effective localization length. The fitting parameters can be found in Table 4.1. 130

Figure 4.15 (a) Seebeck coefficient and electrical conductivity and (b) power factor as a function of PDPP-4T concentration in the PDPP-4T:RR-P3HT blend when E_0 is reduced from 0.15 eV (see Figure 4.14) to 0.10 eV. Dashed lines are the fits to the model as calculated with accounting for effective localization length with the fitting parameters listed in Table 4.1, except here $E_0=0.1$ eV..... 130

Figure 4.16 (a) PDS spectrum of all undoped polymers on a logarithmic scale and their Urbach energies extracted from $Abs = a0eE - EgEu$ ($E < E_g$). (b) PDS (dashed) and UV-Vis (solid line) spectrum of undoped polymers which shows the agreement between two measurements. The dip in absorbance at the absorbance edge is due to polymer photoluminescence..... 132

Figure 4.17 AFM on polymer blend system of RR-P3HT:PDPP:4T (a-f), RRA-P3HT:PDPP-4T (g-l) and PDPP-T-TT-T:PDPP-4T (m-r). Concentration of PDPP-4T in blend system is shown at top each column. Figures g, h and i have different scale which are separated by the red box..... 136

Figure 5.1 Chemical structure of RR-P3HT, RRa-P3HT and PDPP-4T with their IE and hole mobility.	142
Figure 5.2 (a) Schematics of OECT device. (b) Chemical structure of PIL. (c-h) Chemical structure of anions and their radii, Cl^- , BF_4^- , PF_6^- , BPh_4^- , $\text{B}(\text{PhF})_4^-$, $\text{B}(\text{PhCl})_4^-$, $\text{B}(\text{PhMe})_4^-$, $\text{B}(\text{PhF}_5)_4^-$ and $\text{B}(\text{Ph}(\text{CF}_3)_2)_4^-$	143
Figure 5.3 Absorbance spectroelectrochemistry of RRa-P3HT with different anions, (a) Cl^- , (b) BF_4^- , (c) PF_6^- , (d) BPh_4^- and (e) $\text{B}(\text{Ph}(\text{CF}_3)_2)_4^-$. Each color represents a different applied potential with respect to reference electrode, Ag/Ag^+ . The dashed lines are showing the part of data that has been cut out because of high absorbance of acetonitrile in those regions.	145
Figure 5.4 Absorbance spectroelectrochemistry of RR-P3HT with different anions, (a) Cl^- , (b) BF_4^- , (c) PF_6^- , (d) BPh_4^- and (e) $\text{B}(\text{Ph}(\text{CF}_3)_2)_4^-$. Each color represents a different applied potential with respect to reference electrode, Ag/Ag^+ . The dashed lines are showing the part of data that has been cut out because of high absorbance of acetonitrile in those regions.	148
Figure 5.5 Applied potential (vs Ag/Ag^+) vs polaron to neutral peak of polymer for (a) RRa-P3HT and (b) RR-P3HT for 5 anion, Cl^- , BF_4^- , PF_6^- , BPh_4^- and $\text{B}(\text{Ph}(\text{CF}_3)_2)_4^-$	148
Figure 5.6 Absorbance spectroelectrochemistry of polaron absorbance region of (a,b) RRa-P3HT and (c,d) RR-P3TH vs photon energy. (a,c) Showing the polaron absorbance for concnetrioan of polaron to P3HT neutral peak around 0.1 and (b,d) concentraion of 1. In both polymer Cl^- and BPh_4^- couldn't reach concnetraion of 1 even at 1200 mV.	149
Figure 5.7 Absorbance spectroelectrochemistry of (a) RR-P3HT and (b) neutral peak of P3HT absorbance region at 500 mV applied potential with respect to Ag/Ag^+	150

CHAPTER 1. INTRODUCTION TO ORGANIC SEMICODUCTOR

1.1 Brief History and Recent Applications

Studies on electrically conductive organic materials started as early as the 1840s by scientists such as F.F. Runge, C.J. Fritzsche, W. H. Perkin, F. Beissenhirtz^{1,2} working on aniline compounds (such as aniline purple and aniline blue) that led to a discovery in 1862 by Henry Letheby who showed an organic compound (molecules based on carbon and hydrogen bonds), polyaniline prepared by anodic oxidation of aniline, can show electrical conductivity.³ In work done in the 1960s by Kallmann and Pope, anthracene crystals showed current flow by injection of charge carriers with a biased electrode.^{4,5} The need to inject charge carriers is due to the nature of semiconductors in that they are intrinsically electrical insulators and extra charge carriers are needed for them to become electrically conductive. A decade later, in the 1970s, works led by three scientists, Alan J. Heeger, Alan G. MacDiarmid and Hideki Shirakawa showed that doped polyacetylene can become electrically conductive (conductivity over 100 S/cm), which led to them winning the Nobel Prize in chemistry in 2000 "for the discovery and development of conductive polymers."⁶⁻⁹ Although the electrical conductivity of these newly founded materials were much smaller than many metals (10^5 S/cm), this is the beginning to show that organic materials and particularly polymers can be electrically conductive, which opened up a new field of study with interesting and important applications, such as the prevalence of organic light emitting diodes in smart phones and televisions.

With the discovery of electrically conductive polymers, organic semiconductors (OSCs) started to gain the attention of many researchers around the world. In the beginning these materials demonstrated poor stability and performance in various devices, such as

photovoltaics, transistors, and light emitting diodes due to low electrical conductivity (or mobility) or high density of defects. After a few decades of work focused largely on synthesizing and processing new materials, mainly consisting of thiophenes, in the 1990s the performance of OSC materials reached a level where they could be used in electronic devices.¹⁰ Nowadays, we can see OSCs are used next to inorganic materials to improve the performance and reduce the cost of many devices and in some devices the OSCs play the main role. The most common application of OSCs in our daily lives is organic light-emitting diodes (OLED), with the first practical device with brightness over 1000 cd/m² and luminous efficiency of 1.5 lm/W with driving voltage below 10 V was made in 1987.¹¹ The next application of OSCs is found in organic field effect transistors (OFET), when H. Koezuka, A. Tsumura and T. Ando, researchers from Mitsubishi Electric, showed that a polythiophene material can show a source-drain current that increases by a factor of 10²-10³ upon application of a gate voltage.^{12,13} Nowadays we can see OSCs in our displays, sensors (OFET and organic biosensors) and many other emerging applications (e.g., printable solar cells).^{14,15} Organic solar cells, or organic photovoltaics (OPVs), started with a low power conversion efficiency (PCE), less than 1%, from the works done in 1986 by C. W. Tang on copper phthalocyanine and a perylene tetracarboxylic derivative,¹⁶ in 1991 by M. Hiramoto on three-layered OPVs using a perylene tetracarboxylic derivative and metal-free phthalocyanine,¹⁷ and in 1992 by N. S. Sariciftci on a polymer bulk-heterojunction cell composed of Buckminsterfullerene and poly[2-methoxy-5-(2-ethylhexyloxy)-1,4-phenylenevinylene],¹⁸ to recently where they have shown a great improvement in PCE up to 17.5% from Ulsan National Institute of Science and Technology.¹⁹⁻²¹ OPVs now show performance that is approaching that of silicon based

solar cells, and many companies including Epishine Co., OPVIUS GmbH, infinityPV, Raynergy Tek, Heliatek, Phillips 66 and others have started working on mass production of OPV panels through vapor or solution deposition.^{22,23} One of the most recent applications of OSCs is in organic electrochemical transistors (OECTs) for sensors, and especially bio-sensors where organic materials are often less harmful for living organisms.²⁴⁻²⁶ Organic thermoelectric generators (OTEGs), where a temperature difference is converted to electricity (and vice versa) is a fairly new application of OSCs that has received the attention of many researchers and recently shown a significant performance improvement.²⁷⁻²⁹ Most of this new progress and studies on OSCs are due to their unique properties such as mechanical flexibility and the ease and low-cost fabrication process. Another very interesting property of OSCs is their tunability of properties by a simple change in chemical structure, which is often not possible in inorganic materials. Although these are great advantages for OSCs, they still lack efficiency, stability, and the solid understanding of charge transport and electronic properties that exists for many inorganic semiconductors.

1.2 General Chemistry and Physics of Organic Semiconductors

1.2.1 Materials; sp, sp² and sp³ orbitals and conjugation of orbitals

Organic semiconductors are mainly composed of carbon-carbon and carbon-hydrogen bonds and sometimes mixed with heteroatoms such as sulfur, oxygen, and nitrogen. Carbon's (C) atomic number is 6, with 6 neutrons and 6 protons in its nucleus and 6 electrons in its orbitals for its neutral state. In the periodic table, C is in Group 14 with other well-known elements in the world of electronics, including silicon (Si),

germanium (Ge), tin (Sn) and lead (Pb). A carbon atom by itself has 4 electrons in its valence shell with a $2s^2 2p^2$ (or $2s^2 2p_x^1 2p_y^1$) electronic configuration shown in Figure 1.1 (a) and the shapes of these orbitals are shown in Figure 1.1 (b). ACD/ChemSketch from Advanced Chemistry Development, Inc. was used to draw the orbitals.³⁰ In methane, CH_4 , one C atom is bonded to 4 hydrogen (H) atoms. This covalent bond between C and H causes hybridization of orbitals or, in other words, it causes the orbitals to mix. If we denote the wavefunction of each orbital in the 2^{nd} shell in a C atom with ψ_s , ψ_{p_x} , ψ_{p_y} and ψ_{p_z} , the new four wave functions representing orbitals can be shown as below:

$$\psi_{sp_1^3} = \frac{1}{2} (\psi_s + \psi_{p_x} + \psi_{p_y} + \psi_{p_z}) \quad (1.1)$$

$$\psi_{sp_2^3} = \frac{1}{2} (\psi_s + \psi_{p_x} - \psi_{p_y} - \psi_{p_z}) \quad (1.2)$$

$$\psi_{sp_3^3} = \frac{1}{2} (\psi_s - \psi_{p_x} + \psi_{p_y} - \psi_{p_z}) \quad (1.3)$$

$$\psi_{sp_4^3} = \frac{1}{2} (\psi_s - \psi_{p_x} - \psi_{p_y} + \psi_{p_z}) \quad (1.4)$$

So, all these states are 25% s orbital and 75% p orbital. All these states are degenerate, so each orbital is going to be occupied by one electron. The new electronic configuration and orbital shape is shown in Figure 1.1 (c) and (d). These new orbitals are called sp^3 orbitals.^{31,32}

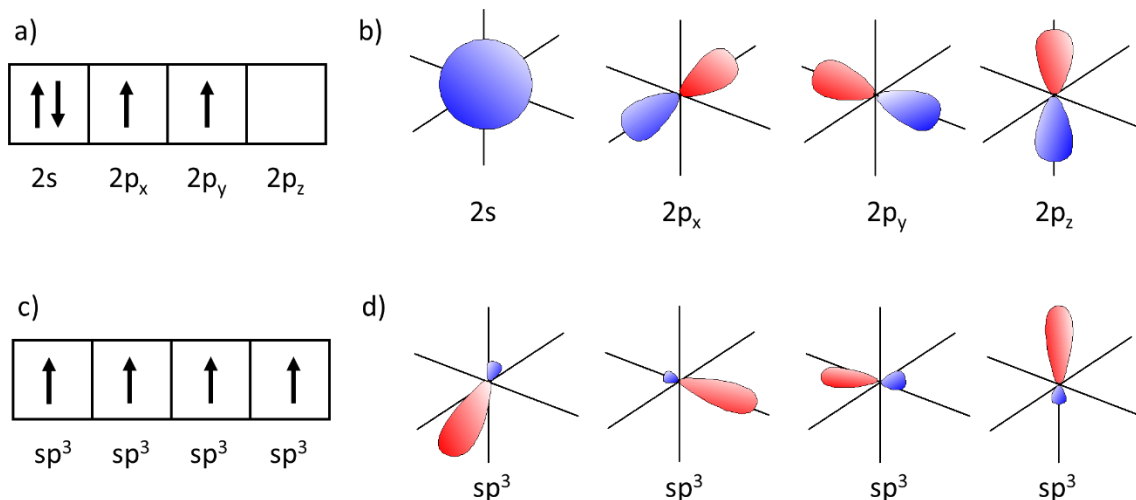


Figure 1.1 (a) Electron configuration of a C atom. (b) Shape of s and p electronic orbitals. Colors show the phase of the wave function. (c) Electronic configuration of C atom in CH₄. (d) shape of 4 sp³ orbital.

Now let's remove one H atom from CH₄ and replace it with another C with bonds to H to form ethane, C₂H₆. Figure 1.2 (a) is showing the schematics of forming a new molecular orbital (MO), σ bonding orbital, and σ* anti-bonding. The two vertically oriented sp³ orbitals on both C atoms in ethane are already filled with two electrons and therefore they will not form any bonds. On the other hand, when these orbitals are not filled, as in ethene, a π-bond can form between the vertically oriented orbitals of both carbons, which leads to a double bond between carbons that is 67% p orbital and 33% s orbital. The wave function for such orbitals is written as:

$$\psi_{sp_1^2} = \sqrt{\frac{1}{3}}(\psi_s + \sqrt{2}\psi_{p_x}) \quad (1.5)$$

$$\psi_{sp_2^2} = \sqrt{\frac{1}{3}}\left(\psi_s - \sqrt{\frac{1}{2}}\psi_{p_x} + \sqrt{\frac{3}{2}}\psi_{p_y}\right) \quad (1.6)$$

$$\psi_{sp_3^2} = \sqrt{\frac{1}{3}} \left(\psi_s - \sqrt{\frac{1}{2}} \psi_{p_x} - \sqrt{\frac{3}{2}} \psi_{p_y} \right) \quad (1.7)$$

This new hybridization is termed sp^2 and is made from mixture of two p orbitals and one s orbital with leaving one p orbital free for each carbon atom. In this case each H atom forms a bond with one sp^2 orbital and carbons form one σ bond with each other through sp^2 orbitals and another with the remaining p orbital, creating new MOs, π bonding and π^* anti-bonding. The schematics of bonds are shown in Figure 1.2 (b). In case of ethyne (acetylene), C_2H_2 , where C atoms are bonded with a triple bond, s and p hybridization lead to a sp hybridization with wave functions shown below which is now 50% p orbital and 50% s orbital:

$$\psi_{sp_1} = \sqrt{\frac{1}{2}} (\psi_s + \psi_{p_x}) \quad (1.8)$$

$$\psi_{sp_2} = \sqrt{\frac{1}{2}} (\psi_s - \psi_{p_x}) \quad (1.9)$$

In this case, there will be two p orbitals left for each C atoms to form π bonds.

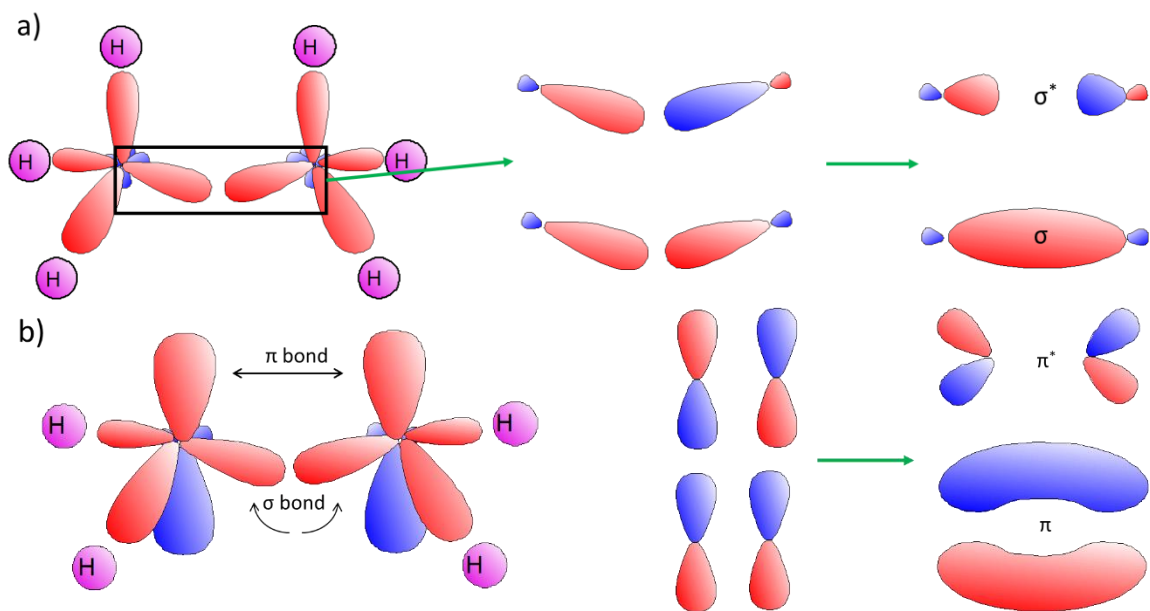


Figure 1.2 (a) showing overlap of two sp^3 orbitals forming a σ orbitals and σ^* anti-bonding orbitals. (b) showing overlap of two sp^2 orbitals forming a π orbitals which form a π bonding and π^* anti-bonding.

This p-orbital overlap can be extended by having more carbons in a chain. Structure of 1,3-Butadiene, C_4H_6 and its π bonding and anti-bonding orbitals are shown in Figure 1.3 (a). In case all the p orbitals have the same phase, the formed π orbital is going to be delocalized over all 4 C atoms. This large delocalization of π orbitals is the reason that OSCs are good electrically conductive material. Similar delocalization of π orbitals can happen in a ring of six C atoms. As shown in Figure 1.3, benzene (C_6H_6) forms a larger (delocalized) π orbital. Adding other electron withdrawing components such as thiophene rings, can further extend the delocalization of π -orbitals, or even more extended conjugation of π orbitals can be formed by polymerizing these molecules (e.g., polythiophene). Polymers are large molecules that are composed of small repeating units (monomers).

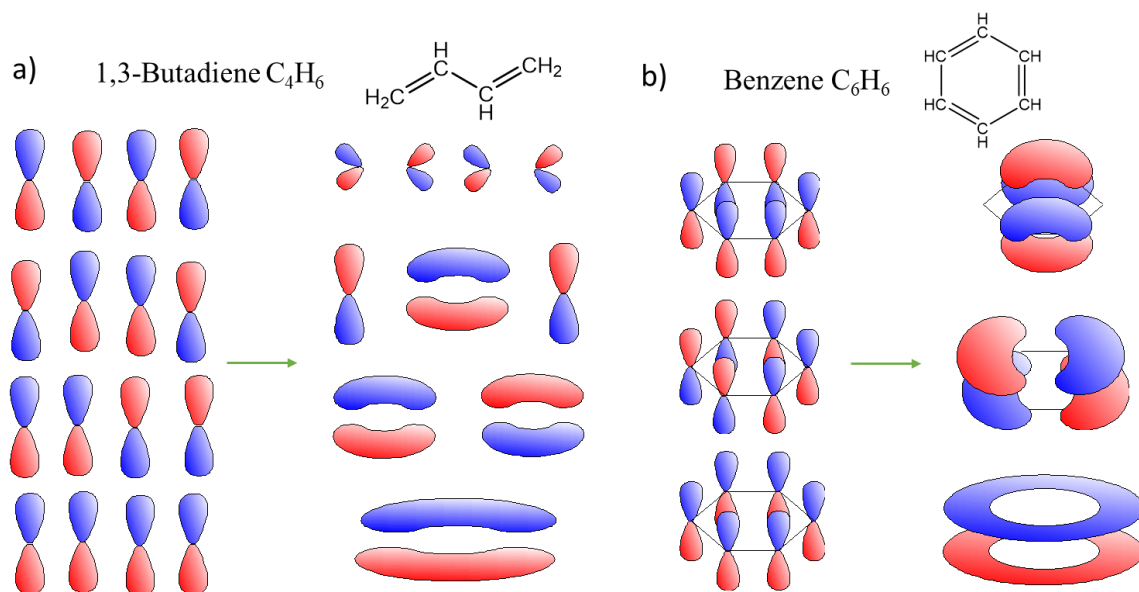


Figure 1.3 Chemical structure and MO of (a) 1,3-Butadiene and (b) benzene. For Benzene only bonding MOs are shown.

1.2.2 Energetics of Organic Semiconductors

In this section we discuss the energetics of OSCs. Starting from the outermost shell of a single C atom, orbital s is filled, and orbital p is occupied by two electrons. The energy diagram of s and p orbitals of the second shell in a C atom is shown in Figure 1.4 (a). C orbitals can go through s-p hybridization. The energy diagram of sp^3 , sp^2 and sp orbitals is shown in Figure 1.4 (b-d).

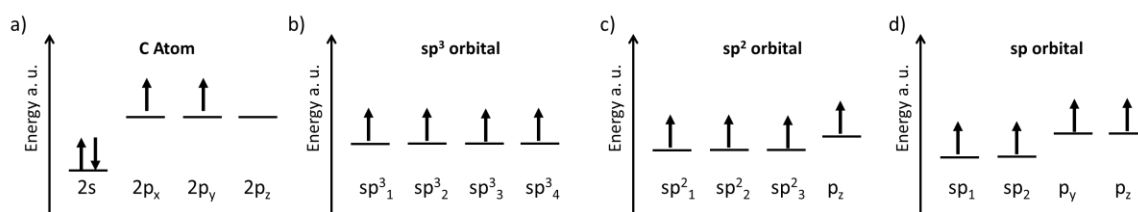


Figure 1.4. energy diagram of (a) s and p orbitals, (b) sp^3 , (c) sp^2 and (d) sp orbitals.

In methane, overlap of sp^3 orbitals from the C atom with s orbitals from H atoms form σ and σ^* bonds. The energy diagram of such bonds is shown in Figure 1.5 (a). The energy of states in new MO of methane is lower than each sp^3 orbital in C atom and s orbital in H atom so electrons first fill the σ MO and leave the σ^* empty. In ethene with a double bond for C atoms, one sp^2 and one p orbital from each C atom are overlapping to form the bonds between them. As discussed, there will be σ , σ^* , π and π^* orbitals form between the two carbon atoms. The energetics of these bonds are shown in Figure 1.5 (b). These details of energetic diagrams with more accurate energetic states can be found elsewhere.³³ Ethyne with a triple bond between carbons will have a similar situation as shown in Figure 1.5 (c).

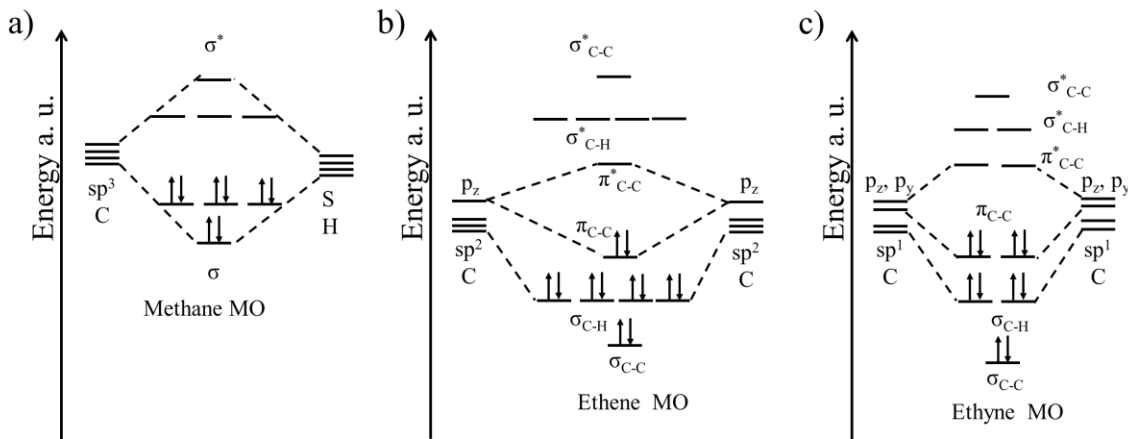


Figure 1.5 Energetic diagram of σ , σ^* , π and π^* orbitals in (a) methane, (b) ethane and (c) ethyne. The accurate energetics can be found elsewhere.³³

All these MO energy diagrams have some properties in common, which are (1) π MO is the highest occupied state energy, (2) π^* is the lowest unoccupied state. These states are especially important in electronics as electrons (or holes) in these states are weakly bound and can move in the material easier than other more-strongly bound electrons. These

MOs are called the highest occupied molecular orbital (HOMO) and lowest unoccupied molecular orbital (LUMO). There are a few other important parameters that we should define here. Vacuum level energy (E_{vac}) is energy level of an electron positioned out of film at rest with zero kinetic energy. The minimum energy required to remove one electron from the molecule or solid film to vacuum is the ionization energy (IE). Based on Koopman's theorem under closed-shell Hartree–Fock calculations,³⁴ the IE is the difference between the energy of HOMO and E_{vac} (with assuming nuclear relaxation is negligible). Koopmans' theorem is an approximation because the correct definition of the ionization energy is the difference between the total energies of the N-1 electron and N electron states. The minimum energy gained by adding an electron to a molecule or solid film is defined as the electron affinity (EA) and is the difference between the energy of the LUMO and E_{vac} (assuming nuclear relaxation is negligible).^{35–37} Schematics of these energetics are shown in Figure 1.6 (a). In electronics we mostly deal with solid state materials where many molecules are near each other and they will feel each other's electric fields. Going from gaseous state to solid state the IE reduces and EA increases by some energy, which is called the polarization energy.^{33,38} The schematics of gas to solid transition is shown in Figure 1.6 (a) and (b). By forming a solid, three more parameters become crucial. As electrons are fermions and obey Fermi-Dirac statistics, the Fermi energy (E_{F}) is defined as the energy at which the probability of finding an electron is 50%. Work function (WF) is defined as the energy required to remove one electron from the Fermi energy out to vacuum, i.e., the WF is the difference between E_{vac} and E_{F} . The energy difference between HOMO and LUMO is called the transport gap energy (E_{tg}). It is

important to mention the equivalent name for HOMO and LUMO in crystalline materials is valence band and conduction band.

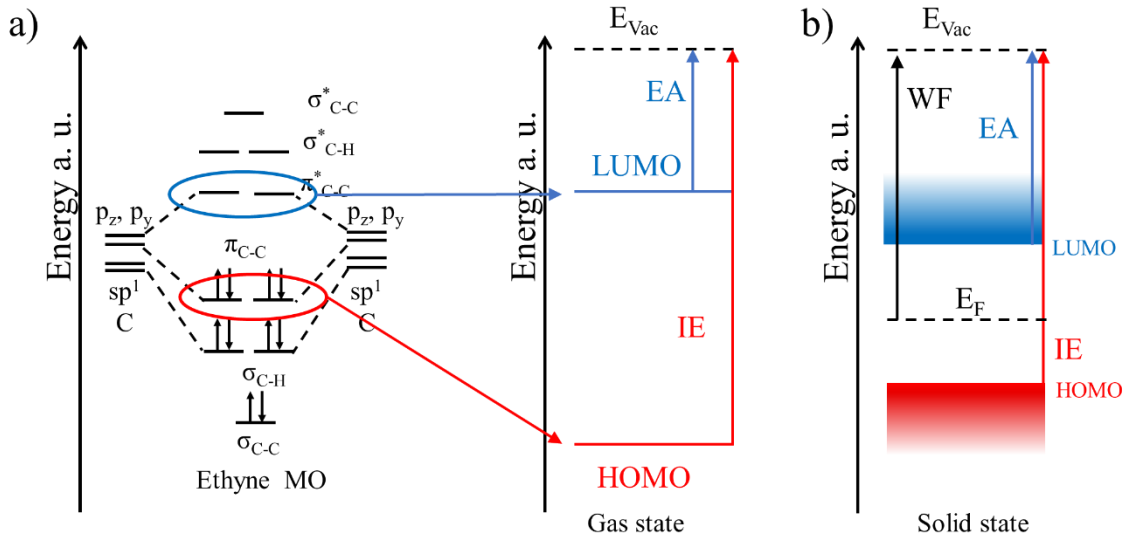


Figure 1.6 Shows schematic of energy diagram of an organic semiconductor if (a) gas phase and (b) in solid state

1.2.3 Charge Carrier Injection

In OSCs, E_{tg} is usually less than 4 eV and greater than 1 eV which still makes it an insulator at room temperature. The reason is, as shown in Figure 1.6 (b), electrons fully occupy the states at lower energy. For the charge carrier to jump to another state and thereby conduct charge, the targeted state should be unoccupied, but the unoccupied states are now at energies above E_{tg} . So, although the occupied and unoccupied states are spatially on top of each other, they are at different energies. The energy gap is large enough that the charge carrier cannot jump to the unoccupied states. For these materials to conduct electricity, there is a need to add electrons to unoccupied states or remove electrons from (add holes to) occupied states. These extra charge carriers can be introduced by various

methods, but here we focus on three different charge-carrier creation methods. The first method is by shining light to excite an electron from HOMO to LUMO, as shown in Figure 1.7 (a). In this method, the electron excited to the unoccupied state acts as a charge carrier that can easily move between other unoccupied states around it; although, this excited electron can also relax back to its ground state in the HOMO because of the columbic attraction to the hole it left in the occupied states distribution. For these systems, by having other materials with appropriate energetic alignment around this light absorbing organic semiconductor the electron and hole may separate and get apart from each other to the desired electrodes. This mechanism will be discussed in more details in Chapter 3. In the second method, which is referred to as chemical doping, another molecule is added to the semiconductor that accepts (or donates) an electron from the semiconductor and leaves a hole (or an electron) as a charge carrier. In most cases, removing an electron from the semiconductor requires that the dopant's EA is larger than the organic semiconductor's IE, while adding an electron requires that the dopant's IE is smaller than the organic semiconductor's EA, as shown in Figure 1.7 (b) and (c). In this doping process the DOS changes and new states are introduced within the gap, which reduces E_{tg} and in some cases the gap completely closes.³⁹ This method and these new states in the band gap is going to be discussed in detail in Chapter 4 and 5. The other method of charge-carrier introduction, which is the basis of OFETs, is by inducing charge carriers into the channel or active area of device by applying a bias to a gate electrode, similar to a capacitor. The applied electric field at the gate, causes the fermi energy to shift towards HOMO (or LUMO) in thin film and so inject holes (or electrons) into the film. In some other device structures, like OEETs, similar to OFETs by applying a bias to the gate electrode the charge carrier are induced

into the channel, but another molecule (counter ion) is also injected into the channel to balance the charges. This effectively increases the capacitance effect and reduces the applied bias voltage to the gate electrode. This method will be discussed in more detail in chapter 5.

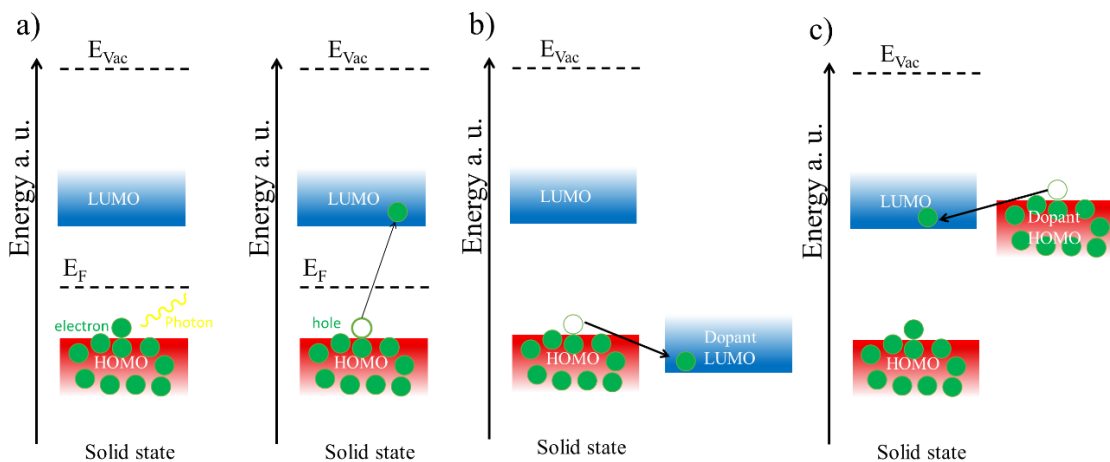


Figure 1.7 (a) Schematic of charge injection by photon absorbance. (b) and (c) Show charge injection by chemical doping. (b) is p-doped and (c) is n-doped.

1.3 Charge Transport in Organic Semiconductors

Charge transport in OSCs is usually described as occurring through hopping between localized sites. The reason for the hopping behavior is that charge carriers are mostly localized on their states and the amount of wave function overlap between the states and their energetic differences mostly determine their hopping rate. There are two theories that are commonly used to describe the charge transport and hopping rate (ν) in OSCs. First is the Miller-Abrahams model and the second is based on Marcus theory, as shown below.^{32,40–42}

$$v_{MA} = \begin{cases} v_0 e^{-\frac{r_{ij}}{\alpha}} & E_j \leq E_i \\ v_0 e^{-\frac{r_{ij}}{\alpha} - \frac{E_j - E_i}{K_B T}} & E_j > E_i \end{cases} \quad (1.10)$$

$$v_{Marcus} = \frac{J_0^2}{\hbar} \sqrt{\frac{1}{4\pi\lambda K_B T}} e^{-\frac{r_{ij}}{\alpha}} e^{\left[-\frac{(E_j - E_i + \lambda)^2}{4\lambda K_B T}\right]} \quad (1.11)$$

v_0 is a prefactor with units of 1/s that partially includes the strength of wavefunction overlap, r_{ij} is the distance between initial site i with energy E_i , and final site j with energy E_j , α is the localization length, which is an indication for amount of wave function size and overlap between two sites, J_0 is transfer integral connecting sites i and j , λ is relaxation energy, K_B is Boltzmann constant and T is absolute temperature. The most accurate charge transport modeling involves heavy simulation of large section of materials which is both expensive and time consuming. In these simulations, to have an accurate prediction of electronic properties, the defined system of states should have as large as possible number of sites, over 1000 sites.⁴³⁻⁴⁶ Meanwhile these sites should be a good representation of the actual organic molecule. These complicated codes for simulating a dynamic system with a large number of sites may takes days to be processed and yet the codes still need more optimization and experimental data to correct for a certain parameter.^{44,47,48} The attempts to model the charge transport in OSCs with analytical equations also faces many problems such as the difficulty in modeling connectivity between crystalline and amorphous regions, various effects of dopants on charge transport such as aggregation, doping efficiency, coulombic interaction between dopant and OSC and morphologic effects of dopant on the film. Also, some studies show, π -conjugated polymers can show band type behavior or a combination of band type and hopping type behaviors which makes it more difficult to

model these transitions without modifying the models to account for morphology. We will discuss the charge transport in more details in chapter 4.

1.4 Dissertation Structure

1.4.1 Chapter 2: Instrumental Setups and Methods of Measurements

Chapter 2 is focused on the instruments. This includes the LabVIEW codes, details of hardware setup that was designed in this lab, calibration methods and finally the process of using them. This chapter also includes details for sample preparations used in the dissertation and other instrument details that were used to take measurements. This chapter consists of two main parts; first is OPV related instrumentation and the second is TE related instruments.

Photoemission spectroscopy instrumentation and analysis is explained and then inverse photoemission spectroscopy (IPES) is explained in more detail, which mostly focuses on LabVIEW codes and instrument connections. Next the LabVIEW codes for characterizing OPV performance under solar simulated irradiation is discussed. Later, setup for measuring external quantum efficiency is explained in detail including each part of the instrument. It follows by LabVIEW code and calibration data. Next, sample preparation and measurements of UV-Vis absorbance, Grazing Incidence Wide-Angle X-ray Scattering (GIWAXS) setup is explained briefly. Finally, device fabrication for OPV devices is discussed.

In the second part, instrumentation for measuring Seebeck coefficients and electrical conductivity is discussed, followed by the setup for measuring TE properties in OECTs. This part includes the schematics of design, calibrations, and LabVIEW codes.

Raman spectroscopy, UV-Vis-NIR and FTIR spectroscopy and film fabrication is explained after.

1.4.2 Chapter 3: Effect of Donor Halogenation on Interfacial Energetics and Charge Transfer State Energies in Model OPVs

In this chapter the effect of halogenation on interface energetics at donor-acceptor heterojunctions in OPVs is investigated.⁴⁹ Halogenation and in particular fluorination, is a commonly used method to manipulate the energetics, stability, and morphology of OSCs. In OPVs, fluorination of electron donor molecules or polymers at appropriate positions has led to improved performance and stability. In this chapter ultraviolet photoemission spectroscopy, EQE measurements of charge-transfer (CT) states, and density functional theory calculations are applied to systematically investigate the effects of halogenation on the bulk solid-state energetics of model anthradithiophene (ADT) materials, their interfacial energetics with C₆₀ (acceptor), and the energetics of various ADT:C₆₀ blend compositions. To probe the effect of blend concentration on the morphology of the films we conducted GIWAXS on all blend compositions. For the ADT:C₆₀ blends, the GIWAXS and UPS data lead us to conclude that halogenated ADT derivatives tend to form crystalline aggregates within C₆₀ at even relatively low concentrations, or in other words halogenation leads to less miscibility with C₆₀. We show that non-halogenated ADT molecules show higher energy CT states in blends with C₆₀ and lower energy CT states in the ADT/C₆₀ bilayers. However, this trend is reversed in the halogenated ADT/C₆₀ systems, wherein the CT state energies of ADT:C₆₀ blends are lower than those in the bilayers. In bulk-heterojunction photovoltaics, the lower energy CT states present in the mixed phase with the halogenated ADT derivatives will likely decrease the probability of charge separation

and increase charge recombination. The less favorable energy landscapes observed upon halogenation suggests that the benefits of fluorination observed in many OPV material systems may be more due to morphological factors.

1.4.3 Chapter 4: Thermoelectric Power Factor Enhancement in Polymer Blend

In this chapter we mainly focus on the theoretical calculation of charge transport. We use Miller-Abrahams jump rate to model the charge-carrier mobility, electrical conductivity and Seebeck coefficient of amorphous π -conjugated polymers by modifying models developed by Arkhipov and Bässler. In this mode a gaussian distribution is assumed for DOS of the polymer where the width of gaussian distribution is representing the degree of disorder of the polymer and the area under the gaussian distribution represents the total number of states in the polymer. Here there is another parameter, localization length representing an average wavefunction overlap between the states. We first study the effect of these parameters on TE properties of a single polymer and later the effect of polymer blends on TE properties is studied by adding another gaussian density of state (DOS) next to the initial one. In these calculations the parameters related to one polymer were fixed while the parameters for the other polymer were varied. The parameters that are varied for the second polymer are width of DOS, localization length and the relative mean energy of its DOS. In all the calculations we assume a homogeneous mixture of polymers and a constant number of charge carriers at a constant temperature. With these assumptions, we show the results produced by these models suggest a power factor improvement can be realized in polymer blends. Later we experimentally probe the TE properties of some selected polymer sets chosen based on the theoretical calculations and widely varying

electronic properties of the polymers.⁵⁰ We show power factors in an appropriate polymer blend are demonstrated to exceed the power factors of the individual polymers by nearly two-fold.

1.4.4 Chapter 5: Effect of Anion Size and Fluorination on Polaron Formation, Polymer Crystallinity, and Thermoelectric Properties in Organic Electrochemical Transistors

In this chapter we focus on the thermoelectric properties of regiorandom and regioregular Poly(3-hexylthiophene) and a diketopyrrolopyrrole (DPP) based polymer in the OECT device structure. In the OECT devices the counterions from the dielectric penetrate the polymer film to balance the induced charges in the channel. By varying the chemical composition of the dielectric we vary the size of the counterions from a small anion (Cl with 1.6 Å in radius) to a much larger anion (tetrakis[3,5-bis(trifluoromethyl)phenyl]borate with 7.9 Å in radius). We first look at the spectroelectrochemistry absorbance spectra to determine how the anions penetrate the crystalline region vs the amorphous region and compare the polaron energy at different doping levels. Here we hypothesize that larger anions have smaller columbic interaction with the polaron so the polaron can be more delocalized.

1.4.5 APPENDIX 1: LabVIEW

In this section there are pictures and short explanations of the LabVIEW codes that control the instruments measuring various parameters such as solar cell characteristics, Seebeck coefficient, TE properties of OECT, and EA.

1.4.6 APPENDIX 2: Calculating Surface coverage using XPS

In this section we explain how surface coverage of surface ligands on MAPbI₃ perovskite films can be measured and calculated using XPS. Here we used a model to calculate the attenuation length of different photoelectrons of existing elements in the perovskite film and surface ligands. The attenuation length of the photoelectrons through the film are uniform, so by increasing the probing angle (with respect to the film normal) we can vary the probing depth. By comparing the results from three different angles we can estimate the surface coverage of the surface modifiers on the film.

CHAPTER 2. INSTRUMENTAL SETUPS AND METHODS OF MEASUREMENTS

2.1 Photoemission Spectroscopy

In Chapter 1 we defined the HOMO, LUMO and E_F (or IE, EA and WF) in OSCs and mentioned their importance in determining electronic transport properties of these materials. There are a few methods that can be used to measure these energetics, including photoemission spectroscopy, cyclic voltammetry, and contact potential difference measurements with Kelvin probe.^{35,36} In cyclic voltammetry the HOMO and LUMO is approximated by the oxidation and reduction potential of film with respect to a reference. Here, the HOMO and LUMO energies measured are influenced by electrolytes and the solvent they are immersed in. On the other hand, Kelvin probe measurements provide an accurate measurement of the WF, but no information about the IE or EA. In the work reported in this dissertation, ultraviolet photoemission spectroscopy (UPS) is used to measure IE and WF and inverse photoemission spectroscopy (IPES) is used to measure EA. In the following section we discuss how these instruments operate with a brief explanation of LabVIEW codes used for IPES. In the last part we introduce X-ray photoemission spectroscopy (XPS) that is used to measure the binding energies of core electrons, which are often used to determine the stoichiometry of the elements composing the material and can be used as a complimentary measurement to show the dipole moment contribution.⁵¹ More details about photoemission spectroscopy can be found elsewhere.^{52–}
⁵⁵ One matter about the notations, here WF is used to show work function, while many other references will use ϕ or Φ . We have reserved this Greek letter for future chapters.

2.1.1 Ultraviolet photoemission Spectroscopy

UPS measurements work based on a simple mechanism known as the photoelectric effect. A photon with enough energy to knock out a valence electron (usually in the vacuum ultraviolet range of 10-30 eV), is incident on the material. Upon absorbing the coming photons, some of the electrons leave the film in all angles away from the film, which are called photoelectrons. Assuming electrons are not scattered inelastically in the film, the photoelectrons' kinetic energy (KE) out of the film purely depends on their binding energy (E_{Bi}) and WF of the film and can be calculated by equation below:

$$KE = E_{Ph} - E_{Bi} - WF \quad (2.1)$$

Where E_{Ph} is energy of the photon ($E_{Ph}=h\nu$; h is Planck's constant, ν is frequency of photon). Let's start our discussion with metals. In metals, there is no band gap and some electrons are at the E_F . Electrons at E_F have zero binding energy ($E_B = 0$ eV with respect to E_F) and so photoelectron coming from states at the E_F have the maximum KE (minimum E_{Bi} corresponds to KE_{max}). For electrons at energy states below E_F , the stronger the electron is bound in the materials, the less energy the photoelectron will have. The energetic schematics of electrons and photoelectrons are shown in Figure 2.1 (a) and (b). The KE of the photoelectron is measure by an electrostatic analyzer shown in Figure 2.1 (c) and is converted to E_{Bi} using Equation (2.1) that is shown in Figure 2.1 (d). In plotting the binding energy, we use the convention that more positive E_{Bi} is plotted towards left and more negative E_{Bi} to the right and zero E_{Bi} is at E_F .

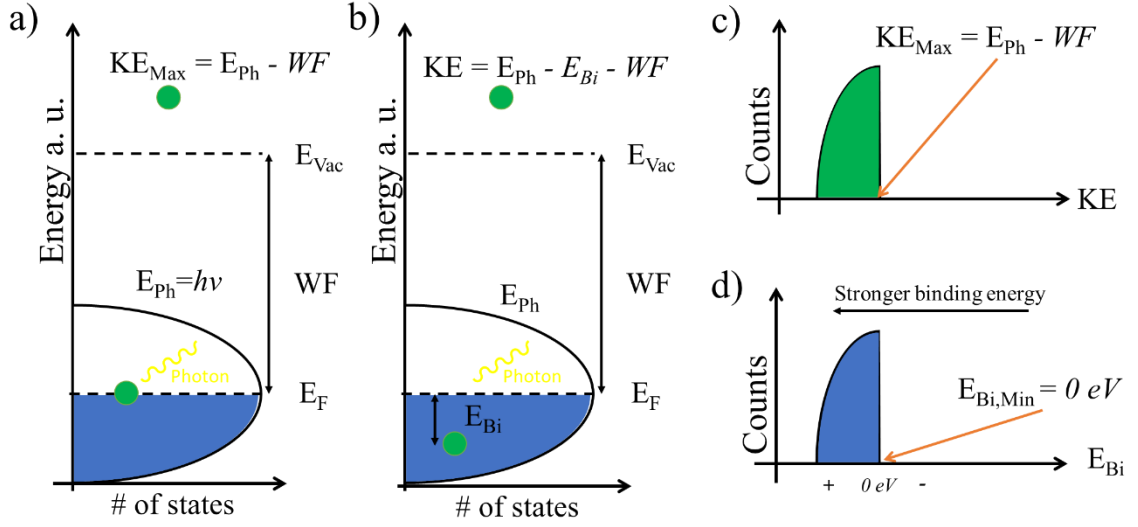


Figure 2.1 Energetic schematics of electrons and photoelectrons in/from a metal at absolute zero. The curve is showing DOS with blue regions indicating occupied states. (a) shows a case with electron as the E_F and (b) the case for electron at states lower than E_F . (c) is showing collected KE spectrum and (d) is showing E_{Bi} spectrum. These spectra doesn't resemble the UPS due to the contribution of inelastically scattered electrons.

For a more realistic analysis and spectrum we should consider the analyzer, scattering in the film and Fermi-Dirac statistics. In the electrical measurements it is important to follow the electrical connections and in particular the ground, especially if the analyzer is electrically isolated from the sample the loss in energy cannot be determined when the photoelectron is absorbed by the analyzer. To resolve this issue in the UPS measurements, both the analyzer and the film are connected to the ground. By doing so, E_F of both will be the same to equilibrate the charges and so the local vacuum around sample and analyzer will shift accordingly. This is also necessary because the electron leaving the film should be replaced and the extra electron absorbed by the analyzer should be removed. Therefore, the KE measured by the analyzer will be:

$$KE = E_{Ph} - E_{Bi} - WF_{Sample} - (WF_{Analyzer} - WF_{Sample}) \quad (2.2)$$

And by rearranging above equation, E_{Bi} is calculated by equation below:

$$E_{Bi} = E_{Ph} - KE - WF_{Analyzer} \quad (2.3)$$

The schematics of how grounding both analyzer and sample help calculating the E_{Bi} is shown in Figure 2.2. This simple and important trick makes the measurements independent of knowing work function of the sample and we just need to determine the work function of analyzer. Later it will be explained why the exact value is not needed and the system can be calibrated by measuring the spectrum of a clean metal. The other great aspect is that E_F of the sample is always at $E_{Bi} = 0$ eV.

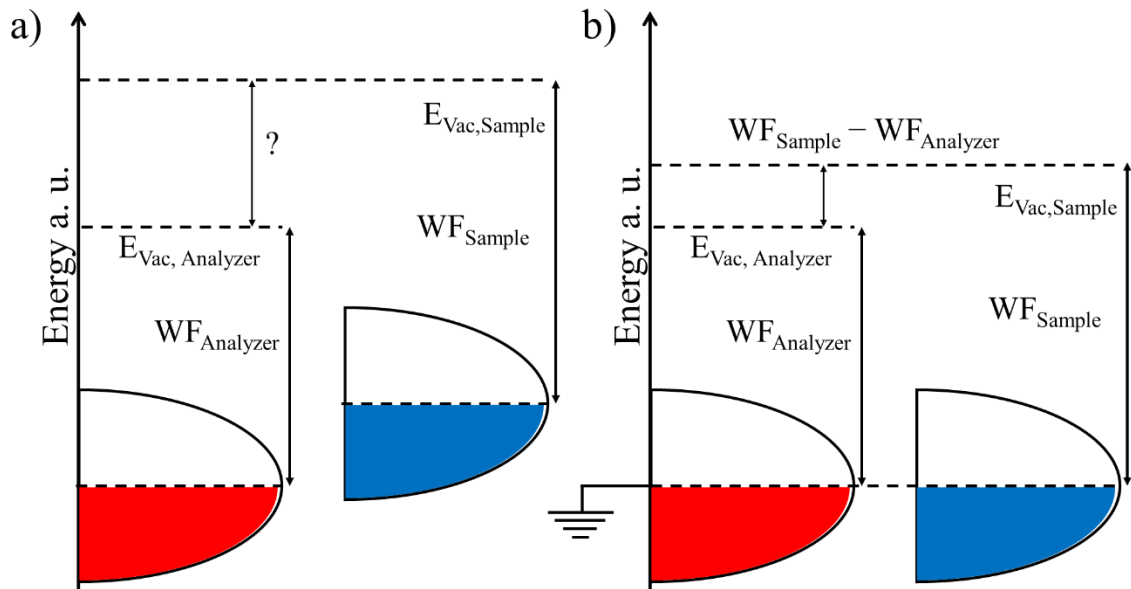


Figure 2.2 Energetics of sample and detector with respect to each other when they are (a) electrically isolated and (b) when they both grounded.

Most electrons will scatter before leaving the materials. The KE of these scattered photoelectrons are smaller than ones that were not scattered inelastically, assuming that the electrons came from states of identical energy. This will result in a large counting of photoelectrons at lower kinetic energies that don't represent any states in the DOS of the sample. This lower KE will translate to a lower E_{Bi} in the spectrum. Figure 2.3 shows the measured spectrum of a 50 nm thick gold thin film. As explained, the spectrum doesn't

represent the DOS of gold because of scattering, though some strong features of the DOS show up. Going towards the lowest KE or highest E_{Bi} in the spectrum, there is a sharp cutoff called the secondary electron cutoff (SECO). With assumption these are the photoelectron with $KE = 0$ eV, their E_{Bi} calculates as:

$$E_{Bi} = E_{Ph} - KE - WF = E_{Ph} - WF \quad (2.4)$$

So WF is equal to:

$$WF = E_{Ph} - E_{Bi}|_{SECO} \quad (2.5)$$

Because of these scattering there are few information that can be extracted from the middle parts of spectrum, so in most presented figure for UPS measurements, only the SECO and around $E_{Bi} = 0$ eV part of spectrum is shown.

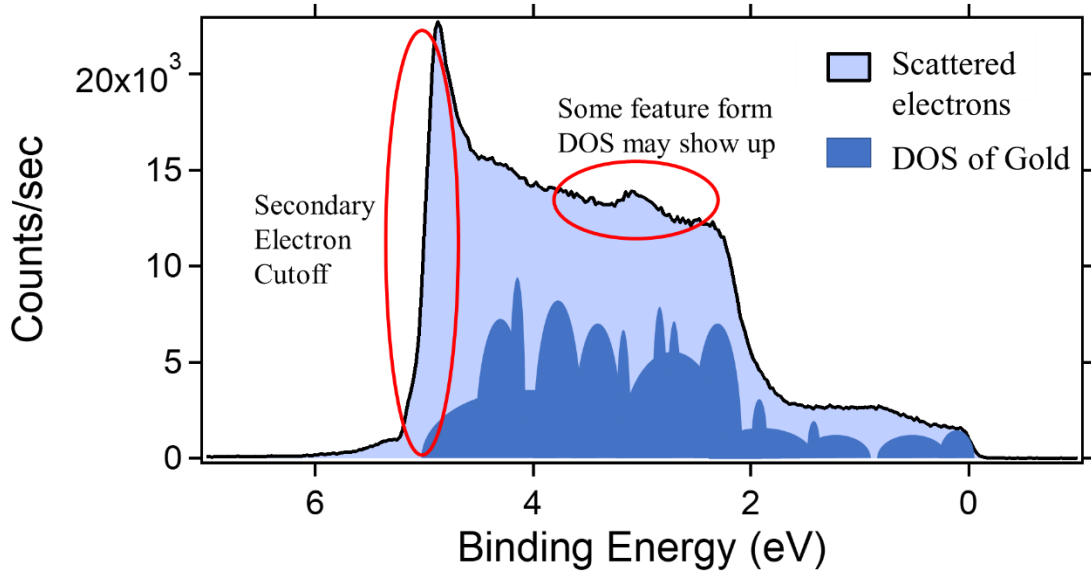


Figure 2.3 UPS spectrum of 50nm gold. Darker blue represents the DOS of gold and light blue represents the scattered electron that show up in spectrum. The DOS of gold shown in dark blue is just a representation for showing the difference between the actual DOS and UPS spectrum.

In the actual experiments there is always a bias voltage applied to the sample with respect to the analyzer. As the KE of photoelectrons at SECO is 0, they often don't reach the analyzer and secondary electrons generated in the analyzer interfere with these photoelectrons; therefore, a negative constant known bias is applied, V_{bias} , to the sample to boost their KE (in the measurements presented in this dissertation V_{bias} is -5V). By applying this bias, Equation (2.2) **Error! Reference source not found.** updates to:

$$\begin{aligned}
 KE &= E_{ph} - E_{Bi} - WF_{Analyzer} - V_{bias} \\
 &= E_{ph} - E_{Bi} - WF_{Analyzer} - (-5)
 \end{aligned}
 \tag{2.6}$$

Now let's focus on the energies around E_F . Figure 2.4 shows regions around $E_F \pm 0.5$ eV. For metal and semi-metal samples, the shape of the spectrum at E_F should obey Fermi-Dirac distribution shape. So, there is an attempt to fit Fermi-Dirac equation to this spectrum shown below:

$$f_1(E) = \frac{A_1}{e^{\frac{E-E_F}{K_B T}} + 1} \quad (2.7)$$

Where E is energy, K_B is Boltzmann constant, T is the temperature in Kelvin and A_1 is a constant to fit to the spectrum. But analyzer will also induce some distortion which usually is represents by a Gaussian convolution shown in equation below:

$$f_2(E) = A_2 \int_{-\infty}^{\infty} \left(\frac{1}{e^{\frac{\omega-E_F}{K_B T}} + 1} \right) \left(\frac{1}{\sqrt{2\pi}\Delta} e^{-\frac{(E-\omega)^2}{2\Delta^2}} \right) d\omega \quad (2.8)$$

Where Δ is width of the Gaussian distribution representing the instrument broadening or resolution. There has been a line multiplied by these equations to account for scattering and simply a better fit. So, equations will change to:

$$f_3(E) = \frac{A_1(aE - b)}{e^{\frac{E-E_F}{K_B T}} + 1} \quad (2.9)$$

$$f_4(E) = A_2 \int_{-\infty}^{\infty} \left(\frac{(a\omega - b)}{e^{\frac{\omega-E_F}{K_B T}} + 1} \right) \left(\frac{1}{\sqrt{2\pi}\Delta} e^{-\frac{(E-\omega)^2}{2\Delta^2}} \right) d\omega \quad (2.10)$$

Where a and b are fitting parameters and A_1 and A_2 in Equations (2.9 and (2.10 is extracted from Equations (2.7 and (2.8 respectively. The fits are shown in Figure 2.4 and the fitting parameter are presented in Table 2.1. For Equation (2.10), T is forced to have values above 290K otherwise the fitting will show lower temperature with compensation of higher Δ . As shown in Table 2.1, E_F is between 0.01-0.03 eV (the difference shows up by multiplying a line to equations), but we know this value should be 0 eV. To correct for this value, we assume the WF of the analyzer has been changed and needs to be corrected. To have a better calibration more spectrums from different regions of the film is needed.

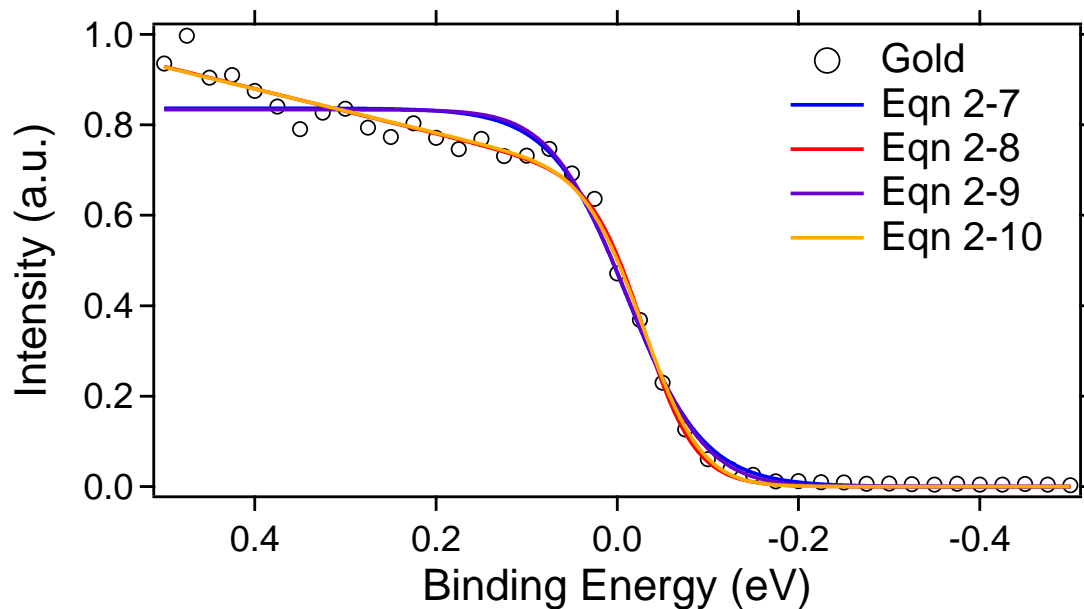


Figure 2.4 UPS spectrum of 50nm gold showing the region around E_F . Solid lines showing fits to the spectrum using the Equations (2.7),(2.8),(2.9) and (2.10).

Table 2.1 Fitting paramant for the fits shown in Figure 2.4

Eqn #	E_F (eV)	T (K)	A_1/A_2	Δ (eV)	a (1/eV)	b
(2.7)	0.0110	492.669	0.836862	-	-	-
(2.8)	0.0116	349.991	0.833632	0.04468	-	-
(2.9)	0.0317	336.317	0.836862	-	-0.59098	-0.814761
(2.10)	0.0310	290.008	0.833632	0.030002	-0.58223	-0.82187

For a semiconductor, E_F is in the middle of the band gap where there is no state for UPS to detect. UPS spectrum of 64 nm C_{60} is shown in Figure 2.5 (a). SECO is shown in Figure 2.5 (b) and HOMO onset in Figure 2.5 (c). To extract WF and HOMO, first a horizontal line is fit to the background and then in both cases, a line is fitted to the onset (shown in dashed red line). For the HOMO onset the fitted line starts approximately 2/3 from the top. The intercepts of these two lines with the background are the desired onsets. Using Equation (2.5), $WF = 4.44$ eV (with $E_{Ph} = 10.2$ eV) and so $IE = 4.44 + 1.975 = 6.415$ eV. In all the analysis this method is used to determine WF, HOMO onset and IE.

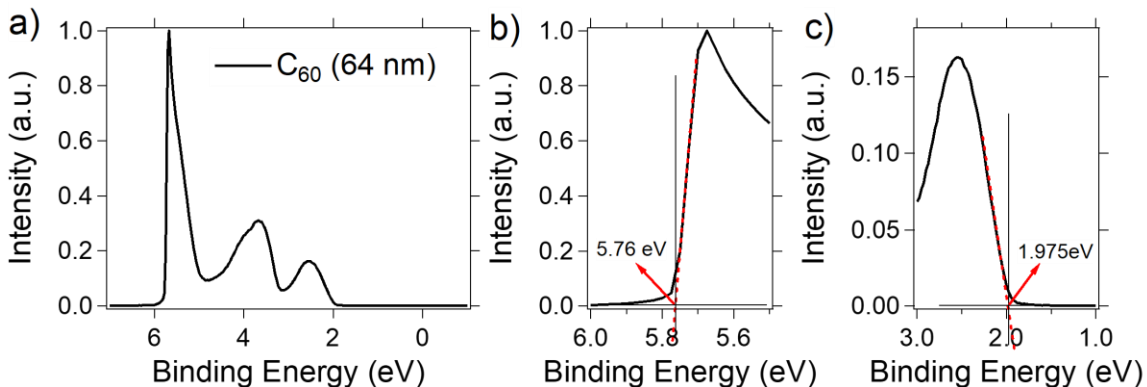


Figure 2.5 (a) UPS spectrum of 64 nm C₆₀, (b) zoomed in view of the SECO region and (c) HOMO onset region.

2.1.1.1 Source, Analyzer, sample preparations and other considerations

The VUV source producing the photons is a H Lyman- α source emitting at 10.2 eV vs. the typical VUV source emitting at 21.22 eV. The advantage of using this low energy VUV lamp is less degradation for organic materials. The details about the source structure and how photon is produced can be found elsewhere.⁵⁶⁻⁵⁹ The analyzer is an 11-inch diameter (180°) hemispherical electron energy analyzer with a multichannel plate detector, PHI 5600 from RBD Instruments, connected to UHV chamber (10^{-9} - 10^{-10} Torr). In this type of analyzer, there is an important parameter called pass energy (PE) and is defined as the KE spread of the photoelectrons entering the hemisphere. PE is set by an electrostatic lens system at the entrance of the hemisphere. Relative energy resolution ($\Delta E/E$, E is the energy of photoelectron entering the hemisphere) in these types of analyzers roughly depend on the average radius and exit slit width of the hemisphere and is a constant value for all the coming photoelectrons. So, higher the energy of the incoming electron results in the higher ΔE (lower absolute energy resolution). In other word, in the first order approximation, intrinsic resolving power become proportional to PE. So, lowering the PE

results in higher resolution (less broadening) but at the same time this causes a lower signal. This effect is most effective in XPS where KE of photoelectron (~ 1000 eV) is much higher than the photoelectron generated of a VUV source (1-10 eV). In the UPS measurement in this work PE is set to 5.85 eV. All the samples have been deposited on the glass coated with ITO to ensure the electrical connection between film and the chamber. Here we are using a monochromatic source, but in the work done by Sato *et.al.* by varying light source energy, they could probe the low density states (impurity/trap states) in the gap.⁶⁰

2.1.2 Inverse Photoemission spectroscopy

The process of IPES is opposite of what it is for UPS. In this process, electrons with a known kinetic energy are directed toward the material and are absorbed by the film and directly occupy one of the unoccupied states. By occupying these states, the electron will lose energy equal to the binding energy of that state with respect to vacuum plus the kinetic energy of the electron. This lost energy can be emitted in the form of a photon. So, electrons absorbed by states closer to E_F emit photons with higher energy. By counting the photons with a photomultiplier tube (PMT) and varying the initial kinetic energy of electrons the density of unoccupied states of a material can be constructed. The schematics of the process are shown in Figure 2.6.

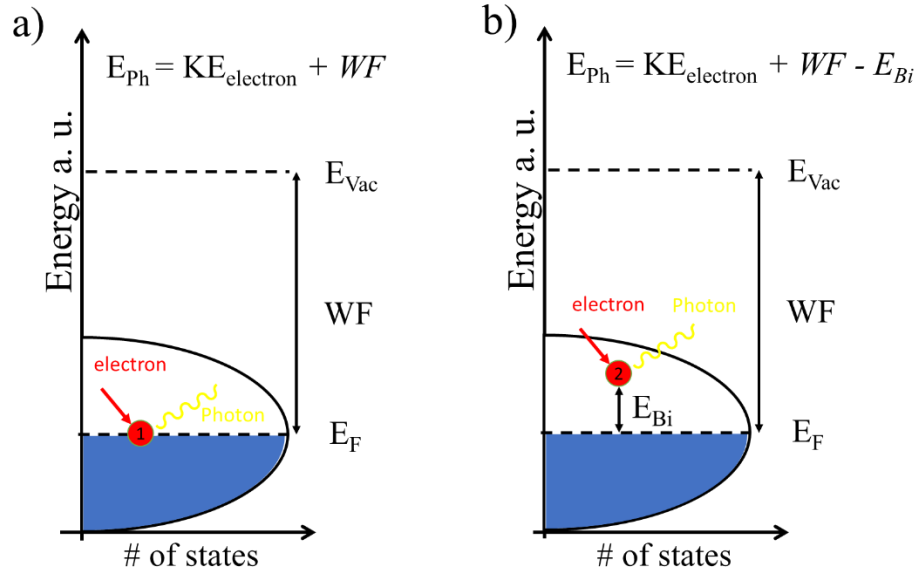


Figure 2.6 Energetic schematics of electrons in a metal. The curve is showing DOS with blue regions indicating occupied states. (a) shows a case where the electron falls into a state at the E_F and (b) shows the case for electron absorbs at states higher than E_F .

Our setup is designed based on the setup proposed by H. Yoshida.⁶¹ In our setup, the kinetic energy of electron is varied between 20 – 30 V and PMT is probing photons in certain wavelength using optical band pass filter (214 nm, 254 nm, or 280 nm and in energy scale 5.79 eV, 4.88 eV, or 4.43 eV). Therefore, to detect any signal, the energy of the photon should be the same as the optical band pass filter. During the measurement, a -20 V bias is applied to the sample to reduce the energy of the coming electrons. To extract the density of unoccupied states of the sample from a signal measured from the PMT, we have to consider two processes. First, we have to find a reference for the kinetic energy of the electron with respect to sample by probing the sample current and second, take account for the energy of the optical filter to convert it into the binding energy of state in the sample. The details can be found elsewhere⁶² and the of LabVIEW codes running these setups can be found in APPENDIX 1.

2.1.2.1 IPES instrumental detail

The electron gun is a Kimball Physics ELG-2 with a BaO cathode. The PMT is R585 from Hamamatsu Photonics which is coupled with a data acquisition system to count the photons. During the measurement the sample is connected to a -20 V bias to reduce the kinetic energy of electrons and stop them from damaging the sample and all the samples are fabricated on an ITO coated glass to ensure electrical connection between film and ground. The measurement is done in UHV chamber with pressure in range of 10^{-10} Torr. More details can be found elsewhere.⁶²⁻⁶⁴

2.1.3 X-ray photoemission spectroscopy

The process of this measurement is similar to what happens in UPS. The difference is that the photon energy is high enough to excite the electrons from the core levels of individual atoms. Therefore, one of the primary applications of XPS is to determine the atomic composition of the film. The binding energies of these core electrons also depend on the type of bonds between elements. Another application of XPS can be determining the surface coverage of a monolayer on top of another material. The detail of surface coverage calculation can be found in APPENDIX 2.

For acquiring the elements constructing the material usually a wide scan range (called a survey scan) from 0 to 1000 eV binding energy is recorded. A sample of a survey scan of regiorandom poly(3-hexylthiophene) (RRa-P3HT) is shown in Figure 2.7 (a). RRa-P3HT is composed of just carbon and sulfur atoms with a 1 to 10 ratio (9% carbon and 91% sulfur). As expected, the only elements showing in the survey are carbon and sulfur.

For a homogenous film the number of electrons per second (the measured value) for an individual peak can be calculated using the equation below:⁶⁵

$$I = nf\sigma\theta'y\lambda AT \quad (2.11)$$

Where n is the number of atoms of the element per cm^3 of the sample, f is the x-ray flux in photons/ cm^2sec , σ is the photoelectric cross-section for the atomic orbital of interest in cm^2 , θ' is an angular efficiency factor for the instrumental arrangement based on the angle between the photon path and detected electron, y is the efficiency of the photoelectric process, λ is the mean free path or attenuation length of the photoelectrons in the sample, A is the area of the sample from which photoelectrons are detected, and T is the detection efficiency for electrons emitted from the sample. We can rewrite Equation (2.11) to:

$$n = I/f\sigma\theta'y\lambda AT = I/SF \quad (2.12)$$

Where SF is called sensitivity factor and it is a parameter that converted the measured peak area to the numbers of atoms in the detected volume to account for varying X-ray absorbance cross-sections, inelastic mean free paths, and analyzer transmission. This parameter mainly depends on the instrumental parameter so by normalizing SF of an element, such as F to 1, the SF of rest of the elements can be determined with respect to F . A list of SF of elements can be found elsewhere.⁶⁵ For two or more elements in a homogenous film, the concentration of each element can be calculated from equation below:

$$X_i = \frac{n_i}{\sum n_j} = \frac{I_i/SF_i}{\sum I_j/SF_j} \quad (2.13)$$

Where X_i is atomic concentration of element i . In most cases since there is a instrumental broadening of signal, I is determined by integrating the area of signal peak. To determine the atomic concentration of RRa-P3HT, a smaller area scan is performed just

for the peaks with highest intensity of each element. Carbon just has one peak around 285 eV representing 1s orbital. Sulfur has two peaks, representing 1s and 2p orbitals with 2p having higher intensity around 165 eV. The results for the small area scans of these two regions is shown in Figure 2.7 (b) and (c). Sulfur 2p consists of two peaks, $2p_{1/2}$ and $2p_{3/2}$. Each subscript is indicating different total angular momentum quantum number j ($j = l+s$). The results show 8.5% sulfur instead of 9%, which this can be result of excess carbon due to organic contamination. This small variation from the actual value (0.5%) is a pretty reasonable measurement even without surface contamination

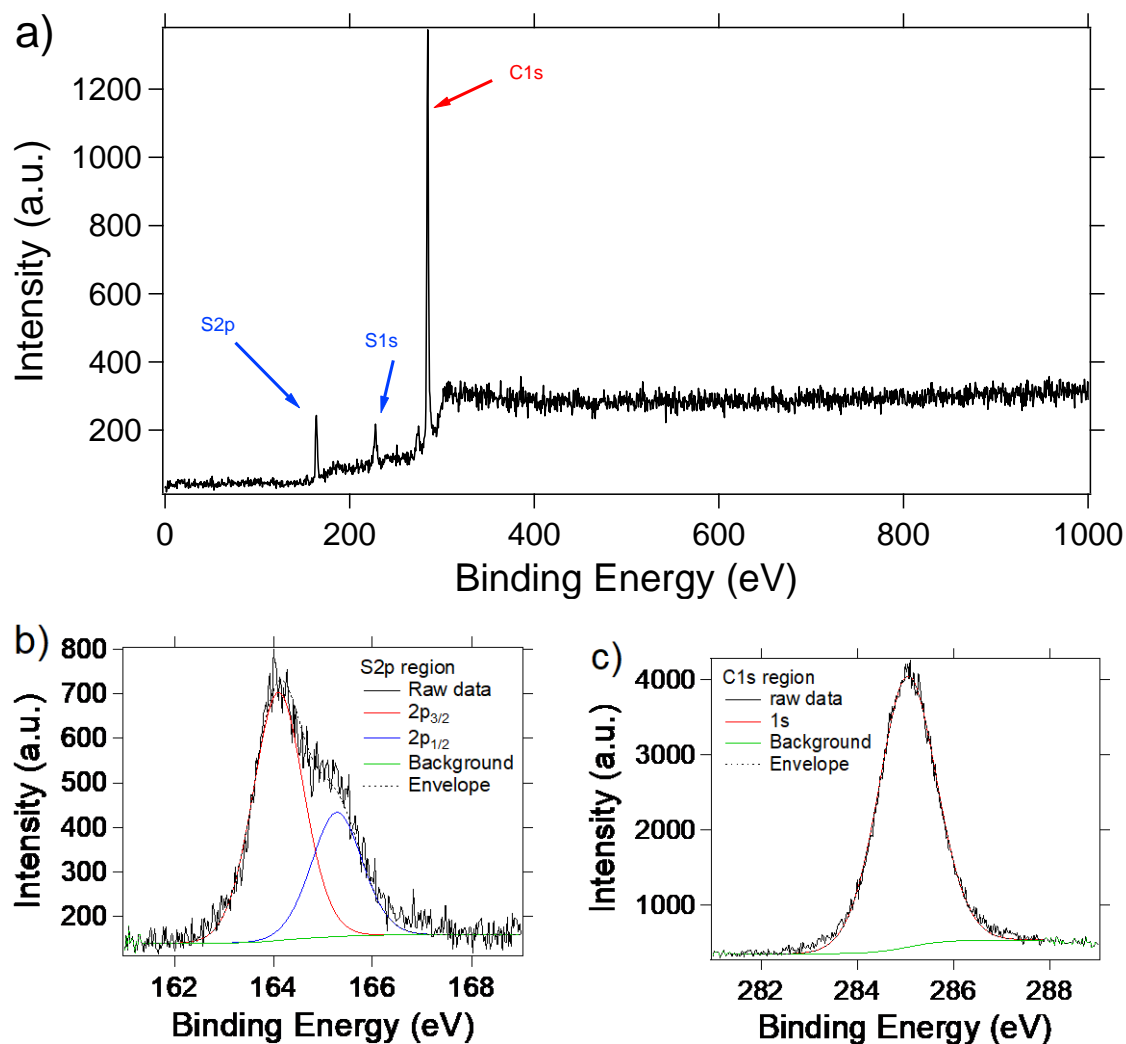


Figure 2.7 (a) XPS survey of Regiorandom Poly(3-hexylthiophene) on ITO coated glass. Small area scan for (b) S 2p and (c) C1s region of same film.

2.1.3.1 XPS instrumental detail

All XPS measurements were performed with a PHI 5600 hemispherical electron energy analyzer in UHV system with an Al K α source at 1486.6 eV or Mg K α source at 1253.6 eV.

2.2 Photovoltaic device fabrication and characterizing

2.2.1 Substrate and substrate cleaning

Substrates are 1mm thick glass slides, coated with a patterned thin layer of indium tin oxide (ITO) (Tinwell Tech., 15 Ω /sq). For cleaning, all the substrates are put in a plastic holder. The cleaning procedure is sequential sonication in aqueous detergent (sodium

dodecyl sulfate, Sigma-Aldrich), acetone and 2-propanol each for 15 minutes. Between sonication in aqueous detergent and acetone, the substrates are rinsed in deionized water multiple times to clean off the remaining detergents. The solvents were refreshed every 2 weeks or earlier. After drying with nitrogen, substrates were exposed to UV–ozone treatment for 10 min to remove organic contaminants. The fabrication process was always started immediately after the last step. This cleaning procedure is applied for all other substrates unless it is mentioned otherwise.

2.2.2 PV Device fabrication process

First a hole transporting layer was deposited on top of a clean substrate. Poly(3,4-ethylenedioxythiophene) polystyrene sulfonate (PEDOT:PSS, CLEVIOS P VP AI 4083) was filtered and was spun-cast at 5000 rpm for 50 s and then annealed on a hot plate at 130 °C for 15 min in air. Active layer is made from anthradithiophene (ADT, synthesized process can be found elsewhere⁴⁹) as donor and Buckminsterfullerene (C₆₀, Nano-C, 99.5%) as acceptor. For bilayer devices, 25 nm of ADT was deposited at a rate of 0.5 Å/s and 40 nm C₆₀ was deposited at a rate of 1 Å/s. For blend films, ADT and C₆₀ were co-deposited at different rates (0.02–1.0 Å/s) to satisfy desired blend ratios with a total thickness of 50 nm. Electron transporting layer was 10 nm bathocuproine (BCP, TCI, >99.0%) deposited at 0.5 Å/s. Finally, electrodes were 100 nm aluminum (Al, 99.99%, Angstrom Engineering) deposited at 1–3 Å/s through a shadow mask that defined four cells of 0.1 cm² area and four cells of 0.2 cm² area per substrate. All thermally evaporated materials were deposited at a typical pressure of 1×10^{-7} mbar. The schematics of patterned ITO, HTL, active layer, ETL and Al electrodes is shown in Figure 2.8. Note that in the case where PEDOT:PSS was used as HTL, the sides are scratched off so Al electrode can have

a direct contact with ITO. In case were none of the layer were spun cast, there was no need for scratching off the extra materials.

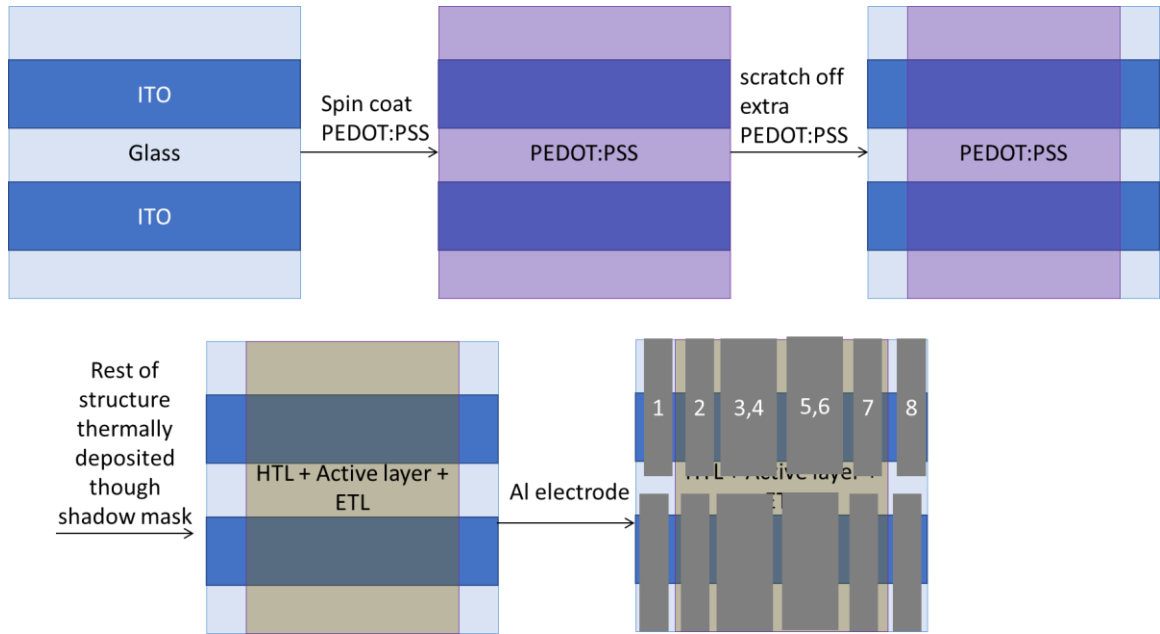


Figure 2.8 Device fabrication process.

2.2.3 Device characterization

Solar cell performance was measured using a solar simulator (ABET Technologies, 11002) at 100 mW/cm² illumination (AM 1.5G). The intensity was adjusted to 100 mW/cm² using a photodiode calibrated with a KG5 filter (ABET Technologies). A 2450 Keithley SourceMeter controlled by LabVIEW was used to characterize the PV devices. The detail of LabVIEW code can be found in APPENDIX 1.

2.3 External quantum efficiency (EQE)

Sensitive EQE measurements were performed in a homemade setup with schematics shown in Figure 2.9. Sensitive EQE measurements were taken at short-circuit conditions under focused monochromatic (CM110, Spectral Products) illumination from a

150 W tungsten–halogen light source (ASBN-W, Spectral Products) chopped by an optical chopper (MC2000, Thorlabs) at 84 Hz. Multiple optical filters were used to prevent unwanted light harmonics in the range of PV device absorbance from interfering with the measurement. The current from the PV device was amplified with a current to voltage amplifier (RDM-Apps) and further amplified with a lock-in amplifier (SR830, Stanford Research Systems). A calibrated silicon photodiode (FDS100) and a calibrated germanium photodiode (FDG03) purchased from Thorlabs were used to measure the incident light intensity at each wavelength. The uncertainty in the absolute EQE is estimated at $\pm 7\%$ due primarily to the uncertainty associated with the photodiode calibration ($\pm 5\%$), light source intensity fluctuations, and small variations in alignment.

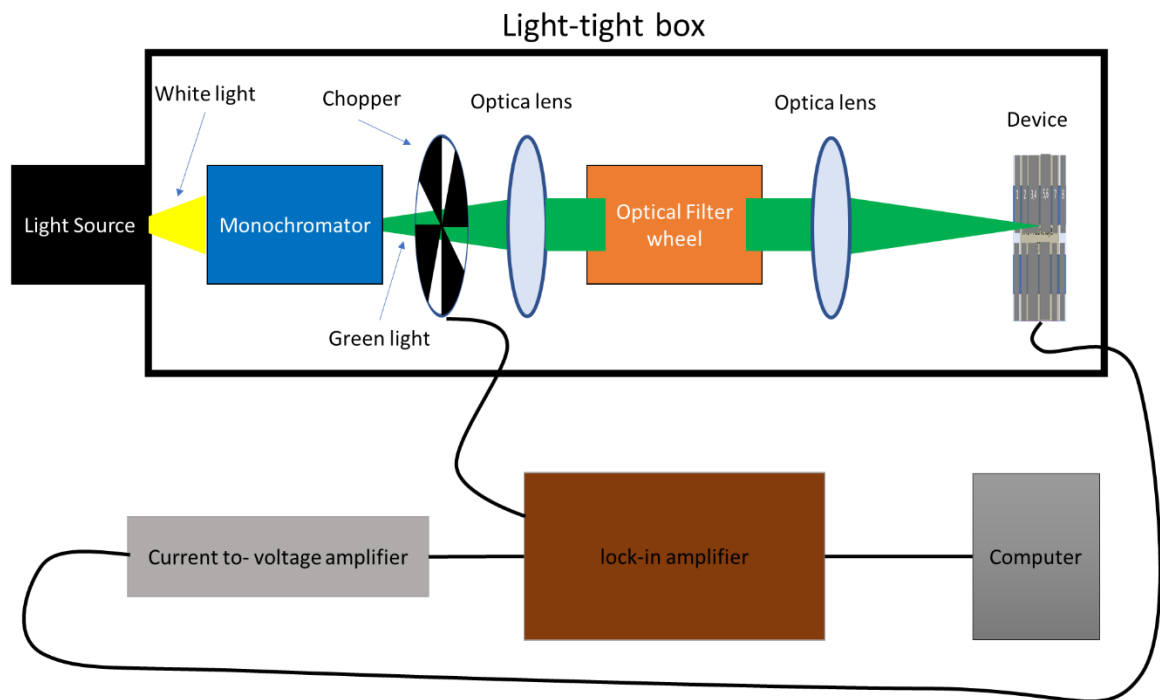


Figure 2.9 Sensitive EQE setup schematics.

2.4 UPS fitting procedure to stepwise deposition of C₆₀ on ADT

For each step in the stepwise deposition of C₆₀ on any of the ADT molecule, the pure X-ADT spectrum was shifted on the x-axis and multiplied or divided by a constant number so it matches the HOMO peak of X-ADT at each step (X-ADT fit), or as much of the HOMO peak as extends out past the C₆₀ HOMO. In the next step, the pure X-ADT fit spectrum was subtracted from the C₆₀ on X-ADT spectrum. The resultant spectrum represents the contribution of C₆₀ in the step, with some variation likely resulting from increased disorder in the X-ADT layer upon C₆₀ deposition. The HOMO onsets for both X-ADT and C₆₀ are then used to determine the IEs at each step. Figure S2 shows an example where the C₆₀ HOMO onsets were extracted from UPS spectra of 2Å, 20Å and 80Å C₆₀ on H-ADT. The figures on the right show the onset of H-ADT in each step and the shifts in the HOMO onset vs. the pure H-ADT film without C₆₀.

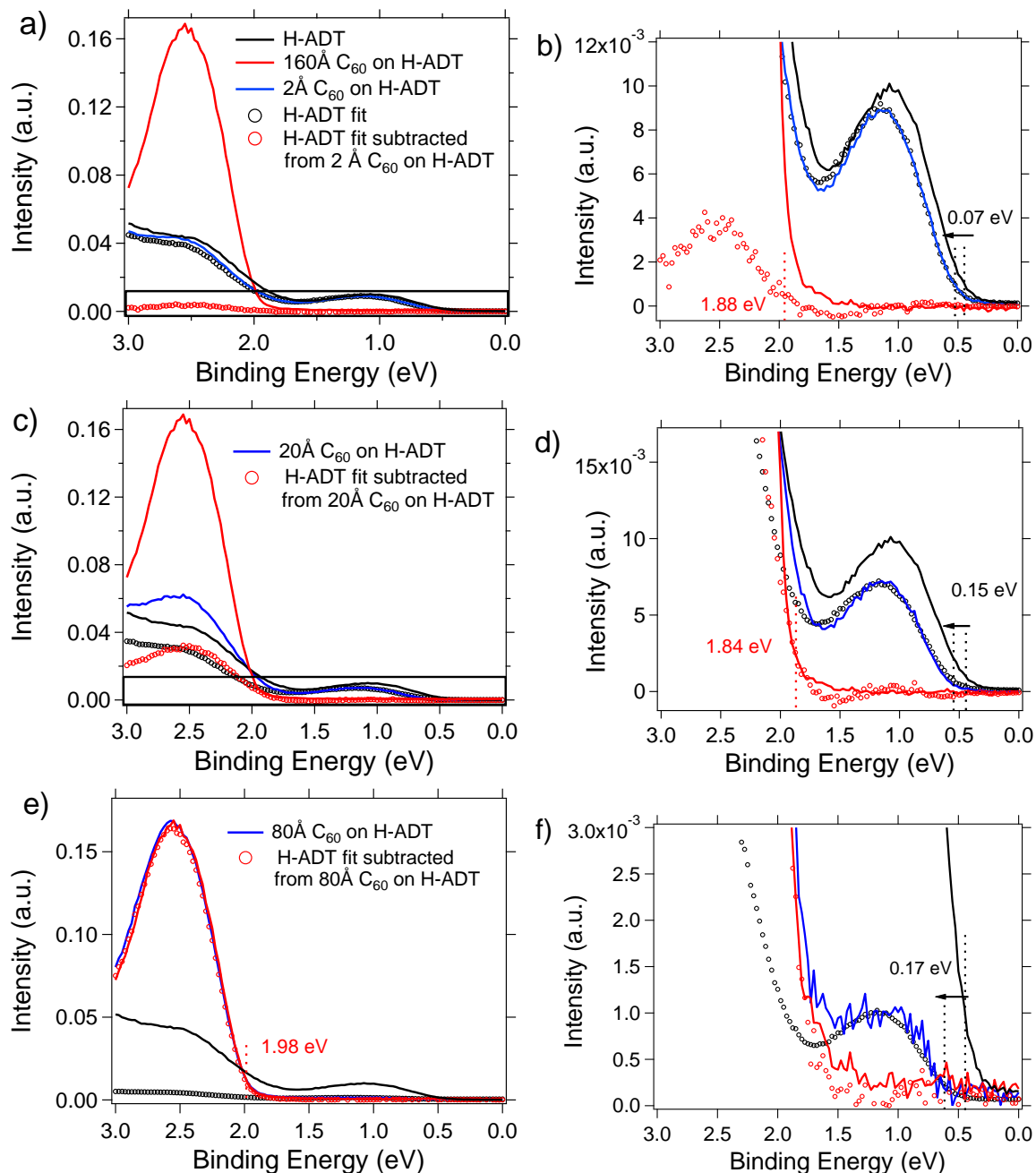


Figure 2.10 Example of H-ADT/ C_{60} stepwise deposition with UPS spectra for 2\AA (a, b), 20\AA (c, d) and 80\AA (e, f) C_{60} on H-ADT. Plots b, d and f show zoomed in regions of the spectrum where the H-ADT onset appears. In all figures the solid black line is pure H-ADT, solid red line is 160\AA C_{60} on H-ADT which represents pure C_{60} , solid blue line shows spectrum of 2, 20 and 80\AA of C_{60} on top of H-ADT, hollow black circles show the shifted and rescaled H-ADT spectrum (H-ADT fit) and hollow red circles show the spectrum of the H-ADT fit subtracted from the 2, 20 and 80\AA C_{60} on H-ADT, which represents the contribution of C_{60} .

2.5 Grazing Incidence Wide-Angle X-ray Scattering (GIWAXS)

Films of Cl-ADT and H-ADT (50 nm thick) were prepared by thermal evaporation at a rate of 0.5 Å/s on silicon wafers with a 300 nm thick oxide layer. Grazing incidence wide-angle X-ray scattering (GIWAXS) measurements were performed at D-line, CHESS at Cornell University. The X-ray beam, with a wavelength of 1.155 Å and a wide band pass (1.47%), was incident on the films at an angle of 0.15°. A PILATUS 200K detector was placed 90 mm from the sample to record the images.

2.6 Density functional theory calculations

Density functional theory calculations were carried out using the Gaussian 09 Rev. E.01 suite at the optimally tuned OT- ω B97X-D/6-31G(d,p) level. Omega tuning was carried out via non-empirical gap tuning of monomers for each ADT of interest and C₆₀ that were geometry optimized at the ω B97X-D/6-31G(d,p) level. The final ω value was obtained as an average over this set. ω values ranged from 0.1538 to 0.1754 bohr⁻¹ with a final value of 0.1637 bohr⁻¹ used in the calculations; using a single ω for all molecular and complex calculations allows us to directly compare molecular orbital energies and state energies across all systems explored. Individual molecular geometries were then re-optimized at this level inside of a diethylether PCM ($\epsilon=4.24$) prior to being placed in dimer configurations. All TD-DFT calculations were completed using the PCM model with a diethylether medium. These calculations have been done by Sean M. Ryno, E. Kirkbride Loya and professor Chad Risko.

2.7 Quadrupole calculations

Molecular quadrupole tensors were determined via the generalized distributed multipole analysis using the GDMA 2.2.11 program.⁶⁶ Density matrices used for analysis were determined at the ω B97xd/6-31G(d,p) level using the Gaussian09 Rev. E.01 program with default ω value using structures optimized at the same level. An atom-centered approach was used including all atoms within the respective molecules and multipoles calculated to the hexadecapole to recreate the molecular electrostatic potential. These calculations have been done by Sean M. Ryno, E. Kirkbride Loya and Professor Chad Risko.

2.8 Thermoelectric device fabrication and characterizing

2.8.1 Substrate and substrate cleaning

Substrates are 1 mm thick glass slides. For cleaning, all the substrates are put in a plastic holder. The cleaning procedure is sequential sonication in aqueous detergent (sodium dodecyl sulfate, Sigma-Aldrich), acetone and 2-propanol each for 15 minutes. Between sonication in aqueous detergent and acetone, the substrates are soaked in deionized water for multiple time to clean off the remaining detergents. The solvents were refreshed every 2 months or earlier. After drying with nitrogen, substrates were exposed to UV–ozone treatment for 10 min to remove organic contaminants. The fabrication process was always started immediate after the last step. This cleaning procedure is applied for all other substrates unless it is mentioned otherwise.

2.8.2 Thermoelectric Device fabrication process

Doped polymer solutions were prepared with a total polymer concentration of 5 mg/mL and a total dopant concentration of 1.16 mg/mL under a nitrogen environment in a glovebox (typically <0.1 ppm H₂O and O₂). Chloroform was degassed prior to use to remove oxygen using three freeze-pump-thaw cycles. Polymer solutions were stirred overnight at 400-500 rpm at 35 °C. The dopant was then added to reach a doping concentration of 5 mole % dopant relative to the repeat unit of P3HT. Based on a polymer density of *ca.* 1.2 g/cm³ and the density of Mo(tfd)₃ as 2.26 g/cm³, this doping concentration is equal to *ca.* 10% by volume for all polymers. This concentration by volume was the same for all solutions to ensure the number of dopants in the solution per unit of volume is kept constant. The mixed solution of polymer and dopant was stirred at 400-500 rpm at 35 °C for an hour. To make the polymer blend solutions, stock solutions of the doped polymers were combined to make solutions with the desired polymer ratios. The polymer ratios are all given as weight ratios. 10×20 mm² glass slides were cleaned with sonication in aqueous detergent (sodium dodecyl sulfate, Sigma-Aldrich), deionized water, acetone, and 2-propanol each for 15 min. After drying them with nitrogen, they were exposed to UV-ozone treatment for 10 minutes to remove any remaining organic contamination. The clean substrates were transferred to the nitrogen filled glovebox and films were spun cast at 1000 rpm for 30 seconds with a 3 second ramp time. For the films used for Seebeck measurements, a Q-tip wet with degassed chloroform was used to clean the doped polymer from regions where electrodes and bismuth were deposited. The film used for electrical conductivity were used as spun cast. Bismuth (100 nm, as temperature reference) and gold

(50 nm, as electrodes) were thermally evaporated under vacuum with a shadow mask. The schematics of the process is shown in Figure 2.11.

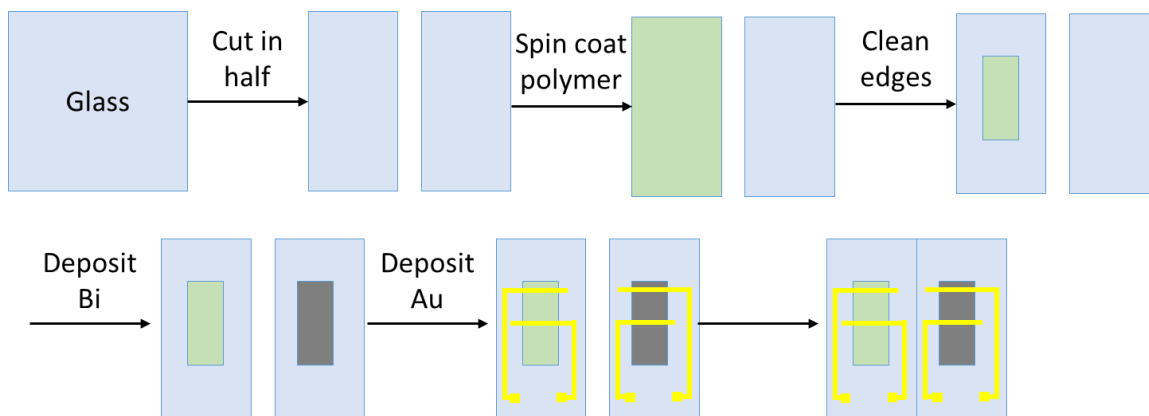


Figure 2.11 Device fabrication schematics for Seebeck coefficient measurement.

2.8.3 Materials

$\text{Mo}(\text{tfd})_3$ was synthesized and supplied by the Marder group at the Georgia Institute of Technology according to a previously reported procedure.⁶⁷ The synthesis of PDPP-4T and PDPP-T-TT-T was performed by the Mei group at Purdue University and also followed previous references.^{68,69} RR-P3HT and RRa-P3HT were purchased from Rieke metals. Bismuth was purchased from Kurt J. Lesker with 99.99% purity. Gold coins with 99.99% purity were thermally evaporated to form electric contacts. Anhydrous degassed chloroform (DriSolv, Ethanol stabilized, 99.8%) was used as a solvent.

2.8.4 Device characterizing

The Seebeck coefficient was measured with a custom built setup.⁷⁰ The details of the Seebeck measurement geometry and system can be found in our previous publication.⁷⁰ The voltage across the polymer film and Bismuth film was measured by two Keithley 2100 multimeters and the temperature of the hot block was resistively heated and controlled with

a TC200 Thorlab temperature controller. Sheet resistance was measured with a four-point probe setup consisting of Signatone S302-4 and Keithley 2450 source meter. To calculate electrical conductivity, film thickness was measured with a Dektak D6M/32 profilometer ($\sigma = \frac{1}{R_{\square}t}$, σ is electrical conductivity, R_{\square} is sheet resistance and t is thickness of film).

2.9 Photothermal Deflection Spectroscopy (PDS)

2.9.1 PDS Device fabrication process

RR-P3HT and RRa-P3HT solutions were prepared with 20 mg/mL polymer concentrations and PDPP-4T and PDPP-T-TT-T were prepared with 10 mg/mL polymer concentration in degassed chloroform. The solutions were stirred at 450 rpm and 35 °C overnight. The solutions were spun cast on cleaned quartz substrates at 800 rpms for 30 seconds in the nitrogen filled glovebox. The samples were sealed in moisture resistant packaging in the glovebox and transferred to Dr. Stephen Johnson at Transylvania University for PDS measurements.

2.9.2 PDS characterizing

PDS is a highly sensitive technique to measure optical absorption in thin films.⁷¹ Chopped, monochromatic light from a 300 W Xe light source was coupled into a monochromator with ± 4 nm wavelength resolution and focused onto the sample surface to cause a periodic temperature change in the focal spot region. The sample was immersed in a fluid (Fluorinert FC72) with a high thermo-optic coefficient and the periodic temperature change of the sample caused a corresponding temperature and index of refraction change in the fluid. A CW probe beam from a HeNe laser passed through the fluid and across the sample surface, deflecting along its path as it encounters variations in index of refraction. The probe beam position was monitored by a quadrant-cell photodiode

that was fed into a lock-in amplifier to measure the periodic deflection. Spectral measurements were achieved by varying the excitation wavelength over the range of interest. The schematic figure and picture of the setup is shown in Figure 2.12. Long-pass optical filters were installed at the input and output of the monochromator to reduce undesired wavelengths at the sample surface. The excitation beam was chopped at 9 Hz for these measurements; further details of the PDS apparatus used in this study can be found elsewhere.⁷²

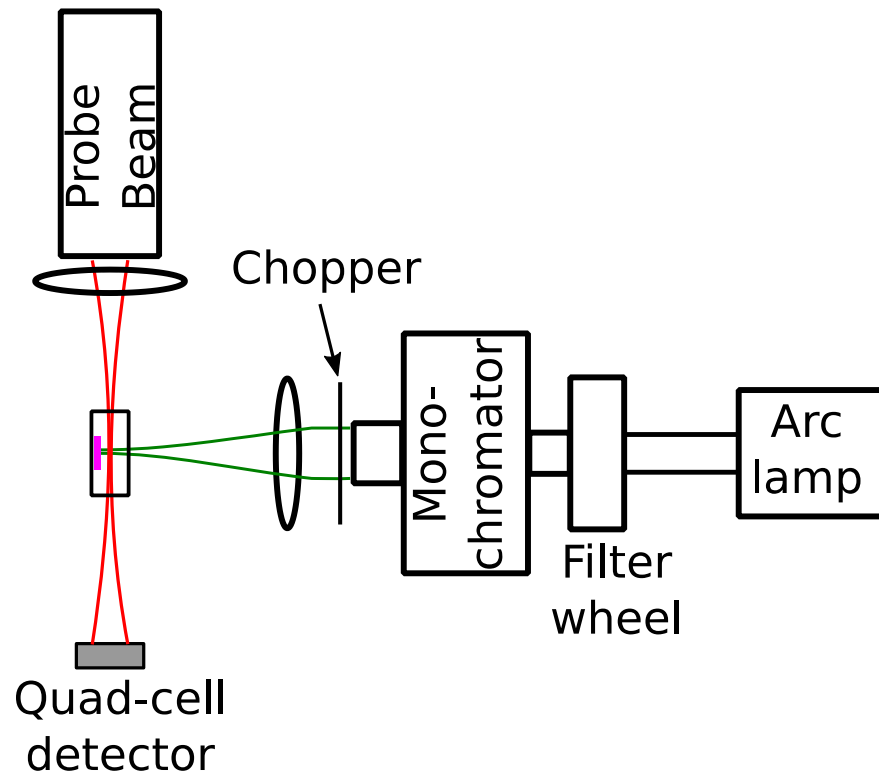


Figure 2.12 Schematic of the PDS setup.

PDS measurements are in good agreement with the optical absorbance. The Urbach energies were extracted using Equation (2.14) to fit the sub-gap region of the PDS spectrum.⁷³

$$Abs = a_0 e^{\frac{E-E_g}{E_u}} \quad (E < E_g) \quad (2.14)$$

Where Abs is absorbance, a_0 is a constant, E is the energy of the absorbed photon, E_g is the band gap energy and E_u is Urbach energy.

2.10 Film fabrication for absorbance spectroelectrochemistry

Polymers were dissolved in chlorobenzene (CB) and stirred at 400-500 rpm at 35 °C overnight. The concentration of P3HT in the CB is 15 mg/ml and PDPP-4T is 7 mg/ml. ITO coated (Sheet resistance = 70 – 100 ohms/sq) alkaline earth boro-aluminosilicate glass were purchased from Delta Technologies and were sequentially cleaned with sonication in aqueous detergent (sodium dodecyl sulfate, Sigma-Aldrich), deionized water, acetone, and 2-propanol each for 15 min. Substrates were dry with nitrogen and exposed to UV-ozone treatment for 10 minutes. Substrates then were transferred to nitrogen filled glovebox and films were spun cast at 1000 rpm for 60 seconds with 3 seconds ramp time. Next, the films were transferred to a petri dish to be seated for an hour with a few drops of CB in them. Then the films were annealed at 120 °C for 10 minutes.

2.11 UV-Vis-NIR absorption spectroelectrochemistry in liquid electrolyte

Absorption spectroelectrochemistry was measured with two different systems in two different environments. UV-Vis absorbance was measured with an Ocean Optics QE Pro high-performance spectrometer in the nitrogen filled glovebox in the range between 350 to 1100 nm and UV-Vis-NIR was measured by Agilent high performance Cary 5000 UV-Vis-NIR spectrophotometers in the air in range between 250 to 3300 nm. A quartz cuvette was used to hold the electrolytes and the film during the measurements as shown in Figure 2.13. All the measurements were performed by a Versastat 4 potentiostat with platinum counter electrode and 10mM Ag(NO₃) reference electrode with difference

counter ions in acetonitrile. All the potential is reported with respect to Ag/Ag^+ . Working electrode voltage was ramped up from -100 mV to 1200 mV with respect to the reference electrode with 50 mV steps. The electrolyte concentration was kept at about 10mM in acetonitrile.

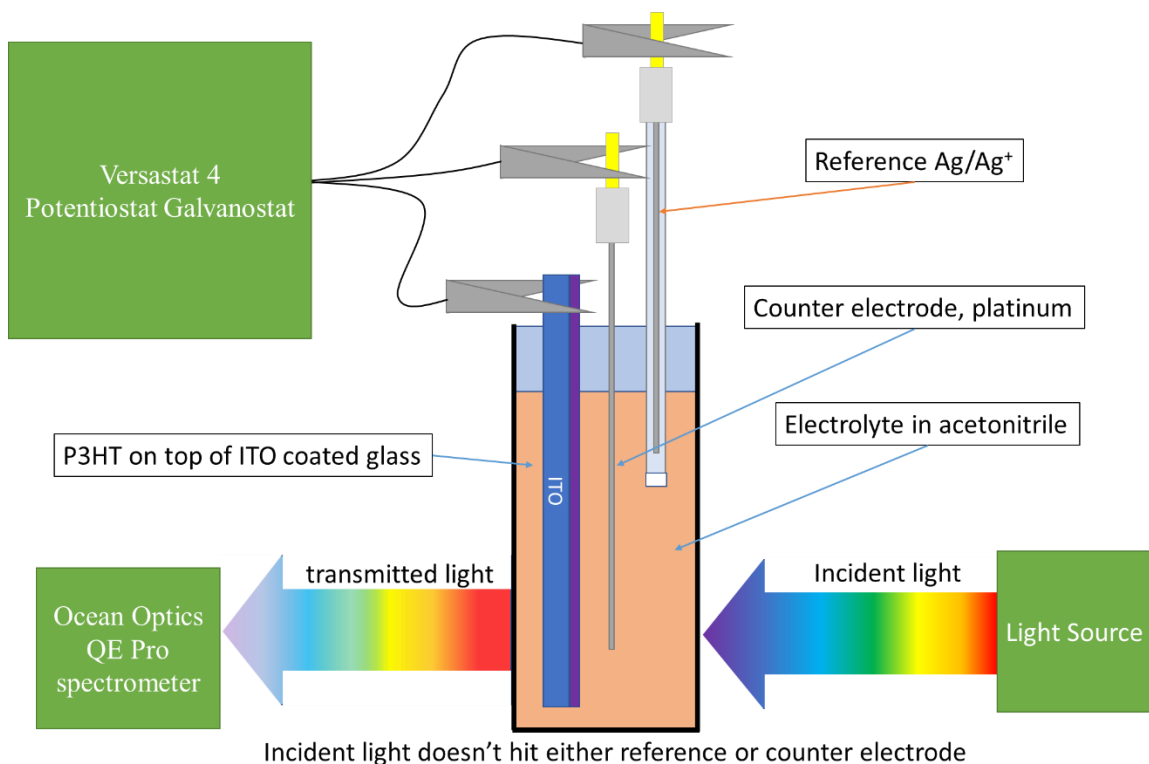


Figure 2.13 Schematic of absorption spectroelectrochemistry setup

2.12 UV-Vis-NIR absorption spectroelectrochemistry on solid state

In this method, similar to absorption spectroelectrochemistry in liquid electrolyte, the measurements are performed by an Ocean Optics QE Pro high-performance spectrometer in the nitrogen filled glovebox. Fabrication of polymer film is explained in section 2.10. After polymer film fabrication, a layer of polymeric ionic liquid is spun cast on top of polymer at 1000 rpm for 60 seconds and annealed at 120 °C for 60 minutes. Later another ITO coated glass was pushed on top of the film and held by two clips as shown in

Figure 2.14 (a). The two ITO coated glass pieces were then connected to a 2450 Keithley source meter with two alligator clips shown in Figure 2.14 (b). By applying voltage, the counter ions are forced to penetrate the polymer film. Since the penetration of the counter ions are very slow, before absorbance measurements there was a couple of minutes delay till the current through the film equals the leakage current.

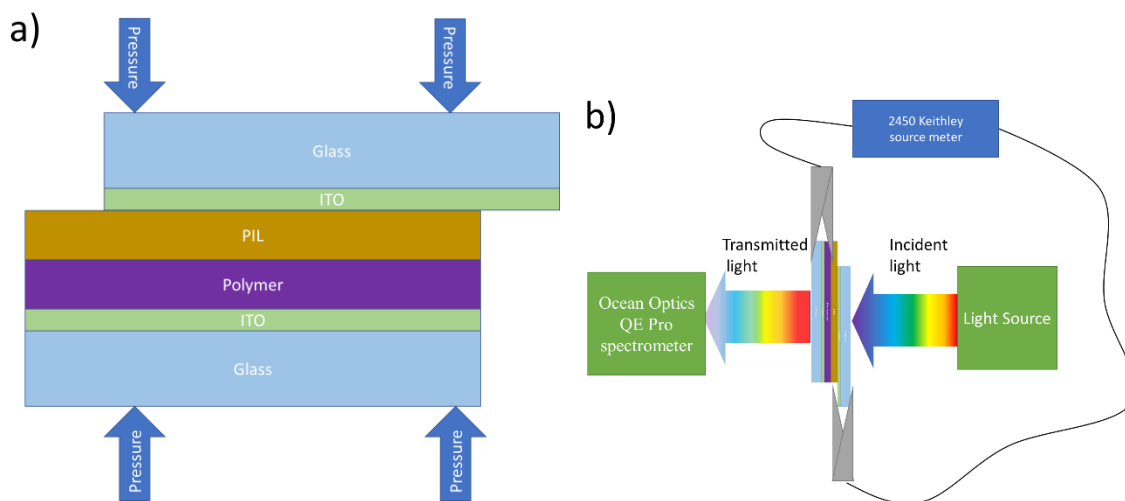


Figure 2.14 (a) Schematic of device for UV-Vis-NIR absorption spectroelectrochemistry on solid state and (b) absorption spectroelectrochemistry setup.

2.13 Raman spectroelectrochemistry

Raman spectroelectrochemistry was measured with a thermo scientific DXR Smart-Raman. The device structure is similar to absorption spectroelectrochemistry on solid state devices explained in the previous section.

2.14 Temperature dependent thermoelectric measurement on OECT

2.14.1 Film fabrication and device structure

Two different glass slides were used in these experiments; first is 1" × 3" × 1 mm glass microscope slides (VWR) and second is 3" × 3-1/4" × (0.19 - 0.25) mm optical grade borosilicate glass. In this dissertation the first one is referred to as a thick substrate and

second one thin substrate. Each substrate is cut into 1" × 1" and sequentially sonication in aqueous detergent (sodium dodecyl sulfate, Sigma-Aldrich), DI water, acetone and 2-propanol each for 15 minutes and then exposed to UV-ozone for 10 minutes and moved to nitrogen filled glove box for gold and polymer deposition.

Two different device structures are used in this section; one is for calibration and measuring temperature dependent Seebeck coefficient of chemically doped polymer and the other is for measuring temperature dependent thermoelectric properties of polymers in OECT device structure. For the first case, 2 nm Cr followed by 50 nm gold is thermally deposited in 10^6 - 10^7 Torr vacuum on glass substrate with a shadow mask. Next 100 nm Bi is deposited using another mask shown in Figure 4.15. Later, polymer is drop cast on the active area region shown in Figure 4.15. During the measurement, 1, 2, 3 and 4 are connected to a voltmeter and 5 and 6 is connected to a power supply for applying heat.

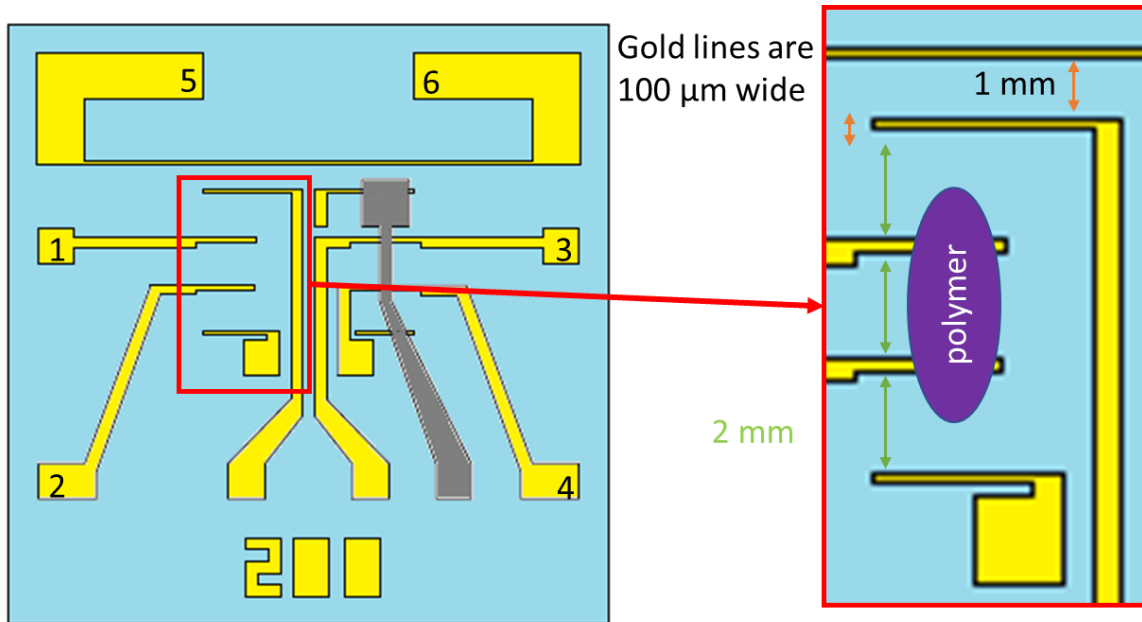


Figure 2.15 Device structure for measuring temperature dependent thermoelectric properties of chemically doped polymers.

For fabricating device for OECT other masks are used. First a 2 nm Cr followed 50 nm gold is thermally deposited using a shadow mask shown in Figure 2.16. The distance between the first electrode and the heater line is set to 1 mm, the heater line is 200 μm and the other gold lines are 50 μm . In the figure below the distance between the gold lines are 50 μm . In other devices the distance can change to 100, 150 and 200 μm .

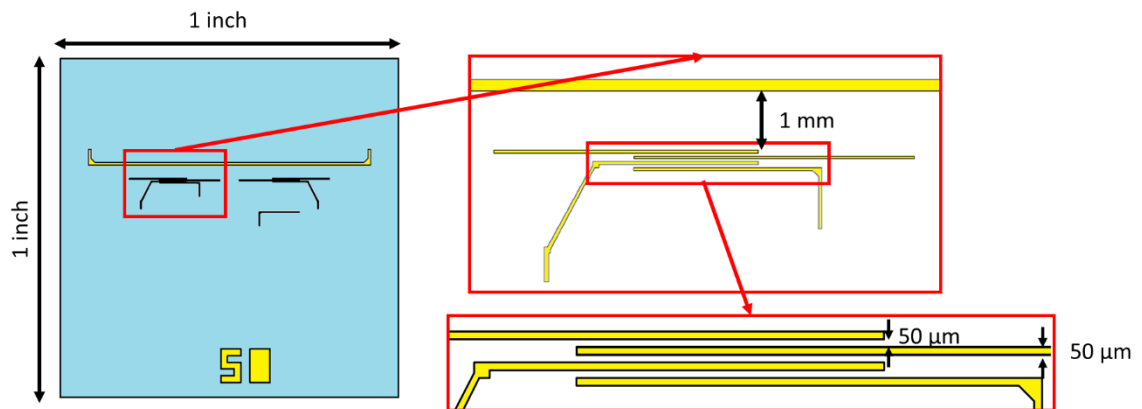


Figure 2.16 schematics of gold deposition of the first layer for OECT device

The complete process of fabrication of the OECT device is shown in Figure 2.17 (a-e). The polymer films are spun cast on the substrate at 4000 rpm for 60 seconds with 3 seconds ramp time. Next, the films were transferred to a petri dish to be sealed for an hour with a few drops of CB in them. Then the films were annealed at 120 °C for 10 minutes. Then PIL was drop cast on top of active area. Then, a Q-tip wet with acetone and CB is used to clean off the extra polymer and PIL so the film is only in the active area shown in Figure 2.17 (c) and there is no contact to other electrodes. Next 50 nm gold is deposited as shown in Figure 2.17 (d) to form the gate contact on top of the active area and the contacts for measuring pins to the electrode. Finally, 100 nm Bi is deposited as shown in Figure 2.17 (e). The final structure of the OECT device is shown in Figure 2.17 (f). There are a total of four electrodes labeled as source and drain. During Seebeck coefficient measurement the two middle electrodes are used and for resistance measurement all four are used as four wire resistance measurements.

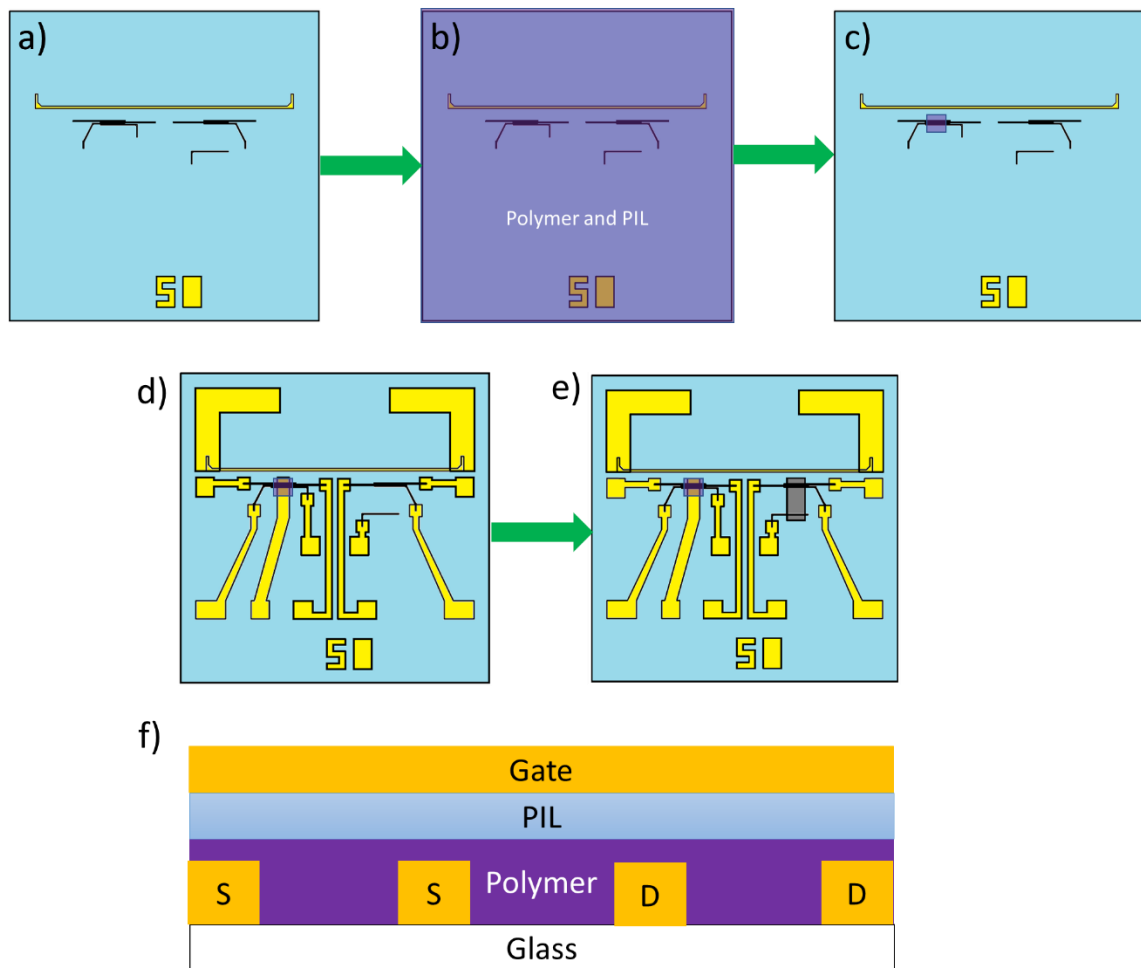


Figure 2.17 (a-e) Schematics of OECT device fabrication. (f) Cross sectional view of an OECT device.

2.14.2 setup for temperature dependent TE properties measurements

We used a custom-built vacuum chamber to measure temperature dependent TE properties of OECTs, as shown in Figure 2.18 and Figure 2.19. A multi stage Peltier module (TE-2-(127-127)-1.15) with operating temperature rated from -40°C to 80°C is coupled with a TC-48-20 controller and MP-3176 thermistor all purchased from TE Technology, Inc. are used to control the temperature of the substrates. The Peltier module is thermally connected with the base of the chamber where 4 cooling fluid lines set at -10°C (with Neslab RTE-140 Recirculating Chiller) are responsible for additional cooling

and heat removal. Since the cooling fluid is in contact with the whole chamber the temperature of the fluid is higher than $-10\text{ }^{\circ}\text{C}$. Two electrical feedthroughs (Belilove Company–Engineers) are used to bring the electrical wires into the vacuum chamber. Noctua NT-H1 thermal paste was used to ensure good thermal contact between the Peltier module and aluminum stage. The pressure is kept at 1-4 Torr during the measurement to minimize the water exposure and oxidation. Thermal conductivity of air at this pressure drops by 20% comparing to atmospheric pressure, so the effect of low vacuum on TE properties measurement is negligible.⁷⁴ For controlling the OECT a dual-channel source meter unit, Keithley 2614B was used and for measuring the thermoelectric voltage of polymer and bismuth two Keithley 2100 (6½-digit resolution multimeter) was used.

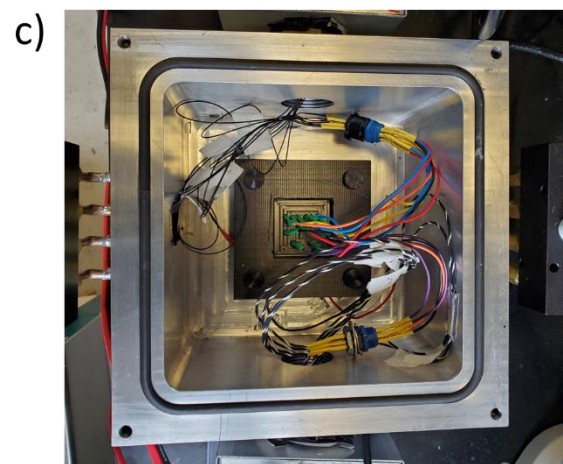
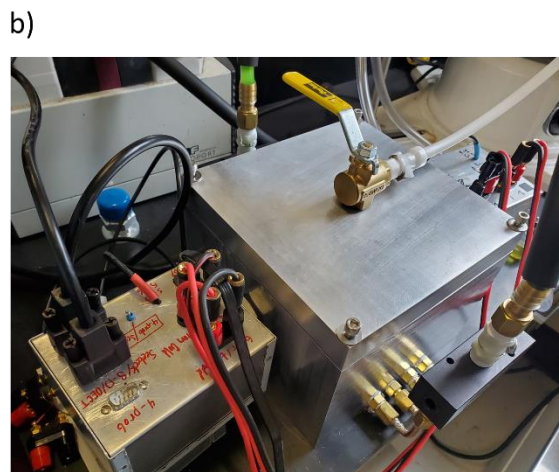
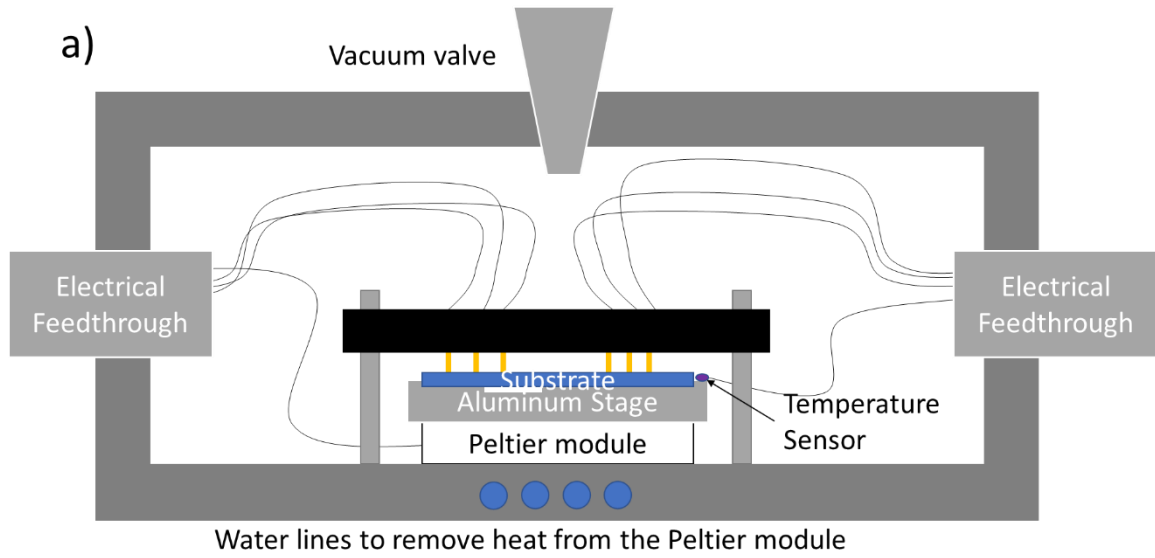


Figure 2.18 (a) Schematics of vacuum chamber for measuring TE properties of OEET. (b) outside view and (c) inside view of vacuum chamber.



Figure 2.19 The vacuum chamber and all the measuring instruments connected.

Figure 2.20 (a) is showing the aluminum stage on top of the Peltier module. There is a cut in the bottom of the chamber so the Peltier module can fit into it. There is also a similar cut under the aluminum stage, so it fits to the Peltier module. Between each part Noctua NT-H1 thermal paste is used for good thermal conduction. Figure 2.20 (b) shows the top view of the aluminum stage and the four posts. The posts are for holding the black measuring stage. On the aluminum stage there is a thermistor held with aluminum tape and a slit placed in the middle. Figure 2.20 (c) shows that the slit is directly under the active area of the measurement. In the next section the importance of position of the slit is going to be discussed. Figure 2.20 (d) and (e) shows the measuring stage which has some gold spring loaded pins for contacting the device.

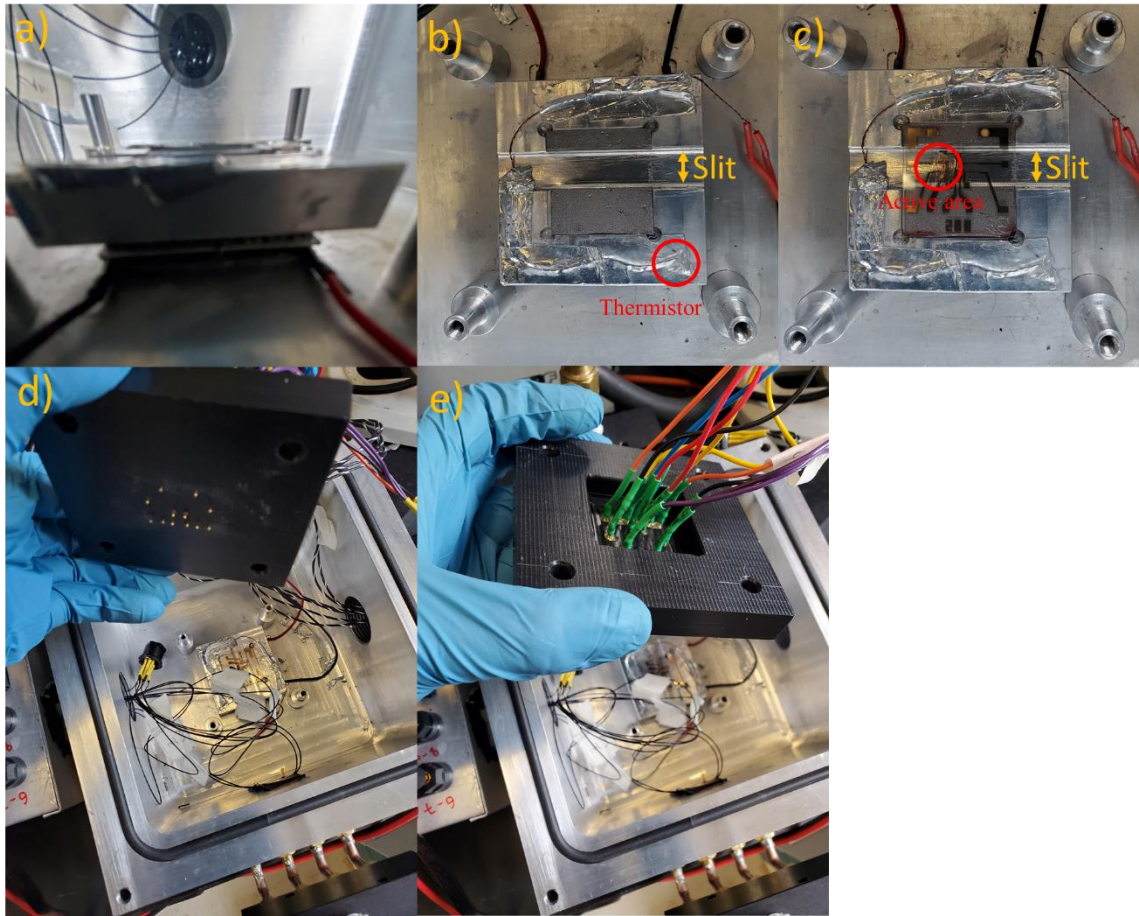


Figure 2.20 (a) Peltier module and aluminum stage. (b) and (c) Top view of aluminum stage with substrate on it. (d) and (e) Bottom and top view of the measuring stage .

2.14.3 Calibration and temperature dependent Seebeck coefficient measurement

The schematic of the device used for calibration is shown in Figure 2.21 (a). Here there are two Bi film deposited on left and right side for a side by side comparison. Temperature gradient is provided by Joule heating of the on-chip heater line with sourcing current to pin 7 and 8. The current is applied by applying a constant voltage of 2, 4, 8, 10 and 15 V. Using the equation $\Delta T = \Delta V_{Bi} / S_{Bi}$ and knowing S_{Bi} at 27°C is $-64.4 \pm 2.6 \mu V/K^{70}$, the temperature across pin 1 and 2 contacts on bismuth is calculated. Figure 2.21 (b) shows the thermoelectric voltage and temperature gradient across the pin 1 and 2 as different

voltages are applied to the heater line. At each heater line power increment, the temperature (following ramp-up) is averaged to obtain a single value.

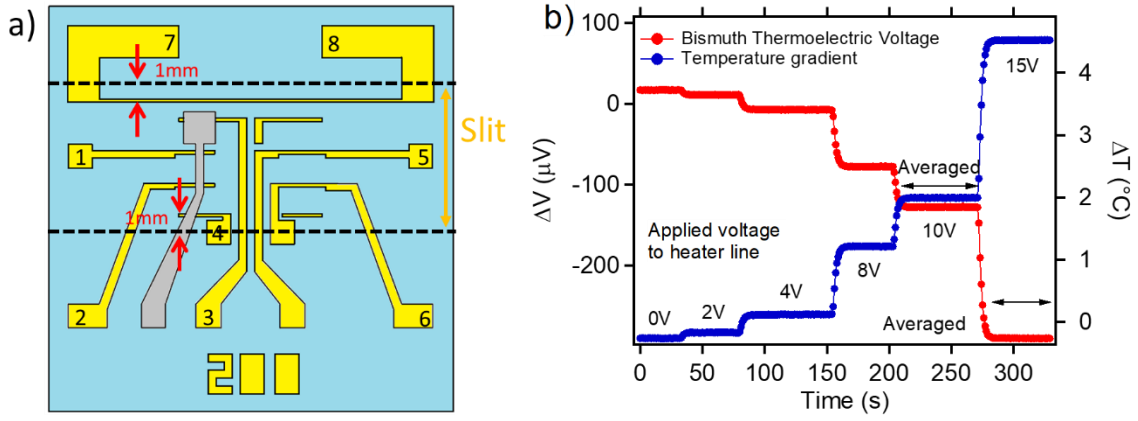


Figure 2.21 (a) Schematic of the device structure. (c) Thermoelectric voltage of bismuth as function of time with varying applied heater line power (each step corresponds to a different power input and the applied voltage is shown next to each step). The temperature gradient is calculated based on the voltage of the bismuth film.

Based on a previous report,⁷⁵ the temperature dependent Seebeck coefficient of 100 nm Bi films, thermally evaporated, is linear between 100 and 400 K and can be approximated as $S_{Bi} = -0.123 \times T + S_0$.⁷⁵ S_0 (equal to $-25.3 \mu\text{V/K}$) was calculated by knowing the Seebeck coefficient of Bi film at room temperature. Additionally, we observed the expected linear dependence of the temperature gradient with respect to the power applied to the on-chip heater line ($P \propto V^2$), as shown in Figure 2.22 (a).⁷⁶ To further check the linearity of temperature gradient in the active area, temperature gradient between pin 3-1, 3-2, 3-1 and 1-2 was measured at -29°C shown in Figure 2.22 (b). As shown in Figure 2.22 (b), the temperature gradient across pins 3 and 2 was equal to sum of temperature gradient between pins 1 and 2 and pins 1 and 3.

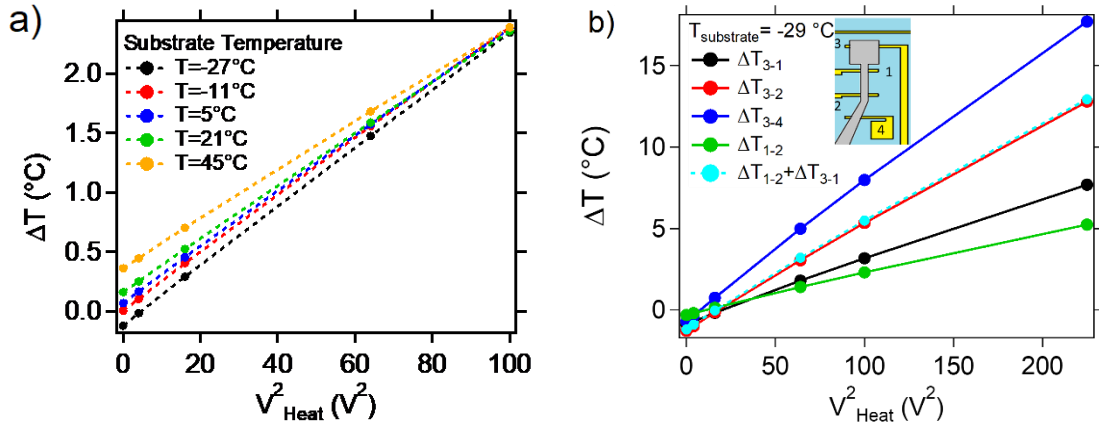


Figure 2.22 (a) Temperature gradient versus applied voltage to heater line squared at different temperatures. (b) Temperature gradient versus applied voltage to heater line squared for different channel length and position in the active area in the slit.

To check the effect of vacuum we switch our pump to a turbo pump capable of achieving pressures around 10^{-6} Torr. Because of poor fittings and seals for high vacuum and pipes with small diameters used in this chamber the pressure will reach to 10^{-3} Torr and likely to only reach 10^{-2} Torr in chamber. The higher vacuum increased the temperature gradients with the same input heater line power by 10-15%. The small increase is expected to be due to small decrease in the vacuum. Next for testing the efficiency of thermal conductance of heat paste, we tried two other thermal pads, IC Graphite Thermal pad and Thermal Grizzly Minus pad 8. Thermal conductivity of Noctua NT-H1 thermal paste is 8 W/mK, thermal conductivity of Thermal Grizzly Minus pad is 8W/mK and thermal conductivity of IC Graphite pad is 35W/mK. Using thick glass substrate, at 650 mW (10 V) power to the heater line the temperature gradients are as follows: IC Graphite is 10.8 $^{\circ}\text{C}$, Grizzly minus 8 is 6.8 $^{\circ}\text{C}$ and paste is 3.7 $^{\circ}\text{C}$. This measurement suggests that using a high thermal conductive pad causes a lower thermal resistance between the film and aluminum stage and results in a greater temperature gradient. The other advantage of using

pad over paste is that every time after changing the substrate the residual paste should be cleaned off with IPA vs. pads that do not need any cleaning.

Another variable considered was the thickness of the glass slide. By decreasing the thickness of glass from a 1mm (1000 μm) to 100-200 μm , the temperature gradient increases by 85%. Next, we tried to look at the effect of slit size and position on the temperature gradient. Dr. Maryam Shahi and Prof. Joseph Brill from the University of Kentucky performed a simulation using MATLAB software to probe the temperature gradient on the glass slide. Figure 2.23 (a) shows temperature profile of glass substrate with different position of heater line. 0 mm indicates the current position of the heater line. The edges of the slits are at 1 mm and -8 mm. As shown in the Figure 2.23 (a), the more heater line is in the center of the slit the higher the temperature gradient would be with a constant power input to the heater line. Figure 2.23 (b) shows the temperature profile of glass substrate with a smaller slit for different thickness of glass. Smaller slit and thinner glass substrate results in a higher temperature gradient as expected.

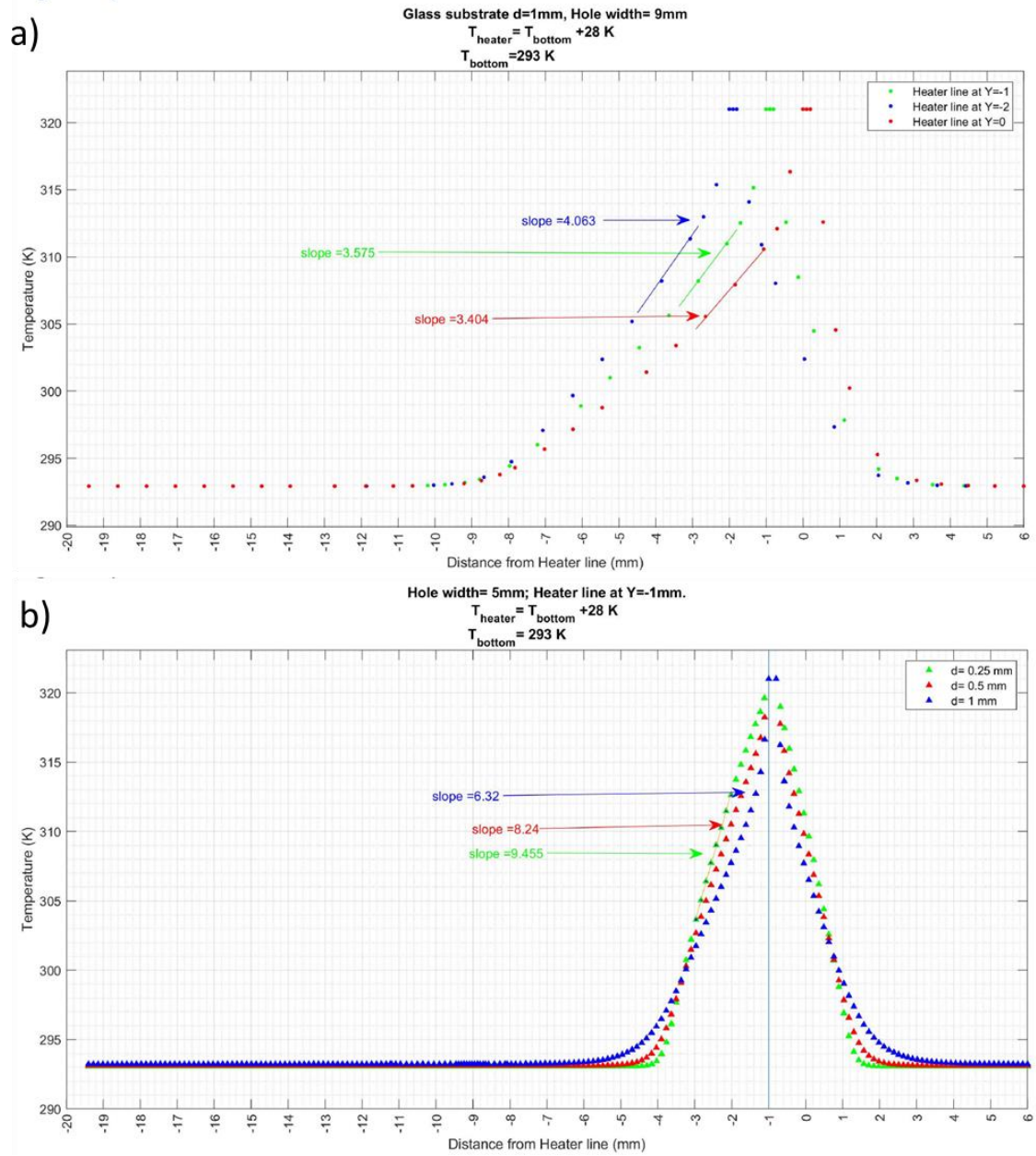


Figure 2.23 (a) Temperature profile of glass substrate for a 1mm thick glass substrate with 9 mm slit for different position of heater line. (b) Temperature profile of glass substrate with 5 mm slit and heater line positioned at -1 mm for different thickness of glass. In both figure the temperature of substrate is at 293 K and temperature heater line at 321 K.

CHAPTER 3. EFFECT OF DONOR HALOGENATION ON INTERFACIAL ENERGETICS AND CHARGE TRANSFER STATE ENERGIES IN MODEL OPVs

This chapter is reprinted with permission from A. Abtahi *et al.*, “Effect of Halogenation on the Energetics of Pure and Mixed Phases in Model Organic Semiconductors Composed of Anthradithiophene Derivatives and C₆₀”, *J. Phys. Chem. C* 2018, 122, 9, 4757–4767, Copyright © 2018 American Chemical Society⁴⁹

3.1 Introduction

Organic photovoltaics (OPVs) present a promising means to harvest solar energy through lightweight, flexible, portable, and environmentally friendly modules. The record power conversion efficiency (PCE) of OPVs has increased from 5 to 13% over the last decade,^{77,78} yet further gains are necessary to enable widespread deployment. As record PCEs have seemingly plateaued,⁷⁸ despite considerable research effort, the largely Edisonian approaches employed thus far appear unlikely to enable further appreciable gains. Rather, more fundamental molecular and morphological design principles must be discovered and utilized. One molecular design strategy that has led to higher efficiencies in bulk-heterojunction OPVs is the replacement of select hydrogen atoms on the electron donor molecules or polymers with fluorine atoms.^{79–89} Given the widely observed beneficial effects of fluorination, it is important to identify the underlying mechanisms behind device performance improvements to further advance the design of OPV materials.

Fluorination influences many properties across varying length scales that help determine the performance of an OPV material system, from the molecular orbital energies through material morphology and topology to OPV-specific device properties.^{79,82,87,89–104} One of the primary motivations for fluorination of donor polymers in OPVs is to alter the ionization energy, and thereby influence the open-circuit voltage.^{81,97,98,105} From a morphological point of view, fluorination of donor polymers can improve phase-purity in

the bulk-heterojunction film and promote the formation of crystalline polymer regions.¹⁰⁰ Fluorination at appropriate positions can also increase the planarity of π -conjugated polymer backbones and alter intermolecular packing,^{79,96,101,102,106} which can lead to higher charge-carrier mobilities. In one report, Tumbleston *et al.* suggested that fluorination alters the molecular orientations and associated intermolecular interactions between polymers and fullerenes from edge-on with the non-fluorinated polymers to face-on with fluorinated polymers.¹⁰⁴ Such changes in the intermolecular interactions at the donor-acceptor (D-A) interface are likely to impact the energy landscape that is critical to photocurrent generation, including the processes of charge separation and recombination. Here, the energy landscape refers primarily to the relative energies of holes and electrons (i.e., sites) at and away from D-A interfaces. Additionally, fluorination will affect intramolecular ground- and excited-state dipoles. For example, Carsten *et al.* reported an increase in OPV performance as the difference between the ground- and excited-state dipole moment of the donor polymer repeat unit increased due to fluorination at selected positions.^{89,95}

The critical processes of charge separation and recombination occur primarily at interfaces between electron donor and electron acceptor molecules or polymers; therefore, changes in intermolecular interactions and the energy landscape that arise from fluorination are expected to influence the probability of charge separation, charge recombination dynamics, and the performance of the PV material system. In a bulk-heterojunction system, the energy landscape will include the site energies for holes and electrons within pure D or A phases, at interfaces between pure D and A phases, and in mixed phases of D and A. Beneficial energy landscapes for promoting charge separation and reducing charge recombination would have lower energy states for holes and electrons within the pure D

and A phases and higher energy states for holes and electrons at D-A interfaces, or in D-A mixed phases; thus, a thermodynamic driving force would exist for interfacial charge-transfer states to separate. Charge separation also appears to be more efficient at interfaces between pure D and A phases,^{107–109} thus it should be advantageous when the lowest energy charge-transfer (CT) states occur between these pure phases as opposed to in mixed D-A phases. Given the importance of the D-A interfacial energy landscape, there is a rapidly growing body of experimental and theoretical work investigating the impact of sD-A interfacial energetics on charge separation and PV performance,^{110–113} and how these energetics are determined at the molecular level.^{113–123} In this manuscript, we show how fluorination and chlorination of model anthradithiophene (X-ADT) derivatives impact the energy landscape at planar D-A interfaces and in mixed phases of varying D and A composition, where C₆₀ is used as the acceptor. We view this contribution as a step in determining if changes in energy landscapes upon fluorination are a primary factor for many of the observed increases in OPV performance.

Several theoretical models have been employed to investigate the influence of the interfacial energy landscape on charge separation and recombination in OPVs.^{110–112,117,124} Many of these studies find that changes in the interfacial energy landscape account in part for how charge separation can be so efficient in OPV materials. For example, kinetic Monte Carlo simulations show that the probability of charge separation depends heavily on the D-A interfacial energy landscape,^{110–112} with interfacial energy offsets of 150 to 300 meV being necessary to explain the high internal quantum efficiencies observed in some OPV materials. Experimentally, cascade energy landscapes have been created in an effort to promote charge separation and minimize charge recombination, with decreased charge

recombination leading to higher V_{OC} values.^{112,125–127} More recently, ultrafast spectroscopic measurements show that the migration of holes from higher to lower energy sites can occur within about 100 fs of excitation.¹²⁸ These ultrafast spectroscopy measurements suggest that in bulk-heterojunction PVs with optimized morphologies, charge separation is in part driven by the migration of holes from higher energy states at D-A interfaces into lower-energy sites within pure D phases.¹²⁸ The combined theoretical and experimental evidence suggests energetics at interfaces and within phases of varying composition play a key role in driving charge separation in OPV devices.

In addition to work on energy cascades, there is an increasingly large body of work on the effects of intermolecular interactions, packing arrangements, and morphology on the energy landscape. Theoretical works have used a wide variety of methods,¹¹⁴ including microelectrostatic simulations,^{116,124,129} density functional theory (DFT) calculations,^{119,124,130–132} and Green's functions theory within the GW approximation and the Bethe–Salpeter equation (GW-BSE).¹²¹ These calculations suggest that the energy landscape at D-A interfaces changes considerably depending on the intermolecular interactions present. Due to significant differences in the electrostatic interactions and polarization energies, different intermolecular arrangements can result in shifts of the interfacial dipole and CT state energy of several hundred meV. Optical, photoelectron, and electrochemical spectroscopies provide additional support for these findings.^{91,122,133–137} Considering both the theoretical and experimental support for these shifts in energetics at D-A interfaces and in mixed phases relative to the pure materials, combined with their potential impact on OPV device performance, it is important to identify the molecular factors giving rise to such energetics. Systematically controlling intermolecular

interactions and energetics will provide a powerful tool to improve the performance of OPV systems.

Here, four model ADT derivatives that can be thermally evaporated with C_{60} were chosen to investigate the influence of halogenation on the energy landscape at interfaces and in mixed phases in OPV devices (Figure 3.1). Importantly, each of these derivatives can be thermally evaporated to form well-defined layered structures with known molecular orientations, thus providing the potential for clean interfaces with C_{60} that reduce the number of unknown variables in the systems. To probe the effects of fluorination, and halogenation in general, at levels commonly used in efficient donor polymers (i.e., one to two fluorine atoms per repeat unit), we compare end-substituted ADT derivatives with hydrogen, methyl, fluorine, and chlorine, as depicted in Figure 3.1. To probe the interfacial energetics between phases of pure materials, we use ultraviolet photoelectron spectroscopy (UPS) during stepwise deposition of C_{60} on top of the varying ADT derivatives combined with external quantum efficiency (EQE) measurements of the CT states in bilayer PV devices. To probe the energetics in the mixed phases, we use UPS measurements of blend films with varying X-ADT: C_{60} composition and EQE measurements of the CT state energies in PV cells based on these X-ADT: C_{60} blends. To provide molecular-level details, these experimental results are compared with results from density functional theory (DFT) calculations at the optimally tuned OT- ω B97X-D/6-31G(d,p) level, where a continuum dielectric ($\epsilon=4.24$) is used to represent the majority C_{60} environment of the mixed phase.

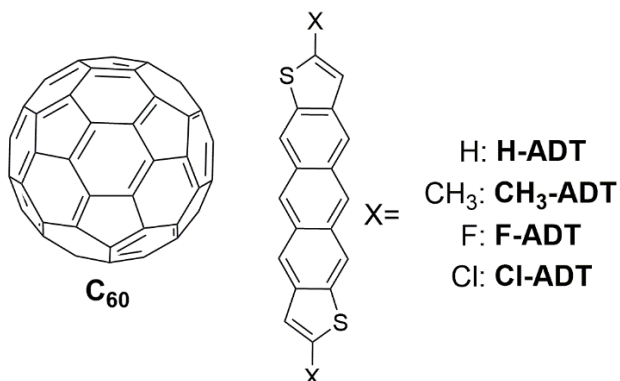
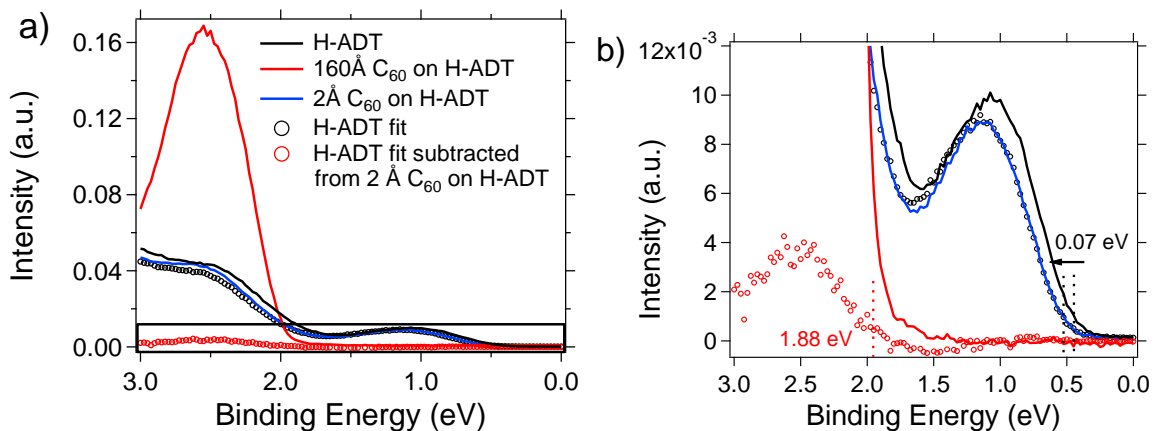


Figure 3.1 Chemical structures of C₆₀ and ADT derivatives used in this work.

3.1 Interfacial Energetics

The results of the UPS measurements are displayed in Figure 3.2 (a-f) for the stepwise deposition of C₆₀ on H-ADT, F-ADT, and Cl-ADT, while the deposition of C₆₀ on CH₃-ADT is shown in Figure 3.3. The ionization energies, HOMO onsets vs. the Fermi energy, and work functions extracted from these measurements are displayed schematically in Figure 3.4 and quantitatively in Figure 3.5. In Section 2.4,



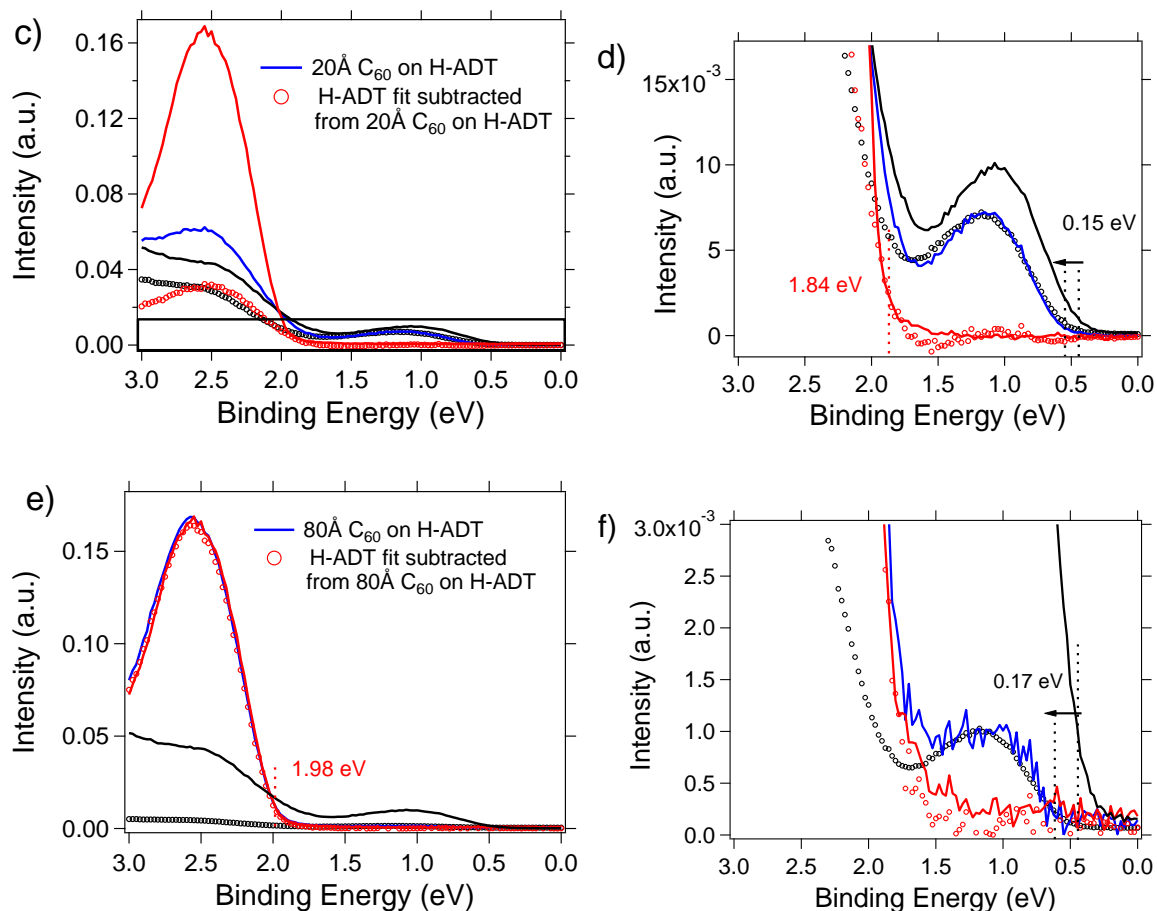


Figure 2.10 shows example UPS spectra demonstrating how both the H-ADT and C_{60} IEs were extracted from the H-ADT/ C_{60} bilayer spectra. Replacing only the two terminal H atoms on the long-axis of the H-ADT molecule with F or Cl atoms results in an increase in the ionization energy (IE) of nearly 1.5 eV, from *ca.* 4.7 eV for CH_3 -ADT and H-ADT to 5.83 and 6.21 eV for Cl-ADT and F-ADT, respectively. The dramatic increase in IE between the non-halogenated and halogenated ADT derivatives is in part attributed to the tip-on orientation of the ADT derivatives on the substrate and the differing quadrupoles (see below) along the long axis of the molecule. These tip-on orientations are confirmed by grazing incidence wide angle X-ray scattering (GIWAXS) measurements for H-ADT and Cl-ADT, as displayed in Figure 3.6; the tip-on orientation of F-ADT was

previously reported.¹³⁸ Crystal structures, as determined from single-crystal X-ray diffraction measurements and displayed in Figure 3.7, show that the ADT derivatives all adopt a similar herringbone packing structure with the main variation occurring in d_{001} , which increases from 14.35 Å for H-ADT to 16.82 Å for Cl-ADT.

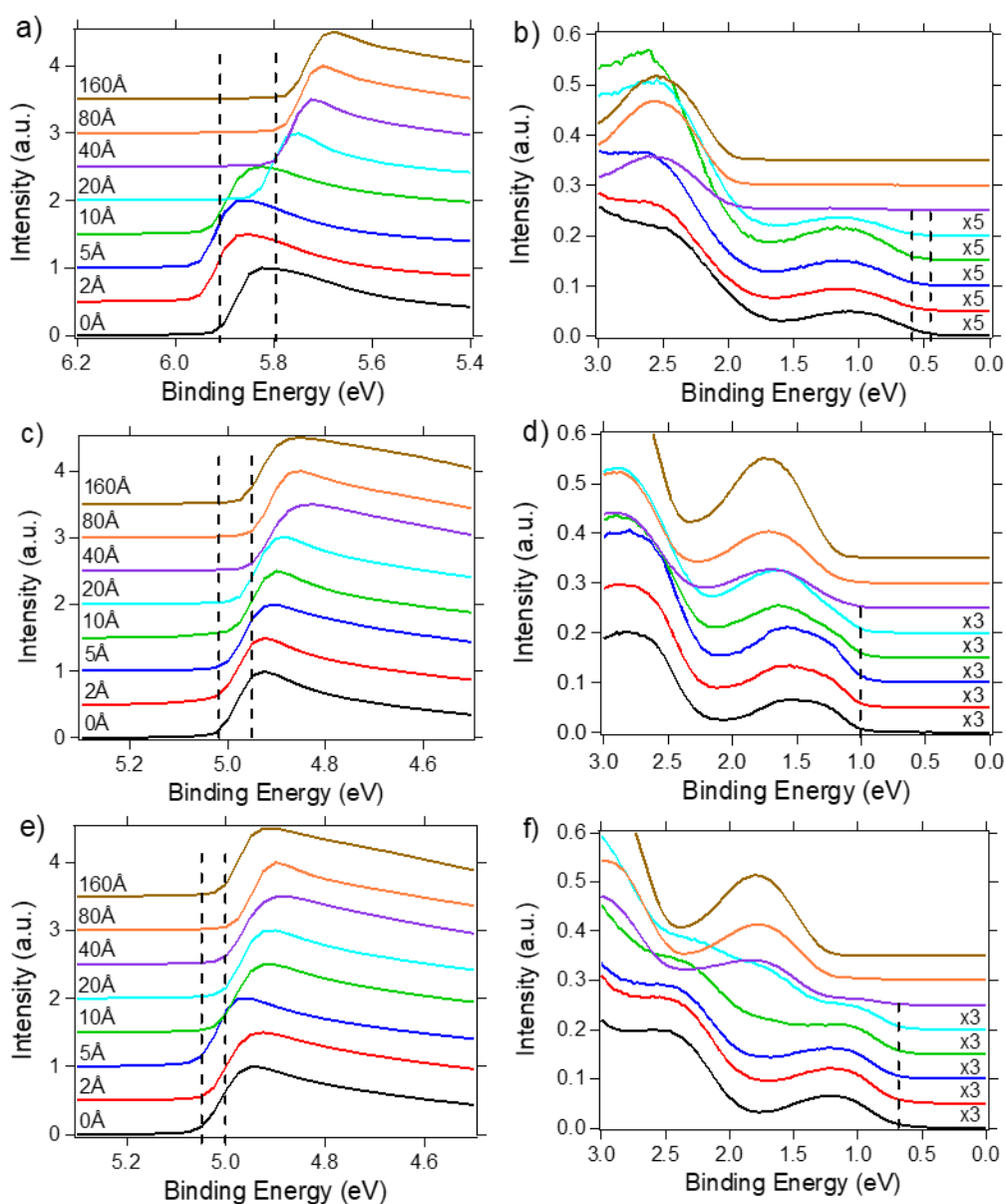


Figure 3.2 UPS spectra showing the secondary electron cut-off (a, c, e) and HOMO onset (b, d, f) regions for H-ADT/C₆₀, F-ADT/C₆₀, and Cl-ADT/C₆₀ bilayers during stepwise C₆₀ deposition. The UPS measurements were recorded with a H Lyman- α source emitting at 10.2 eV.⁵⁹

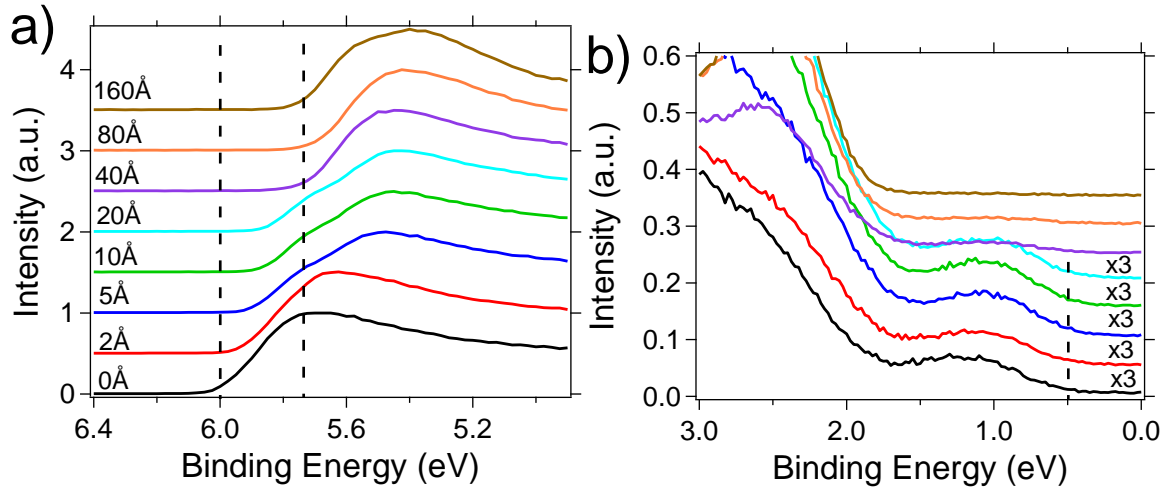


Figure 3.3 UPS spectra showing the secondary electron cut-off (a) and HOMO onset (b) regions for a CH₃-ADT/C₆₀ bilayer during stepwise C₆₀ deposition.

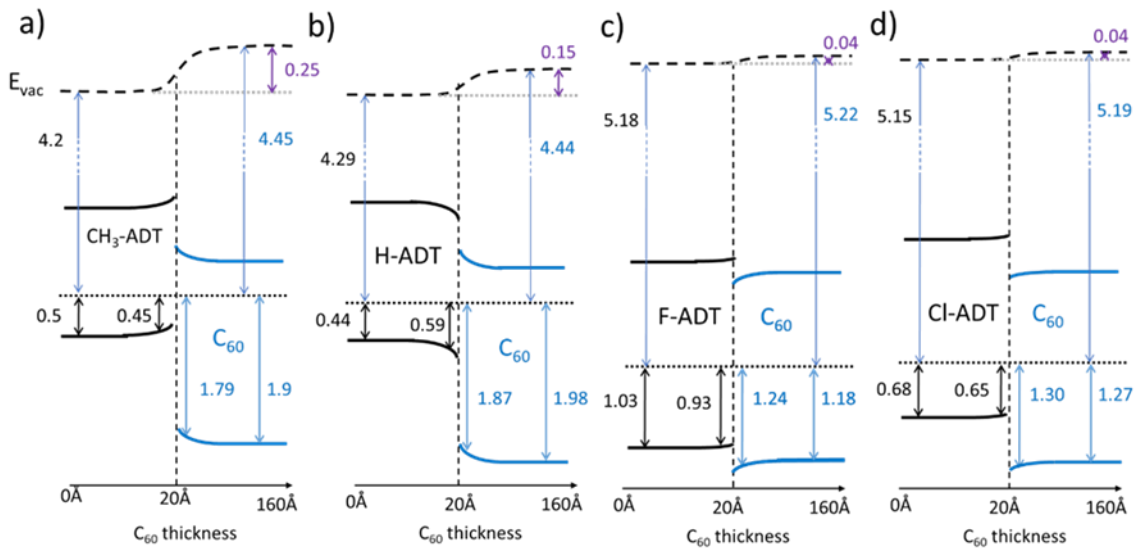


Figure 3.4 Resulting energy diagrams for CH₃-ADT/C₆₀ (a), H-ADT/C₆₀ (b), F-ADT/C₆₀ (c) and Cl-ADT/C₆₀ (d) bilayers during stepwise C₆₀ deposition.

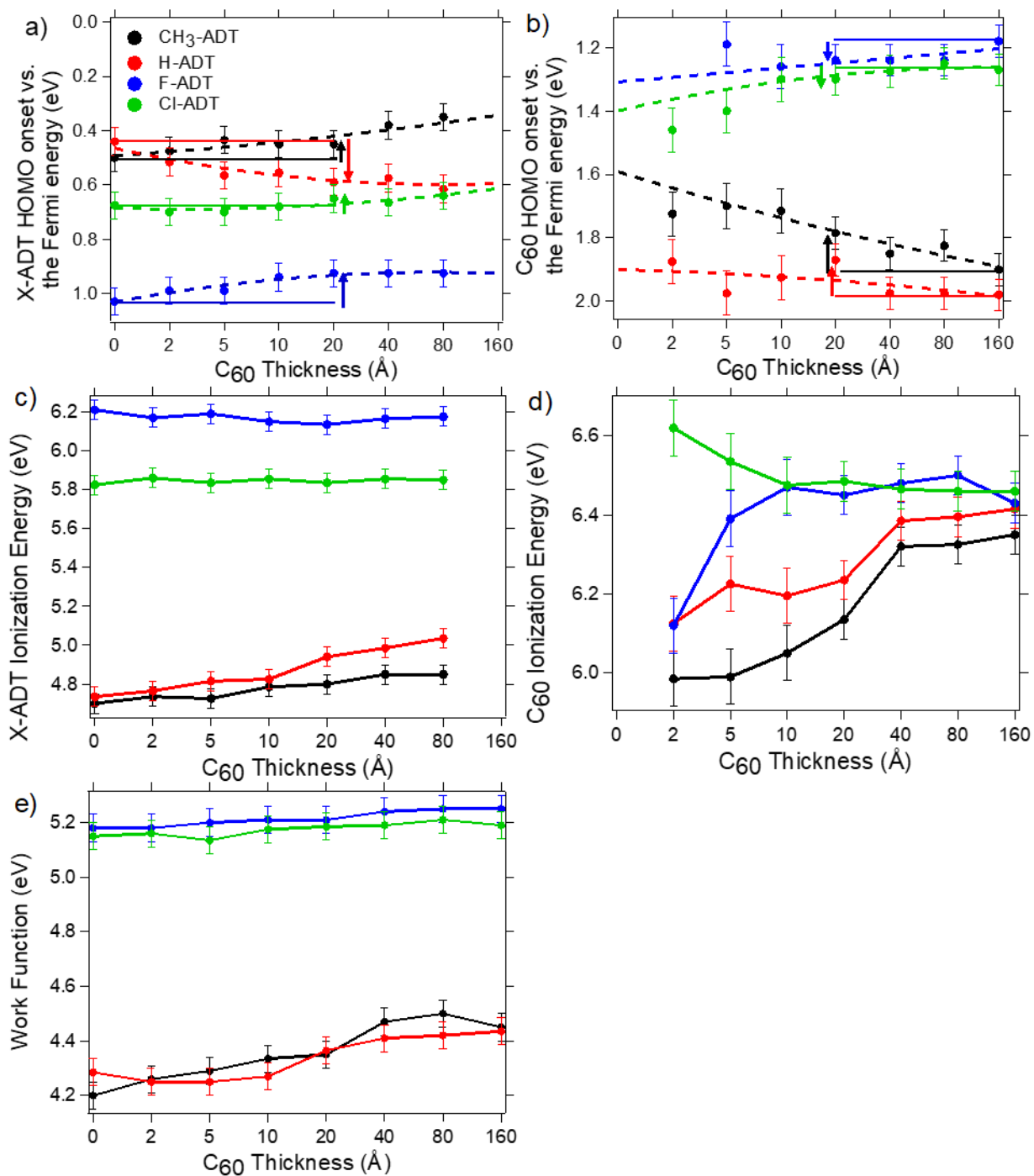


Figure 3.5 HOMO onsets vs. Fermi energy of ADT derivatives (a) and C₆₀ (b), Ionization energies of ADT derivatives (c) and C₆₀ (d) and work functions (e) as a function of C₆₀ thickness. Dashed lines show an approximate trend for the points. Solid lines simply have connected the points in the graph.

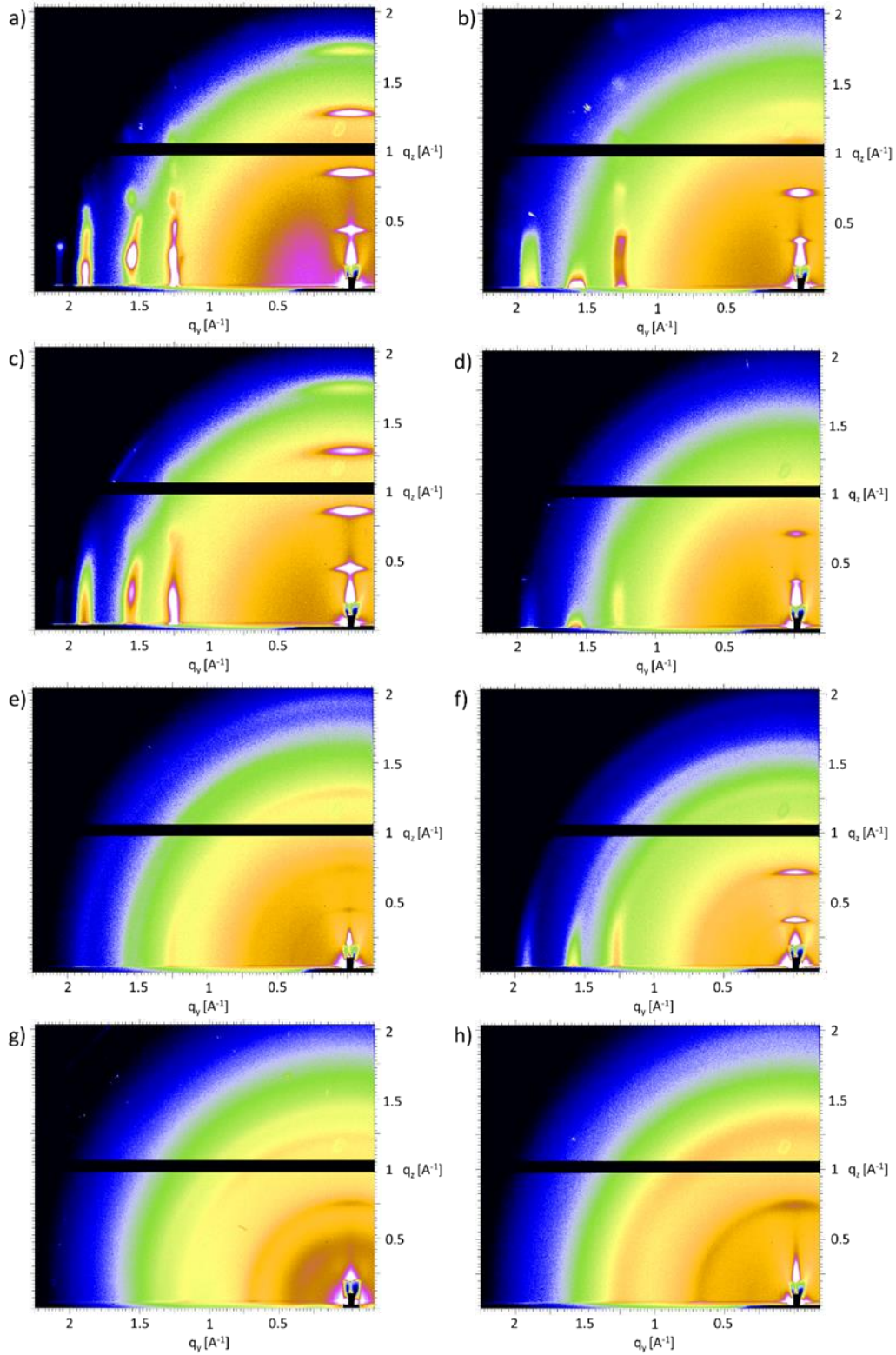


Figure 3.6 GIWAXS measurements of H-ADT:C₆₀ (a,c,e,g) and Cl-ADT:C₆₀ (b,d,f,h) blends with different ratio of C₆₀. Pure X-ADT (a,b), 9:1 (c,d), 1:1 (e,f) and 1:9 (g,h)

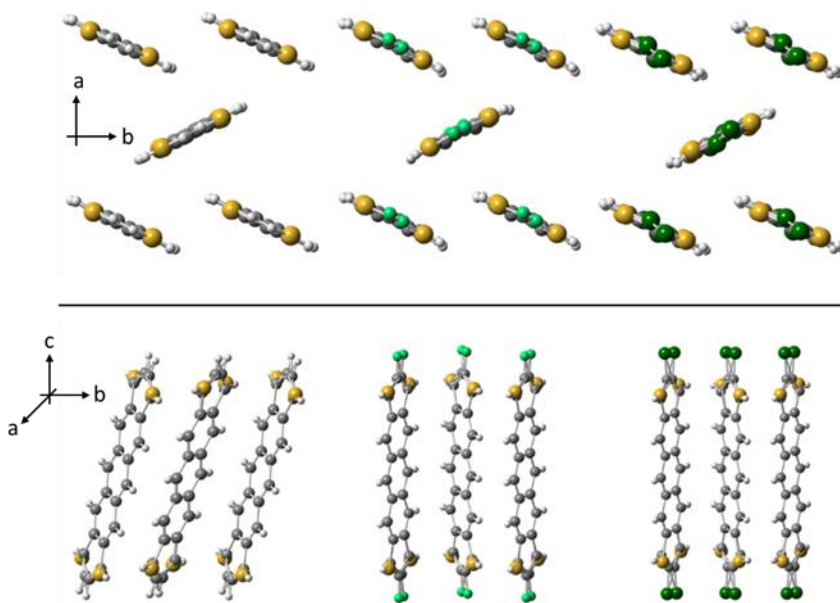


Figure 3.7 Crystal structures for H-ADT, F-ADT, and Cl-ADT in order from left to right. The crystal structure for H-ADT is taken from Mamada, *et al.*¹³⁹ and the structures for F-ADT and Cl-ADT were experimentally determined in our laboratories using single crystal X-ray diffraction.

DFT calculations of the isolated ADT derivatives show that the HOMO of H-ADT lies 0.13 eV and 0.19 eV higher than the HOMOs of Cl-ADT and F-ADT, respectively. While this trend does mirror the UPS measurements, the overall difference is greatly reduced; experimentally, we measure differences of 1.1 and 1.48 eV between the IEs of H-ADT and Cl-ADT or F-ADT, respectively. These large differences are most likely explained by the fact that we are comparing gas-phase calculations to macroscopic solid-state experimental measurements. We contend that the significant differences in the molecular quadrupoles, as listed in Table 3.1, are key factors for the massive difference in IEs between the CH₃ or H terminated ADTs and the Cl or F terminated ADTs.^{140,141} A quintessential example demonstrating the effect of quadrupole sign and resulting surface dipole on IE is the large (up to 0.6 eV) change in IE for the same molecule as the molecular orientation changes from edge-on to face-on.^{93,140} In our X-ADT series the long-axis

quadrupole along the conjugated core shifts from large and positive for CH₃-ADT (29.55 D-Å) to significantly smaller and positive H-ADT (13.99 D-Å) to increasingly negative for F-ADT (-17.53 D-Å) and Cl-ADT (-21.80 D-Å), indicating that the ends of the molecules shift from positive charge to negative charge. Additionally, we see the normal component of the quadrupole (i.e., that due to the π -electron cloud) is largely reduced from H-ADT/CH₃-ADT (-23.92/-30.01 D-Å) to F-ADT/Cl-ADT (-8.24/-6.69 D-Å) indicating that the π electron density is being pulled from the conjugated core to the halogenated end groups. Using the trends from our DFT calculated quadrupoles, the molecular orientations determined by GIWAXS, and the formulas presented in the work by the Koch group,^{140,141} we predict that the IEs of H-ADT and CH₃-ADT will be less than Cl-ADT and F-ADT based purely on quadrupolar and surface dipole/orientation effects. Alternative models,¹⁴²⁻¹⁴⁴ whereby orientation dependent variations in IEs are attributed primarily to how molecular orientations affect the polarization energies in thin films without explicitly accounting for surface dipoles, should also predict a lower IE of H-ADT and CH₃-ADT vs. Cl-ADT and F-ADT based primarily on the tip-on orientations and quadrupolar interactions.

Table 3.1 Molecular quadrupole principal components for H-ADT, CH₃-ADT, F-ADT, and Cl-ADT determined via distributed multipole analysis of the ω B97X-D/6-31G(d,p) density matrix. θ_{XX} , θ_{YY} , and θ_{ZZ} correspond to the molecular long axis, short axis, and normal axis, respectively. All data are given in units of Debye-Angstroms.

System	θ_{XX}	θ_{YY}	θ_{ZZ}
H-ADT	13.99	9.93	-23.92
CH ₃ -ADT	29.55	0.46	-30.01
F-ADT	-17.53	25.77	-8.24
Cl-ADT	-21.80	28.49	-6.69

The UPS results and plots of energy levels presented in Figure 3.2, Figure 3.3, Figure 3.4 and Figure 3.5 show that the dipole at the X-ADT/C₆₀ interface varies as CH₃-ADT > H-ADT > F-ADT = Cl-ADT. Here, the interface dipole is taken as the shift in the work function between the pure X-ADT film and the film with 40 Å C₆₀. In the case of H-ADT the interface dipole points towards the ADT side, following the convention used in most UPS studies with the interface dipole pointing towards the positive end. Initially, we expected that the interface dipole for F-ADT and Cl-ADT would point in the opposite direction as H-ADT and CH₃-ADT, owing to the greater electronegativity of the F and Cl atoms and the predicted effects on the molecular quadrupole. Indeed, this assumption is supported by the sign change in the long-axis quadrupole component from theoretical calculations. Instead, we find that there is almost no interface dipole between the halogenated ADTs and C₆₀, and the small 0.04 eV dipole points in the same direction as the CH₃-ADT/C₆₀ and H-ADT/C₆₀ interface dipoles.

The energy landscapes displayed in Figure 3.4 and Figure 3.5 show that the CH₃-ADT/C₆₀ and H-ADT/C₆₀ interfacial energetics appear more favorable for dissociating interfacial charge-transfer states. Here, the HOMO of H-ADT bends away from the Fermi level as C₆₀ is deposited. This, combined with the shift in vacuum level, leads to an increase in the IE of H-ADT from 4.73 eV without C₆₀ to 4.96 eV with 20 Å C₆₀. Furthermore, the HOMO of C₆₀ bends upwards at the interface with H-ADT. Assuming that the LUMO parallels the HOMO for C₆₀, this upward bending of the HOMO at the interface would mean that the LUMO also bends upwards at the interface. Accordingly, it is more energetically favorable for both holes in H-ADT and electrons in C₆₀ to move away from the interface. By contrast, for the halogenated ADTs the energy landscape is nearly flat,

with a small amount of unfavorable upward bending of the X-ADT HOMOs and downward bending of the C₆₀ LUMO at the interface. Contrary to our expectations, these bilayer studies indicate that halogenation leads to a less favorable energy landscape for charge separation in the halogen-ADT/C₆₀ systems. These interfacial energetic shifts most likely arise primarily from a combination of interfacial electrostatic interactions (e.g., quadrupole-induced dipole) and interfacial disorder. For example, it was shown through both experiment and theoretical calculations that interfacial energetic disorder may contribute to interfacial energetic shifts,^{145,146} while theoretical calculations have shown how interfacial electrostatic interactions can lead to shifts in energy states at donor-acceptor interfaces.^{38,124,147,148}

To further probe interfacial energetics in the materials, we fabricated bilayer OPV devices and utilized sensitive EQE measurements to probe the CT state absorbance, with the EQE and current-voltage characteristics presented in Figure 3.8. The bilayer OPV results show higher short-circuit current densities (J_{SC}) for the H-ADT/C₆₀ devices as compared to the F-ADT/C₆₀ and Cl-ADT/C₆₀ devices. This increased J_{SC} for H-ADT/C₆₀ bilayers is consistent with a more favorable energetic landscape for charge separation. However, due to the number of variables that can influence J_{SC} (e.g., exciton diffusion length, charge carrier mobilities, absorption coefficients, charge-transfer state dissociation probability) it is not possible to definitively say whether the increased J_{SC} for H-ADT/C₆₀ devices arises from the more favorable energetic landscape.

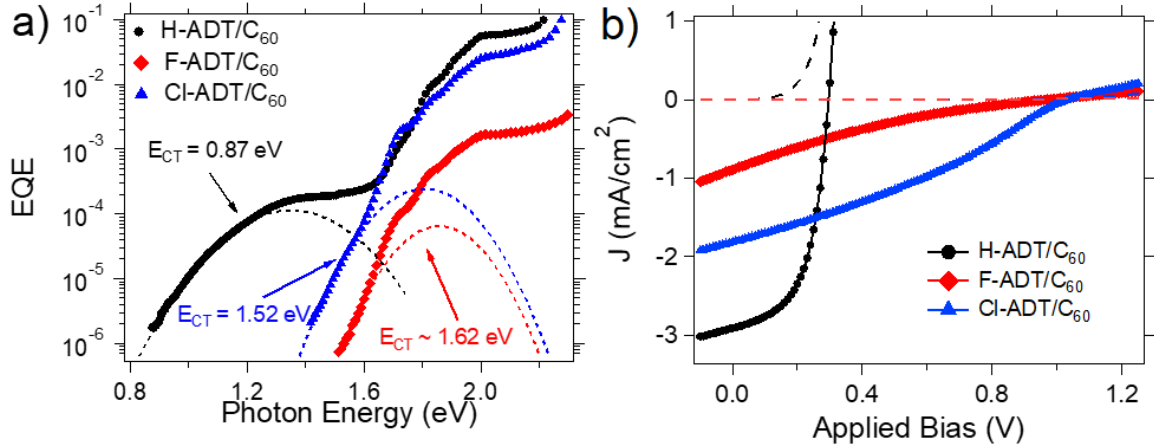


Figure 3.8 a) Sensitive EQE of H-ADT/C₆₀, F-ADT/C₆₀ and Cl-ADT/C₆₀ bilayer PV devices. The fit to the CT states is shown with dashed lines. b) Current density vs. voltage characteristics in the dark and under AM1.5G illumination.

The CT absorbance bands in the EQE spectra are fit with Equation (3.1).¹⁴⁹ Here, E_{CT} is the charge-transfer state energy; f is related to the electronic coupling between the molecules in the CT state, the internal quantum efficiency, and the number of CT states; and λ is related to energetic disorder and the reorganization energy.^{149,150} As shown in Figure 3.8 (a), the CT state energy of the H-ADT/C₆₀ bilayer is 0.87 eV, compared to 1.52 eV for the Cl-ADT/C₆₀ bilayer. Only a small edge of the CT state absorbance is evident in the Cl-ADT/C₆₀ bilayer, which makes it difficult to accurately determine all fitting parameters. However, regardless of what values of λ and f are used, E_{CT} remains near 1.52 eV as shown in Figure 3.9. The F-ADT/C₆₀ bilayer CT state is higher in energy than the Cl-ADT/C₆₀ CT state, but with most of the CT absorbance buried under the C₆₀ absorbance we cannot accurately quantify E_{CT} .

$$EQE_{CT} \propto \frac{f}{E\sqrt{4\pi\lambda kT}} \exp\left(-\frac{(E_{CT} + \lambda - E)^2}{4\lambda kT}\right) \quad (3.1)$$

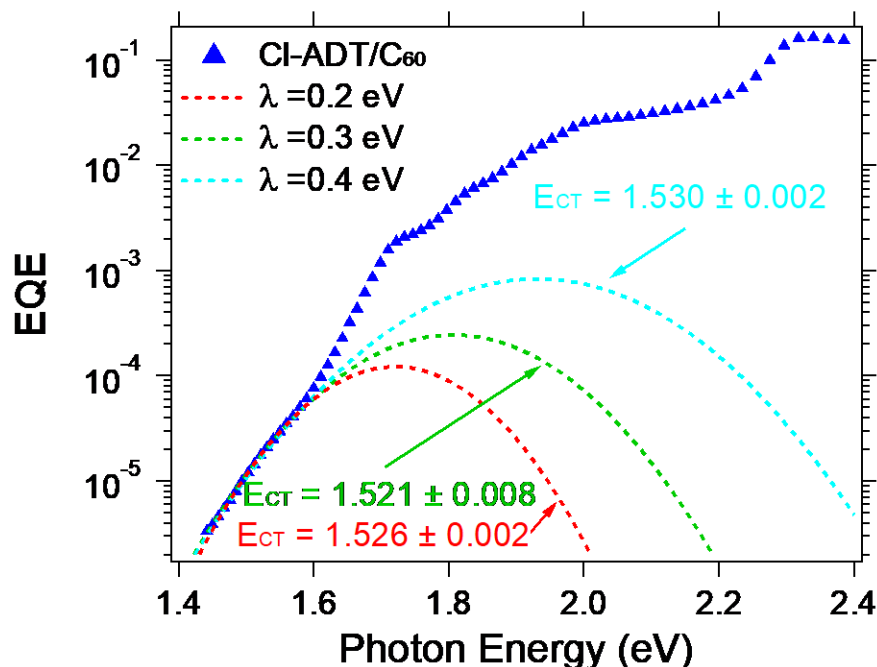


Figure 3.9 EQE of Cl-ADT/C₆₀ bilayer PV device. This graph shows fitting with different λ and f values yield similar CT state energies

Typically, as the CT state primarily involves the HOMO of the donor and LUMO of the acceptor, E_{CT} will vary directly with the IE of the donor if the same acceptor is used. Notably, this is a simplified approximation as it does not account for polarization energy differences between the different donors and C₆₀. Based on the pure H-ADT and Cl-ADT IEs, it is predicted that the H-ADT/C₆₀ and Cl-ADT/C₆₀ CT state energies differ by 1.1 eV, which is 0.45 eV greater than the observed 0.65 eV difference in CT state energies. This discrepancy further supports the interfacial energetic shifts as observed in the UPS measurements. In these UPS measurements the H-ADT IE increases at the interface with C₆₀, while the EA of C₆₀ decreases. These changes in interfacial energetics result in a larger energy difference between the H-ADT HOMO and C₆₀ LUMO at the interface. Based on the HOMO and LUMO levels of H-ADT and C₆₀ at a C₆₀ thickness of 20 Å, our UPS measurements predict that E_{CT} for H-ADT/C₆₀ will be 1.12 eV and E_{CT} for Cl-ADT/C₆₀

will be 1.75 eV. With these energetic shifts accounted for, the measured E_{CT} difference of 0.65 eV agrees well with the predicted E_{CT} difference of 0.63 eV. These results highlight the importance of accounting for the interfacial energetics in determining E_{CT} .

To obtain further insight into these charge transfer states we used time-dependent density functional theory (TDDFT) calculations to evaluate the CT state energies for a tip-on ADT:C₆₀ configuration. Our results follow the same general trends observed in the experimental data; H-ADT:C₆₀ possesses the lowest E_{CT} at 3.20 eV, while F-ADT:C₆₀ and Cl-ADT:C₆₀ have larger E_{CT} s of 3.49 and 3.61 eV, respectively. The absolute values of these calculated results are significantly higher than the experimentally measured E_{CT} values due to only accounting for a single X-ADT molecule and single C₆₀ per configuration. As has previously been demonstrated, expanding the system to include multiple donor and acceptor molecules leads to decreased E_{CT} values through delocalization and polarization effects,^{131,151,152} though the trends are not fully consistent within a given computational method for a broad set of materials.

3.2 Blend Energetics

Blend PV cells and blend films for UPS measurements were fabricated to further experimentally probe the effects of halogenation on material energetics. Specifically, these measurements were carried out to simulate the mixed phases that are present in BHJ PVs. H-ADT and CH₃-ADT display similar trends in E_{CT} and IE values with varying X-ADT:C₆₀ composition, as do F-ADT and Cl-ADT (see Figure 3.10, Figure 3.11, Figure 3.12, Figure 3.13 and Table 3.2). Thus, we primarily focus our discussion on H-ADT:C₆₀ and Cl-ADT:C₆₀ blends. The blends were initially fabricated with both donor rich (9:1 X-ADT:C₆₀) and acceptor rich (1:9 X-ADT:C₆₀) compositions. As shown by the data in

Figure 3.10 and Figure 3.12 and Table 3.2, the H-ADT blends show relatively large changes in IE and E_{CT} between the blends of both compositions and the pure material/bilayers, with the lowest energy states for holes, electrons, and CT states lying in the pure H-ADT phase, pure C_{60} phase, and at interfaces between these pure phases, respectively. This trend is in agreement with previous reports, where IEs, oxidation potentials, and CT energies increase in mixed phases.^{91,122} Whereas, the CI-ADT blends show similar IEs and E_{CT} values in blends of both compositions and the pure materials/bilayers.

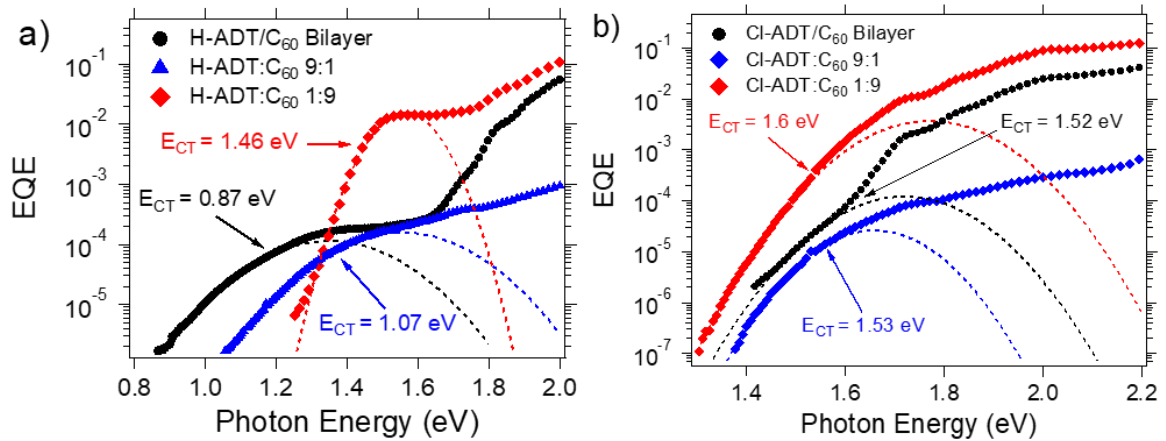


Figure 3.10 EQE of H-ADT/ C_{60} (a) and CI-ADT/ C_{60} (b) bilayers, 9:1, and 1:9 blends with fits to the CT state component indicated by dashed lines.

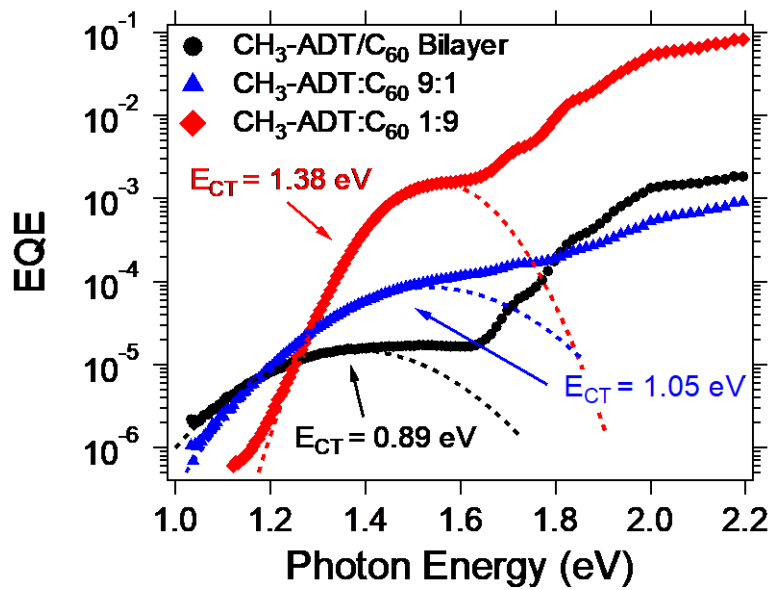


Figure 3.11 EQE spectra of CH₃-ADT:C₆₀ blend and bilayer devices with the fits to the CT band shown with dashed lines.

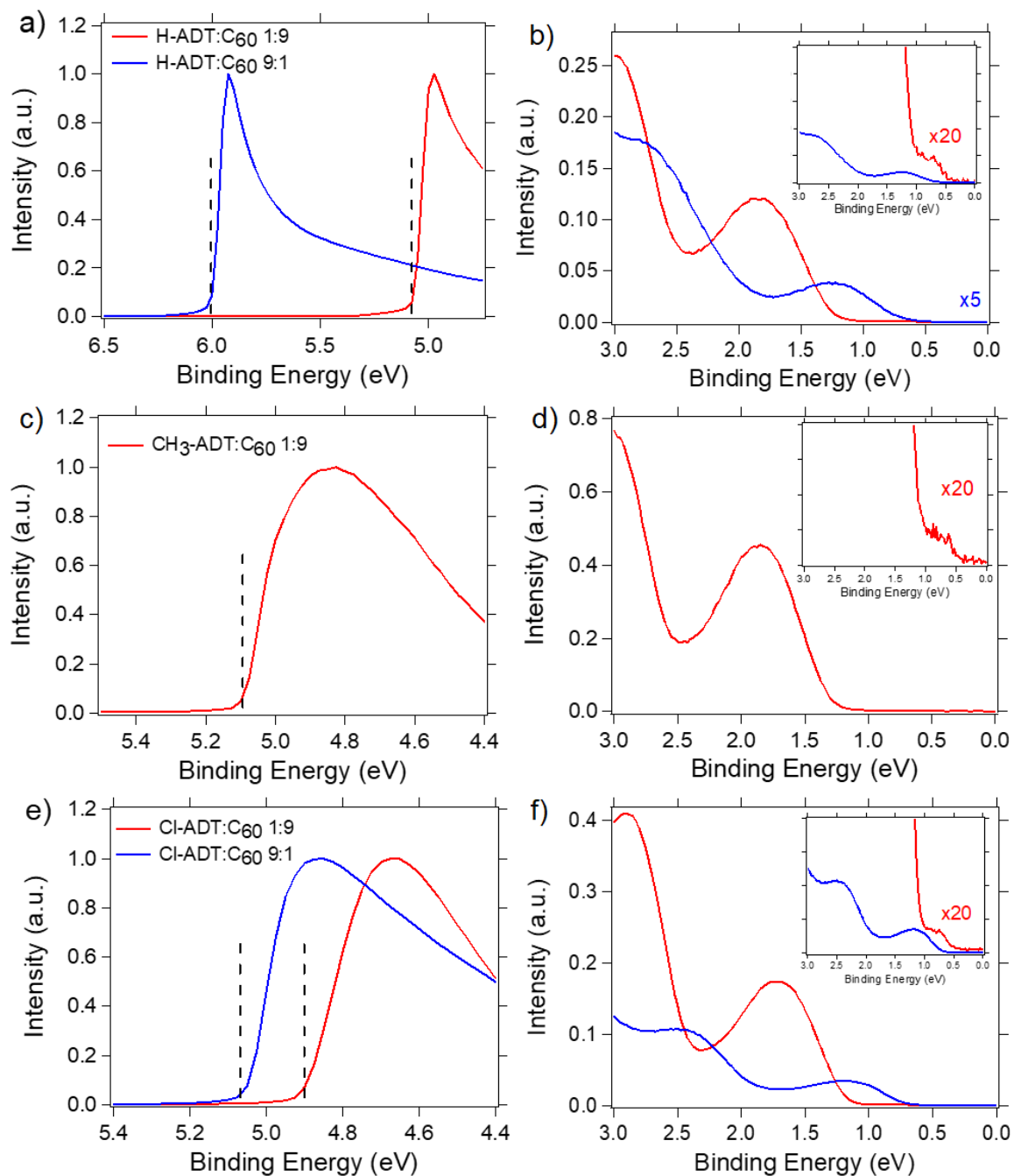


Figure 3.12 UPS spectra of H-ADT:C₆₀ (a,b), CH₃-ADT:C₆₀ (c,d) and Cl-ADT:C₆₀ (e,f) at 1:9 and 9:1 ratios. Plots a,c and e show the SECO regions whereas plots b,d and f show the HOMO onset regions.

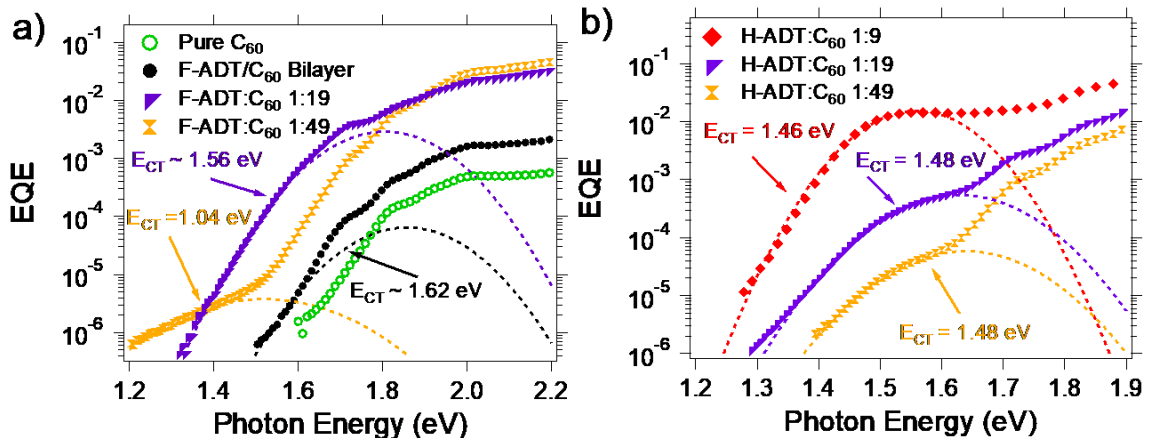


Figure 3.13 EQE spectra of F-ADT:C₆₀ bilayer and blend films (a). The 1:49 F-ADT:C₆₀ blend shows the appearance of a new low-energy CT band. EQE spectra of H-ADT blend films (b).

Table 3.2 Summary of experimentally measured CT state energies, λ , f , and IEs.

Device/Material	E _{CT} [*] (eV)	λ (eV)	$f \times 10^{-3}$ (eV ²)	IE [#] of X-ADT (eV)	IE [#] of C ₆₀ (eV)
H-ADT Bilayer	0.87	0.5	0.066	4.73	6.42
H-ADT 9:1 Blend	1.07	0.5	0.099	4.89	5.94
H-ADT 1:9 Blend	1.46	0.1	4.313	5.51	6.37
H-ADT 1:19 Blend	1.48	0.16	0.198	5.55	6.475
H-ADT 1:49 Blend	1.48	0.17	0.047	-	6.45
Cl-ADT Bilayer	1.52	0.3	0.155	5.83	6.46
Cl-ADT 9:1 Blend	1.53	0.25	0.042	5.85	6.61
Cl-ADT 1:9 Blend	1.6	0.25	5.85	5.8	6.49
Cl-ADT 1:19 Blend	1.4	0.13	0.295	5.54	6.43
Cl-ADT 1:49 Blend	1.39	0.18	0.03	-	6.45
F-ADT Bilayer	1.62	0.25	0.035	6.21	6.4
F-ADT 1:19 Blend	1.56	0.25	1.479	5.77	6.2
F-ADT 1:49 Blend	1.04	0.5	0.002	-	6.4
CH3-ADT bilayer	0.89	0.5	0.008	4.7	6.35
CH3-ADT 9:1	1.05	0.5	0.052	-	-
CH3-ADT 1:9	1.38	0.18	0.557	5.45	6.41

*Uncertainty in E_{CT} is ± 0.03 eV. #Uncertainty in IEs is ± 0.05 eV.

In the donor-rich blends with a 9:1 X-ADT:C₆₀ ratio by volume, the IE of Cl-ADT remains the same as it is in the pure state (*ca.* 5.85 eV), while the IE of H-ADT increases from 4.73 eV in the pure state to 4.89 eV in the 9:1 blend. More drastically, the IE of C₆₀ decreases from 6.42 eV for pure C₆₀ to 5.94 eV in the 9:1 H-ADT blend and increases to 6.61 eV in the 9:1 Cl-ADT blend. Qualitatively, these are similar trends as observed in energetics for the X-ADT/C₆₀ bilayer interfaces, i.e., the IE of H-ADT and C₆₀ increase and decrease, respectively, at the H-ADT/C₆₀ interface, while the IE of Cl-ADT and C₆₀ show more minimal changes at the Cl-ADT/C₆₀ interface. In the acceptor-rich blends with a 1:9 X-ADT:C₆₀ ratio, both the IE of Cl-ADT and C₆₀ remain close to their values in the pure materials; however, the IE of H-ADT increases by nearly 0.8 eV to 5.5 eV. These changes in IEs may arise due to the expected mixture of ADT orientations now present in the film and the molecular orientation effects on the surface dipole,^{140,141} and due to the differing polarization energies afforded by the surrounding C₆₀ molecules.

To further probe energetics in the blend materials, we again performed sensitive EQE measurements on the PV cells and fit the CT state region according to Equation (3.1), as shown in Figure 3.13. The extracted E_{CT} values follow a similar trend as predicted from the UPS measurements of the IEs. Here, E_{CT} increases from 0.87 eV to 1.46 eV in going from the H-ADT bilayer to the 1:9 blend, which largely parallels the increasing IE of H-ADT. Similarly, as the Cl-ADT and C₆₀ IEs varied little between the bilayers and blends, the E_{CT} values for Cl-ADT:C₆₀ blends and bilayers display similar E_{CT} values ranging from 1.52 to 1.6 eV.

One explanation for the significant difference in energetics between the H-ADT:C₆₀ and Cl-ADT:C₆₀ blends is the difference in donor aggregation behavior. For example, one

reason that Cl-ADT may remain the same in bilayer and blend films could be that Cl-ADT has a strong tendency to aggregate and form small crystallites. In this case, the energetics of Cl-ADT are likely to be similar between the blends and bilayers. On the other hand, H-ADT may be well dispersed in the 1:9 blend, thus resulting in a significant change in energetics relative to the pure polycrystalline material. To determine if aggregation is responsible for the nearly constant E_{CT} value in the Cl-ADT:C₆₀ blends, we compare the GIWAXS data for H-ADT and Cl-ADT in the 1:9 C₆₀ blends, as shown in Figure 3.6. For both blends we do not observe any diffraction spots or rings from the ADT derivatives. The diffraction rings that are evident are from C₆₀.¹⁵³ However, small clusters of a handful of molecules are likely to be invisible to GIWAXS, but these small aggregates are likely to show different energetic properties than dispersed single molecules. To further examine if small scale aggregation may be occurring in the 1:9 Cl-ADT:C₆₀ blends, we prepared PV devices with 1:19 and 1:49 ratios. With 19 and 49 times more C₆₀ than Cl-ADT (by volume), the Cl-ADT molecules are more likely to be molecularly dispersed in the C₆₀ matrix than in the 1:9 blend. Surprisingly, in both higher-ratio Cl-ADT:C₆₀ blend devices a lower energy CT state clearly emerges in the EQE spectrum, as shown in Figure 3.14 (a). The most likely explanation for the appearance of this new lower-energy CT state is that the Cl-ADT transitioned from being primarily in small clusters in the 1:9 blend to being primarily molecularly dispersed in the 1:19 and 1:49 blends. The CT state in both blends is 0.13 eV lower than in the bilayer device. To the best of our knowledge, this is the first example where E_{CT} decreases in moving from donor/C₆₀ bilayers to blends. To verify that this trend was not unique to Cl-ADT devices, we also prepared blend devices with F-ADT at 1:19 and 1:49 F-ADT:C₆₀ ratios. As evident in Figure 3.13, the 1:49 F-ADT:C₆₀ blend

shows the appearance of a low energy CT state at 1.04 eV that is not apparent in the bilayer devices.

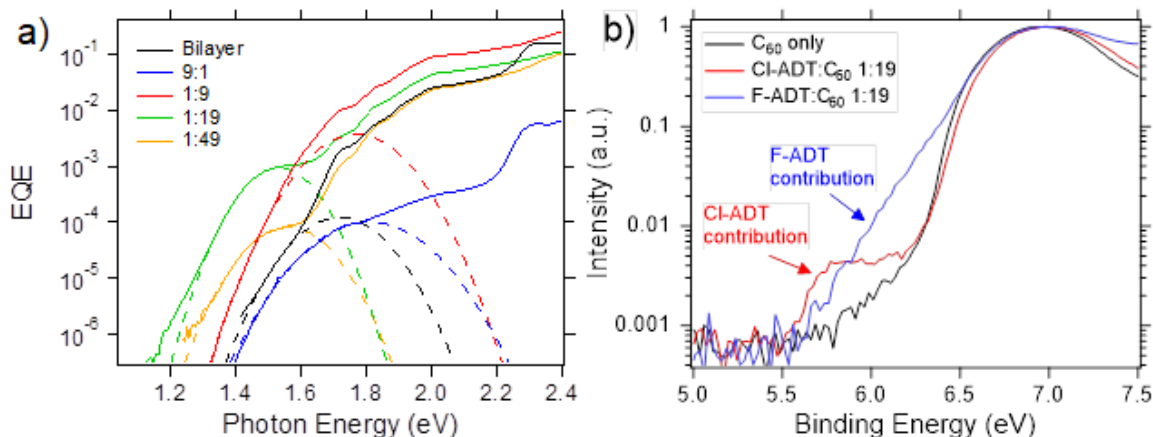


Figure 3.14 EQE spectra of CI-ADT:C₆₀ blend and bilayer PVs with fits to the CT absorbance band shown (a), and UPS spectra of pure C₆₀, CI-ADT:C₆₀, and F-ADT:C₆₀ blends at a 1:19 ratio (b). In the UPS spectra the binding energy is referenced to the vacuum level at 0 eV.

The energetics in the 1:19 and 1:49 blend films with CI-ADT and F-ADT were further investigated by UPS. In the 1:49 blends the signal from the ADT derivatives is below our limit of detection, as shown in Figure 3.15, but in the 1:19 blends a clear signal from the ADT derivatives is apparent. Figure 3.14(b) shows the UPS spectra of these 1:19 blends on a semi-log plot, with the spectra shifted by the work functions to put the vacuum levels at 0 eV. In agreement with the EQE measurements of the CT states, both F-ADT and CI-ADT show lower IEs in these blends with C₆₀. Fitting of these spectra with a linear y-axis shows IEs for F-ADT and CI-ADT of ca. 5.77 and 5.54 eV, which are 0.44 and 0.29 eV lower than in the pure F-ADT and CI-ADT films, respectively. Overall, this combination of CT state measurements and IE measurements clearly shows that both energies are lowered in these dilute X-ADT:C₆₀ blends.

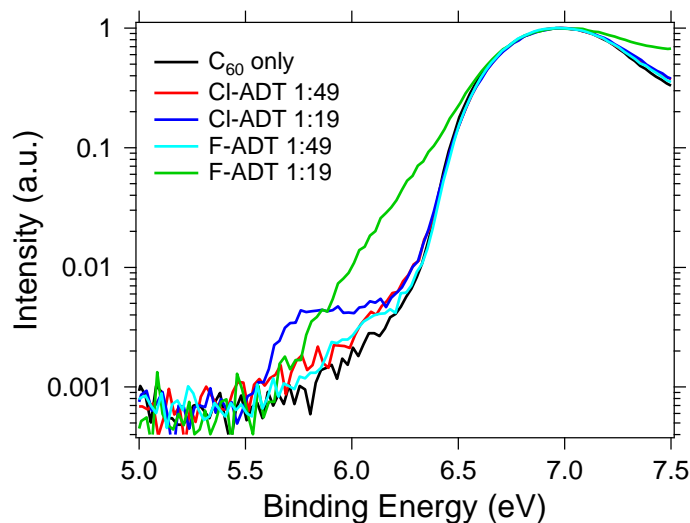


Figure 3.15 UPS spectra for pure C₆₀, CI-ADT:C₆₀ 1:19 and 1:49 blend, and F-ADT:C₆₀ 1:19 and 1:49 blend. The data are plotted with the vacuum level at 0 eV.

We turn again to TDDFT calculations to determine if the opposite trends in E_{CT} in going from bilayers to blends observed for the non-halogenated and halogenated ADT derivatives may in part arise due to the molecular arrangement of the CT state (tip-on for bilayer vs. all orientations present in the blend) and associated electrostatic interactions. In the bilayer systems, GIWAXS shows that CI-ADT molecules are oriented tip-on with respect to the substrate and deposited C₆₀ layer. Although we assume that the CT states are predominantly tip-on for the bilayers based on the GIWAXS measurements, we note that GIWAXS is a bulk measurement and is not specific to molecules at the surface (where the CT states will form) or molecules in amorphous regions. TDDFT results show the face-on and edge-on orientations have larger CT state oscillator strengths (Table 3.3), and thus these face-on and edge-on CT complexes are expected to be the dominant contributors to the CT absorbance in the low donor blends. Therefore, the CT absorbance band is viewed as representing the tip-on orientation in the bilayers and the face-on and edge-on orientations for the dilute blends. Looking at the orientation dependence of the CT state energy in H-

ADT:C₆₀ and Cl-ADT:C₆₀ complexes (Figure 7 and Table 3.3), the calculated E_{CT} values do show a strong dependence on the molecular orientation. However, the dependence of the CT state energy of these dimers alone are insufficient to fully explain the experimental results. For example, the calculated CT state energies of all X-ADT:C₆₀ tip-on configurations are 0.71 to 0.89 eV higher than for the face-on configurations; yet, experimentally the tip-on CT states (bilayers) are lower in energy than the face-on CT states (blends) for the CH₃-ADT:C₆₀ and H-ADT:C₆₀ systems. This disagreement suggests that orientation effects alone cannot explain the observed experimental data. Rather, polarization and delocalization effects due to gross changes in the molecular environments must be accounted for and are likely responsible for the shifts in CT energies when comparing the bilayer and blend configurations.

Table 3.3 Calculated E_{CT} and oscillator strengths (f) values of X-ADT:C₆₀ complexes with varying orientations. Details of calculations are provided in the Methods section of the main document.

X-ADT and orientation	E_{CT} (eV)	f
H-ADT:C ₆₀ face-on	2.49	0.0155
H-ADT:C ₆₀ tip-on	3.20	0.0012
H-ADT:C ₆₀ edge-on	2.71	0.0179
Cl-ADT:C ₆₀ face-on	2.72	0.0252
Cl-ADT:C ₆₀ tip-on	3.61	0.0000
Cl-ADT:C ₆₀ edge-on	2.94	0.0254
CH ₃ -ADT:C ₆₀ face-on	2.46	0.0205
CH ₃ -ADT:C ₆₀ tip-on	3.21	0.0146
CH ₃ -ADT:C ₆₀ edge-on	2.91	0.0299
F-ADT:C ₆₀ face-on	2.69	0.0229
F-ADT:C ₆₀ tip-on	3.49	0.0017
F-ADT:C ₆₀ edge-on	2.83	0.0181

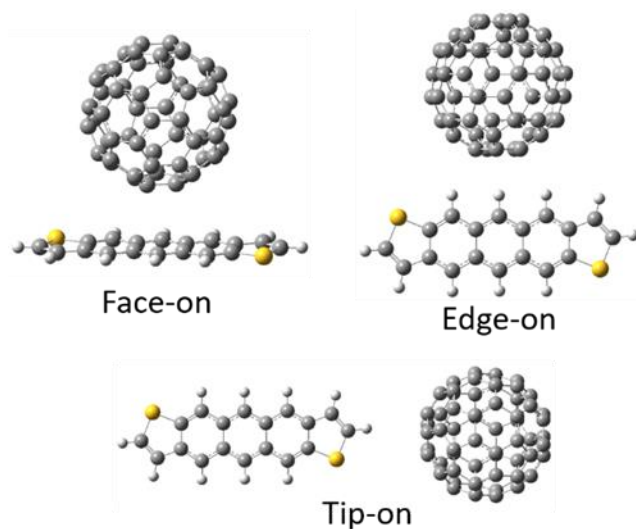


Figure 3.16 Schematic of the intermolecular orientations investigated in the DFT calculations.

3.3 Conclusion

The dipole at the X-ADT/C₆₀ interface does not reverse in direction when the terminal hydrogen atom is substituted by either fluorine or chlorine, rather this dipole is reduced from 0.15 to 0.04 eV. Whereas previous theoretical calculations indicated more favorable energy landscapes for charge separation when C₆₀ is interacting with the more electronegative part of a molecule, our UPS measurements indicate that the energy landscape is more favorable for charge separation when C₆₀ is interacting with a more electropositive end group, e.g., hydrogen. Furthermore, our measurements of blend material systems indicate that halogenation of ADT molecules can lead to lower CT state energies in the mixed phase relative to at interfaces between pure phases. However, the halogenated compounds appear to have a high propensity to aggregate, with the molecularly dispersed phase only evident at ADT concentrations of around 5% and below. In this ADT material system, the less favorable energy landscape for high PV performance upon halogenation suggests that commonly observed performance improvements in OPV materials upon fluorination are not due to energetics, and thus may be attributed more to morphological effects. For example, lower fullerene miscibility in the donor phase and *vice versa*, or a more favorable intermolecular arrangement between donor and acceptor (e.g., face-on).¹⁰⁴ Furthermore, as the energetics will likely vary with molecular orientation, fluorination may lead to more favorable energy landscapes for BHJ PVs if a face-on donor-acceptor orientation is adopted at the interfaces between donor rich and acceptor rich domains. Future directions involve seeing if these same trends apply to high-performing fluorinated polymers used in BHJ PVs.

CHAPTER 4. THERMOELECTRIC POWER FACTOR ENHANCEMENT IN POLYMER BLEND

This chapter is reprinted with permission from A. Abtahi *et. al.*, “Designing π -conjugated polymer blends with improved thermoelectric power factors”, *J. Mater. Chem. A*, 2019,7, 19774-19785, Copyright © 2019 Royal Society of Chemistry⁵⁰

4.1 Introduction

Increasing energy efficiency and providing continuous power for remote sensors or wearable electronic devices is a continuously growing challenge. Thermoelectric (TE) devices are an appealing technology to address this challenge, as these devices can convert waste heat produced by various mechanical, chemical, biological and other processes into electricity.¹⁵⁴⁻¹⁵⁶ Inorganic TE materials such as bismuth chalcogenides and lead telluride have been studied for half a century and show relatively high performance over a wide temperature range, but the high cost of materials and device fabrication, as well as their rigid form factors, have limited their practical use.^{157,158} OSCs, and particularly π -conjugated polymers, are emerging as promising alternative TE materials for low grade waste heat recovery owing to the use of potentially low-cost materials and fabrication methods, mechanical flexibility, and low weight.^{27,29,159-163}

The maximum energy conversion efficiency achievable by a TE device is proportional to the thermoelectric figure of merit ZT , $ZT = T \frac{S^2 \sigma}{\kappa}$, where S is the Seebeck coefficient, σ the electrical conductivity, κ the thermal conductivity and T the temperature.¹⁶⁴ The Seebeck effect refers to the electromotive force created by a temperature difference across a material, with S defined as the electrical potential difference induced by a 1 K temperature differential (with units of volt per Kelvin). The

Seebeck coefficient is determined by the average energy of charge carriers (with respect to the Fermi energy) contributing to the electrical conductivity at a certain temperature. Since polymers are generally poor thermal conductors, and have similar thermal conductivity ($0.1\text{-}0.3 \text{ Wm}^{-1}\text{K}^{-1}$),^{162,165-169} the power factor ($P=S^2\sigma$) is the primary metric that must be improved to increase the efficiency of organic TE devices.

Most intrinsic π -conjugated polymers have low electrical conductivities, which limits their TE performance. By introducing additional charge carriers in π -conjugated polymers, typically through molecular doping, σ increases significantly and they can reach reasonably high TE performance, with record ZT values in the range of $0.1\text{-}0.42$ at room temperature, with some uncertainty due to potential artifacts arising from the Seebeck coefficient measurement geometry.^{162,170,171} Increasing the charge carrier concentration, as is typically accomplished through increasing the dopant concentration, can lead to higher σ , but the increase in σ typically comes at the expense of S . This trade-off between σ and S limits the power factor.^{163,168,172,173} Commonly, σ in π -conjugated polymers varies much more drastically than S , which has driven extensive efforts to increase σ by choosing different dopants,^{27,162,168,170,172,174-177} manipulating the doping method,^{163,178,179} designing new polymer structures,^{27,180,181} or varying the material processing conditions.^{159,160,168,172,173}

Another method to improve the power factor of both organic and inorganic TE materials is through manipulating the density of states (DOS),¹⁸²⁻¹⁸⁴ such as may be accomplished by blending two different polymers or a polymer with carbon nanotubes or graphene.^{185,186} These blend systems provide a potential means to surpass the power factors of the individual materials imposed by the trade-off between σ and S . The idea with

polymer blends is that by adding a polymer with a different energetic distribution of states to the initial polymer, the energy difference between the Fermi energy and the transport states can be more controllably adjusted and even increased. To date, this approach has primarily led to higher Seebeck coefficients in blends of π -conjugated polymers, but not significantly higher power factors. Previously Zuo *et al.*⁴³ showed that by blending different polymers the Seebeck coefficient in the blend can surpass S of the individual polymers. In their work, blends of P3HT_{0.1}:PTB7_{0.9} and P3HT_{0.05}:TQ1_{0.9} reached S of $\approx 1100 \mu\text{VK}^{-1}$ and $\approx 2000 \mu\text{VK}^{-1}$, which surpassed S for the single polymers ($S_{\text{P3HT}}=142 \mu\text{VK}^{-1}$, $S_{\text{PTB7}}=469 \mu\text{VK}^{-1}$ and $S_{\text{TQ1}}=1560 \mu\text{VK}^{-1}$). Conceptually, the polymer with the lower energy states can pin the Fermi energy, which results in the other polymers DOS lying further from the Fermi energy. When the polymer with the lower energy states is included at a low concentration, a significant amount of transport may occur through the material with states at higher energies with respect to the Fermi energy. Thus, the charge carriers contributing to σ have a higher average energy and S increases.^{43,182,183}

The Seebeck coefficient is not only determined by the distribution of the mobile charge carriers relative to the Fermi energy; rather, it is determined by how the charge carriers in these different energy states contribute to the total electrical conductivity. In other words, S is determined by the energy dependence of σ . Thus, the Seebeck coefficient should increase as the mobility of higher energy charge carriers increases relative to the mobility of lower energy charge carriers. Polymer blends provide an ideal platform for systematically manipulating the energy dependence of charge transport through blending polymers with different transport energies and charge-carrier mobilities. In this work we combine theory and experiments to investigate how the mobility ratio between the

polymers, combined with the energy offsets between the DOS distributions and the width of the DOS distributions, contribute to the Seebeck coefficient, electrical conductivity, and the power factor in polymer blends. Notably, processing conditions, dopant choice, polymer structures, and film morphology will also all influence the thermoelectric properties in these blends, but they are beyond the scope of this current work.

From the theoretical side, we apply a slightly modified version of the model introduced by Arkhipov and Bässler to model how transport occurs in a single polymer and in polymer blends.¹⁸⁷ In this model we use the Miller-Abrahams jump rate equation to account for jump distance and energetic differences between localized states, combined with Gaussian disorder, to model charge carrier transport in OSCs.⁴⁰ Using this model, we primarily focus on how the width of the DOS, the localization length, and the energy offset between the DOS of the different polymers in the blend impact S , σ , and the power factor. We find that in a single polymer a narrow DOS is the most important requirement for achieving high power factors. Calculations of polymer blends show that power factors can be improved over both individual polymers. For this improvement to be realized, the polymer with its DOS centered at a higher energy should have a higher localization length and broader DOS than the polymer with its DOS centered at a lower energy. Experimentally, we investigate 3 different polymer blend systems, where in each blend the ratio of the two polymers is varied from 1:0 to 0:1. Our experimental results are in agreement with theoretical predictions and show that power factors in polymer blends can indeed exceed those of the individual polymers at the same doping concentrations.

4.2 Theoretical model

Since the discovery of electrically conducting polymers, many groups have investigated charge transport in disordered systems using different models of transport mechanisms.^{27,42,44,178,183,187–195,195–207} In π -conjugated polymers, charge transport occurs through jumping between localized states that are typically described as having a Gaussian distribution, especially at high charge-carrier concentrations when most of the low energy trap states are populated.^{44,60,187,190,194,208,209} The jump rate between these states depends on both the spatial distance, localization length, and energy difference between an occupied starting state and the nearby unoccupied target states.^{44,187,190,195,196} Using the generalized Einstein equation we can calculate the average charge-carrier mobility as a function of the energy of the charge carrier and from there we can calculate σ and S .^{187,200}

The Gaussian DOS is given by Equation (4.1):

$$g(E) = \frac{N_t}{\sqrt{2\pi}\Delta} \exp\left[-\frac{(E - E_0)^2}{2\Delta^2}\right] \quad (4.1)$$

Where $g(E)$ is the distribution of states as a function of energy, N_t is the total number of states per unit volume, Δ is the width of the DOS, and E_0 is the mean energy of all states. N_t for most polymers is usually in the range of 10^{20} - 10^{21} cm^{-3} and Δ , which is a characteristic of the energetic disorder,⁷³ is in the range of a few $K_B T$ (K_B is the Boltzmann constant).^{73,190,194,200,209} We use the Miller-Abrahams jump rate equations to explain the jump rate (v) between states, as given by Equation (4.2):^{40,188,190}

$$v(r_{ij}, E_i, E_j) = v_0 \exp[-R(r_{ij}, E_i, E_j)] = v_0 \exp\left[-2 \frac{r_{ij}}{\alpha} - \frac{(E_j - E_i) + |E_j - E_i|}{2 K_B T}\right] \quad (4.2)$$

Where ν_0 is the attempt to jump frequency, R the hopping parameter, α the localization length, r_{ij} the jump distance, and E_i and E_j are energies for the starting and final states of a charge carrier. The localization length defines the decay length between wave functions of localized states, which for polymers are generally in the range of 1 to 5 Å.^{184,190,195,206,207,210,211} To make a connection between α and the DOS, we define a parameter called the intrinsic length a ($a=N_i^{-1/3}$). The intrinsic length has the same units as α , as it is defining an average length between localized states. In a polymer, α is expected to be smaller than a .^{190,194,195,200,209,210} In the model introduced by Arkhipov and Bässler, which we use in this work to calculate the energy dependent mobility of charge carriers, the average number of available hoping sites for a charge carrier starting at energy E_i whose hopping parameter is smaller than R is calculated by Equation (4.3).

$$\begin{aligned}
n(E_i, R) &= 4\pi \int_0^{R\frac{\alpha}{2}} r^2 dr \int_{-\infty}^{E_i+K_B T \left(R-r\frac{2}{\alpha}\right)} g_u(E_j, E_F) dE_j \\
&= 4\pi \left[\int_0^{R\frac{\alpha}{2}} r^2 dr \int_{-\infty}^{E_i} g_u(E_j, E_F) dE_j \right. \\
&\quad \left. + \int_0^{R\frac{\alpha}{2}} r^2 dr \int_{E_i}^{E_i+K_B T \left(R-r\frac{2}{\alpha}\right)} g_u(E_j, E_F) dE_j \right] \tag{4.3}
\end{aligned}$$

The first term can be integrated separately and the second term can be simplified by changing the order of integration:

$$\begin{aligned}
n(E_i, R) &= 4\pi \left[\frac{1}{3} \left(R \frac{\alpha}{2} \right)^3 \int_{-\infty}^{E_i} g_u(E_j, E_F) dE_j \right. \\
&\quad \left. + \int_{E_i}^{E_i + K_B T (R)} g_u(E_j, E_F) dE_j \int_0^{\frac{\alpha}{2} \left(R - \frac{E_j - E_i}{K_B T} \right)} r^2 dr \right] \\
&= 4\pi \left[\frac{1}{3} \left(R \frac{\alpha}{2} \right)^3 \int_{-\infty}^{E_i} g_u(E_j, E_F) dE_j \right. \\
&\quad \left. + \int_{E_i}^{E_i + K_B T (R)} g_u(E_j, E_F) dE_j \frac{1}{3} \left(\frac{\alpha}{2} \left(R - \frac{E_j - E_i}{K_B T} \right) \right)^3 \right] \\
&= \frac{4\pi}{3} \left(R \frac{\alpha}{2} \right)^3 \left[\int_{-\infty}^{E_i} g_u(E_j, E_F) dE_j \right. \\
&\quad \left. + \int_{E_i}^{E_i + K_B T R} \left(1 - \frac{E_j - E_i}{R K_B T} \right)^3 g_u(E_j, E_F) dE_j \right]
\end{aligned} \tag{4.4}$$

Further simplification will lead to (4.5).

$$\begin{aligned}
n(E_i, R) &= \frac{\pi}{6} \alpha^3 R^3 \left(\int_{-\infty}^{E_i} g_u(E_j, E_F) dE_j + \int_{E_i}^{E_i + K_B T R} g_u(E_j, E_F) \left(1 - \right. \right. \\
&\quad \left. \left. \frac{E_j - E_i}{K_B T R} \right)^3 dE_j \right)
\end{aligned} \tag{4.5}$$

Here, $g_u(E, E_F)$ is the density of unoccupied states and E_F is the Fermi energy. The density of unoccupied states is calculated using the Fermi-Dirac distribution:

$$g_u(E, E_F) = g(E)(1 - f_{FD}(E, E_F)) \tag{4.6}$$

Where f_{FD} is the Fermi-Dirac distribution ($f_{FD}(E, E_F) = (1 + \text{Exp}(\frac{E - E_F}{K_B T}))^{-1}$). The

Fermi energy can be determined by solving the following equation:

$$N_C = \int_{-\infty}^{\infty} g(E) f_{FD}(E, E_F) dE \quad (4.7)$$

Where N_C is the total number of charge carriers per unit volume. For simplicity, in this study we neglect the effect of backwards jumps.¹⁸⁷ By using a Poisson distribution, the average hopping parameter $\langle R \rangle$ and average squared jump distance $\langle r^2 \rangle$ can be calculated. The probability density of hopping with hopping parameter R is shown by Poisson distribution as below:

$$P(E_i, R) = \frac{\partial n(E_i, R)}{\partial R} e^{-n(E_i, R)} \quad (4.8)$$

So, the average hopping parameter is equal to:

$$\langle R \rangle(E_i) = \int_0^{\infty} R P(E_i, R) dR = \int_0^{\infty} R \frac{\partial n(E_i, R)}{\partial R} e^{-n(E_i, R)} dR \quad (4.9)$$

Using integration by parts we arrive at:

$$\langle R \rangle(E_i) = -R e^{-n(E_i, R)} \Big|_0^{\infty} - \int_0^{\infty} (-e^{-n(E_i, R)}) dR = \int_0^{\infty} e^{-n(E_i, R)} dR \quad (4.10)$$

First term is zero at both limits ($\lim_{R \rightarrow \infty} n(E_i, R) = \infty$), so average R is simply equal to:

$$\langle R \rangle(E_i) = \int_0^{\infty} e^{-n(E_i, R)} dR \quad (4.11)$$

Average squared jump distance is equal to:

$$\langle r^2 \rangle(E_i) = \frac{4\pi \int_0^{\langle R \rangle(E_i) \frac{\alpha}{2}} (r^2) r^2 dr \int_{-\infty}^{E_i + K_B T (\langle R \rangle(E_i) - r \frac{2}{\alpha})} g_u(E_j, E_F) dE_j}{4\pi \int_0^{\langle R \rangle(E_i) \frac{\alpha}{2}} r^2 dr \int_{-\infty}^{E_i + K_B T (\langle R \rangle(E_i) - r \frac{2}{\alpha})} g_u(E_j, E_F) dE_j} \quad (4.12)$$

Using the same methods as in Equations (4.3) and (4.4), $\langle r^2 \rangle(E)$ is simplified to:

$$\langle r^2 \rangle(E_i) = \frac{3}{20} (\langle R \rangle(E_i))^2 \alpha^2 \frac{\int_{-\infty}^{E_i} g_u(E_j, E_F) dE_j + \int_{E_i}^{E_i + K_B T \langle R \rangle(E_i)} g_u(E_j, E_F) \left(1 - \frac{E_j - E_i}{K_B T \langle R \rangle(E_i)}\right)^5 dE_j}{\int_{-\infty}^{E_i} g_u(E_j, E_F) dE_j + \int_{E_i}^{E_i + K_B T \langle R \rangle(E_i)} g_u(E_j, E_F) \left(1 - \frac{E_j - E_i}{K_B T \langle R \rangle(E_i)}\right)^3 dE_j} \quad (4.13)$$

From there we calculate the energy dependent mobility, $\mu(E)$, using the Einstein relationship.

$$\mu(E) = \frac{ev_0}{K_B T} \langle r^2 \rangle(E) \text{Exp}[-\langle R \rangle(E)] (1 - f_{FD}(E, E_F)) \quad (4.14)$$

Where e is the elementary charge. Using the energy dependent mobility, the average charge-carrier mobility and electrical conductivity can be calculated with Equations **Error! Reference source not found.**) and **Error! Reference source not found.**)

$$\bar{\mu} = \frac{1}{N_C} \int_{-\infty}^{\infty} g(E) f_{FD}(E, E_F) \mu(E) dE \quad (4.15)$$

$$\sigma = e N_C \bar{\mu} = \int_{-\infty}^{\infty} \sigma(E) dE = e \int_{-\infty}^{\infty} g(E) f_{FD}(E, E_F) \mu(E) dE \quad (4.16)$$

The Seebeck coefficient is proportional to the average energy (with respect to the Fermi energy) of conducting charge-carriers weighted by their contribution to the total electrical conductivity, as given by Equation (4.17).

$$S = \frac{1}{T_e} \int_{-\infty}^{\infty} \frac{\sigma(E)}{\sigma} (E - E_F) dE = \frac{1}{T_e} (E_T - E_F) \quad (4.17)$$

Here, the transport energy, E_T , is the average energy of charge carriers weighted by their contribution to the total electrical conductivity. To allow more direct comparison

between π -conjugated polymers with varying charge-carrier mobility and DOS distributions, the total density of charge carriers is kept constant in further calculations. The other two remaining parameters, the localization length and DOS width, are variable. To make the calculations as comparable as possible, we keep the ratio between the average distance between states (a) and α constant in our initial calculations.

4.3 Single polymer

Figure 1a and b show the results of calculations performed with Equations **Error! Reference source not found.**) and (4.17) as a function of the width of the DOS and α . The intrinsic length is calculated such that the total number of states is between 1×10^{20} and $1 \times 10^{21} \text{ cm}^{-3}$ and α adjusted such that $\frac{a}{\alpha}$ equals 10. Changing the $\frac{a}{\alpha}$ ratio does affect the trends in TE properties. Higher localization lengths for the same DOS width lead to higher electrical conductivity, while a narrower DOS width for the same localization length will also lead to higher electrical conductivity. As Figure 4.1 shows, as the electrical conductivities increase the effect of both localization length and DOS width on the Seebeck coefficient and electrical conductivity become smaller. For ratios of $\frac{a}{\alpha}$ larger than 3, trends in the Seebeck coefficient are as explained in the main text, i.e., higher disorder and smaller localization lengths will result in higher Seebeck coefficients. By going to ratios of $\frac{a}{\alpha}$ smaller than 3, the Seebeck coefficient will increase as the DOS width decreases and the localization length decreases. The reason for this is that at high charge carrier concentration in a broader DOS there are more charge carriers located at energies below the Fermi energy. In the situation where the localization length is small compared to the intrinsic length (which defines the total number of states), the charge carriers in the low energy states are partially trapped and cannot contribute to the transport, but if the localization length is large

enough, in theory, they can contribute to the transport. In this case, these low energy charge carriers decrease the Seebeck coefficient. To maintain consistency with previous work¹⁹⁰ and prevent changes in trends due to the $\frac{a}{\alpha}$ ratio, we maintain $\frac{a}{\alpha} > 3$ in all calculations presented in the paper. Additionally, the trends in the Seebeck coefficient for $\frac{a}{\alpha} > 3$ are consistent with trends found with Monte Carlo simulations, where the Seebeck coefficient increases with increasing energetic disorder.¹⁹⁵ Figure S2 highlights how the $\frac{a}{\alpha}$ ratio influences the power factor. As we mentioned above, for $\frac{a}{\alpha} > 3$ the trends in the power factor are the same as we explained above. However, when $\frac{a}{\alpha} < 3$, as the DOS narrows the power factor still increases, but as the localization length increases the power factor decreases for a constant DOS width within all DOS widths examined.

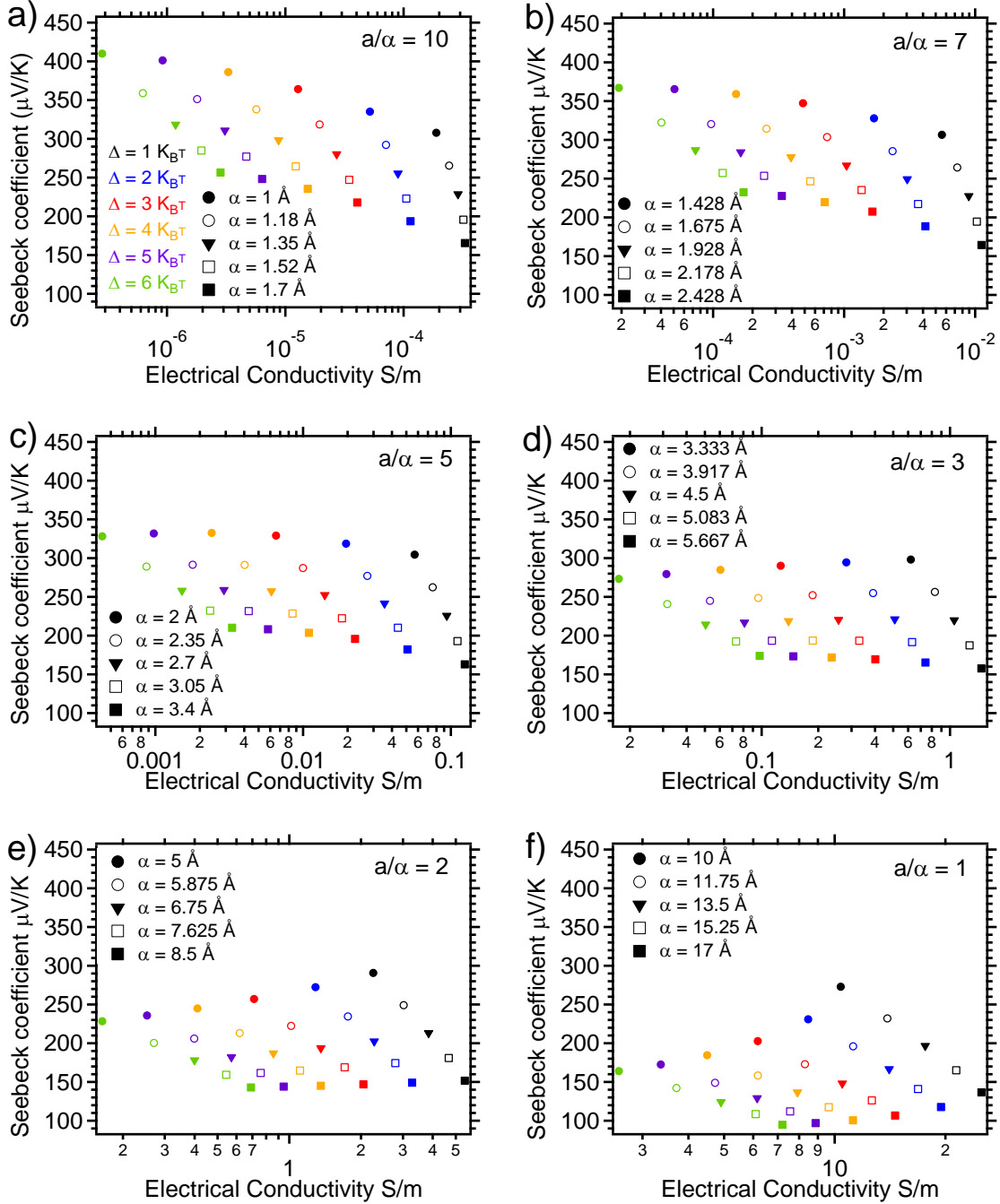


Figure 4.1 Seebeck coefficient vs. electrical conductivity. Parameters are $N_C = 3 \times 10^{19} \text{ cm}^{-3}$, $v_0 = 10^{12} \text{ s}^{-1}$, a has values of 1, 1.18, 1.35, 1.52 and 1.7 nm (corresponding to $N_t = 10, 6.09, 4.06, 2.85$ and $2.06 \times 10^{20} \text{ cm}^{-3}$), and Δ has values of ranging from 1 to $6 K_B T$. α is chosen such that the ratio between a and α is constant for each figure, $\frac{a}{\alpha}$ is 10 for (a), 7 for (b), 5 for (c), 3 for (d), 2 for (e) and 1 for (f).

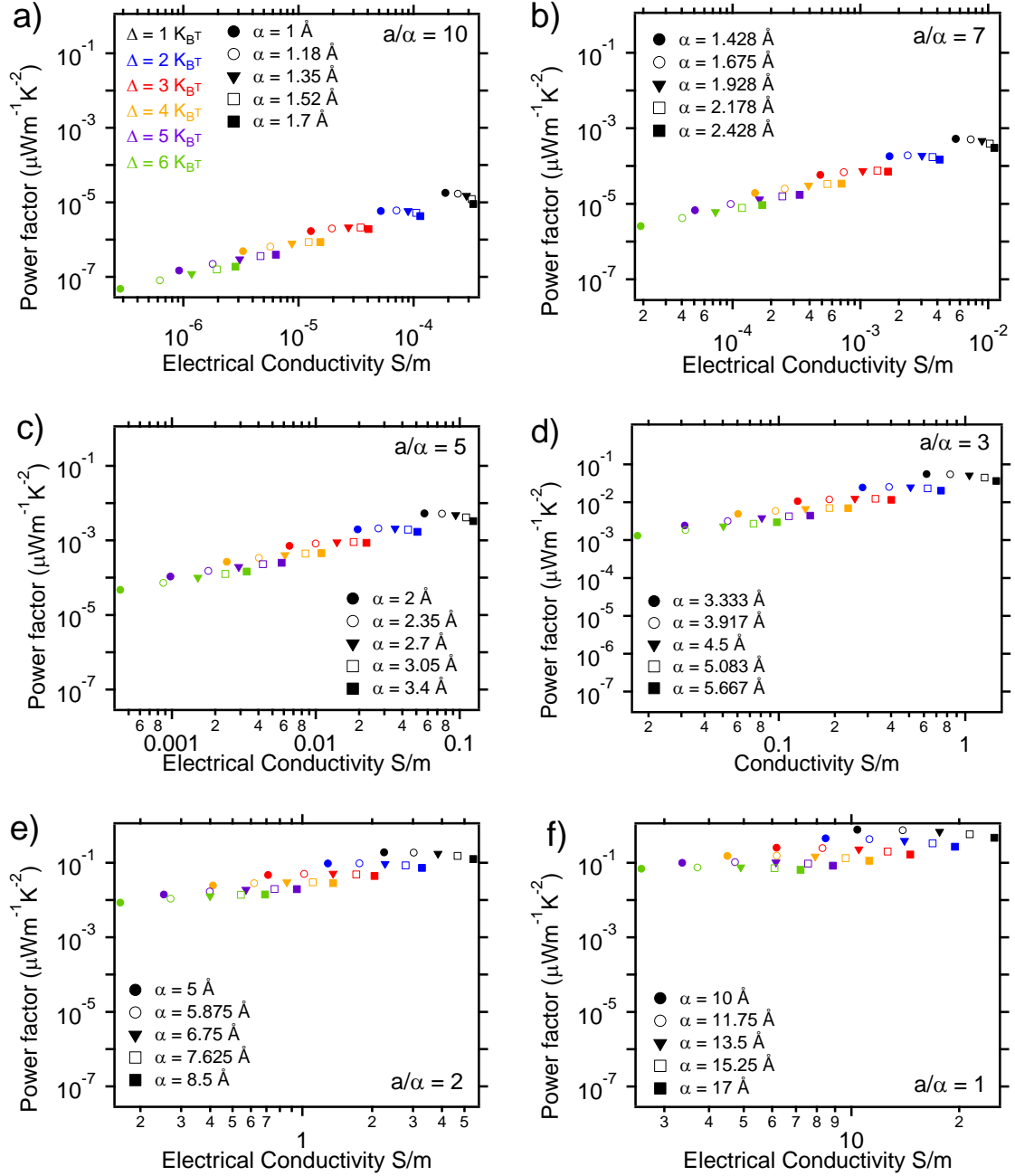


Figure 4.2 Power factor vs. electrical conductivity. Parameters are $N_C = 3 \times 10^{19} \text{cm}^{-3}$, $v_0 = 10^{12} \text{s}^{-1}$, a has values of 1, 1.18, 1.35, 1.52 and 1.7nm (corresponding to $N_t = 10, 6.09, 4.06, 2.85$ and $2.06 \times 10^{20} \text{cm}^{-3}$), Δ has values of 1-6 $K_B T$. α is chosen in such way that the ratio between a and α is constant for each figure, $\frac{a}{\alpha}$ is 10 for (a), 7 for (b), 5 for (c), 3 for (d), 2 for (e) and 1 for (f).

The results presented in Figure 4.3 (a) show that as the DOS narrows for a particular localization length σ increases and S decreases. Additionally, as α increases for a given

DOS width, σ increases and S decreases. Figure 4.3 (b) shows that the power factor increases by approximately two orders of magnitude as the DOS width of the polymer decreases from 6 to 1 $K_B T$, which is primarily attributed to the change in σ . A more specific discussion follows to rationalize the various trends, but in general the modeling shows that for a single polymer it is most beneficial to have a narrow DOS.^{73,195,200} Although the trends are accurate, the absolute value of the electrical conductivity will depend heavily on the value of v_0 .

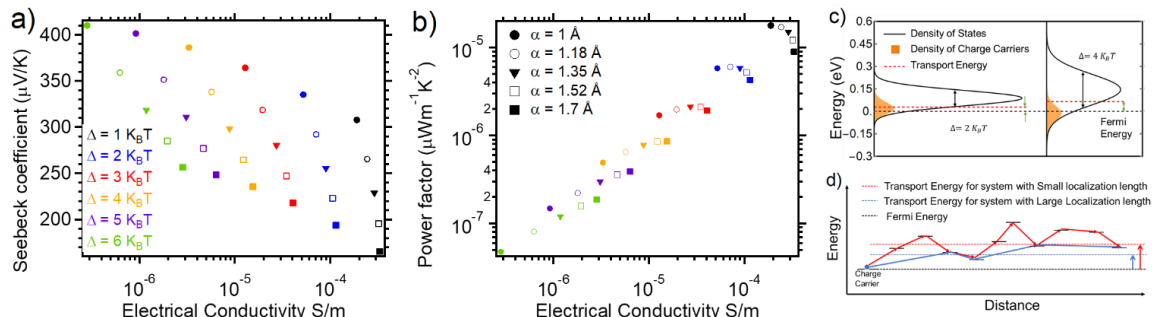


Figure 4.3 (a) Seebeck coefficient and (b) power factor as a function of electrical conductivity for varying DOS widths (indicated by color) and localization lengths (indicated by symbol). Here $N_C=3 \times 10^{19} \text{ cm}^{-3}$, $v_0=10^{12} \text{ s}^{-1}$, α has values of 1, 1.18, 1.35, 1.52 and 1.7 nm (correspondent to $N_t=10, 6.09, 4.06, 2.85$ and $2.06 \times 10^{20} \text{ cm}^{-3}$), Δ has values of 1-6 $K_B T$ and α values of 1, 1.18, 1.35, 1.52, and 1.7 \AA . For each point, the intrinsic length is chosen so $\frac{\alpha}{a}=10$. (c) Schematic illustration comparing average transport energy of two DOS distributions with the same α but different DOS widths. (d) Schematic illustrating how α affects the average transport energy.

The increase in σ with narrowing of the DOS is rationalized by considering that on average there will be more available states nearby that are energetically accessible for a charge carrier to jump to. To put it more quantitatively, according to Equation (4.2) a smaller energetic offset in a jump will lead to an exponential increase in the jump rate. The decrease in S with decreasing width of the DOS can be explained by considering that charge carriers at lower energies will contribute more to the electrical conductivity in a narrow

DOS. As illustrated in Figure 4.3 (c), when the DOS is narrow the average transport energy is lower since there are more lower energy states available for the carriers to move through. By contrast, when the DOS is wide charge carriers are forced to move through higher energy states more often due to a lack of nearby lower energy states.

Figure 4.3 (a) also shows that as the localization length increases for a particular DOS width, σ increases and S decreases. The increase in σ is rationalized by the increased available sites to hop to (i.e., the charge carrier can access more states due to the larger localization length), while the decrease in S arises from a lowering of the average transport energy due to the ability to access more lower energy states from a given site. Figure 4.3 (d) illustrates two cases, one with a larger localization length (blue arrows) and one with a smaller localization length (red arrows). If these two polymers have the same DOS width, the one with the larger localization length will allow a charge carrier to access more states around it. As a result, in the polymer with the larger localization length transport will occur on average through lower energy states and S will be smaller. Regardless of the DOS width, going from a localization length of 1 Å to 1.7 Å results in a similar S change of *ca.* 150 μVK^{-1} . By contrast, the changes in electrical conductivity resulting from the increased localization length are much more pronounced when the DOS is broader.

The primary variable influencing the power factor is the DOS width, which is consistent with previous findings.^{200,201} As the DOS width decreases from 6 to 1 $\text{K}_\text{B}T$, the power factor increases by a factor of 100. Interestingly, the trend in power factor with localization length variations is not consistent across the varying DOS widths. For a broad DOS the greatest localization length leads to the highest power factor, whereas for a narrow DOS the smallest localization length gives rise to the highest power factor. This trend

arises due to the larger influence of the localization length on σ for the broad DOS relative to the narrow DOS. For a broad DOS ($6 K_B T$), as the localization length increases from 1 to 1.7 \AA , σ increases by a factor of 10 and S decreases by a factor of 1.6. As a result of the large changes in σ , the power factor increases with localization length when the DOS is broad. On the other hand, for the narrow DOS ($1 K_B T$) as the localization length increases from 1 to 1.7 \AA , σ increases by a factor of 1.7 and S decreases by a factor of 1.9. Owing to the dependence of the power factor on S^2 , the increase in electrical conductivity with increasing localization length is outweighed by the decrease in the Seebeck coefficient and the power factor reaches a maximum at lower localization lengths when the DOS is narrow.

4.4 Polymer blends

Our model of polymer blends expands upon the single polymer model described in previous section. The two polymers are treated as a homogenous blend and the total density of states is described by Equation (4.18).

$$g_{blend}(E) = C_A g_A(E) + C_B g_B(E) = C_A \frac{N_{t,A}}{\sqrt{2\pi}\Delta_A} \text{Exp}\left[-\frac{(E-E_{0,A})^2}{2\Delta_A^2}\right] + C_B \frac{N_{t,B}}{\sqrt{2\pi}\Delta_B} \text{Exp}\left[-\frac{(E-E_{0,B})^2}{2\Delta_B^2}\right] \quad (4.18)$$

Where C is the concentration of polymer and the indices A and B refer to the different polymers in the blend ($C_A + C_B = 1$). The average number of available hopping sites is described with Equation (4.19).

$$n(E_i, R) = \frac{\pi}{6} R^3 \left(C_A \alpha_A^3 \int_{-\infty}^{E_i} g_{u,A}(E_j, E_F) dE_j + \int_{E_i}^{E_i + K_B T R} g_{u,A}(E_j, E_F) \left(1 - \frac{E_j - E_i}{K_B T R}\right)^3 dE_j \right) + \quad (4.19)$$

$$\frac{\pi}{6} R^3 \left(C_B \alpha_B^3 \int_{-\infty}^{E_i} g_{u,B}(E_j, E_F) dE_j + \int_{E_i}^{E_i + K_B T R} g_{u,B}(E_j, E_F) \left(1 - \frac{E_j - E_i}{K_B T R} \right)^3 dE_j \right)$$

The first term correlates with polymer A and second term is for polymer B. Unoccupied states are denoted as $g_{u,A}$ or $g_{u,B}$, ($g_{u,i}(E, E_F) = g_i(E)(1 - f_{FD}(E, E_F))$). The Fermi energy is derived from Equation (4.7), but instead of Equation (4.1), Equation (4.18) is used. For simplicity, the DOS in the blends is treated as a linear combination of the individual polymer DOS, which neglects any broadening or energetic shifts that may occur as a result of interactions between the different polymers. Experimentally, ultraviolet and inverse photoelectron spectra of organic semiconductor blends have been fit well with a linear combination of the two individual pure materials, albeit the energies of the individual components can shift in the blends.^{122,212} Equations (4.10) and (4.12) are used to find the average jump parameter and the average squared jump distance. These parameters are then used to calculate the energy dependent mobility using Equation (4.14), followed by the charge carrier mobility, σ , and S using Equations **Error! Reference source not found.**, **Error! Reference source not found.** and (4.17).

According to Equation (4.19), the localization length of initial states is neglected, i.e., the available hopping sites are determined based on the energy distribution and localization length of the final states. Since we have two different polymers, the hopping parameter for a jump from polymer A to B should be different from a jump from polymer A to A. To more appropriately account for jumps between polymer A and polymer B, we have extended Equation (4.19) to include the probability of the charge carrier starting from

polymer A or polymer B and an effective localization length that accounts for jumps between polymer A and polymer B, as discussed briefly in the next section.

The equations for modeling the polymer blends include 10 independent variables at a constant temperature: C_B , $N_{t,A}$, $N_{t,B}$, Δ_A , Δ_B , $E_{0,B} - E_{0,A}$ (ΔE_0), α_A , α_B , N_C and v_0 . To make the results as directly comparable as possible, we keep the concentration of charge carriers constant at $3 \times 10^{19} \text{ cm}^{-3}$ and $v_0 = 10^{12} \text{ s}^{-1}$, as we did for a single polymer. The concentration of polymer B is varied from 0 to 100% in increments of 2.5%, which provides sufficient resolution to display general trends. The total number of states in the polymer blends is kept constant, which leaves 5 independent variables, Δ_A , Δ_B , α_A , α_B and ΔE_0 . The DOS width is varied between 1.5 and 6 $K_B T$ and α between 1 and 5 \AA . The DOS width and α of polymer A are kept constant near the middle of the range, $\Delta_A = 2.5 K_B T$ and $\alpha = 2.5 \text{\AA}$. The DOS width and α of polymer B are varied through the specified ranges and ΔE_0 is set to 0.15 eV. These parameters allow analysis of a wide range of scenarios with varying DOS widths and charge-carrier mobility ratios.

When two polymers are blended together the Fermi energy relative to the individual polymers DOS distributions will vary, and thereby the average transport energy of the charge carriers will change. This variation in the Fermi energy obtained through blending two polymers together was the motivation for the Katz group's initial work on polymer blend thermoelectrics.¹⁸² Figure 4.4 and Figure 4.5 depict how the Fermi energy changes as the polymer blend composition changes when Δ_B is broad (6 KBT) and narrow (1.5 KBT), respectively, with a constant ΔE_0 of 0.15 eV. As is evident, when the DOS of polymer B is broad, there is minimal change in the Fermi energy as the concentration of polymer B increases. Alternatively, when the DOS of polymer B is narrow there is a

relatively large change (0.18 eV) in the position of the Fermi energy as the blend composition is varied. Accounting for the Fermi energy relative to the DOS in these two situations, when Δ_B is broad the charge carriers will be relatively distributed between the two polymers; however, when Δ_B is narrow most charge carriers will remain on polymer A. Thus, polymer A will dominate charge transport until polymer B reaches high concentrations. Intuitively, it can be expected that when one polymer dominates charge transport it is unlikely that the power factor in the blends will improve over the single polymers. Thereby, we expect that the most likely scenario to show an improved power factor for the blends is one where the Fermi energy changes gradually and charge carriers are distributed over both polymers.

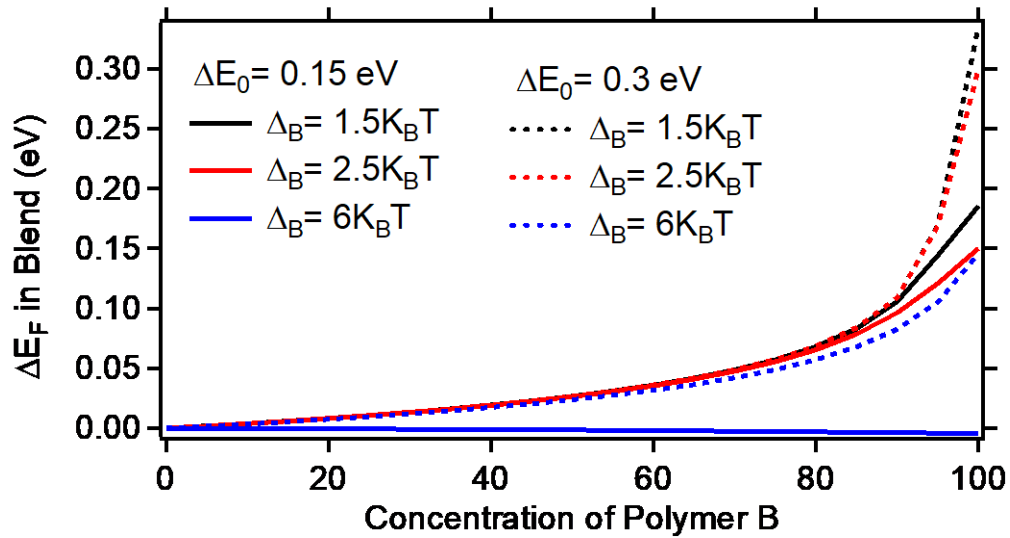


Figure 4.4 Fermi energy as a function of polymer concentration for added polymer with the same, narrower and broader DOS width at 0.15 and 0.3 eV offset. The Fermi energy of pure polymer A is set to be zero. Fitting parameters are $N_{t,A}=N_{t,B}= 1 \times 10^{21} \text{ cm}^{-3}$, $\Delta_A=2.5 K_B T$, $\Delta_B=1.5, 2.5$ and $6 K_B T$, $\Delta E_0=0.15$ and 0.3 eV , $T=300 \text{ K}$ and $N_C=3 \times 10^{19} \text{ cm}^{-3}$.

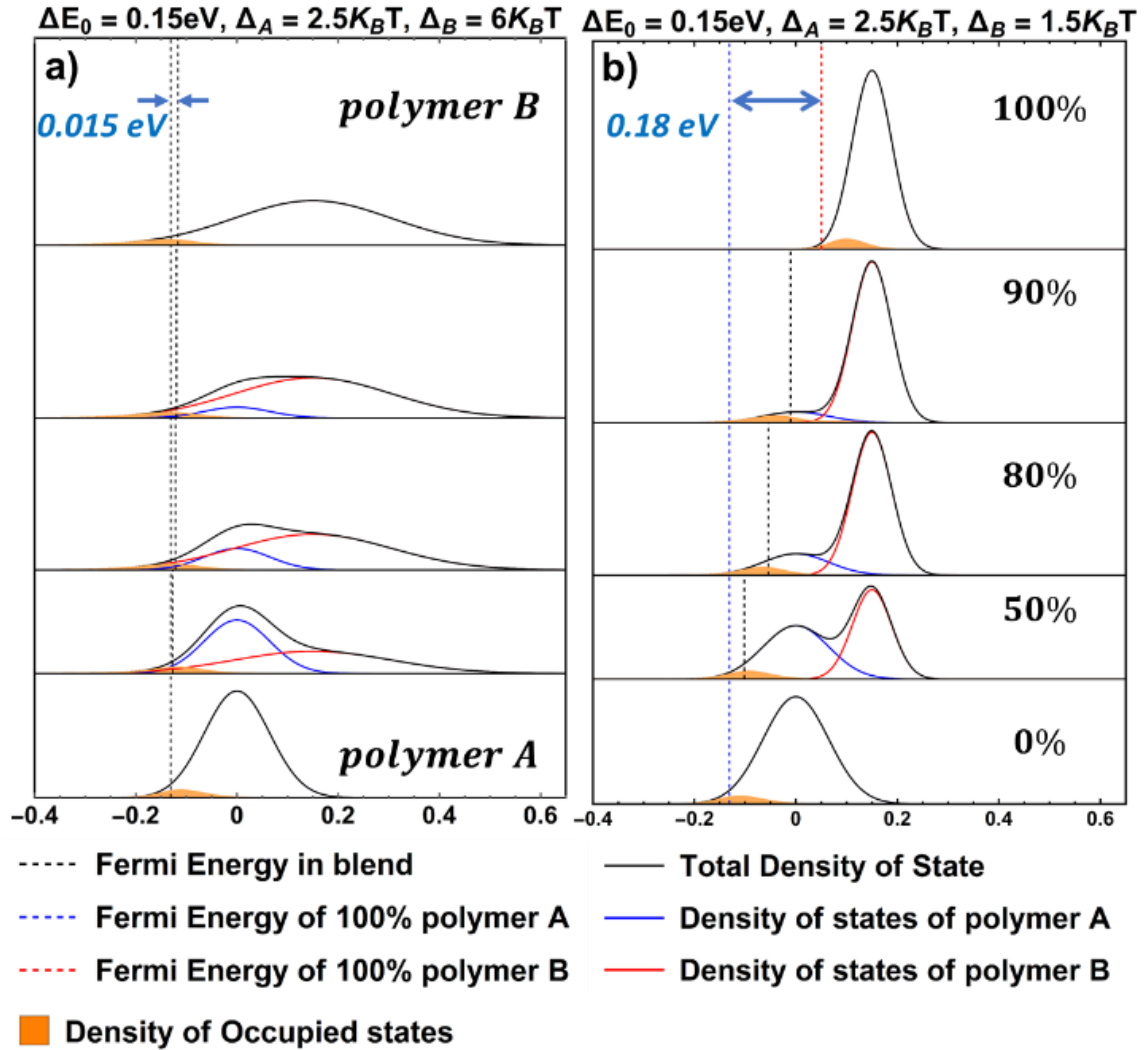


Figure 4.5 DOS of two polymer blends with varying compositions. In (a) the polymer with its DOS centered at higher energies has a broader DOS than the polymer with its DOS centered at lower energies and in (b) the polymer with the higher energy DOS has a narrower DOS. In both cases the DOS distributions of the polymers display a 0.15 eV energy offset.

Figure 4.6 shows how the calculated S , σ , and power factor vary as a function of the DOS width and α of polymer B. Here, the DOS width and α of polymer A are kept constant at $2.5 K_B T$ and 2 \AA , respectively. In pure polymer A S is $190 \mu\text{V/K}^{-1}$ and σ is 0.005 Sm^{-1} , while in pure polymer B S is $377, 240, \text{ and } 217 \mu\text{V/K}$ and σ is $6.2 \times 10^{-8} \text{ Sm}^{-1}, 0.035 \text{ Sm}^{-1}$ and 0.12 Sm^{-1} for localization lengths of $1, 4, \text{ and } 5 \text{ \AA}$, respectively. The primary findings from these calculated parameters are 1) when the DOS of polymer B is

narrow, the Seebeck coefficient in the blend can exceed that of either polymer by *ca.* 60%; 2) the Seebeck coefficient improvements in the blend are higher when polymer B has a larger delocalization length; 3) electrical conductivity improvements are only seen when polymer B has a broad DOS ($6K_B T$) and a large localization length; and 4) power factors in the blend can surpass the power factors of the pure polymers when polymer B has a broad DOS and larger localization length.

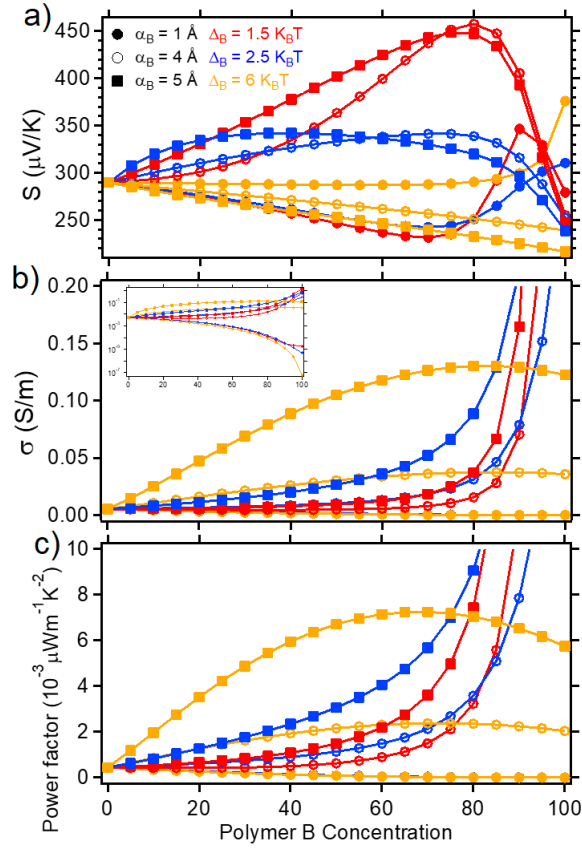


Figure 4.6 (a) Seebeck coefficient, (b) electrical conductivity and (c) power factor of polymer blend systems. Polymer A has fitting parameters of $\alpha_A=2 \text{ \AA}$, $N_{t,A}=6.1 \times 10^{20} \text{ cm}^{-3}$, $\Delta_A=2.5 K_B T$ and $E_{0,A}=0 \text{ eV}$ and polymer B has fit parameters of $\alpha_B=1, 4$ and 5 \AA , $N_{t,B}=6.1 \times 10^{20} \text{ cm}^{-3}$, $\Delta_B=1, 2.5$ and $6 K_B T$ and $E_{0,B}=0.15 \text{ eV}$ ($\Delta E_0=0.15 \text{ eV}$). Other fit parameters are $v_0=1012 \text{ s}^{-1}$, $T=300 \text{ K}$ and $N_C=3 \times 10^{19} \text{ cm}^{-3}$.

When polymer B has a narrower DOS and higher localization length, an improvement in S appears in the blends. This observation is similar to results presented by

Zuo et al.⁴³ and J. Sun et al.²¹³ The improvements are more pronounced when the DOS of polymer B is narrower and the localization length of polymer B is greater. These trends can be rationalized by considering the energy separation between the Fermi energy and the available states in polymer B combined with the charge transport properties of polymer B. As highlighted in Figure 4.5, the energetic separation between the DOS of polymer B and the Fermi energy increases as Δ_B becomes narrower. When the electronic states in polymer B are further separated from the Fermi energy and have higher localization lengths than states in polymer A, the average energy (transport energy) of charge carriers that contribute to conduction increases. In other words, when states at higher energies with higher charge-carrier mobilities are introduced S increases. The transport and Fermi energies for the blends with varying DOS width and α , as shown in Figure 4.7, highlight how both DOS width and α impact the transport energy relative to the Fermi energy and thereby the Seebeck coefficient.

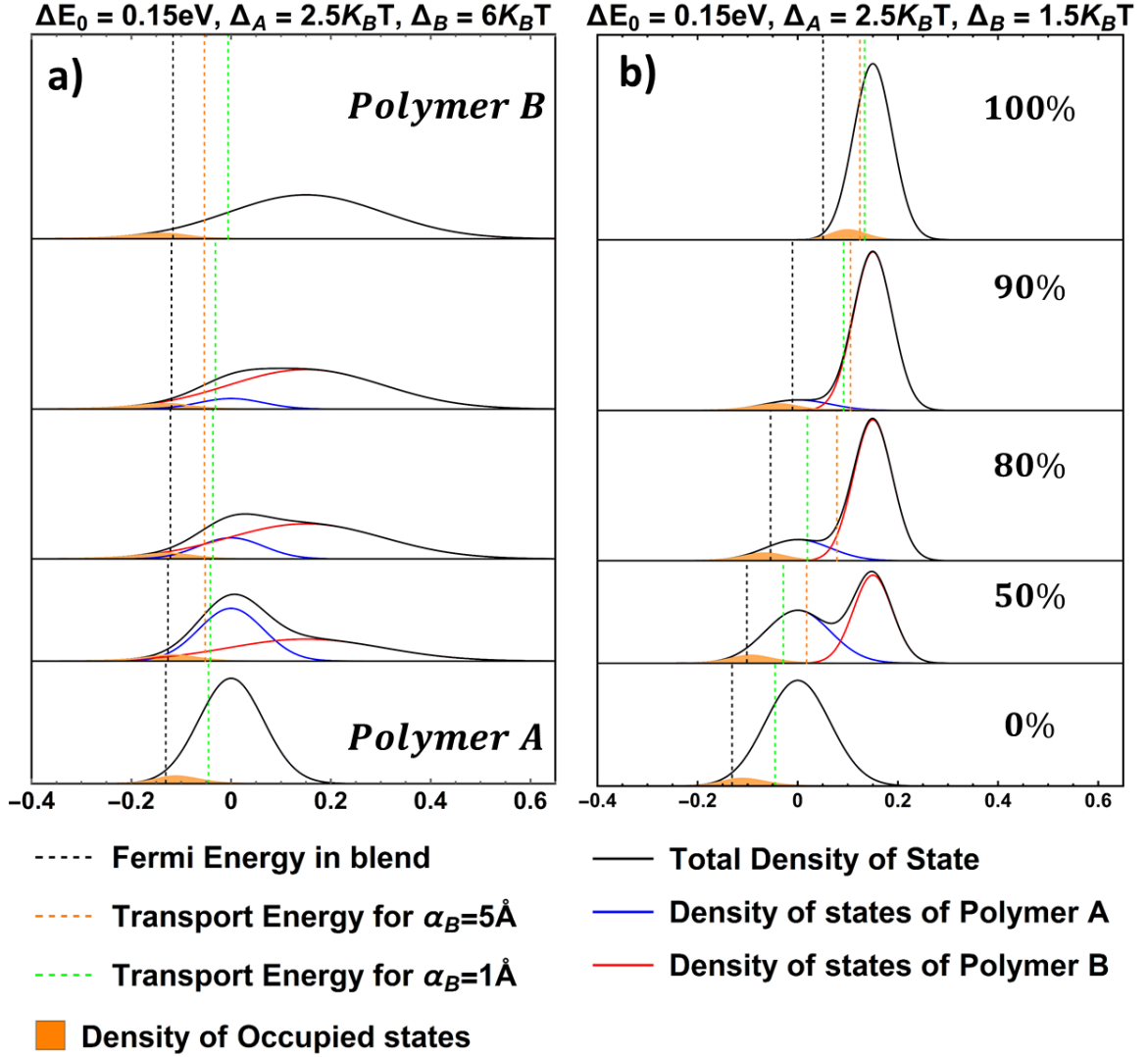


Figure 4.7 Transport energy in polymer blends with varying compositions. In (a) the polymer with its DOS centered at higher energies has a broader DOS ($\Delta_B = 6 K_B T$) than the polymer with its DOS centered at lower energies and in (b) the polymer with the higher energy DOS has a narrower DOS ($\Delta_B = 1.5 K_B T$). In both cases the DOS distributions of the polymers display a 0.15 eV energy offset. To calculate transport energy from equation 9, Polymer A parameters are $\alpha_A = 2\text{\AA}$, $N_{t,A} = 6.1 \times 10^{20} \text{ cm}^{-3}$, $\Delta_A = 2.5 K_B T$ and $E_{0,A} = 0 \text{ eV}$ and parameters for Polymer B are $N_{t,B} = 6.1 \times 10^{20} \text{ cm}^{-3}$, $\alpha_B = 1\text{\AA}$ (Dashed green line) and 5\AA (Dashed orange line) and $E_{0,B} = 0.15 \text{ eV}$ ($\Delta E_0 = 0.15 \text{ eV}$) and the common parameters are $v_0 = 10^{12} \text{ s}^{-1}$, $T = 300 \text{ K}$ and $N_C = 3 \times 10^{19} \text{ cm}^{-3}$

Although the Seebeck coefficient in the blends increases as Δ_B decreases, the opposite is true for σ . As highlighted in Figure 4.5, the separation between the DOS of

polymer B and the Fermi energy increases with decreasing DOS width, and thus there are less charge carriers populating the states on polymer B. On the other hand, Figure 4.6 (b) shows that when Δ_B is broad ($6 K_B T$) the electrical conductivity of the blend can slightly exceed the electrical conductivity of either of the two pure polymers. As a result of the increased electrical conductivity and Seebeck coefficient trend, the power factor for blends with a Δ_B of $6 K_B T$ and α_B of 4-5 Å exceed those of either of the individual polymers. For the parameters examined in Figure 4.6, the highest power factor gains in the blend relative to the two polymers independently is *ca.* 20% and occurs for $\Delta_B=6 K_B T$ and $\alpha_B=5$ Å.

A more complete analysis of how the TE properties of polymer blends vary as a function of polymer concentration (x-axis) and mobility ratio of added polymer (y-axis) to the host polymer ($\frac{\mu_B}{\mu_A}$) is displayed in Figure 4.8. Here, we compare TE properties based on the mobility ratio since it is an experimentally measurable parameter and therefore provides a more concrete guide for selecting polymers. As displayed in Equations (4.3) and (4.14) the charge-carrier mobility in a single polymer increases as α increases or the DOS narrows. In these calculations, polymer A has a localization length of 2 Å and DOS width of 2.5 $K_B T$ with $N_{t,A}= 6.1 \times 10^{20} \text{ cm}^{-3}$ ($a_A=1.18 \text{ nm}$) which gives a ratio of $\frac{a}{\alpha} = 5.9$. The maximum of the DOS for polymer B is located at 0.15 eV above the maximum of the DOS of polymer A. To study the effects of energetics and localization length on the TE properties, the total number of states and charge carrier density are kept constant in all calculations. A wide range of localization lengths (from 0.9 to 5 Å) for polymer B are used so the ratio of $\frac{a}{\alpha}$ will range from 3.5 to 18. As discussed, $\frac{a}{\alpha}$ ratios above 3 lead to reasonable results. Each column in Figure 4.8 represents a constant DOS width for polymer B and varying localization lengths. For a constant Δ_B , the localization length is the parameter that affects the mobility.

Thus, higher localization lengths correspond to higher mobility and higher mobility ratios between polymers B and A.

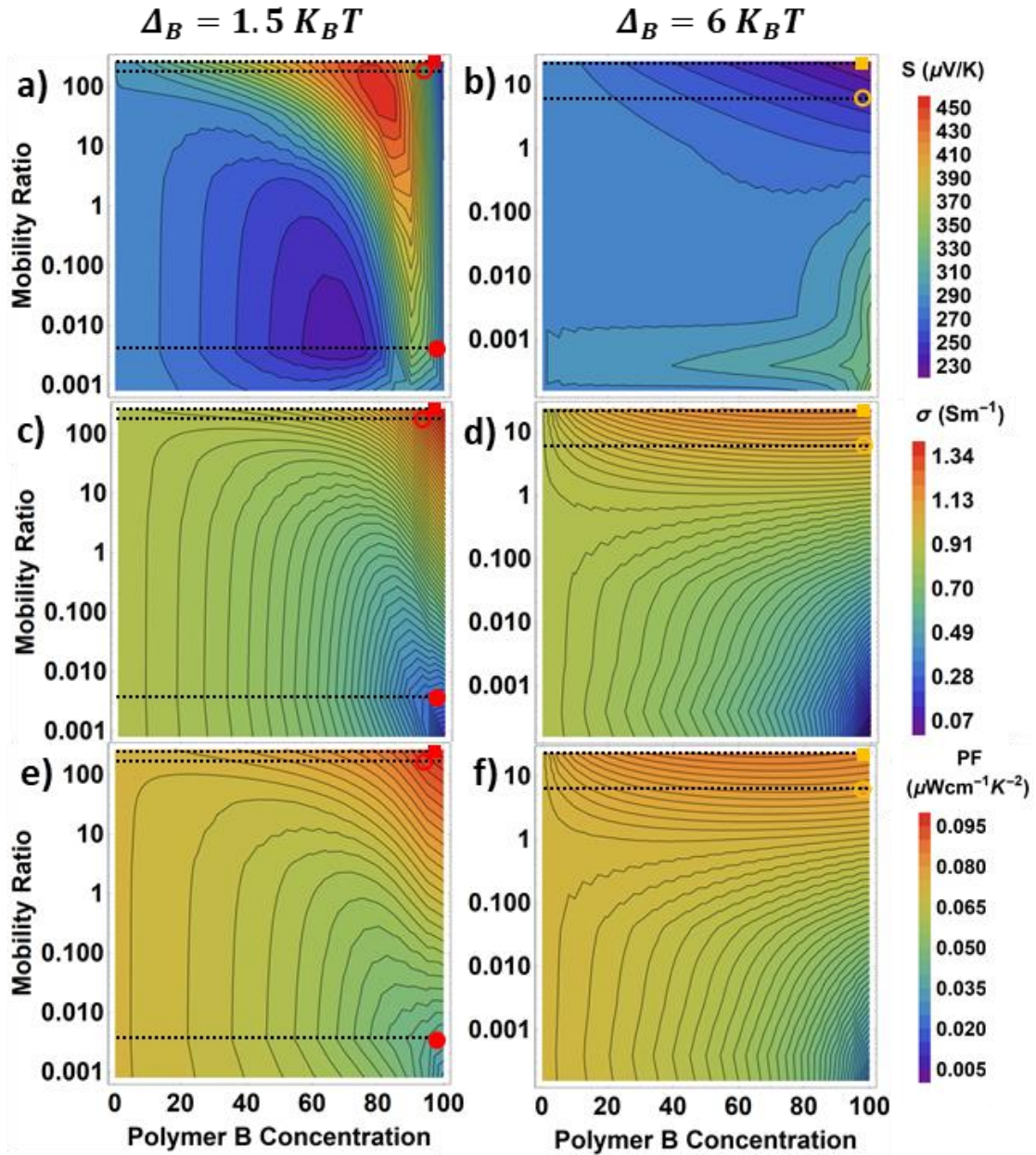


Figure 4.8 (a,b) Seebeck coefficient, (c,d) electrical conductivity, and (e,f) power factor calculated for polymer blends. Polymer A fitting parameters are $\alpha_A=2\text{\AA}$, $N_{t,A}=6.1\times 10^{20}\text{ cm}^{-3}$, $\Delta_A=2.5\text{ K}_B T$ and $E_{0,A}=0\text{ eV}$. Each column has a different DOS width for polymer B, $\Delta_B=1.5\text{ K}_B T$ (a,c,e), and $\Delta_B=6\text{ K}_B T$ (b,d,f). The other parameters for polymer B are $N_{t,B}=6.1\times 10^{20}\text{ cm}^{-3}$ and $E_{0,B}=0.15\text{ eV}$ ($\Delta E_0=0.15\text{ eV}$) and the common parameters are $v_0=10^{12}\text{ s}^{-1}$, $T=300\text{ K}$ and $N_C=3\times 10^{19}\text{ cm}^{-3}$. The results for $\Delta_B=2.5\text{ K}_B T$ can be found in Figure 4.9. Dashed lines correspond to the data presented in Figure 3. One data line for $\Delta_B=6\text{ K}_B T$ was less than 10^{-3} , which is out of the range shown in the heat map.

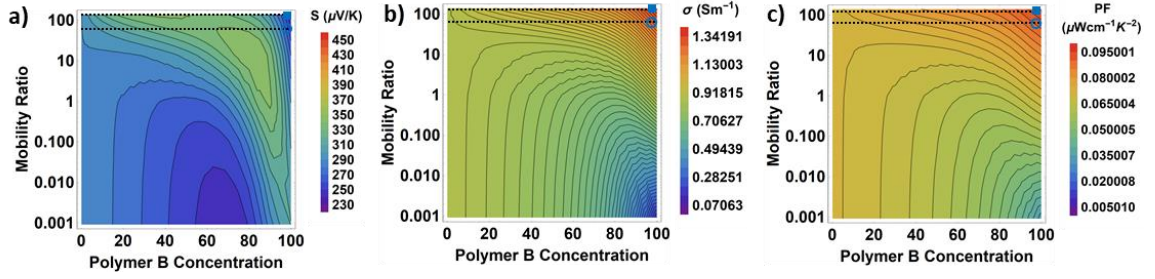


Figure 4.9 (a) Seebeck coefficient, (b) electrical conductivity, and (c) power factor calculated for polymer blends. Polymer A fitting parameters are $\alpha_A=2\text{\AA}$, $N_{t,A}=6.1\times 10^{20}\text{ cm}^{-3}$, $\Delta_A=2.5\text{ K}_B\text{T}$ and $E_{0,A}=0\text{ eV}$ and fitting parameters for Polymer B are $N_{t,B}=6.1\times 10^{20}\text{ cm}^{-3}$, $\Delta_B=2.5\text{ K}_B\text{T}$ and $E_{0,B}=0.15\text{ eV}$ ($\Delta E_0=0.15\text{ eV}$) and the common parameters are $v_0=10^{12}\text{ s}^{-1}$, $T=300\text{ K}$ and $N_C=3\times 10^{19}\text{ cm}^{-3}$. Dashed lines correspond to calculations from Fig3. One data line was less than 10^{-3} , so it has been cut from the heat map.

Focusing on the Seebeck coefficient, Figure 4.8 a shows that blending a polymer with a narrower DOS width at higher energies will lead to up to a 58% improvement in S in the blends compared to the pure polymers. The gain in S in the blends relative to the pure polymers increases as the charge-carrier mobility of polymer B increases. This result is in line with expectations, as the relative contribution of the higher energy charge carriers to σ increases as the mobility of those higher energy charge carriers increases. As Δ_B increases to $2.5\text{ K}_B\text{T}$ (Figure 4.9), the increase in S in the blends becomes smaller, and at $6\text{ K}_B\text{T}$ S no longer increases for the blends. For this wide DOS, the Seebeck coefficient changes gradually to lower values as the concentration of polymer B is increased with mobility ratios above 1. However, when the mobility ratio decreases below 1 the Seebeck gradually increases to higher values as the concentration of polymer B is increased. These trends arise due to the influence of localization length on transport and the Seebeck coefficient, as discussed previously and highlighted in Figure 4.1 (d).

The electrical conductivity varies more drastically across the blend composition space when Δ_B is smaller and when the mobility ratio is further from 1. Furthermore, σ

varies over a much greater range than the Seebeck coefficient, as discussed previously in regards to Figure 4.6. Therefore, in the blends with Δ_B of 1.5 and 2.5 the electrical conductivity changes more drastically and dominates the power factor, which results in maximum power factors occurring for either pure polymer A or pure polymer B. On the other hand, when Δ_B is 6 $K_B T$ the maximum power factors are reached with a mixture of both polymer A and polymer B. Overall, these models show that power factor enhancements over pure polymers should be attainable in polymer blends with the right combination of energy offset, DOS widths, and charge-carrier mobility differences.

4.5 Effective localization length

In case of charge transfer between two localized states with localization length of α_A and α_B , we treat the jump rate with the following equation:

$$v \propto \text{Exp} \left[-\frac{r_{ij}}{\alpha_A} \right] \times \text{Exp} \left[-\frac{r_{ij}}{\alpha_B} \right] = \text{Exp} \left[-\frac{2 r_{ij}}{\frac{2 \alpha_A \alpha_B}{\alpha_A + \alpha_B}} \right] = \text{Exp} \left[-\frac{2 r_{ij}}{\alpha_{eff}} \right] \quad (4.20)$$

α_{eff} represents an effective localization length for a jump between two localized states with different localization lengths. Here we assume the localization length of each individual polymer is the same in the blend as in the pure materials. If a charge carrier is located on polymer A initially, the average number of available hopping sites for such charge carrier starting at energy E_i whose hopping parameter is smaller than R can be written as:

$$\begin{aligned}
n_A(E_i, R) = & \frac{\pi}{6} R^3 C_A \alpha_A^3 \left(\int_{-\infty}^{E_i} g_{u,A}(E_j, E_F) dE_j \right. \\
& + \int_{E_i}^{E_i + K_B T R} g_{u,A}(E_j, E_F) \left(1 - \frac{E_j - E_i}{K_B T R} \right)^3 dE_j \Big) \\
& + \frac{\pi}{6} R^3 C_B \alpha_{eff}^3 \left(\int_{-\infty}^{E_i} g_{u,B}(E_j, E_F) dE_j \right. \\
& + \int_{E_i}^{E_i + K_B T R} g_{u,B}(E_j, E_F) \left(1 - \frac{E_j - E_i}{K_B T R} \right)^3 dE_j \Big)
\end{aligned} \tag{4.21}$$

And if the charge carrier is located on polymer B, the same parameter for such charge carrier can be calculated as:

$$\begin{aligned}
n_B(E_i, R) = & \frac{\pi}{6} R^3 C_A \alpha_{eff}^3 \left(\int_{-\infty}^{E_i} g_{u,A}(E_j, E_F) dE_j \right. \\
& + \int_{E_i}^{E_i + K_B T R} g_{u,A}(E_j, E_F) \left(1 - \frac{E_j - E_i}{K_B T R} \right)^3 dE_j \Big) \\
& + \frac{\pi}{6} R^3 C_B \alpha_B^3 \left(\int_{-\infty}^{E_i} g_{u,B}(E_j, E_F) dE_j \right. \\
& + \int_{E_i}^{E_i + K_B T R} g_{u,B}(E_j, E_F) \left(1 - \frac{E_j - E_i}{K_B T R} \right)^3 dE_j \Big)
\end{aligned} \tag{4.22}$$

We can define the parameter n in the polymer blend based on the weighted probability of finding the charge carrier in either polymer:

$$n(E_i, R) = C'_A n_A + C'_B n_B \tag{4.23}$$

here C'_A and C'_B are the probabilities of finding a charge carrier on polymer A and B, respectively, which can be calculated as below:

$$C'_A = \frac{\int_{-\infty}^{\infty} C_A g_A(E) f_{FD}(E, E_F) dE}{N_C} \quad (4.24)$$

$$C'_B = \frac{\int_{-\infty}^{\infty} C_B g_B(E) f_{FD}(E, E_F) dE}{N_C} = 1 - C'_A \quad (4.25)$$

Further we can calculate TE properties using Equations (4.11), (4.13), (4.15), (4.16) and (4.17). Figure 4.10 compares the calculations without (a,c,e) and with (b,d,f) an effective localization length is included. As shown in Figure 4.10, including an effective localization length in the calculations has a large impact on TE properties of the blend system, particularly at lower concentrations of polymer B with Δ_B equal to $1.5K_B T$, $2.5K_B T$. In the model introduced here, we added a weighted probability to account for whether the charge carriers start from polymer A or polymer B based on their energetics. As shown in Figure 4.3, when polymer B has a narrower DOS centered at higher energies than polymer A, the charge carriers will mostly be localized on polymer A rather than polymer B. Therefore, the probability of a charge carrier to jump from polymer B to another site on polymer B is reduced for two reasons. First, the probability of the charge carrier starting on polymer B is low, and second, the unoccupied states on polymer B are at higher energies. This will cause a drop in the Seebeck coefficient and electrical conductivity in Figure 4.10 (b) and d at low concentrations of polymer B. In the case that polymer B has a broader DOS width, the Seebeck coefficient in the blend will not change as much since the probability of finding a charge carrier on polymer A or B will be comparable to the concentrations of polymer A or B in the blend. Accounting for jumps between polymers with this method has a larger impact on electrical conductivity, particularly in the case where α_B is larger, e.g., 5 \AA . The drop in σ rises from the effective

localization length that is smaller than α_B (α_A is 2\AA , α_B is 5\AA and so α_{eff} is 2.86\AA). The drop in electrical conductivity is significant enough that it reduces the improvement in power factor from 26% to 3%.

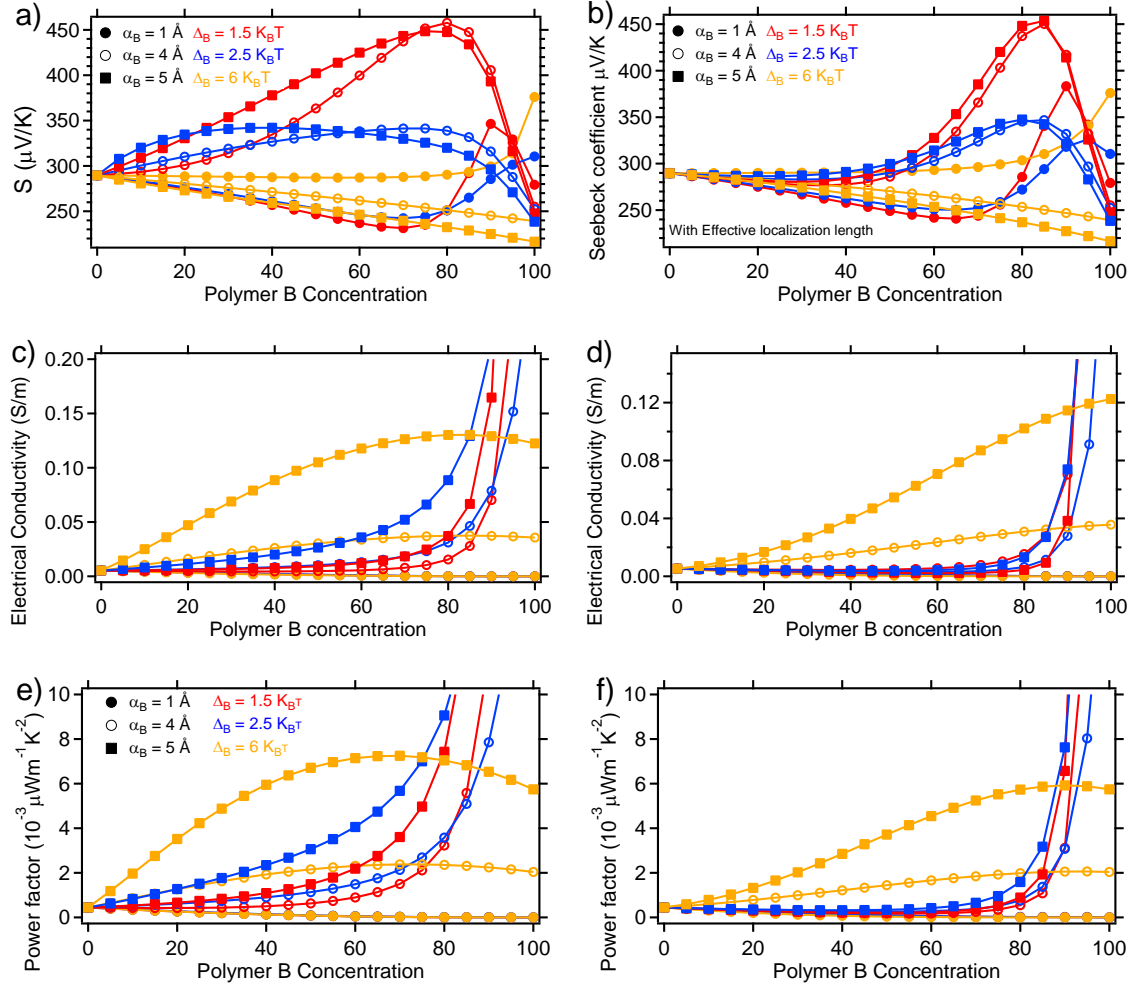


Figure 4.10 (a,b) Seebeck coefficient, (c,d) electrical conductivity and (e,f) power factor of polymer blend systems calculated as described in the paper (a,c,e) and calculated based on an effective α as described in the SI (b,d,f). Polymer A has fitting parameters of $\alpha_A=2\text{\AA}$, $N_{l,A}=6.1\times 10^{20}\text{ cm}^{-3}$, $\Delta_A=2.5 K_B T$ and $E_{0,A}=0\text{ eV}$ and polymer B has fitting parameters of $\alpha_A=1,4$ and 5\AA , $N_{l,B}=6.1\times 10^{20}\text{ cm}^{-3}$, $\Delta_A=1, 2.5$ and $6 K_B T$ and $E_{0,B}=0.15\text{ eV}$ ($\Delta E_0=0.15\text{ eV}$). Other fit parameters are $v_0=10^{12}\text{ s}^{-1}$, $T=300\text{ K}$ and $N_C=3\times 10^{19}\text{ cm}^{-3}$.

By including an effective localization length and accounting for the probability of a charge carrier starting on polymer A or B, the modeled TE properties in polymer blends changes, especially the magnitude of power factor improvement. To determine if we could

achieve the same improvement when an effective localization length is accounted for, we probed additional combinations where the two mentioned effects are minimized. To increase the contribution of polymer B to charge carriers conduction, the DOS width of polymer B can be increased or the energetic offset between the two DOS decreased. As is shown in Figure 4.11 (a, d) and g, by increasing the DOS width of polymer B from $6K_B T$ to $7K_B T$, similarly large power factor improvements in the blends are achievable again. Similarly, Figure 4.11 (h) suggests by reducing the energetic offset from 0.15 eV to 0.1 eV we can reproduce the power factor improvement. The other effect from this revised model is that the effective localization length is some number between α_A and α_B , so by reducing the difference we can reduce the effect of α_{eff} . As Figure 4.11(i) shows, by reducing the difference between the two localization lengths from 2\AA to 1\AA , we can reproduce the power factor improvement. In this section we show that by differentiating between hopping between two different polymers, the parameters where power factor improvements are observed shift slightly. These variations still follow the same trends which are reported in manuscript with one additional comment, the localization length between two polymers should not be overly different.

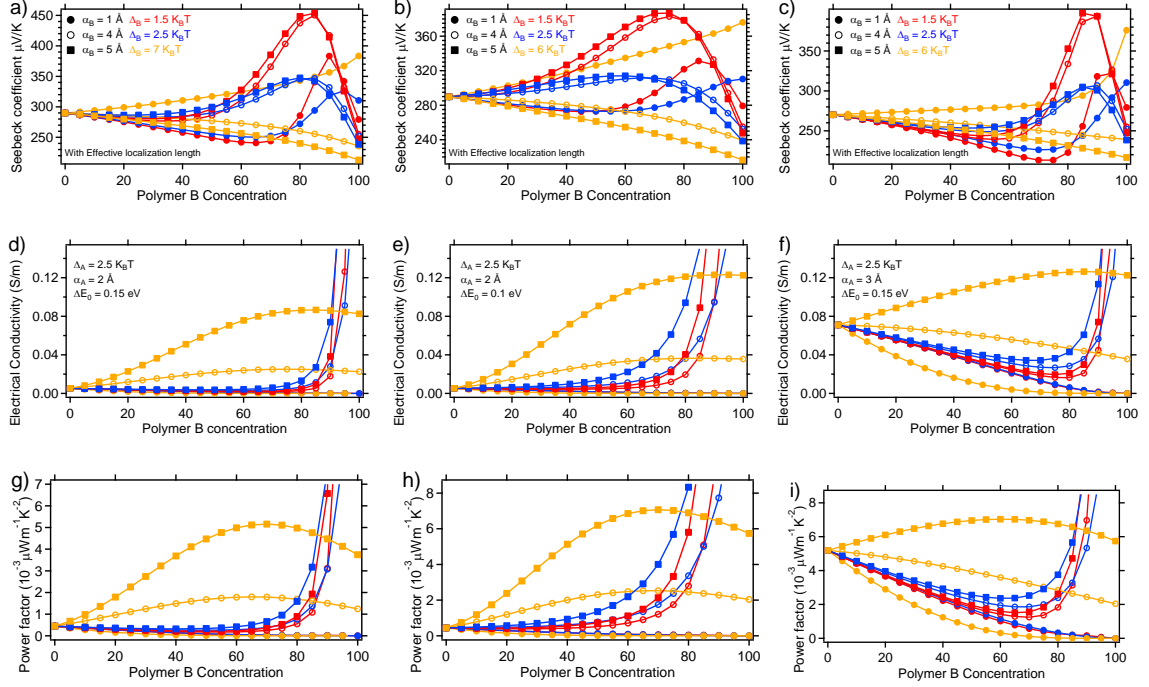


Figure 4.11 (a, b, c) Seebeck coefficient, (d, e, f) electrical conductivity and (g, h, i) power factor of polymer blend systems. Each column presents slight variations in parameters where power factor improvements in the blends are expected. In figures a, b, d, e, g and h polymer A has fitting parameters of $\alpha_A=2 \text{ \AA}$, $N_{t,A}=6.1 \times 10^{20} \text{ cm}^{-3}$, $\Delta_A=2.5 \text{ K}_B T$ and $E_{0,A}=0 \text{ eV}$ and figures c, f and i all parameters for polymer A are same except for localization length which the value is $\alpha_A=3 \text{ \AA}$. Polymer B has fit parameters of $\alpha_B=1, 4$ and 5 \AA , $N_{t,B}=6.1 \times 10^{20} \text{ cm}^{-3}$, $\Delta_B=1, 2.5$ and $6 \text{ K}_B T$ ($6 \text{ K}_B T$ for figure a, d and g) and $E_{0,B}=0.15 \text{ eV}$ ($\Delta E_0=0.15 \text{ eV}$, for figure b, e and h the value is $\Delta E_0=0.1 \text{ eV}$). Other fit parameters are $v_0=10^{12} \text{ s}^{-1}$, $T=300 \text{ K}$ and $N_C=3 \times 10^{19} \text{ cm}^{-3}$.

Based on Figure 4.10 and Figure 4.11, we conclude that including these additional parameters to account for jumps between polymers A and B changes the absolute values of the TE properties and results in maximum TE power factors in the blends occurring with slightly different parameters, but they do not change the general trends or resulting conclusions.

4.6 Experimental results

We selected polymers for this study with varying charge-carrier mobilities, ionization energies (IE), and extents of disorder, as shown in Figure 4.12. Regioregular and regiorandom poly(3-hexylthiophene) (RR-P3HT and RRa-P3HT, respectively) are structurally similar polymers with charge-carrier mobilities that differ by several orders of magnitude and IEs that differ by *ca.* 0.2 eV.^{177,214} The hole mobility of RR-P3HT can reach $0.1 \text{ cm}^2\text{V}^{-1}\text{s}^{-1}$ and we have measured its IE to be $4.56\pm 0.05 \text{ eV}$.²¹⁵ On the other hand, RRa-P3HT has a lower hole mobility of 10^{-5} - $10^{-4} \text{ cm}^2\text{V}^{-1}\text{s}^{-1}$ and a higher IE of $4.73\pm 0.05 \text{ eV}$.²¹⁶ The other two polymers are based on diketopyrrolopyrrole (DPP) and thiophene units and show high hole mobilities of *ca.* $1 \text{ cm}^2\text{V}^{-1}\text{s}^{-1}$,^{69,217} and have similar IEs of 5.03 ± 0.05 and $5.09\pm 0.05 \text{ eV}$ for PDPP-4T and PDPP-T-TT-T, respectively. With PDPP-4T and PDPP-T-TT-T both having relatively high IEs, we use the dopant molybdenum tris-[1,2-bis(trifluoromethyl) ethane-1,2-dithiolene] ($\text{Mo}(\text{tfd})_3$),²¹⁸ which we recently measured by inverse photoemission spectroscopy to have an EA of 5.59 eV .¹⁷⁷ All polymer blends are doped at *ca.* 10% by volume in an attempt to maintain similar charge-carrier concentrations. In this series of blends, PDPP-4T serves as the host polymer and the polymer blended with PDPP-4T is varied. The measured S and σ values for the three different blend systems are presented in Figure 6.

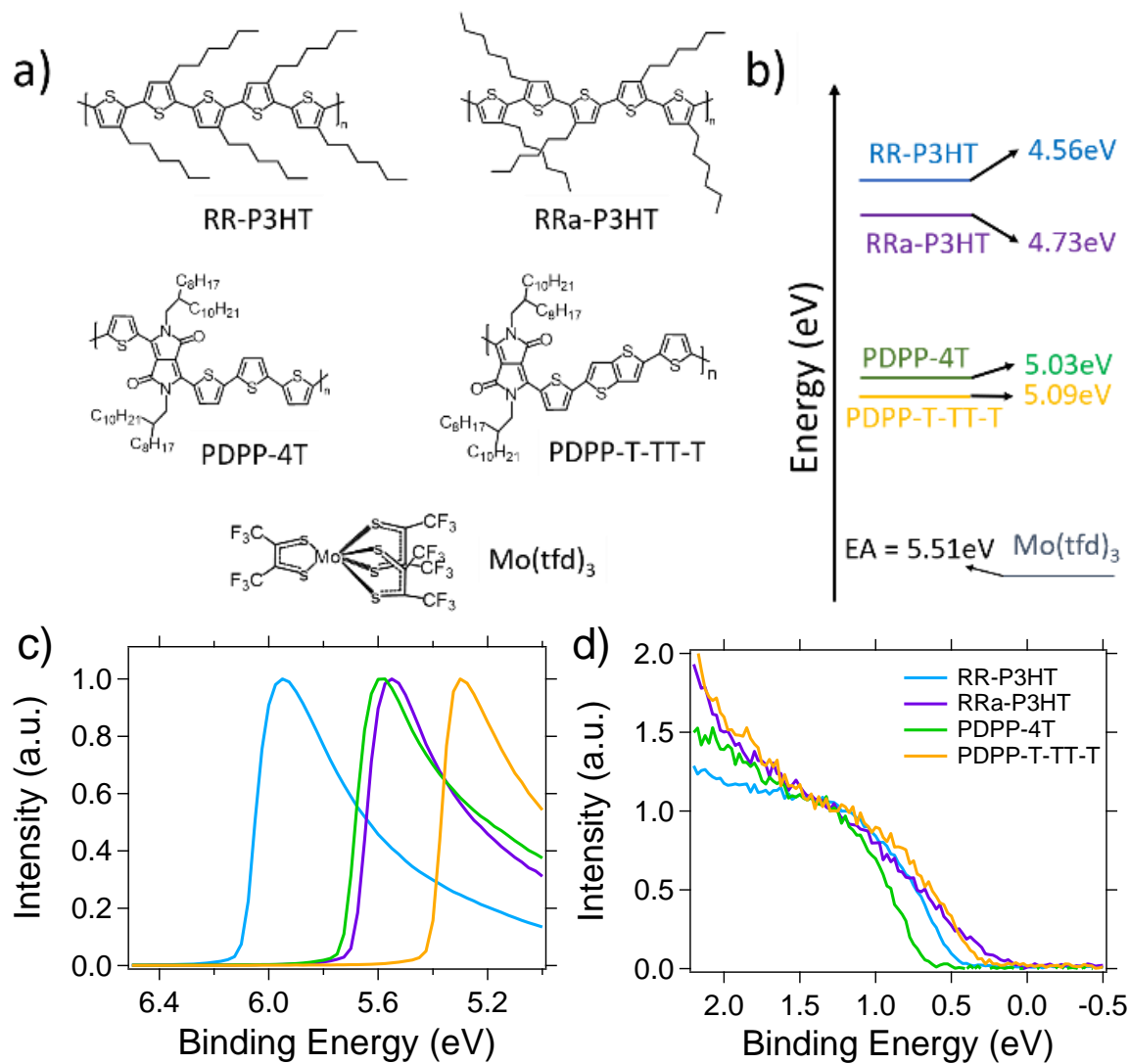


Figure 4.12 (a) Molecular structure of polymers and dopant, RR-P3HT, RRa-P3HT, PDPP-4T, PDPP-T-TT-T and Mo(tfd)₃. (b) Ionization energy (IE) of polymers and electron affinity (EA) of dopant¹⁷⁷. Normalized (c) secondary cutoff and (d) HOMO onset regions of undoped polymers measured by ultraviolet photoemission spectroscopy (UPS).

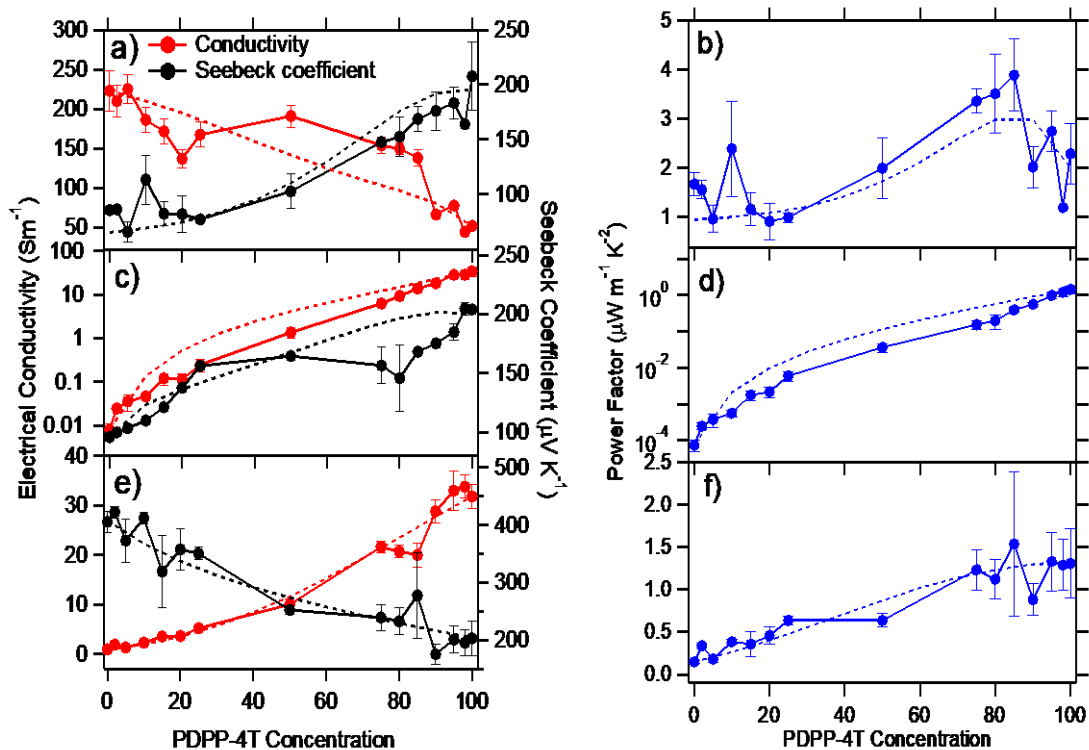


Figure 4.13 (a,c,e) Seebeck coefficient and electrical conductivity and (b,d,f) power factor as a function of PDPP-4T concentration in polymer blend. The blends are PDPP-4T:RR-P3HT (a,b) and PDPP-4T:RRa:P3HT (c,d) and PDPP-4T:PDPP-T-TT-T (e,f). Dashed lines are the fits to the model as calculated with Equations (4.16) and (4.17). The fitting parameters can be found in Table 4.1.

Table 4.1 fitting parameters for each polymer in each individual blend system

PDPP-4T:RR-P3HT								
Polyme r	Δ ($K_B T$)	α (\AA)	a (nm)	N_t (10^{20} cm^{-3})	N_C (10^{19} cm^{-3})	a/α	E_0	ν_0 (10^{15} s^{-1})
PDPP-4T	4	2.8	1.4	3.64	6	5	0	3.52
RR-P3HT	1.2	2	1.5	2.96	12	12.5	-0.15	44.8
PDPP-4T:RRa-P3HT								
Polyme r	Δ ($K_B T$)	α (\AA)	a (nm)	N_t (10^{20} cm^{-3})	N_C (10^{19} cm^{-3})	a/α	E_0	ν_0 (10^{15} s^{-1})
PDPP-4T	4	2.5	1.4	3.64	6	5.6	0	5.43
RRa-P3HT	2	1.2	1.5	2.96	12	12.5	-0.15	2.41
PDPP-4T:PDPP-T-TT-T								
Polyme r	Δ ($K_B T$)	α (\AA)	a (nm)	N_t (10^{20} cm^{-3})	N_C (10^{19} cm^{-3})	a/α	E_0	ν_0 (10^{15} s^{-1})
PDPP-4T	3.5	2.5	1.35	4.06	6	5.4	0	4.06
PDPP-T-TT-T	4.5	1.8	1	10	1.5	10	0.08	2.83

In the first case, PDPP-4T is blended with RR-P3HT. Here, there is a large offset between the IEs of the two polymers and the higher IE polymer, PDPP-4T, has a hole mobility that is approximately an order of magnitude greater than that of RR-P3HT. In the second case, PDPP-4T is blended with RRa-P3HT. In this case there is a large energy offset between the two polymer IEs and the lower IE polymer, RRa-P3HT, has a hole

mobility that is three to four orders of magnitude lower than that of PDPP-4T. In the final case PDPP-4T is blended with PDPP-T-TT-T. In this blend the IE difference between the polymers is small and both polymers display similar charge-carrier mobilities. PDPP-4T:RR-P3HT follows one of the theoretically predicted guidelines for observing enhanced PFs in the blends, i.e., the polymer with the higher IE has a charge-carrier mobility that is an order of magnitude higher than that of the mobility in the lower IE polymer. According to the theoretical modeling, the other two blends do not have electronic properties that would lead to enhanced power factors.

The PDPP-4T:RR-P3HT blend indeed shows an improvement in power factor, as the blend with 85% PDPP-4T displays a power factor that is nearly double that of the pure polymers. At 10% doping by volume, pure PDPP-4T displays an electrical conductivity (52 Sm^{-1}) that is four times lower than pure RR-P3HT (223 Sm^{-1}) at the same doping ratio. In this blend the increase in S and decrease in σ are more comparable, which means that neither parameter will overwhelm the power factor. These more gradual changes lead to a higher power factor in the blend than in either of the two pure materials. The fitting parameters shown in Table 4.1 suggest RR-P3HT has a narrower DOS ($1.2 \text{ K}_B\text{T}$ compared with $4 \text{ K}_B\text{T}$) with slightly higher localization length ($2.8\text{\AA} > 2\text{\AA}$) located at lower energies. The ratio in the DOS width (3.3) is similar to the scenario shown in the second column of Figure 4.8 (2.4), and as modeled for the higher mobility ratios there is an increase in the power factor.

Next, we examine the other two blend systems that are not expected to give rise to higher power factors. For the PDPP-4T:RRa-P3HT blend system, the charge-carrier mobility of RRa-P3HT is 3 to 4 orders of magnitude smaller than that in PDPP-4T, and

thus the contribution of PDPP-4T is likely to dominate over RRa-P3HT in determining the power factor. Indeed, the 3+ order of magnitude difference in the electrical conductivity and the higher Seebeck coefficient for PDPP-4T leads to PDPP-4T dominating transport and the power factor in the blends. The fitting parameters for the PDPP-4T and RRa-P3HT blends (Table 4.1) suggest that PDPP-4T has a broader DOS with higher localization length at higher energies.

The final blend system we examine is PDPP-4T:PDPP-T-TT-T, where there is almost no charge-carrier mobility difference. Surprisingly, the electrical conductivity of PDPP-T-TT-T is much smaller than that of PDPP-4T (0.9 Sm^{-1} compared to 31.8 Sm^{-1}). Increasing the ratio of PDPP-4T in the blend leads to a constant decrease in S from $404 \mu\text{VK}^{-1}$ to $204 \mu\text{VK}^{-1}$, which opposes the changes in electrical conductivity. The large Seebeck coefficient and low electrical conductivity in pure PDPP-T-TT-T suggests a low charge-carrier concentration and high total number of states, which agrees with the fitting parameters ($N_{t,\text{PDPP-T-TT-T}}=10^{21}\text{cm}^{-3}$ and $N_{c,\text{PDPP-T-TT-T}}=1.5\times 10^{19}\text{cm}^{-3}$ or $\frac{N_{c,\text{PDPP-T-TT-T}}}{N_{t,\text{PDPP-T-TT-T}}}=1.5\%$). Furthermore, the fitting parameters for these two polymers suggest we have blended two polymers with almost similar disorder and similar localization length with 0.08 eV energetic offset. This scenario can be best represented by the calculated data in Figure 4.9 when the mobility ratio is small, and as predicted by the model there is not any improvement in the power factor.

The theoretical fitting to the experimental data from the manuscript and the revised version from this section where α_{eff} is applied are shown in Figure 4.14 to show how accounting for jumps between polymer A and B alters the results. Figure 4.14 shows that using an effective localization length has a minimum effect on PDPP-4T:RRa-P3HT and

PDPP-4T:PDPP-T-TT-T blend systems. The effect is minimized in PDPP-4T:PDPP-T-TT-T blends because PDPP-T-TT-T has a similar DOS width with a small energetic offset compared to PDPP-4T. The new theoretical approach doesn't change the trend in PDPP-4T:RRa-P3HT blend because RRa-P3HT already has very small localization length, so the effect on the power factor is negligible. As we can see in Figure 4.14 (a,b), using the same parameters as Table 4.1 with the new theoretical approach applied the calculated data deviates more from the experimental data and does not show as much improvement in the power factor for the reasons explained previously. However, as shown in Figure 4.15, reducing the energetic offset from 0.15 to 0.1eV between PDPP-4T and RR-P3HT does fit the experimental data well and shows a similar improvement in power factor as the data reported in the manuscript.

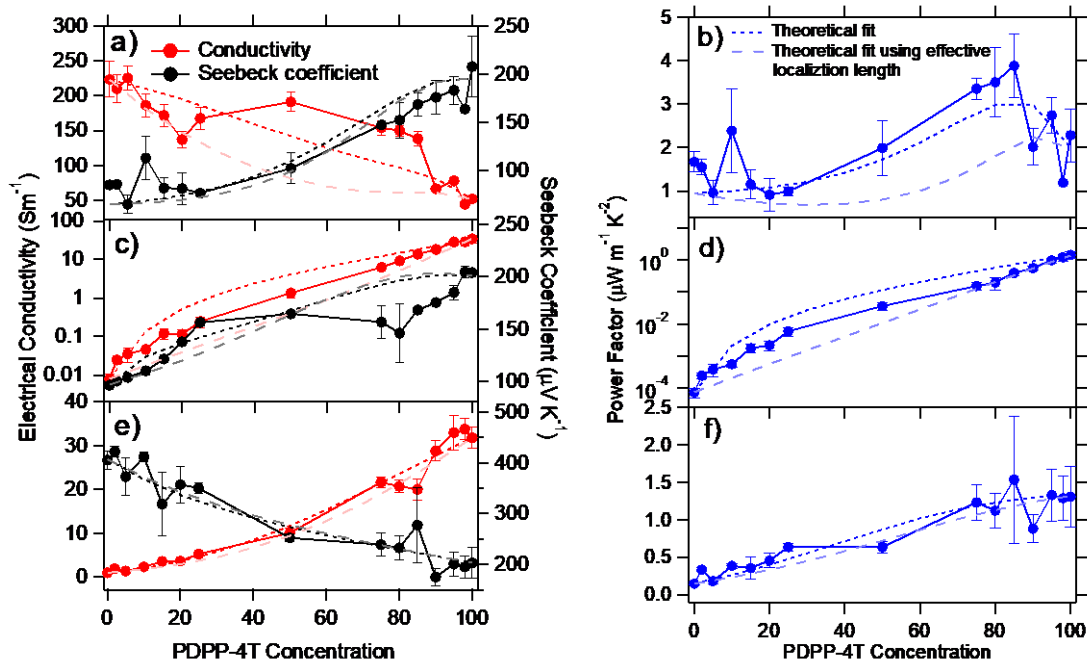


Figure 4.14 (a,c,e) Seebeck coefficient and electrical conductivity and (b,d,f) power factor as a function of PDPP-4T concentration in the polymer blend. The blends are PDPP-4T:RR-P3HT (a,b) and PDPP-4T:RRa:P3HT (c,d) and PDPP-4T:PDPP-T-TT-T (e,f). Darker dashed lines with shorter dashes are the fits to the model as calculated with Equations (4.16) and (4.17) and lighter dashed lines with longer dashes are the fits to the model accounting for effective localization length. The fitting parameters can be found in Table 4.1.

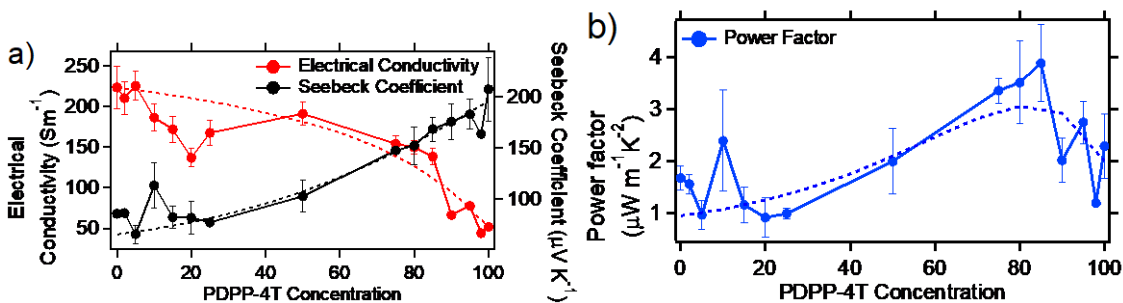


Figure 4.15 (a) Seebeck coefficient and electrical conductivity and (b) power factor as a function of PDPP-4T concentration in the PDPP-4T:RR-P3HT blend when E_0 is reduced from 0.15 eV (see Figure 4.14) to 0.10 eV. Dashed lines are the fits to the model as calculated with accounting for effective localization length with the fitting parameters listed in Table 4.1, except here $E_0=0.1$ eV.

Photothermal deflection spectroscopy (PDS) measurements,^{71,72} as shown in Figure 4.16, were carried out in an effort to obtain experimental evidence into the DOS widths for the different polymers.⁷³ From these PDS spectra the Urbach energy was extracted, where the Urbach energy provides a quantitative measurement of the extent of disorder. Unfortunately, the polaron absorbance in the polymers extends beyond the limits of the PDS system and therefore the un-doped polymers were investigated. In the un-doped polymers, the Urbach energies of RR-P3HT, PDPP-4T, and PDPP-T-TT-T are similar at 42 to 45 meV, whereas RRa-P3HT is significantly higher at 170 meV. Considering that the Urbach energy should reflect the DOS width, these values are in disagreement with the values extracted through fitting the experimental data with the theoretical model. We suspect that this discrepancy arises from the PDS measurements being performed on the un-doped polymers. Adding chemical dopants has previously been shown both experimentally and theoretically to significantly alter the relative disorder and DOS widths in the polymers.^{201–203,209} Experimentally probing disorder in these doped systems is a direction that we will pursue in future work.

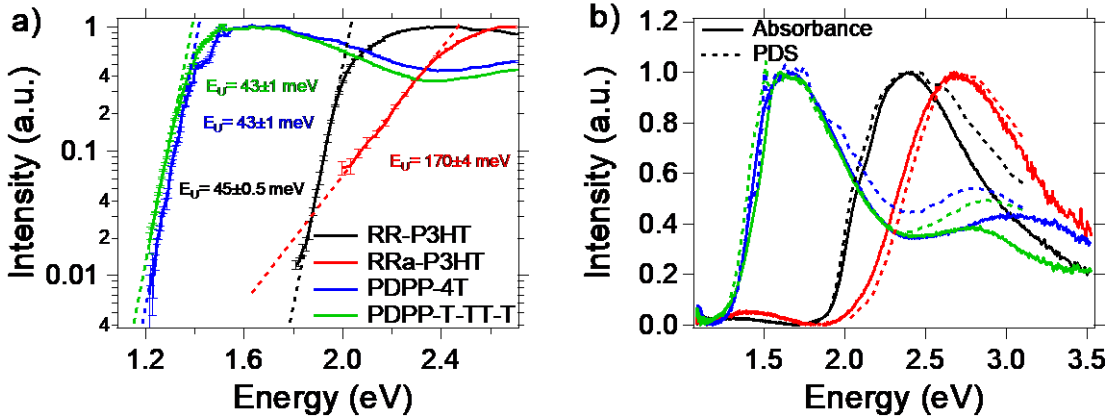


Figure 4.16 (a) PDS spectrum of all undoped polymers on a logarithmic scale and their Urbach energies extracted from $Abs = a_0 e^{\frac{E-E_g}{E_U}}$ ($E < E_g$). (b) PDS (dashed) and UV-Vis (solid line) spectrum of undoped polymers which shows the agreement between two measurements. The dip in absorbance at the absorbance edge is due to polymer photoluminescence.

There are three additional fitting parameters that differ between the polymers and have major contributions to the observed experimental trends. These include the total density of states, the density of charge carriers and attempt to jump frequency. The total number of states is equal to the total number of states that have some contribution to charge transport. The total number of states is highest for PDPP-T-TT-T ($10 \times 10^{20} \text{cm}^{-3}$) and lowest for RRa-P3HT ($2.96 \times 10^{20} \text{cm}^{-3}$) and their value can be affected by multiple parameters, including morphological factors that restrict transport or the presence of energetic traps. Despite keeping the concentration of the dopant constant (Table 4.2) in the films, the concentration of charge carriers is not the same for all polymers. RR-P3HT and RRa-P3HT have the highest charge carrier concentration ($12 \times 10^{19} \text{cm}^{-3}$) versus PDPP-4T ($6 \times 10^{19} \text{cm}^{-3}$) and PDPP-T-TT-T ($1.5 \times 10^{19} \text{cm}^{-3}$). There are a few possible reasons for these differences, such as dopant aggregation^{219,220} or lower energetic offsets between the EA of the dopant and IE of the polymer,⁴³ both of which can decrease the doping efficiency. The

extracted charge-carrier concentration does correspond with the doping efficiency expected based purely on the IE of the polymers, with the carrier concentration decreasing as the polymer IE increases; however, it is difficult to experimentally verify the exact concentration of charge carriers. Attempt to jump frequency should be in order of 10^{11} - 10^{13} s^{-1} (i.e., order of phonon vibration frequency), but the fitting parameters used to fit to our experimentally measured electrical conductivity are about two orders of magnitude higher. The number of electronic states per unit volume were calculated based on the density and molecular weight of the polymer and dopant using Equations (4.26) and (4.27)

$$N_d = \left(\gamma^{-1} \frac{MW_p}{\rho_p} + \frac{MW_d}{\rho_d} \right)^{-1} N_A \quad (4.26)$$

$$N_p = \left(\frac{MW_p}{\rho_p} + \gamma \frac{MW_d}{\rho_d} \right)^{-1} N_A x \quad (4.27)$$

Where N_d is the number of dopant molecules per unit volume, N_p the maximum number of aromatic rings in the polymer backbone per unit volume of polymer, N_A is Avogadro's number, MW_p is the molecular weight of a repeat unit in the polymer, MW_d the molecular weight of dopant, ρ_p the density of polymer, ρ_d the density of dopant, γ the ratio of dopant molecules to polymer repeat units and x is equal to the number of aromatic rings in the polymer repeat unit. The total number of states is always smaller than the maximum number of aromatic rings contributed by the polymer ($N_t \leq N_p$) and the number of charge carriers are always smaller than the number of dopants ($N_c \leq N_d$). Table 4.2 shows these parameters for the four polymers we used in this study.

Table 4.2 The molecular weight of a polymer repeat unit and the density of polymers (estimated) and dopant. γ is extracted from solution preparation and concentration of dopant and maximum number of states are calculated using equation S15 and S16.

material	MW (g/mol)	ρ (g/cm^3)	$\gamma\%$	x	N_d ($10^{19} cm^{-3}$)	N_p ($10^{20} cm^{-3}$)
PDPP-4T	1024.6	1.2	32	6	20.2	37
PDPP-T- TT-T	1110.71	1.2	35	6	20.3	35
RR-P3HT	166.28	1.2	5.3	1	20.3	38
RRa- P3HT	166.28	1.2	5.3	1	20.3	38
Mo(tfd) ₃	774.43	2.27				

To calculate the number of charge carriers in the polymer blends, we used Equation (4.28):

$$N_{C,Blend} = C_A N_{C,A} + C_B N_{C,B} \quad (4.28)$$

$N_{C,Blend}$ is the number of charge carriers in the blend, C_A and C_B are the concentrations of polymer A and B and $N_{C,A}$ and $N_{C,B}$ are the number of charge carriers for pure polymer A and pure polymer B.

Predicting a correct prefactor for electrical conductivity has been a challenge for analytical models.^{44,183,221,222} Here we have used a linear combination ν_0 of two pure polymers to fit to blend systems. To estimate the attempt to jump frequency in the blend system we have used a similar equation:

$$\vartheta_{0,Blend} = C_A \vartheta_{0,A} + C_B \vartheta_{0,B} \quad (4.29)$$

Where

$$\vartheta_{0,A} = \frac{\sigma_{Exp,A}}{\sigma_{Theory,A}} \quad (4.30)$$

$$\vartheta_{0,B} = \frac{\sigma_{Exp,B}}{\sigma_{Theory,B}} \quad (4.31)$$

σ_{Exp} is the experimentally measured electrical conductivity and σ_{Theory} is the theoretical electrical conductivity assuming ϑ_0 in Equation (4.14) is equal to 10^{12}s^{-1} .

AFM images of these polymer blends, as displayed in Figure 4.17, show large aggregates in both pure PDPP-T-TT-T and PDPP-4T films and in the blends at or above a PDPP-4T composition of 0.5. These aggregates are absent in the undoped polymer, and thereby we suspect that they are dopant rich, either consisting entirely of the dopant or consisting of highly doped polymers that are rendered insoluble upon heavy doping.²²³ Dopant aggregation would also agree with lower carrier concentration in these DPP containing polymers as compared to both P3HT polymers. The morphology of the films can play a large role in determining the thermoelectric performance, particularly in polymer blends.¹⁸⁴ Importantly for comparison purposes, the blend systems in this work show similar aggregated morphologies at higher (>0.5) PDPP-4T compositions where the increased power factors are observed for the RR-P3HT:PDPP-4T blends. The analytical model presented provides a nice framework for understanding the thermoelectric properties of polymer blends, but moving forward it will be important to experimentally investigate the morphologies in detail and incorporate the influence of morphology into the theoretical model. For example, the current analytical model may be expanded to include a

perturbation of the probability of hopping between the two polymers (C'_A and C'_B) based on the morphology.

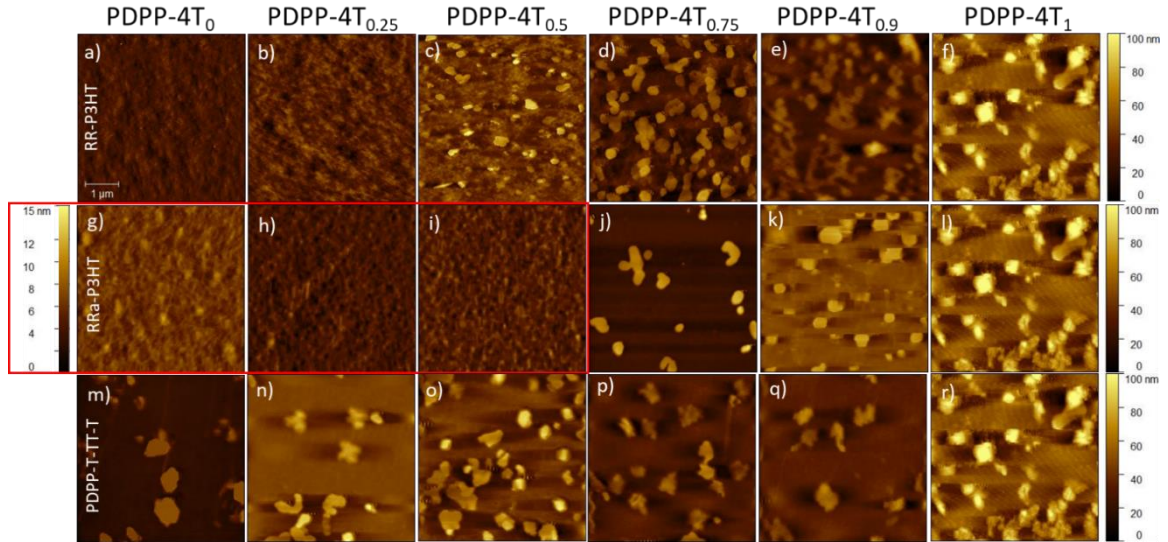


Figure 4.17 AFM on polymer blend system of RR-P3HT:PDPP:4T (a-f), RRa-P3HT:PDPP-4T (g-l) and PDPP-T-TT-T:PDPP-4T (m-r). Concentration of PDPP-4T in blend system is shown at top each column. Figures g, h and i have different scale which are separated by the red box.

4.7 Conclusion

The results presented show that polymer blends are capable of reaching higher power factors than either of the individual polymers. For higher power factors to be realized in the blend, the polymer with its DOS centered at higher energies should have a broader DOS and higher charge-carrier mobility. Furthermore, the electrical conductivities of the two polymers should not be drastically different, as this leads to the polymer with the higher electrical conductivity dominating charge transport and minimizing the influence of the other polymer. From a simple experimental viewpoint of selecting candidate polymers, the polymers should have similar electrical conductivities (within an

order of magnitude) and Seebeck coefficients (within a factor of two), and the polymer with the higher IE should have a higher mobility.

In terms of guiding the design of thermoelectric polymers, our results indicate that polymers with low energetic disorder (i.e., a narrow density of states distribution) and large localization lengths should be targeted for both polymer blends and pure polymers. In the case of blends, increases in performance should be obtainable regardless of the DOS width and localization length of the lower energy polymer, so long as the polymer with the higher energy DOS has a broader DOS and comparable or larger localization length. There are numerous factors that this work did not account for, such as the morphology of the polymer blends and the effects of blending polymers together on the width of the DOS of each individual polymer, that are likely to be important in determining the thermoelectric performance of polymer blends. Future work that accounts for morphology, doping induced disorder, and polymer interactions will be helpful in further guiding the design of polymer blend thermoelectrics.

CHAPTER 5. EFFECT OF ANION SIZE AND FLUORINATION ON POLARON FORMATION, POLYMER CRYSTALLINITY, AND THERMOELECTRIC PROPERTIES IN ORGANIC ELECTROCHEMICAL TRANSISTORS

5.1 Introduction

π -conjugated polymers (CPs) have shown promising potential for use in thermoelectric (TE) applications, where heat can be converted into electricity and vice versa, due to their potential inexpensive fabrication process, mechanical flexibility, large area application and their light weight nature.^{27–29,50,162,171,176,224–226} However, the performance must be increased to enable commercial applications. The performance of TE materials is determined by a unitless figure of merit, ZT , which is defined as $ZT = T\sigma S^2/\kappa$, where T is absolute temperature, σ is the electrical conductivity, S is the Seebeck coefficient and κ is thermal conductivity.²²⁷ Since CPs have the advantage of low thermal conductivity,¹⁶² increasing the power factor, $PF = \sigma S^2$, is currently the primary focus for optimization of CP TEs. The common approach to improve PF is by increasing σ with increasing charge carrier concentration by adding dopants with the expense of a decrease in S .^{50,178,205,228} Understanding the variables that affect charge transport in CPs can help to minimize this trade-off.

Doping of OSCs is a method to enhance the charge-carrier mobility, charge-carrier density, and thereby the electrical conductivity.^{226,229–232} A common way to dope CPs is by adding a dopant molecule to the CP to oxidize or reduce the polymer. The enhancement of electrical conductivity in such systems depends on various factors, including the doping method, doping efficiency,^{178,179} dopant aggregation, and dopant size and structure.^{44,177,231–235} In the process of oxidizing or reducing the CP, polarons and/or bipolarons are formed on the CP backbone. These polarons and/or bipolarons are typically

delocalized over multiple aromatic units of the polymer, which is a key factor in determining charge-carrier transport properties in CPs.^{39,236–242} This delocalization involves different extents of interchain and intrachain contributions and the amount of delocalization that occurs will have a huge effect on determining the charge-carrier mobility in the polymer.^{239–245} For example, in >98% regioregular poly(3-(2'-ethyl)hexylthiophene) P3EHT the mobility is around $10^{-5} \text{ cm}^2\text{V}^{-1}\text{s}^{-1}$,²⁴⁶ yet in regioregular Poly(3-hexylthiophene) (RR-P3HT) the mobility can reach up to $10^{-1} \text{ cm}^2\text{V}^{-1}\text{s}^{-1}$.^{247,248} Both of these polymers are semi-crystalline and share the same backbone, but they show large differences in the extent of polaron delocalization, and particularly in the interchain direction.²³⁹ In RR-P3EHT the polaron is delocalized over 4.8 thiophene units in the intrachain direction (N_{intra}) and only 1.1 units in the interchain direction (N_{inter}). By contrast, 100% RR-P3HT with similar crystallinity displays a more 2D polaron with $N_{\text{intra}}=3-4.8$ and $N_{\text{inter}}=1.8-2.8$.^{239,243,244} The high-mobility polymer poly(3-([2,2':5',2''-terthiophen]-5-yl)-2,5-bis(6-dodecyloctadecyl)-2,5-dihydropyrrolo[3,4-c]pyrrole-1,4-dione-6,5''-diyl) (P(DPP6DOT2-T)) also shows significant polaron delocalization in both the interchain and intrachain direction ($N_{\text{intra}}=3.8-4.3$ and $N_{\text{inter}}=2.3-3.3$).²⁴⁰ By contrast, in the work done by Milner's group^{242,245,241}, in the crystalline region of P3HT the polaron was calculated to be mostly localized along the chain with a negligible activation energy in this direction, $0.25 \times 10^{-5} \text{ eV}$ and larger activation energy, 0.09 eV for interchain hopping due to the calculated small delocalization in the interchain direction. In general, these works highlight how important the degree of polaron delocalization is in both the inter- and intrachain directions for determining charge transport behavior and how there is still disagreement and uncertainty regarding the extent of polaron delocalization.

In addition to the polymer conformation and morphology, the dopant size also affects polaron delocalization and the electrical conductivity.^{177,235,240,249–251} Here, the general idea is that larger dopants can increase the distance between the charges on the dopant and polymer; thereby, reducing Coulombic interactions between the charges and increasing charge-carrier delocalization on the CP. Liang *et.al.* showed that that larger dopants, such as molybdenum tris-[1,2-bis(trifluoromethyl) ethane-1,2- dithiolene] ($\text{Mo}(\text{tfd})_3$), lead to more delocalized polarons than smaller dopants, such as FeCl_3 , which results in higher electrical conductivity and improved TE performance.¹⁷⁷ Increasing dopant size to increase charge-carrier delocalization was a primary goal in the work done by Aubry *et. al.*,²⁴⁹ where a large spherical dopant, DDB- F_{72} (a pseudoicosahedral dodecaborane core with each vertex functionalized with a 3,5-bis(trifluoromethyl)benzyloxy substituent) with a diameter of 2 nm was developed and compared with 2,3,5,6-tetrafluoro-7,7,8,8-tetracyanoquinodimethane (F_4TCNQ), which has a smaller size with a length of 0.8 nm and width of 0.4 nm. The larger DDB- F_{72} dopant led to nearly an order of magnitude higher electrical conductivity in RR-P3HT when compared to F_4TCNQ .²⁵¹ Although these works strongly support the impact of dopant size on charge-carrier delocalization, more quantitative conclusions are difficult due to competing variables such as different doping efficiencies and significantly different polymer morphologies.

Organic electrochemical transistors (OECTs) provide an ideal platform for developing a more definitive understanding of counterion size effects on charge-carrier delocalization and TE properties of CPs. Multiple groups have shown that OECTs provide a viable and well-controlled platform for studying TE properties of CPs.^{201,252,253} Using

OECT has some advantages over using field effect transistors in studying TE properties such as; the counter ions penetrate into the bulk of the film so more representative measurements of TE properties can be achieved, because of high capacitance of ionic liquid, with lower gate voltage more counter ions can penetrate into the film and so measurements can be done for higher charge-carrier concentration. Using OECTs to probe the effect of counterion size on TE properties of CPs has several advantages; including (1) direct control of charge carrier concentration by adjusting the gate voltage , (2) minimal impact on disturbing the CP morphology relative to chemical doping and (3) the electron affinity (EA) of anions becomes irrelevant in the doping process as the charge-carrier concentration is controlled by the gate voltage. In this study we used UV-Vis-NIR absorbance spectroelectrochemistry to probe polaron delocalization and ion penetration into crystalline region versus amorphous region. Tuning the polaron delocalization by varying the anion size can help us to gain a better understanding of charge transport in doped CPs and potentially provide guidelines for improvement of thermoelectric power factors.

5.2 Materials and device structure

In this study we selected 3 p-type polymers, Regiorandom P3HT (RRa-P3HT) and regioregular P3HT (RR-P3HT) and PDPP-4T. RRa-P3HT and RR-P3HT are two well-known and well-studied polymers with charge carrier mobilities that are different by several orders of magnitude. Hole mobility of RR-P3HT can reach up to $0.1 \text{ cm}^2\text{V}^{-1}\text{s}^{-1}$ vs. the RRa-P3HT with hole mobilities in the range of 10^{-5} to $10^{-4} \text{ cm}^2\text{V}^{-1}\text{s}^{-1}$.^{215,216} The other key difference between these two polymers is their structure. RRa-P3HT forms a fully amorphous structure vs. RR-P3HT shows a system of both crystalline and amorphous

phases. This difference in morphology is apparent in the UV-Vis-NIR absorbance, Raman spectra and GIWAXS measurements.^{216,254–256} PDPP-4T is a high mobility ($1 \text{ cm}^2\text{V}^{-1}\text{s}^{-1}$) polymer with semi-crystalline structure.^{69,217,257,258} The structure of polymers are shown in Figure 5.1.

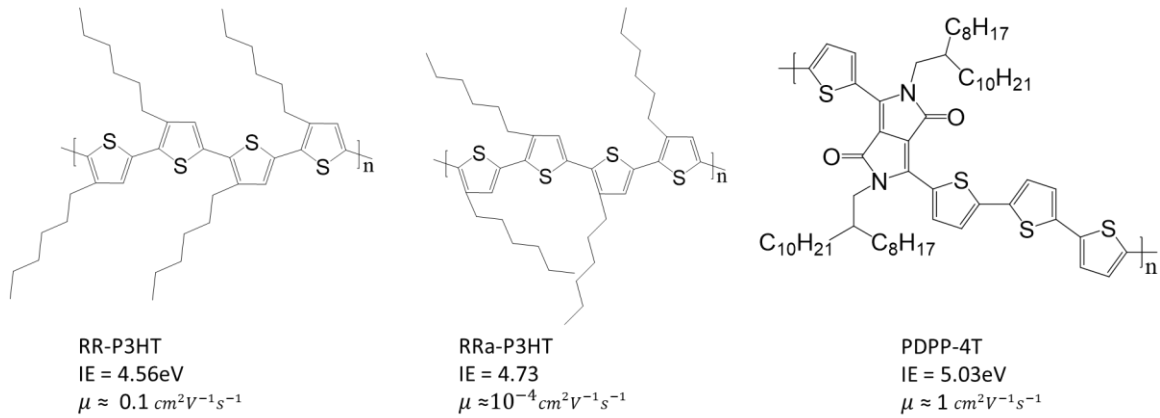


Figure 5.1 Chemical structure of RR-P3HT, RRa-P3HT and PDPP-4T with their IE and hole mobility.

As shown in Figure 5.2 (a), OECT device structure consists of source and drain electrodes, gate electrodes, CP, and polymeric ionic liquid (PIL) as the gate dielectric. Here we used poly(diallyldimethylammonium) as PIL with chloride as the smallest anion which has been used as OECTs before and the chemical structure is shown in Figure 5.2 (b).²⁵⁹ X can be replaced by another anion. A list of anions we used in this work is shown in Figure 5.2 (c-h). Here we are using chloride (Cl^-) with radius 1.6 \AA , tetrafluoroborate (BF_4^-) with radius 2.6 \AA , hexafluorophosphate (PF_6^-) with radius 2.9 \AA , tetrphenylborate (BPh_4^-) with radius 4.4 \AA , tetrakis(4-fluorophenyl)borate (B(PhF)_4^-) with radius 7 \AA , tetra(p-tolyl)borate (B(PhMe)_4^-) with radius 7.1 \AA , tetrakis(4-chlorophenyl)borate (B(PhCl)_4^-) with radius 7.9 \AA , tetrakis(pentafluorophenyl)borate ($\text{B(PhF}_5)_4^-$) with radius 7 \AA and tetrakis[3,5-bis(trifluoromethyl)phenyl]borate ($\text{B(Ph(CF}_3)_2)_4^-$) with radius 7.3 \AA .²⁶⁰ All of the anions here are bulky anions and they cover a range from 1.6 \AA to 7.9 \AA in radius. These selections

of polymers with the anions allow us to systematically study the effect of anion size and electrostatic charge of the anion on the polaron formation in the crystalline and amorphous regions of polymers.

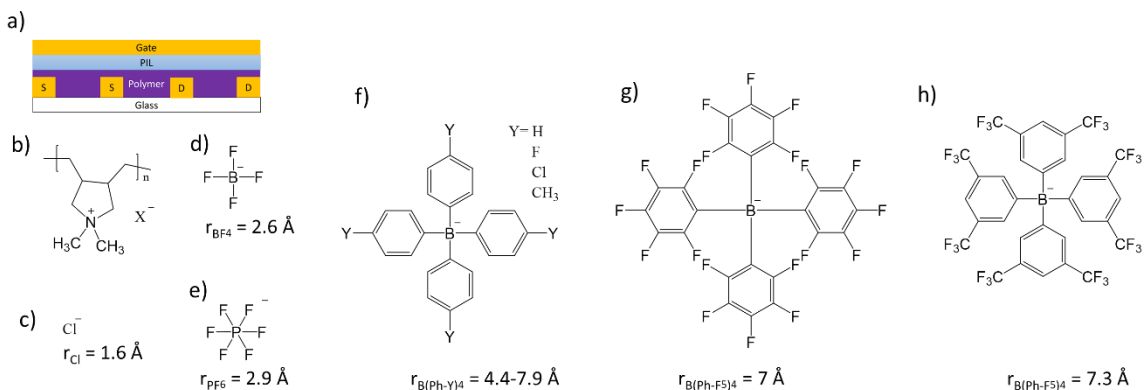
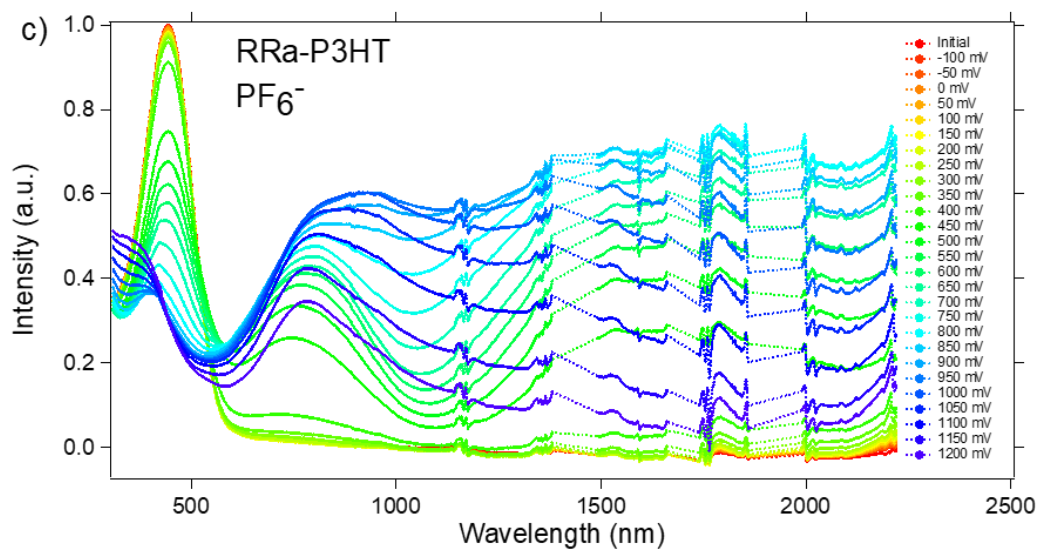
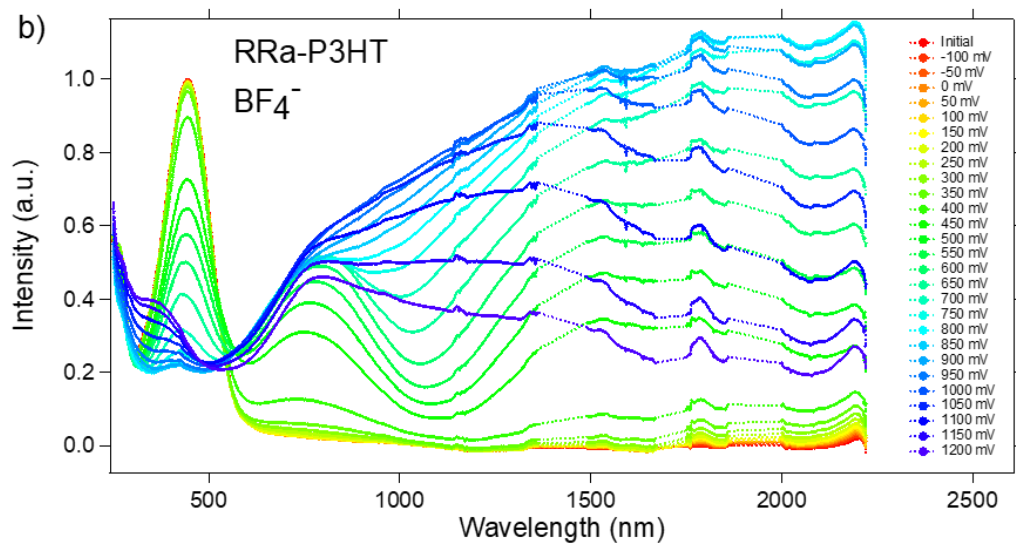
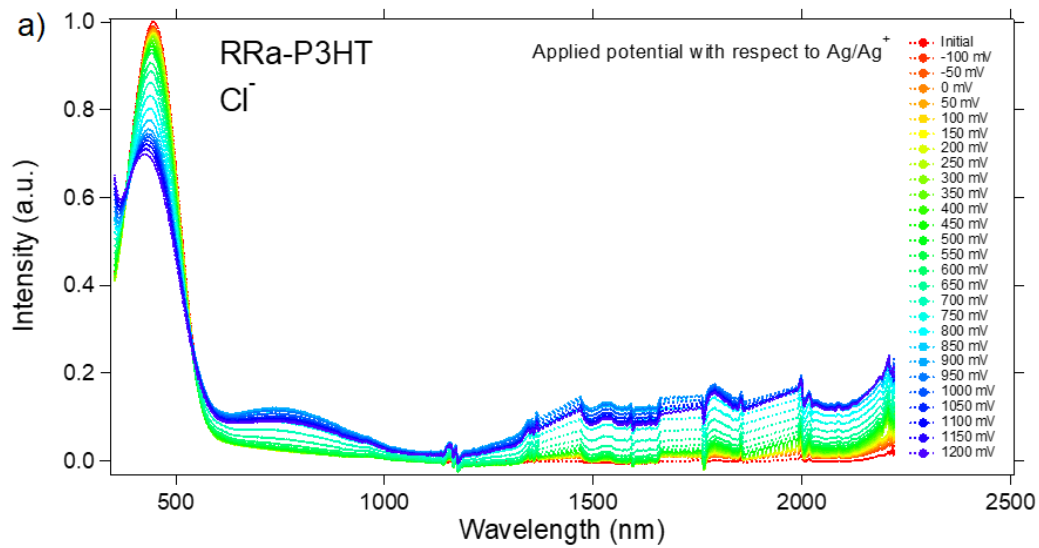


Figure 5.2 (a) Schematics of OECT device. (b) Chemical structure of PIL. (c-h) Chemical structure of anions and their radii, Cl^- , BF_4^- , PF_6^- , BPh_4^- , B(PhF)_4^- , B(PhCl)_4^- , B(PhMe)_4^- , $\text{B(PhF}_5)_4^-$ and $\text{B(Ph(CF}_3)_2)_4^-$.

5.3 Absorbance spectroelectrochemistry

Here we used absorbance spectroelectrochemistry to probe the penetration of anion from the electrolyte into amorphous and crystalline regions of the polymer film as potential is applied. Using absorbance spectra, we also probe the polaron concentration with respect to neutral peak of the polymer and polaron energy as a function of applied potential. Absorbance spectroelectrochemistry of RRA-P3HT with 5 different anions is shown in Figure 5.3. Surprisingly, the anions containing fluorine have a higher doping efficiency observed in Figure 5.3 (b), (c) and (e).



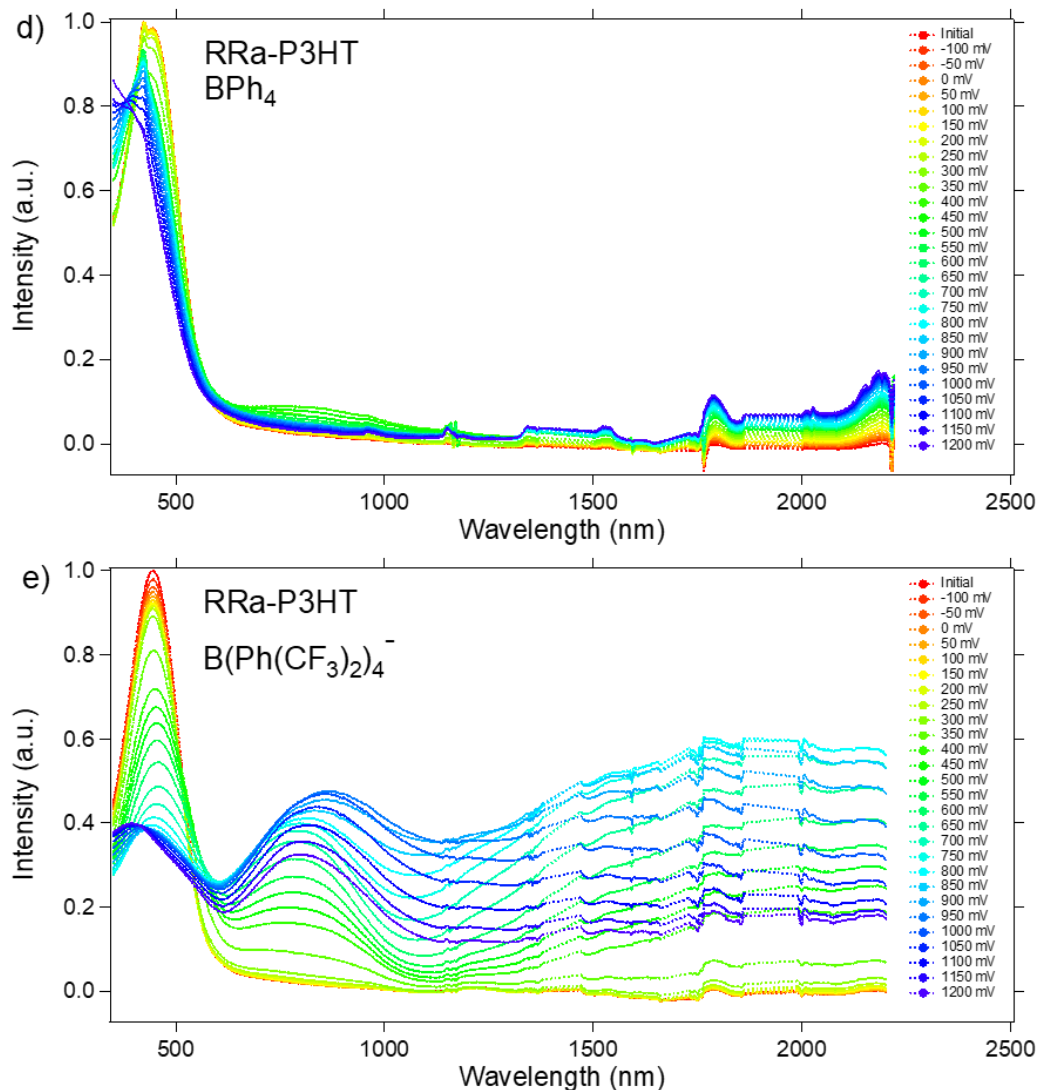
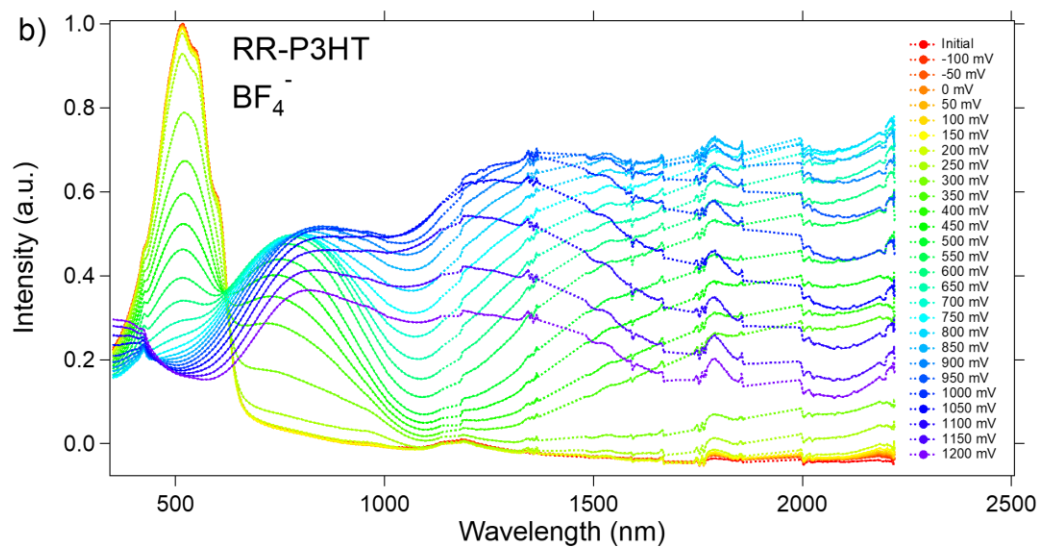
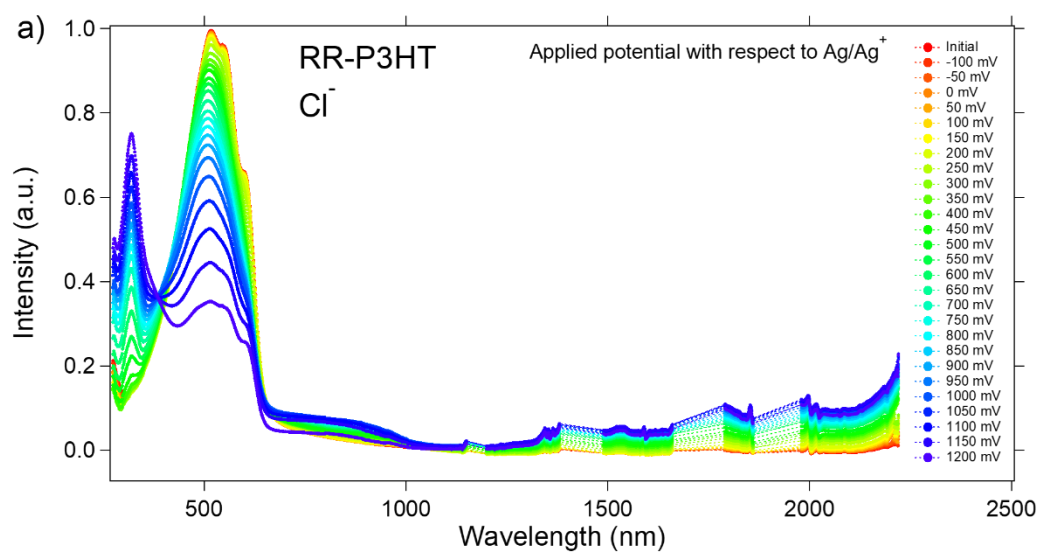


Figure 5.3 Absorbance spectroelectrochemistry of RRa-P3HT with different anions, (a) Cl^- , (b) BF_4^- , (c) PF_6^- , (d) BPh_4^- and (e) $\text{B}(\text{Ph}(\text{CF}_3)_2)_4^-$. Each color represents a different applied potential with respect to reference electrode, Ag/Ag^+ . The dashed lines are showing the part of data that has been cut out because of high absorbance of acetonitrile in those regions.

Figure 5.4 showing the absorbance spectroelectrochemistry of RR-P3HT with Cl^- , BF_4^- , PF_6^- , BPh_4^- and $\text{B}(\text{Ph}(\text{CF}_3)_2)_4^-$ anions. RR-P3HT has a strong absorbance shoulder at about 600 nm indicating the crystalline region of the polymer. Similarly, as RRa-P3HT, the anions with the fluorine atom in their structure had a higher doping efficiency.



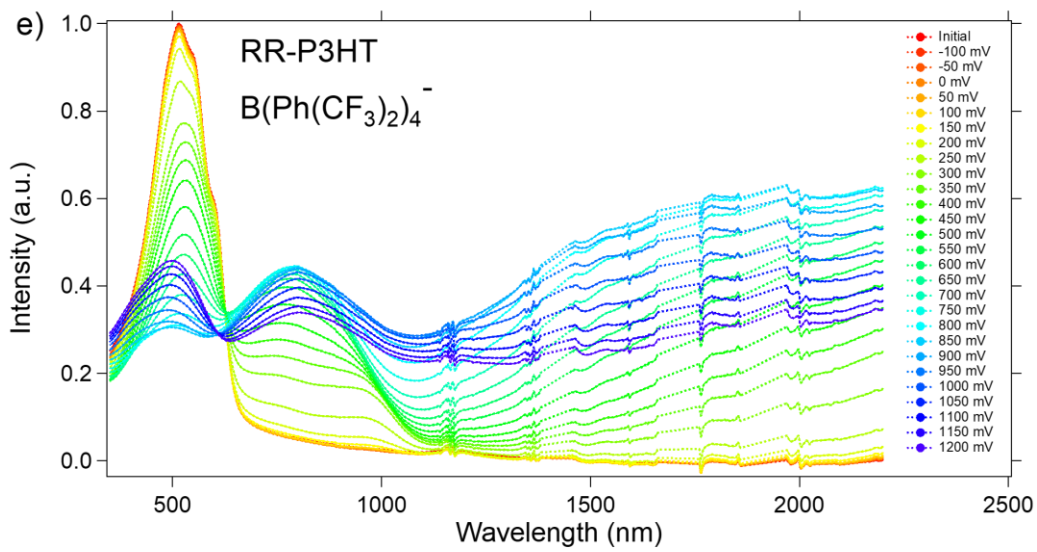
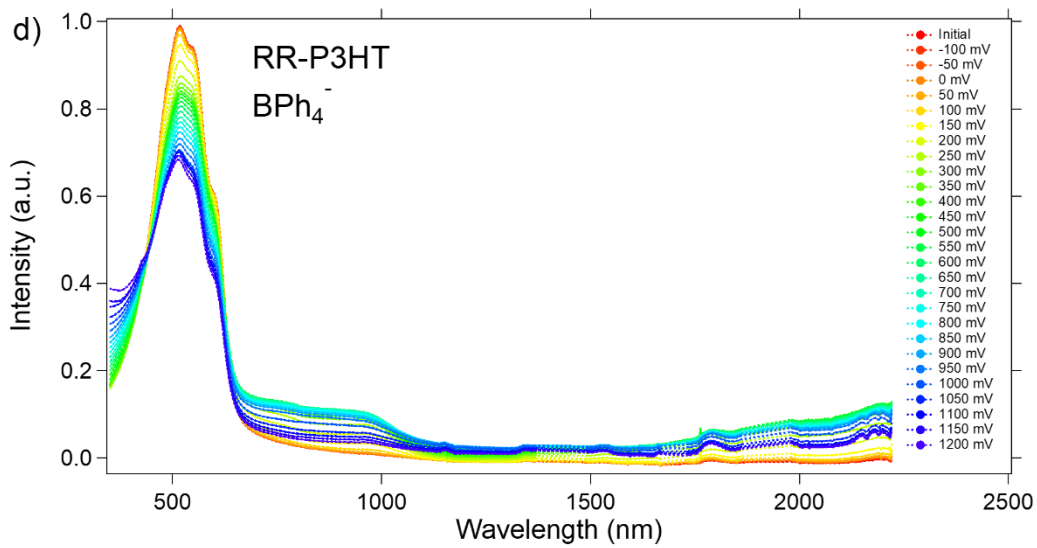
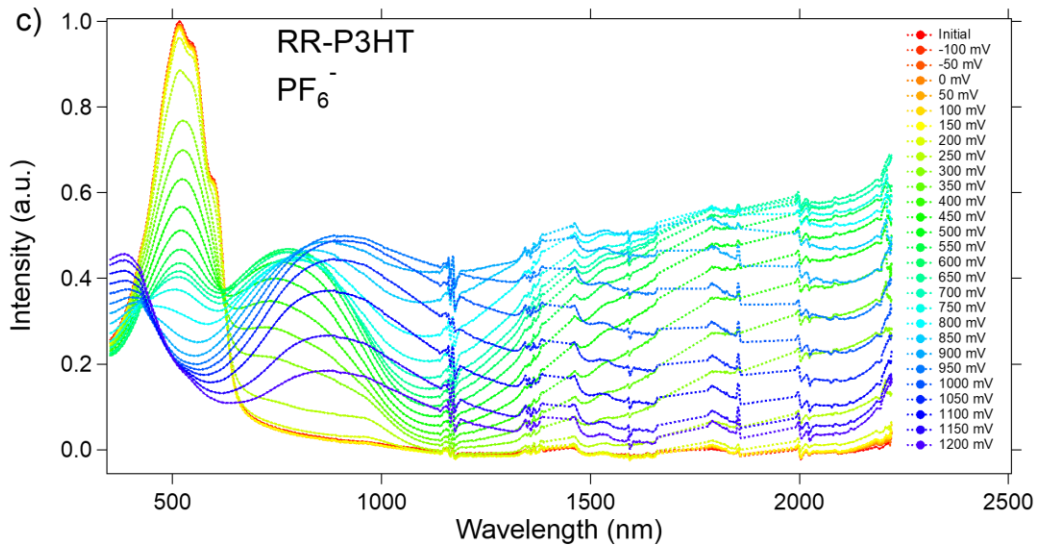


Figure 5.4 Absorbance spectroelectrochemistry of RR-P3HT with different anions, (a) Cl^- , (b) BF_4^- , (c) PF_6^- , (d) BPh_4^- and (e) $\text{B}(\text{Ph}(\text{CF}_3)_2)_4^-$. Each color represents a different applied potential with respect to reference electrode, Ag/Ag^+ . The dashed lines are showing the part of data that has been cut out because of high absorbance of acetonitrile in those regions.

To have a good comparison between the spectra, we find the ratio between the polaron peak intensity to neutral absorbance peak of P3HT. Figure 5.5 shows the applied potential (vs Ag/Ag^+) vs polaron to neutral peak intensity ratio of RRa-P3HT and RR-P3HT. As shown, anions containing fluorine have a much higher doping efficiency by almost one order of magnitude. Between BF_4^- , PF_6^- and $\text{B}(\text{Ph}(\text{CF}_3)_2)_4^-$, smaller anions have higher doping efficiency. To further see the effect of fluorine atoms in the doping efficiency we will compare these results with $\text{B}(\text{PhCl})_4^-$, $\text{B}(\text{PhMe})_4^-$, $\text{B}(\text{PhF}_5)_4^-$ where we have Cl, methyl group or 4 more fluorine atoms. As expected, for RRa-P3HT at about 400 mV the polaron start to form which is 150 mV higher than for RR-P3HT. This is due to lower IE of crystalline regions of RR-P3HT vs the amorphous regions of RRa-P3HT.

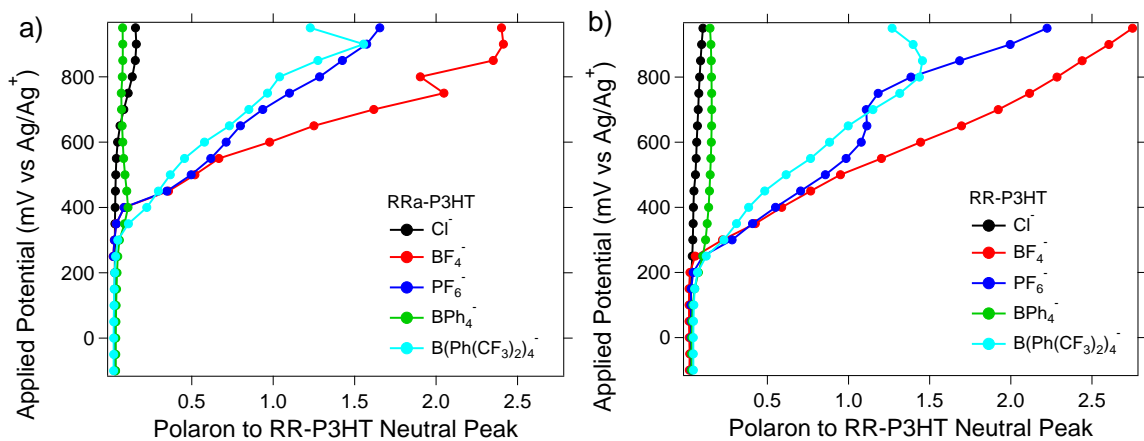


Figure 5.5 Applied potential (vs Ag/Ag^+) vs polaron to neutral peak of polymer for (a) RRa-P3HT and (b) RR-P3HT for 5 anion, Cl^- , BF_4^- , PF_6^- , BPh_4^- and $\text{B}(\text{Ph}(\text{CF}_3)_2)_4^-$.

Figure 5.6 shows the polaron absorbance region of RRa-P3HT and RR-P3HT. In both polymers and at same polaron concentrations, the larger anion leads to a polaron with its absorbance edge at lower energy. We suspect this is due to the smaller columbic

interaction between the larger anion and the polaron which causes the polaron to be more delocalized and show a lower absorbance energy.

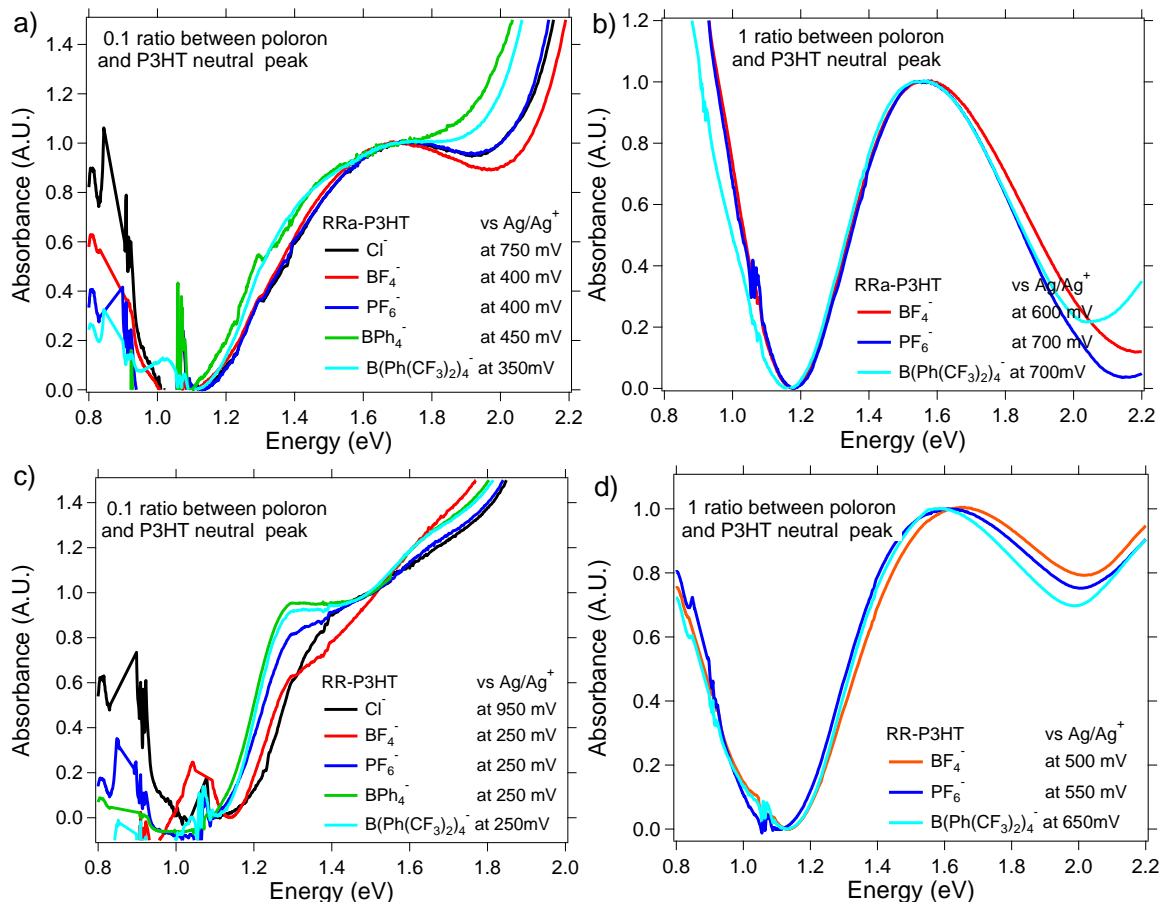


Figure 5.6 Absorbance spectroelectrochemistry of polaron absorbance region of (a,b) RRa-P3HT and (c,d) RR-P3HT vs photon energy. (a,c) Showing the polaron absorbance for concentration of polaron to P3HT neutral peak around 0.1 and (b,d) concentration of 1. In both polymer Cl^- and BPh_4^- couldn't reach concentration of 1 even at 1200 mV.

To determine if the anion size affects the degree of anion penetration into the crystalline region vs amorphous region, we looked at the absorbance region of RR-P3HT neutral peak shown in Figure 5.7 (a) at 500 mV applied potential with respect to Ag/Ag^+ . As indicated in Figure 5.7 (b) the larger anion shows a shift in the neutral state peak position of RR-P3HT to lower energy. This lower energy absorbance may indicate that the

larger anions could be selectively bleaching the higher-energy amorphous regions and resulting in a peak shift towards lower energy.

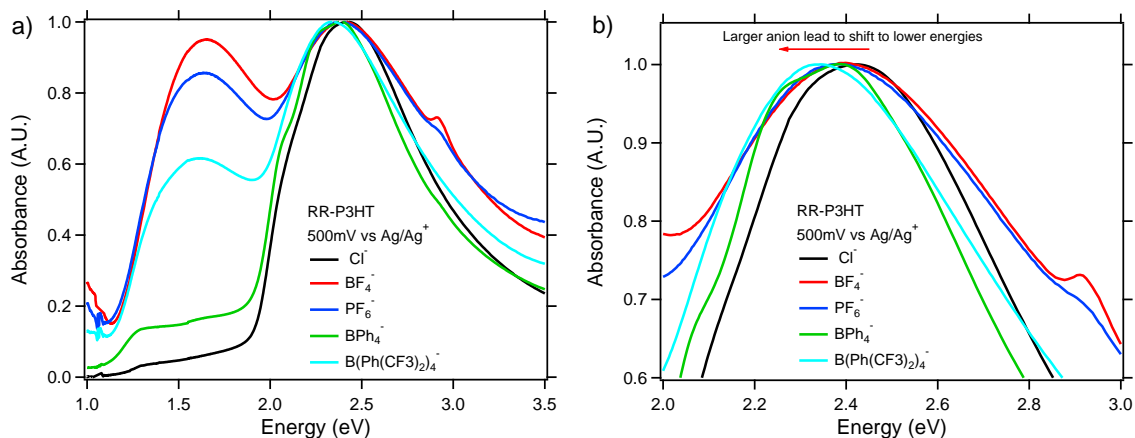


Figure 5.7 Absorbance spectroelectrochemistry of (a) RR-P3HT and (b) neutral peak of P3HT absorbance region at 500 mV applied potential with respect to Ag/Ag^+ .

5.4 Conclusion

By looking at the absorbance edge of polarons in spectroelectrochemical data from various anions for both RR-P3HT and RRA-P3HT, we concluded that larger anions cause the polarons to form at lower energies. Also, we concluded that fluorinated anions have higher doping efficiency comparing to non-fluorinated anions. In absorbance spectrums of RR-P3HT using larger anions, as anions penetrate into the film, the neutral peak intensity of P3HT shifts towards the lower energies. These trends for larger anions suggest that they prefer to enter the amorphous region earlier than crystalline region of P3HT due to their size.

In summary, as expected, larger anions will have less columbic interaction with polarons and lead to lower energy polaron, this causes the polaron to be more delocalized and potentially improve the electrical conductivity. Similarly, larger anions prefer to

penetrate and dope the amorphous region first which may also lead to a higher Seebeck coefficient as charge carriers at these higher energy states become more delocalized. More experiments needed to be done to confirm this delocalization of polarons such as Raman spectroelectrochemistry to look at the stretching modes on thiophenes and measuring Seebeck coefficient in OECT devices.

APPENDICES

APPENDIX 1. LabVIEW

In this section the LabVIEW codes for various setups is discussed.

First is LabVIEW code for IPES setup. This code was mainly a modification to the main LabVIEW codes provides by the company for controlling the electron gun. The modification was done to be able to count the sample current and PMT signal as the electron gun energy is changing without disrupting the codes which run the electron gun and ensure its safety parameters. The modified LabVIEW diagram is shown in Figure A1.1. The block diagram was too large and complicated to be shown here.

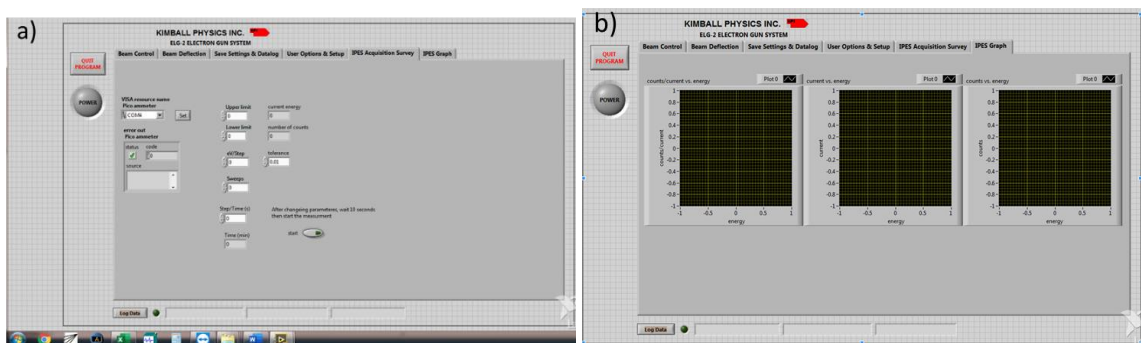


Figure A1.1 LabVIEW diagram for IPES. (a) controlling the electron gun and (b) measured figures from left to right PMT counts/Sample current, Sample current and PMT counts all vs. energy of electron.

Second is presented the LabVIEW code for the PV characterizing.

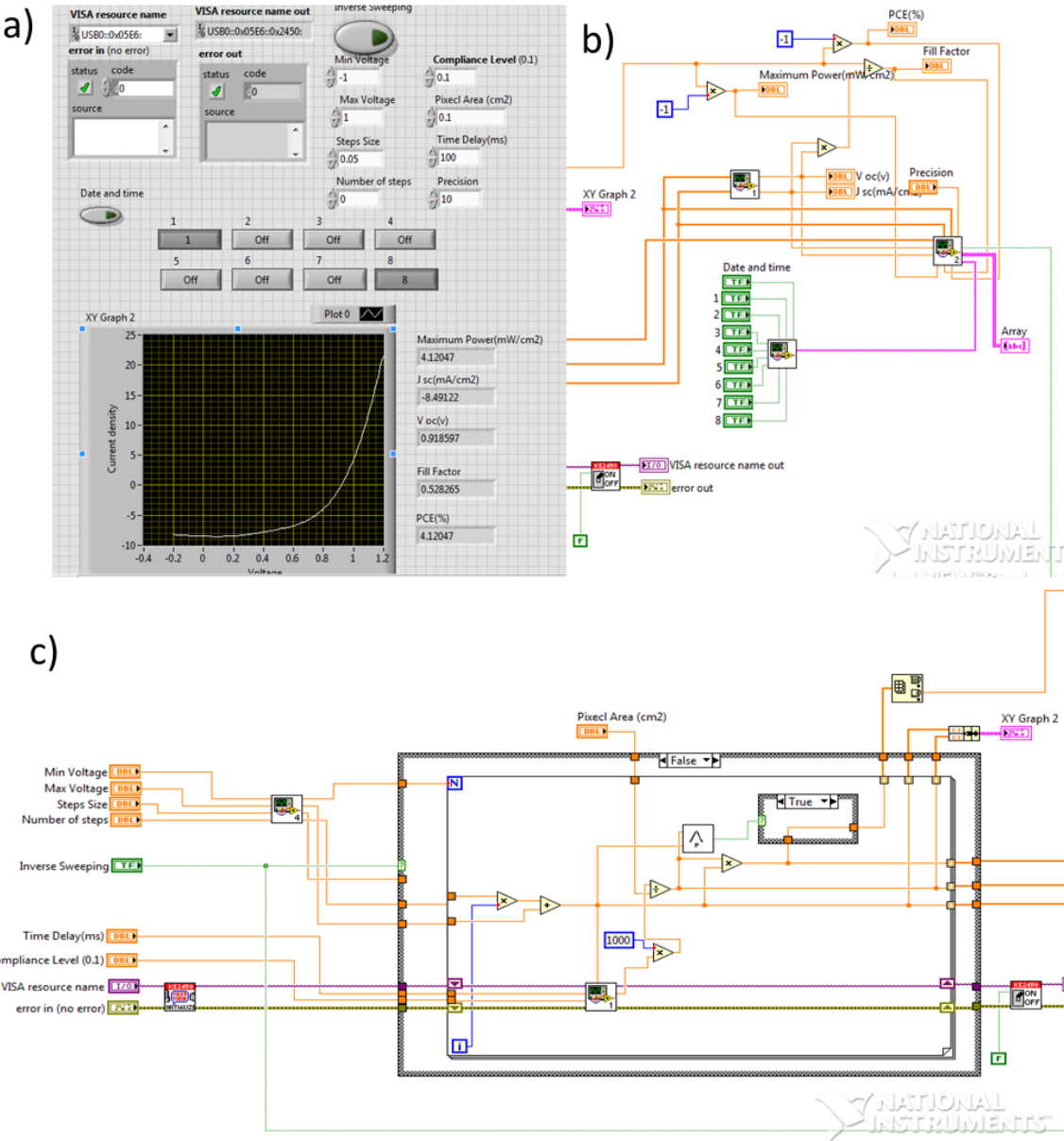
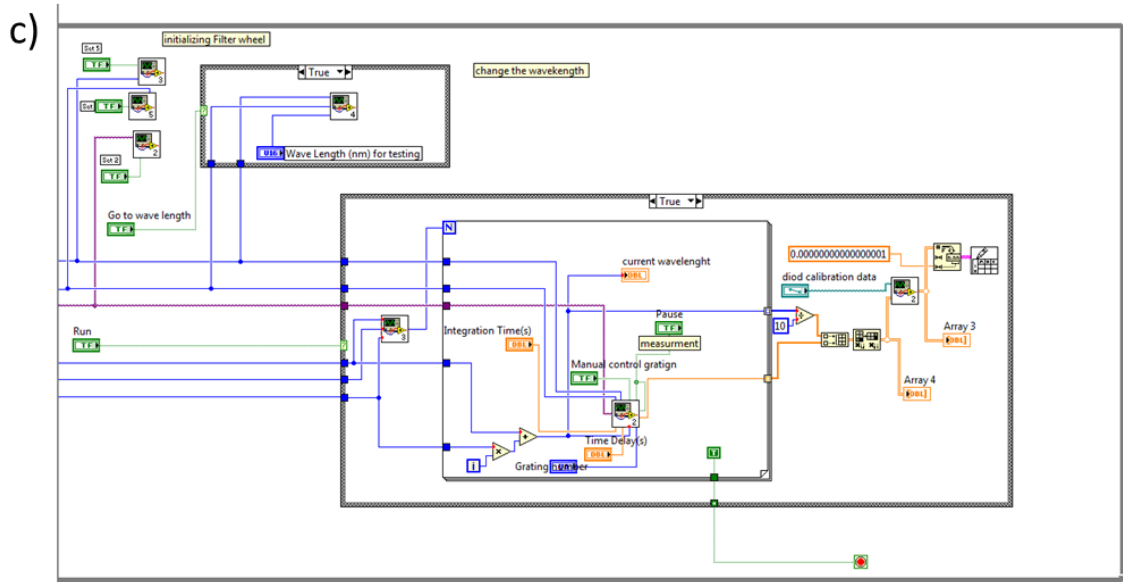
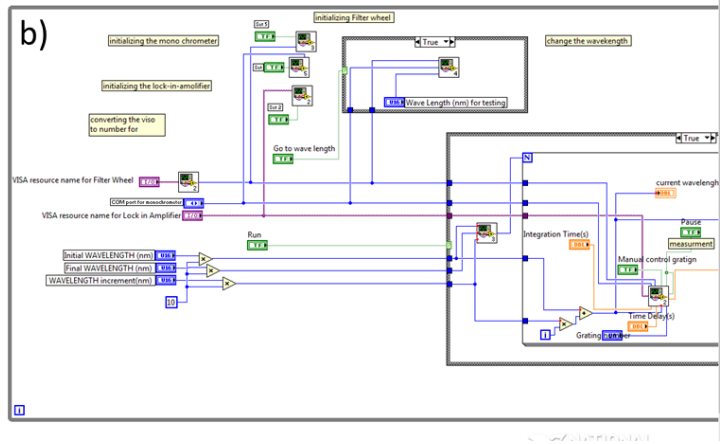
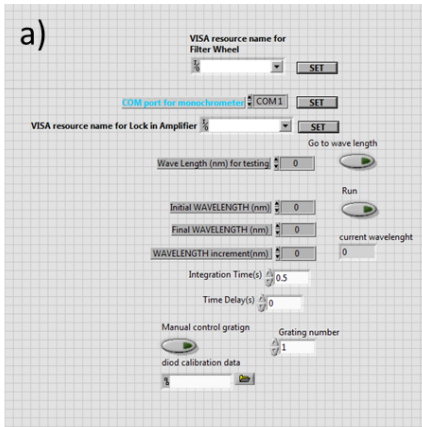


Figure A1.2 LabVIEW diagram for PV characterizing. (a) controlling the Keithley 2450 for voltage sweep and (b) block diagram of calculating FF and PCE and (c) block diagram of initializing the Keithley and applying the voltage and measuring the current.

Third is presented the LabVIEW code for the EQE measurements shown in Figure A1.3. In this code first the light source is calibrated with a silicon and germanium photodiode. First Lock-In-Amplifier, filter wheel and monochromator are initialized to check for a good connection. Then the range and steps for changing the wavelength of monochromator is selected. A text file containing the photodiode calibration should be loaded to the program before the start. The code will export a file that should be used in another LabVIEW code (Figure A1.3 (d)) to measure the EQE of the sample. The parameter to measure EQE is similar to one for light source calibration.



APPENDIX 2. Calculating Surface coverage using XPS

Adapted with permission from S. M. Park, A. Abtahi, A. M. Boehm, and K. R. Graham, "Surface Ligands for Methylammonium Lead Iodide Films: Surface Coverage, Energetics, and Photovoltaic Performance", *ACS Energy Lett.* 2020, 5, 7, 2265. Copy right © 2020 American Chemical Society.⁶⁴

XPS can be used to estimate the surface coverage of a functional group or surface ligand on a substrate using a substrate overlayer model.²⁶¹ The substrate overlayer model is used to convert XPS peak area ratios of one element from the overlayer and from the substrate into a fractional monolayer coverage based upon the surface ligand (overlayer) structure.^{262–264} As shown in Equation (5.1), the ratio of XPS peak areas arising from the overlayer (I_{Ov}^x) and the substrate (I_{Sub}^y) are related to the fractional coverage (Φ) of the overlayer, where the overlayer is the surface ligand layer and the substrate is MAPbI₃. Here, I_{Ov}^x and I_{Sub}^y correspond to XPS peaks from elements that are unique to the overlayer or substrate, respectively.

$$\frac{I_{Ov}^x}{I_{Sub}^y} = \frac{SF^x}{SF^y} \frac{\rho_{a,Ov}^x}{\rho_{a,Sub}^y} \frac{\lambda_{Ov}^x}{\lambda_{Sub}^y} \frac{\phi (1 - \exp\left[-\frac{d_{Ov} \cos(\beta)}{\lambda_{Ov, self}^x \cos(\theta)}\right])}{1 - \phi + \phi \exp\left[-\frac{(d_{Ov} + D) \cos(\beta)}{\lambda_{Sub, Ov}^y \cos(\theta)}\right]} \quad (5.1)$$

In equation (1), $\rho_{a,i}^x$ is the atomic density of an element (x or y) from the overlayer (Ov) or substrate (Sub), λ_i^x is the attenuation length of an element x in an infinitely thick layer i, SF^x is the sensitivity factor of element x, d_{Ov} is the thickness of the layer from which photoelectrons of element x are passing through, D is the thickness of the region where the photoemitted electrons of interest in the overlayer are emitted from, $\lambda_{Ov, self}^x$ is the attenuation length of photoelectrons from element x passing through the overlayer itself, $\lambda_{Sub, Ov}^y$ is the attenuation length of photoelectrons from element y passing through the surface ligand layer with length of $d_{Ov} + D$, and the electron take-off angle (θ) is the angle

between the detector and the substrate surface normal. β indicates the tilt angle of the ligand with respect to the surface normal, which shortens d_{Ov} and D by their product with $\text{Cos}(\beta)$. Self-assembled monolayers (SAM) typically do not stand straight up and so a title angle, β , is included.

For simplicity here we assume the surface ligand to be Octylphosphonic acid (OPA) and substrate to be MAPbI₃. By following the work done by Gao et. al.²⁶⁵ we can approximate the ratio of atomic densities by assuming they bind to Pb atoms. We expect that all ligands except for the ammonium containing ligands will indeed bind to Pb. In case of a cubic crystal structure, Figure A2. (a), for each unit cell (3 iodide and 1 Pb) there will be 1 ligand adsorption cite. As shown in Figure A2.1 (b) and (c), by assuming a tetragonal crystal structure for MAPbI₃ (100 and 001 face), for each unit cell there can be 2 Pb atoms on the surface that can bind to 2 ligands (i.e., one ligand per Pb atom) at 100% coverage. In each unit cell there are a total of 12 iodide atoms and for each PA containing ligand there are 3 oxygen atoms (total of 6 oxygens for a unit cell):

$$Cubic^{PbI_2}: \frac{\rho_{a,modifier}^O}{\rho_{a,MAPbI_3}^I} = \frac{\frac{3}{Area \times d_{PA} \text{Cos}(\beta)}}{\frac{3}{Area \times a_{cubic}}} = \frac{a_{cubic}}{d_{PA} \text{Cos}(\beta)} \quad (5.2)$$

$$Tetragonal_{100}^{MA_2Pb_2I_2}: \frac{\rho_{a,modifier}^O}{\rho_{a,MAPbI_3}^I} = \frac{\frac{6}{Area \times d_{PA} \text{Cos}(\beta)}}{\frac{12}{Area \times \sqrt{2} a_{cubic}}} = \frac{\sqrt{2}}{2} \frac{a_{cubic}}{d_{PA} \text{Cos}(\beta)} \quad (5.3)$$

$$Tetragonal_{001}^{Pb_2I_4}: \frac{\rho_{a,modifier}^O}{\rho_{a,MAPbI_3}^I} = \frac{\frac{6}{Area \times d_{PA} \text{Cos}(\beta)}}{\frac{12}{Area \times 2 a_{cubic}}} = \frac{a_{cubic}}{d_{PA} \text{Cos}(\beta)} \quad (5.4)$$

In these equations d_{PA} is the length of phosphonic acid (PA) group, a_{cubic} is the lattice unit cell length for a cubic MAPbI₃ crystal structure, which equals 0.635 nm, and $Area$ is the cross sectional area of the particular plane for the unit cell. The details of the

length of modifiers are shown in Figure S6 on average, we use a ratio of $0.9 \frac{a_{cubic}}{d_{PA} \cos(\beta)}$.

Sensitivity factors for I 3d_{5/2} and O 1s are 6.206 and 0.711 respectively.²⁶⁴

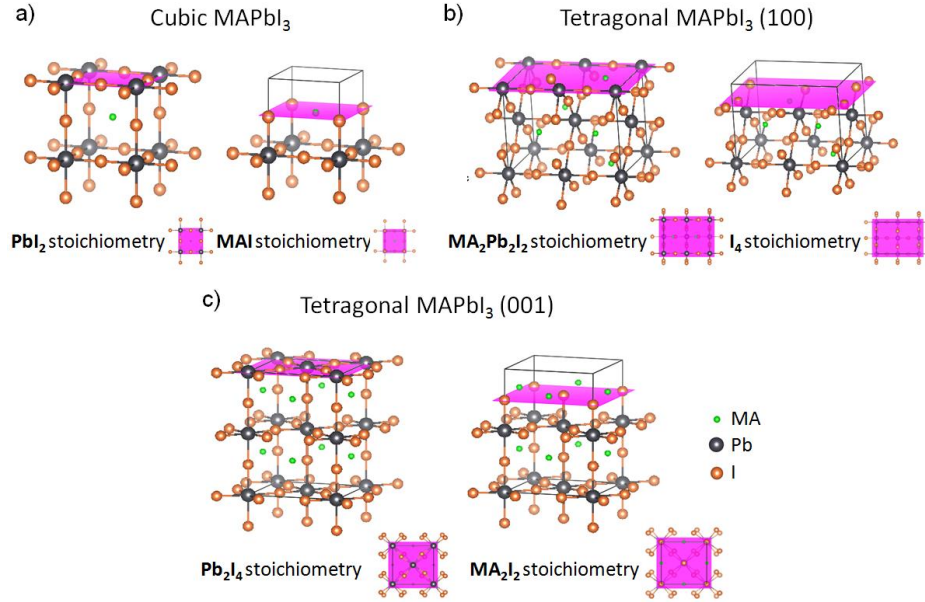


Figure A2.1 (a) MAPbI₃ cubic crystal structure with the (001) and (002) planes shown in pink. MAPbI₃ tetragonal crystal structure showing the (b) (100) and ($\bar{4}00$) planes and (a) the (001) and (00 $\bar{4}$) planes. Pb atoms are shown in black, I in orange and MA molecule in green. The indicated planes were used in surface coverage calculations.

The attenuation lengths can be approximated by equation (S4).^{266,267}

$$\lambda = 0.316 \times 10^{12} \left(\frac{A}{\rho_m N} \right)^{1/2} \left[\frac{E}{Z^{0.45} (3 + \ln \frac{E}{27})} + 4 \right] \quad (5.5)$$

Where A is the atomic molar mass in g mol⁻¹, ρ_m is mass density in kg m⁻³, N is Avogadro's number, Z is the total atomic number of the layer and E is kinetic energy of the element of interest.

We are probing the integrated intensity of the I 3d_{5/2} photoelectrons from MAPbI₃ and the oxygen signal from the OPA ligand. The equation for calculating surface coverage is shown below:

$$\lambda \frac{I_{PA}^O}{I_{MAPbI_3}^I} = \frac{SF^O}{SF^I} \frac{\rho_{a,PA}^O}{\rho_{a,MAPbI_3}^I} \frac{\lambda_{PA}^O}{\lambda_{MAPbI_3}^I} \frac{\phi (1 - \exp\left[-\frac{d_{Octyl} \cos(\beta)}{\lambda_{Octyl}^O \cos(\theta)}\right])}{1 - \phi + \phi \exp\left[-\frac{d_{OPA} \cos(\beta)}{\lambda_{OPA}^I \cos(\theta)}\right]} \quad (5.6)$$

The photoelectrons generated from O in the PA group are attenuated by λ_{PA}^O , and photoelectrons from I generated in MAPbI₃ are attenuated by $\lambda_{MAPbI_3}^I$. Oxygen's signal is further attenuated by passing through the octyl group with $d_{Octyl} \cos(\beta)$ thickness and attenuation length of λ_{Octyl}^O , and the iodide signal is attenuated by passing through OPA with $d_{OPA} \cos(\beta)$ thickness. We note that this modeling is based on a flat surface and local variations in surface roughness can result in deviations in the modeled vs. actual surface coverage. The calculated I_O/I_I ratios as a function of surface coverage of the OPA ligand is displayed in Figure A2.2.

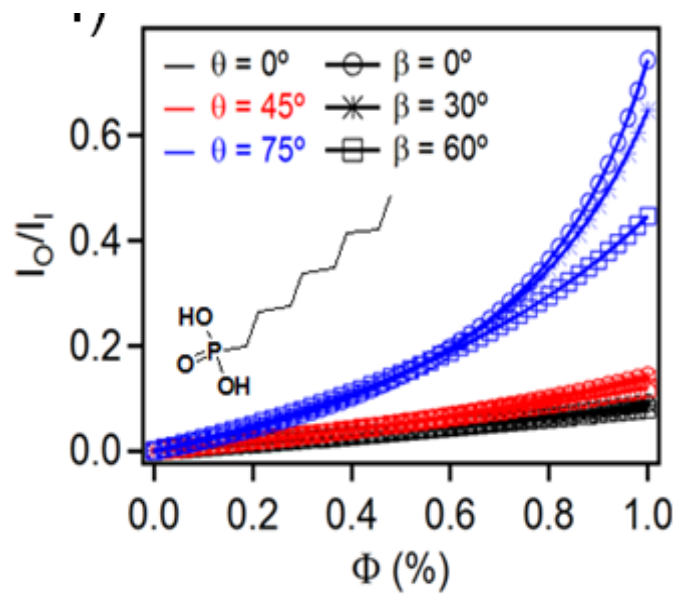


Figure A2.2 (a) Calculated I_0/I_1 vs. surface coverage (Φ) for varying tilt angles (β) and take-off angles (θ) for OPA.

BIBLIOGRAPHY

1. Plater, M. J. & Raab, A. Who Made Mauveine First: Runge, Fritsche, Beissenhirtz or Perkin? *J. Chem. Res.* **40**, 758–762 (2016).
2. Rasmussen, S. C. Conjugated and Conducting Organic Polymers: The First 150 Years. *Chempluschem* **85**, 1412–1429 (2020).
3. Inzelt, G. Rise and rise of conducting polymers. *J. Solid State Electrochem.* **15**, 1711–1718 (2011).
4. Kallmann, H. & Pope, M. Positive Hole Injection into Organic Crystals. *J. Chem. Phys.* **32**, 300–301 (1960).
5. KALLMANN, H. & POPE, M. Bulk Conductivity in Organic Crystals. *Nature* **186**, 31–33 (1960).
6. Shirakawa, H., Louis, E. J., MacDiarmid, A. G., Chiang, C. K. & Heeger, A. J. Synthesis of electrically conducting organic polymers: halogen derivatives of polyacetylene, (CH)_x. *J. Chem. Soc. Chem. Commun.* 578 (1977) doi:10.1039/c39770000578.
7. Diaz, A. F., Kanazawa, K. K. & Gardini, G. P. Electrochemical polymerization of pyrrole. *J. Chem. Soc. Chem. Commun.* 635 (1979) doi:10.1039/c39790000635.
8. Chiang, C. K. *et al.* Electrical Conductivity in Doped Polyacetylene. *Phys. Rev. Lett.* **39**, 1098–1101 (1977).
9. McGinness, J., Corry, P. & Proctor, P. Amorphous Semiconductor Switching in Melanins. *Science (80-.)*. **183**, 853–855 (1974).
10. Shaw, J. M. & Seidler, P. F. Organic electronics: Introduction. *IBM J. Res. Dev.* **45**, 3–9 (2001).
11. Tang, C. W. & VanSlyke, S. A. Organic electroluminescent diodes. *Appl. Phys. Lett.* **51**, 913–915 (1987).
12. Tsumura, A., Koezuka, H. & Ando, T. Macromolecular electronic device: Field-effect transistor with a polythiophene thin film. *Appl. Phys. Lett.* **49**, 1210–1212 (1986).
13. Suputra, O. Summary for Policymakers. in *Climate Change 2013 - The Physical Science Basis* (ed. Intergovernmental Panel on Climate Change) vol. 53 1–30 (Cambridge University Press, 2013).
14. Bellis, M. OLED Technology Guidelines and History. *houghtCo*. thoughtco.com/who-invented-oled-technology-1992208. (2020).
15. Metalgrass. OLED companies: the comprehensive list. *Metalgrass Co*. <https://www.oled-info.com/companies> (2019).
16. Tang, C. W. Two-layer organic photovoltaic cell. *Appl. Phys. Lett.* **48**, 183–185

- (1986).
17. Hiramoto, M., Fujiwara, H. & Yokoyama, M. Three-layered organic solar cell with a photoactive interlayer of codeposited pigments. *Appl. Phys. Lett.* **58**, 1062–1064 (1991).
 18. Wudl, F., Sariciftci, N., Smilowitz, L. & Heeger, A. . Photoinduced Electron Transfer from a Conducting Polymer to Buckminsterfullerene. *Science (80-.)*. **258**, 1474–1476 (1992).
 19. Hiramoto, M. & Shinmura, Y. Organic Solar Cells. in *Springer Handbook of Electronic and Photonic Materials* (eds. Kasap, S. & Capper, P.) 1–1 (Springer International Publishing, 2017). doi:10.1007/978-3-319-48933-9_54.
 20. Reese, M. O., Marshall, A. R. & Rumbles, G. CHAPTER 1 Reliably Measuring the Performance of Emerging Photovoltaic Solar Cells. in *Nanostructured Materials for Type III Photovoltaics* 1–32 (The Royal Society of Chemistry, 2018). doi:10.1039/9781782626749-00001.
 21. best-research-cell-efficiencies.20200919_3.pdf. *NREL Best Research-cell Efficiencies* <https://www.nrel.gov/pv/assets/images/efficiency-chart.png>. (2020).
 22. NREL. Best Research-Cell Efficiencies: Rev. 04-06-2020. *NREL* <https://www.nrel.gov/pv/cell-efficiency.html> (2020).
 23. Rollet, C. An organic solar cell with 25% efficiency. *pv magazine* <https://www.pv-magazine.com/2020/03/24/an-organic-solar-cell-with-25-efficiency/> (2020).
 24. Hopkins, J., Fidanovski, K., Lauto, A. & Mawad, D. All-Organic Semiconductors for Electrochemical Biosensors: An Overview of Recent Progress in Material Design. *Front. Bioeng. Biotechnol.* **7**, 1–8 (2019).
 25. Tingley, K. The Body Electric. *newyorker* (2013).
 26. Sugama, S. *et al.* Dynamic aberrant NF- κ B spurs tumorigenesis: a new model encompassing the microenvironment Spiros. *Sci. Transl. Med.* **26**, 39–46 (2017).
 27. Russ, B., Glaudell, A., Urban, J. J., Chabinyk, M. L. & Segalman, R. A. Organic thermoelectric materials for energy harvesting and temperature control. *Nat. Rev. Mater.* **1**, 16050 (2016).
 28. Chabinyk, M. Behind organics' thermopower. *Nat. Mater.* **13**, 119–121 (2014).
 29. Du, Y., Xu, J., Paul, B. & Eklund, P. Flexible thermoelectric materials and devices. *Appl. Mater. Today* **12**, 366–388 (2018).
 30. Advanced Chemistry Development, I. ACD/ChemSketch. (2019).
 31. Miessler, G. L. *Inorganic chemistry*. (Upper Saddle River, N.J. : Pearson Education, 2004).
 32. Bassler, H. & Kohler, A. Charge Transport in Organic Semiconductors. *Unimolecular Supramol. Electron. I Chem. Phys. Meet A* **312**, 1–65 (2012).

33. Albright, T. A., Burdett, J. K. & Whangbo, M. Orbital Interactions in Chemistry. (2013) doi:10.1002/9781118558409.
34. Koopmans, T. Über die Zuordnung von Wellenfunktionen und Eigenwerten zu den Einzelnen Elektronen Eines Atoms. *Physica* **1**, 104–113 (1934).
35. Bredas, J.-L. Mind the gap! *Mater. Horiz.* **1**, 17–19 (2014).
36. Kahn, A. Fermi level, work function and vacuum level. *Mater. Horizons* **3**, 7–10 (2016).
37. Heimel, G., Salzmann, I., Duhm, S. & Koch, N. Design of organic semiconductors from molecular electrostatics. *Chem. Mater.* **23**, 359–377 (2011).
38. D'Avino, G. *et al.* Electrostatic phenomena in organic semiconductors: fundamentals and implications for photovoltaics. *J. Phys. Condens. Matter* **28**, 433002 (2016).
39. Zozoulenko, I. *et al.* Polarons, Bipolarons, And Absorption Spectroscopy of PEDOT. *ACS Appl. Polym. Mater.* **1**, 83–94 (2019).
40. Miller, A. & Abrahams, E. Impurity conduction at low concentrations. *Phys. Rev.* **120**, 745–755 (1960).
41. Marcus, R. A. Electron Transfer Reactions in Chemistry: Theory and Experiment (Nobel Lecture). *Angew. Chemie Int. Ed. English* **32**, 1111–1121 (1993).
42. Coropceanu, V. *et al.* Charge Transport in Organic Semiconductors. *Chem. Rev.* **107**, 926–952 (2007).
43. Zuo, G., Liu, X., Fahlman, M. & Kemerink, M. High Seebeck Coefficient in Mixtures of Conjugated Polymers. *Adv. Funct. Mater.* **28**, 1703280 (2018).
44. Zuo, G., Abdalla, H. & Kemerink, M. Impact of doping on the density of states and the mobility in organic semiconductors. *Phys. Rev. B* **93**, 235203 (2016).
45. Volpi, R., Nassau, R., Nørby, M. S. & Linares, M. Theoretical Study of the Charge-Transfer State Separation within Marcus Theory: The C 60 -Anthracene Case Study. *ACS Appl. Mater. Interfaces* **8**, 24722–24736 (2016).
46. Melianas, A. *et al.* Photo-generated carriers lose energy during extraction from polymer-fullerene solar cells. *Nat. Commun.* **6**, 8778 (2015).
47. van der Kaap, N. J. & Koster, L. J. A. Massively parallel kinetic Monte Carlo simulations of charge carrier transport in organic semiconductors. *J. Comput. Phys.* **307**, 321–332 (2016).
48. Groves, C. Simulating charge transport in organic semiconductors and devices: a review. *Reports Prog. Phys.* **80**, 026502 (2017).
49. Abtahi, A. *et al.* Effect of Halogenation on the Energetics of Pure and Mixed Phases in Model Organic Semiconductors Composed of Anthradithiophene Derivatives and C 60. *J. Phys. Chem. C* **122**, 4757–4767 (2018).

50. Abtahi, A. *et al.* Designing π -conjugated polymer blends with improved thermoelectric power factors. *J. Mater. Chem. A* **7**, 19774–19785 (2019).
51. Schlaf, R., Parkinson, B. a., Lee, P. a., Nebesny, K. W. & Armstrong, N. R. HOMO/LUMO Alignment at PTCDA/ZnPc and PTCDA/ClInPc Heterointerfaces Determined by Combined UPS and XPS Measurements. *J. Phys. Chem. B* **103**, 2984–2992 (1999).
52. Hüfner, S., Schmidt, S. & Reinert, F. Photoelectron spectroscopy—An overview. *Nucl. Instruments Methods Phys. Res. Sect. A Accel. Spectrometers, Detect. Assoc. Equip.* **547**, 8–23 (2005).
53. Hüfner, S., Hüfner, S. & Service, S. (Online. *Very High Resolution Photoelectron Spectroscopy*. (Berlin, Heidelberg : Springer Berlin Heidelberg : Imprint: Springer, 2007).
54. Greiner, M. T. *et al.* Universal energy-level alignment of molecules on metal oxides. *Nat. Mater.* **11**, 76–81 (2012).
55. Hüfner, S. *Photoelectron spectroscopy: principles and applications*. (Springer Berlin Heidelberg, 2003). doi:10.1007/978-3-662-09280-4.
56. Wieser, J. *et al.* Vacuum ultraviolet rare gas excimer light source. *Rev. Sci. Instrum.* **68**, 1360–1364 (1997).
57. Wieser, J. *et al.* Lyman-alpha emission via resonant energy transfer. *J. Phys. B At. Mol. Opt. Phys.* **31**, 4589–4597 (1998).
58. Morozov, A., Krücken, R., Ulrich, A., Wieser, J. & McCarthy, T. Energy-transfer processes in neon-hydrogen mixtures excited by electron beams. *J. Chem. Phys.* **123**, 234311 (2005).
59. Boehm, A. M., Wieser, J., Butrouna, K. & Graham, K. R. A new photon source for ultraviolet photoelectron spectroscopy of organic and other damage-prone materials. *Org. Electron.* **41**, 9–16 (2017).
60. Sato, T., Kinjo, H., Yamazaki, J. & Ishii, H. 10¹⁵ cm⁻³ eV⁻¹ level detection of density of states of a p-type polymer by h ν -dependent high-sensitivity ultraviolet photoemission spectroscopy. *Appl. Phys. Express* **10**, 011602 (2017).
61. Yoshida, H. Near-ultraviolet inverse photoemission spectroscopy using ultra-low energy electrons. *Chem. Phys. Lett.* **539–540**, 180–185 (2012).
62. Boehm, A. INTERFACES IN LEAD-FREE TIN PEROVSKITE PHOTOVOLTAICS: AN INVESTIGATION OF ENERGETICS, ION MOBILITY, SURFACE MODIFICATION, AND PERFORMANCE. (University of Kentucky, 2020). doi:<https://doi.org/10.13023/etd.2020.372>.
63. Boehm, A. M., Liu, T., Park, S. M., Abtahi, A. & Graham, K. R. Influence of Surface Ligands on Energetics at FASnI₃/C₆₀ Interfaces and Their Impact on Photovoltaic Performance. *ACS Appl. Mater. Interfaces* **12**, 5209–5218 (2020).

64. Park, S. M., Abtahi, A., Boehm, A. M. & Graham, K. R. Surface Ligands for Methylammonium Lead Iodide Films: Surface Coverage, Energetics, and Photovoltaic Performance. *ACS Energy Lett.* **5**, 799–806 (2020).
65. J.F. Moulder, W.F. Stickle, P. Sobol, K.D. Bomben, J. C. *PHI-Handbook of X-ray Photoelectron Spectroscopy*. Perkin-Elmer Corporation (1992). doi:9780962702624.
66. Stone, A. J. Distributed Multipole Analysis: Stability for Large Basis Sets. *J. Chem. Theory Comput.* **1**, 1128–1132 (2005).
67. Davison, A., Holm, R. H., Benson, R. E. & Mahler, W. Metal Complexes Derived from cis -1,2-dicyano-1,2-ethylenedithiolate and Bis(Trifluoromethyl)-1,2-dithiete. in *Inorganic Syntheses* vol. X 8–26 (2007).
68. Zhao, Y. *et al.* Conjugation-break spacers in semiconducting polymers: Impact on polymer processability and charge transport properties. *Macromolecules* **48**, 2048–2053 (2015).
69. Schroeder, B. C. *et al.* Taming Charge Transport in Semiconducting Polymers with Branched Alkyl Side Chains. *Adv. Funct. Mater.* **27**, 1701973 (2017).
70. Liang, Z., Boland, M. J., Butrouna, K., Strachan, D. R. & Graham, K. R. Increased power factors of organic–inorganic nanocomposite thermoelectric materials and the role of energy filtering. *J. Mater. Chem. A* **5**, 15891–15900 (2017).
71. Jackson, W. B., Amer, N. M., Boccara, A. C. & Fournier, D. Photothermal deflection spectroscopy and detection. *Appl. Opt.* **20**, 1333 (1981).
72. Couch, B., Meyer, A., Heller, B. & Johnson, S. L. Absolute fluorescence quantum yield determined by photothermal deflection spectroscopy. *Methods Appl. Fluoresc.* **7**, 015004 (2018).
73. Venkateshvaran, D. *et al.* Approaching disorder-free transport in high-mobility conjugated polymers. *Nature* **515**, 384–388 (2014).
74. Lang, S., Gerschitzka, M., Bauer, D. & Drück, H. Thermal Conductivity of Vacuum Insulation Materials for Thermal Energy Stores in Solar Thermal Systems. *Energy Procedia* **91**, 172–181 (2016).
75. Mikolajczak, P., Piasek, W. & Subotowicz, M. Thermoelectric power in bismuth thin films. *Phys. Status Solidi* **25**, 619–628 (1974).
76. Yoshida, M. *et al.* Gate-Optimized Thermoelectric Power Factor in Ultrathin WSe₂ Single Crystals. *Nano Lett.* **16**, 2061–2065 (2016).
77. Cui, Y. *et al.* Fine-Tuned Photoactive and Interconnection Layers for Achieving over 13% Efficiency in a Fullerene-Free Tandem Organic Solar Cell. *J. Am. Chem. Soc.* **139**, 7302–7309 (2017).
78. Wilson, G. National Center for Photovoltaics, www.nrel.gov/ncpv/. 2016 (2013).
79. Son, H. J. *et al.* Synthesis of Fluorinated Polythienothiophene- co -

- benzodithiophenes and Effect of Fluorination on the Photovoltaic Properties. *J. Am. Chem. Soc.* **133**, 1885–1894 (2011).
80. Chen, H.-C. *et al.* Prominent Short-Circuit Currents of Fluorinated Quinoxaline-Based Copolymer Solar Cells with a Power Conversion Efficiency of 8.0%. *Chem. Mater.* **24**, 4766–4772 (2012).
 81. Chen, H.-Y. *et al.* Polymer solar cells with enhanced open-circuit voltage and efficiency. *Nat. Photonics* **3**, 649–653 (2009).
 82. Nguyen, T. L. *et al.* Semi-crystalline photovoltaic polymers with efficiency exceeding 9% in a ~300 nm thick conventional single-cell device. *Energy Environ. Sci.* **7**, 3040–3051 (2014).
 83. Zhao, J. *et al.* Efficient organic solar cells processed from hydrocarbon solvents. *Nat. Energy* **1**, 15027 (2016).
 84. Bin, H. *et al.* Non-Fullerene Polymer Solar Cells Based on Alkylthio and Fluorine Substituted 2D-Conjugated Polymers Reach 9.5% Efficiency. *J. Am. Chem. Soc.* **138**, 4657–4664 (2016).
 85. Huang, J. *et al.* Highly Efficient Organic Solar Cells with Improved Vertical Donor-Acceptor Compositional Gradient Via an Inverted Off-Center Spinning Method. *Adv. Mater.* **28**, 967–974 (2016).
 86. Schroeder, B. C. *et al.* Silaindacenodithiophene-based low band gap polymers - The effect of fluorine substitution on device performances and film morphologies. *Adv. Funct. Mater.* **22**, 1663–1670 (2012).
 87. Price, S. C., Stuart, A. C., Yang, L., Zhou, H. & You, W. Fluorine substituted conjugated polymer of medium band gap yields 7% efficiency in polymer-fullerene solar cells. *J. Am. Chem. Soc.* **133**, 4625–4631 (2011).
 88. Zhou, H. *et al.* Development of Fluorinated Benzothiadiazole as a Structural Unit for a Polymer Solar Cell of 7 % Efficiency. *Angew. Chemie Int. Ed.* **50**, 2995–2998 (2011).
 89. Carsten, B. *et al.* Examining the Effect of the Dipole Moment on Charge Separation in Donor–Acceptor Polymers for Organic Photovoltaic Applications. *J. Am. Chem. Soc.* **133**, 20468–20475 (2011).
 90. Calvo-Castro, J., Morris, G., Kennedy, A. R. & McHugh, C. J. Effects of Fluorine Substitution on the Intermolecular Interactions, Energetics, and Packing Behavior of N-Benzyl Substituted Diketopyrrolopyrroles. *Cryst. Growth Des.* **16**, 2371–2384 (2016).
 91. Sweetnam, S. *et al.* Characterization of the Polymer Energy Landscape in Polymer:Fullerene Bulk Heterojunctions with Pure and Mixed Phases. *J. Am. Chem. Soc.* **136**, 14078–14088 (2014).
 92. Burke, T. M., Sweetnam, S., Vandewal, K. & McGehee, M. D. Beyond Langevin Recombination: How Equilibrium Between Free Carriers and Charge Transfer

- States Determines the Open-Circuit Voltage of Organic Solar Cells. *Adv. Energy Mater.* **5**, 1500123 (2015).
93. Chen, W., Qi, D.-C., Huang, H., Gao, X. & Wee, A. T. S. Organic-Organic Heterojunction Interfaces: Effect of Molecular Orientation. *Adv. Funct. Mater.* **21**, 410–424 (2011).
 94. Yang, P. *et al.* Influence of fluorine substituents on the film dielectric constant and open-circuit voltage in organic photovoltaics. *J. Mater. Chem. C* **2**, 3278–3284 (2014).
 95. Carsten, B. *et al.* Mediating Solar Cell Performance by Controlling the Internal Dipole Change in Organic Photovoltaic Polymers. *Macromolecules* **45**, 6390–6395 (2012).
 96. McGarry, K. A. *et al.* Rubrene-based single-crystal organic semiconductors: Synthesis, electronic structure, and charge-transport properties. *Chem. Mater.* **25**, 2254–2263 (2013).
 97. Tada, A., Geng, Y., Wei, Q., Hashimoto, K. & Tajima, K. Tailoring organic heterojunction interfaces in bilayer polymer photovoltaic devices. *Nat. Mater.* **10**, 450–5 (2011).
 98. Nakano, K. & Tajima, K. Organic Planar Heterojunctions: From Models for Interfaces in Bulk Heterojunctions to High-Performance Solar Cells. *Adv. Mater.* **29**, 1603269 (2017).
 99. Liu, P. *et al.* Effect of fluorine content in thienothiophene-benzodithiophene copolymers on the morphology and performance of polymer solar cells. *Chem. Mater.* **26**, 3009–3017 (2014).
 100. Tumbleston, J. R., Stuart, A. C., Gann, E., You, W. & Ade, H. Fluorinated Polymer Yields High Organic Solar Cell Performance for a Wide Range of Morphologies. *Adv. Funct. Mater.* **23**, 3463–3470 (2013).
 101. Jiang, B. *et al.* Synthesis of fluorinated diphenyl-diketopyrrolopyrrole derivatives as new building blocks for conjugated copolymers. *Polym. Chem.* **7**, 3311–3324 (2016).
 102. Do, K. *et al.* Impact of Fluorine Substituents on π -Conjugated Polymer Main-Chain Conformations, Packing, and Electronic Couplings. *Adv. Mater.* **28**, 8197–8205 (2016).
 103. Zhao, F. *et al.* Single-Junction Binary-Blend Nonfullerene Polymer Solar Cells with 12.1% Efficiency. *Adv. Mater.* **29**, 1700144 (2017).
 104. Tumbleston, J. R. *et al.* The influence of molecular orientation on organic bulk heterojunction solar cells. *Nat. Photonics* **8**, 385–391 (2014).
 105. Verstappen, P. *et al.* Fluorination as an effective tool to increase the open-circuit voltage and charge carrier mobility of organic solar cells based on poly(cyclopenta[2,1-b:3,4-b']dithiophene-alt-quinoxaline) copolymers. *J. Mater.*

- Chem. A* **3**, 2960–2970 (2015).
106. Nguyen, T. L. *et al.* Semi-crystalline photovoltaic polymers with efficiency exceeding 9% in a ~300 nm thick conventional single-cell device. *Energy Environ. Sci.* **7**, 3040–3051 (2014).
 107. Gélinas, S. *et al.* Ultrafast long-range charge separation in organic semiconductor photovoltaic diodes. *Science* **343**, 512–6 (2014).
 108. Lin, Y. L., Fusella, M. A. & Rand, B. P. The Impact of Local Morphology on Organic Donor/Acceptor Charge Transfer States. *Adv. Energy Mater.* 1702816 (2018) doi:10.1002/aenm.201702816.
 109. Bernardo, B. *et al.* Delocalization and dielectric screening of charge transfer states in organic photovoltaic cells. *Nat. Commun.* **5**, 3245 (2014).
 110. Burke, T. M. & McGehee, M. D. How High Local Charge Carrier Mobility and an Energy Cascade in a Three-Phase Bulk Heterojunction Enable >90% Quantum Efficiency. *Adv. Mater.* **26**, 1923–1928 (2014).
 111. Groves, C. Suppression of geminate charge recombination in organic photovoltaic devices with a cascaded energy heterojunction. *Energy Environ. Sci.* **6**, 1546 (2013).
 112. Kipp, D. & Ganesan, V. Exploiting the Combined Influence of Morphology and Energy Cascades in Ternary Blend Organic Solar Cells Based on Block Copolymer Additives. *Macromolecules* **49**, 5137–5144 (2016).
 113. D’Avino, G. *et al.* Energetics of Electron–Hole Separation at P3HT/PCBM Heterojunctions. *J. Phys. Chem. C* **117**, 12981–12990 (2013).
 114. Few, S., Frost, J. M. & Nelson, J. Models of charge pair generation in organic solar cells. *Phys. Chem. Chem. Phys.* **17**, 2311–2325 (2015).
 115. Shoaee, S. *et al.* Acceptor Energy Level Control of Charge Photogeneration in Organic Donor/Acceptor Blends. *J. Am. Chem. Soc.* **132**, 12919–12926 (2010).
 116. Linares, M. *et al.* On the Interface Dipole at the Pentacene–Fullerene Heterojunction: A Theoretical Study. *J. Phys. Chem. C* **114**, 3215–3224 (2010).
 117. Verlaak, S. *et al.* Electronic Structure and Geminate Pair Energetics at Organic–Organic Interfaces: The Case of Pentacene/C 60 Heterojunctions. *Adv. Funct. Mater.* **19**, 3809–3814 (2009).
 118. Yost, S. R. & Van Voorhis, T. Electrostatic Effects at Organic Semiconductor Interfaces: A Mechanism for “Cold” Exciton Breakup. *J. Phys. Chem. C* **117**, 5617–5625 (2013).
 119. Few, S., Frost, J. M., Kirkpatrick, J. & Nelson, J. Influence of Chemical Structure on the Charge Transfer State Spectrum of a Polymer:Fullerene Complex. *J. Phys. Chem. C* **118**, 8253–8261 (2014).
 120. Ryno, S. M., Risko, C. & Brédas, J.-L. Impact of Molecular Packing on Electronic

- Polarization in Organic Crystals: The Case of Pentacene vs TIPS-Pentacene. *J. Am. Chem. Soc.* **136**, 6421–6427 (2014).
121. Baumeier, B., Andrienko, D. & Rohlfing, M. Frenkel and charge-transfer excitations in donor-acceptor complexes from many-body Green's functions theory. *J. Chem. Theory Comput.* **8**, 2790–2795 (2012).
 122. Graham, K. R. *et al.* The Roles of Structural Order and Intermolecular Interactions in Determining Ionization Energies and Charge-Transfer State Energies in Organic Semiconductors. *Adv. Energy Mater.* **6**, 1601211 (2016).
 123. Westacott, P. *et al.* On the role of intermixed phases in organic photovoltaic blends. *Energy Environ. Sci.* **6**, 2756 (2013).
 124. Ryno, S. M., Fu, Y., Risko, C. & Brédas, J.-L. Polarization Energies at Organic–Organic Interfaces: Impact on the Charge Separation Barrier at Donor–Acceptor Interfaces in Organic Solar Cells. *ACS Appl. Mater. Interfaces* **8**, 15524–15534 (2016).
 125. Endres, J., Pelczer, I., Rand, B. P. & Kahn, A. Determination of Energy Level Alignment within an Energy Cascade Organic Solar Cell. *Chem. Mater.* **28**, 794–801 (2016).
 126. Schlenker, C. W. *et al.* Cascade Organic Solar Cells. *Chem. Mater.* **23**, 4132–4140 (2011).
 127. Stevens, M. A. & Arango, A. C. Open-circuit voltage exceeding the outermost HOMO-LUMO offset in cascade organic solar cells. *Org. Electron.* **37**, 80–84 (2016).
 128. Jakowetz, A. C. *et al.* Visualizing excitations at buried heterojunctions in organic semiconductor blends. *Nat. Mater.* **16**, 551–557 (2017).
 129. Castet, F. *et al.* Electronic polarization effects on charge carriers in anthracene: A valence bond study. *Phys. Rev. B - Condens. Matter Mater. Phys.* **77**, 1–14 (2008).
 130. Yost, S. R., Voorhis, T. Van & Van Voorhis, T. Electrostatic Effects at Organic Semiconductor Interfaces: A Mechanism for “Cold” Exciton Breakup. *J. Phys. Chem. C* **117**, 5617–5625 (2013).
 131. Zheng, Z., Tummala, N. R., Fu, Y.-T., Coropceanu, V. & Brédas, J.-L. Charge-Transfer States in Organic Solar Cells: Understanding the Impact of Polarization, Delocalization, and Disorder. *ACS Appl. Mater. Interfaces* **9**, 18095–18102 (2017).
 132. Gjergji Sini*, Marcel Schubert*, Chad Risko*, Steffen Roland, Olivia P. Lee, Zhihua Chen, Thomas V. Richter, Daniel Dolfen, Veaceslav Coropceanu, Sabine Ludwigs, Ullrich Scherf, Antonio Facchetti, Jean M. J. Fréchet, and D. N. On the Molecular Origin of Charge Separation at the Donor–Acceptor Interface. *Adv. Energy Mater.* **1702232**, 1–15 (2018).
 133. Shoaee, S. *et al.* Charge Photogeneration for a Series of Thiazolo-Thiazole Donor Polymers Blended with the Fullerene Electron Acceptors PCBM and ICBA. *Adv.*

- Funct. Mater.* **23**, 3286–3298 (2013).
134. Akaike, K., Kanai, K., Ouchi, Y. & Seki, K. Influence of ionization energy change on valence band offset in organic p-n junction. *Appl. Phys. Lett.* **95**, 1–4 (2009).
 135. Lau, K. M. *et al.* Interfacial electronic structure of copper phthalocyanine and copper hexadecafluorophthalocyanine studied by photoemission. *Appl. Phys. Lett.* **88**, 10–13 (2006).
 136. Brumbach, M., Placencia, D. & Armstrong, N. R. Titanyl phthalocyanine/C60 heterojunctions: Band-edge offsets and photovoltaic device performance. *J. Phys. Chem. C* **112**, 3142–3151 (2008).
 137. Ran, N. A. *et al.* Impact of interfacial molecular orientation on radiative recombination and charge generation efficiency. *Nat. Commun.* **8**, 79 (2017).
 138. Storzer, T. *et al.* Growth, Structure, and Anisotropic Optical Properties of Difluoro-anthradithiophene Thin Films. *J. Phys. Chem. C* **121**, 21011–21017 (2017).
 139. Mamada, M. *et al.* *syn* -/ *anti* -Anthradithiophene Derivative Isomer Effects on Semiconducting Properties. *ACS Appl. Mater. Interfaces* **5**, 9670–9677 (2013).
 140. Duhm, S. *et al.* Orientation-dependent ionization energies and interface dipoles in ordered molecular assemblies. *Nat. Mater.* **7**, 326–332 (2008).
 141. Heimel, G., Salzmann, I., Duhm, S., Rabe, J. P. & Koch, N. Intrinsic Surface Dipoles Control the Energy Levels of Conjugated Polymers. *Adv. Funct. Mater.* **19**, 3874–3879 (2009).
 142. Yoshida, H., Yamada, K., Tsutsumi, J. & Sato, N. Complete description of ionization energy and electron affinity in organic solids: Determining contributions from electronic polarization, energy band dispersion, and molecular orientation. *Phys. Rev. B* **92**, 075145 (2015).
 143. Topham, B. J. & Soos, Z. G. Ionization in organic thin films: Electrostatic potential, electronic polarization, and dopants in pentacene films. *Phys. Rev. B* **84**, 165405 (2011).
 144. Schwarze, M. *et al.* Impact of molecular quadrupole moments on the energy levels at organic heterojunctions. *Nat. Commun.* **10**, 2466 (2019).
 145. Akaike, K., Koch, N., Heimel, G. & Oehzelt, M. The Impact of Disorder on the Energy Level Alignment at Molecular Donor-Acceptor Interfaces. *Adv. Mater. Interfaces* **2**, 1500232 (2015).
 146. Ngongang Ndjawa, G. O. *et al.* Impact of Molecular Orientation and Spontaneous Interfacial Mixing on the Performance of Organic Solar Cells. *Chem. Mater.* **27**, 5597–5604 (2015).
 147. Poelking, C. *et al.* Impact of mesoscale order on open-circuit voltage in organic solar cells. *Nat. Mater.* **14**, 434–439 (2015).

148. Idé, J. *et al.* Interfacial dipole and band bending in model pentacene/C 60 heterojunctions. *Int. J. Quantum Chem.* **113**, 580–584 (2013).
149. Vandewal, K., Tvingstedt, K., Gadisa, A., Inganäs, O. & Manca, J. V. Relating the open-circuit voltage to interface molecular properties of donor:acceptor bulk heterojunction solar cells. *Phys. Rev. B* **81**, 125204 (2010).
150. Pivrikas, A. *et al.* Langevin recombination and space-charge-perturbed current transients in regiorandom poly(3-hexylthiophene). *Phys. Rev. B - Condens. Matter Mater. Phys.* **71**, 1–5 (2005).
151. Yang, B. *et al.* Impact of Electron Delocalization on the Nature of the Charge-Transfer States in Model Pentacene/C 60 Interfaces: A Density Functional Theory Study. *J. Phys. Chem. C* 141121074201008 (2014) doi:10.1021/jp5074076.
152. Chen, X.-K., Ravva, M. K., Li, H., Ryno, S. M. & Brédas, J.-L. Effect of Molecular Packing and Charge Delocalization on the Nonradiative Recombination of Charge-Transfer States in Organic Solar Cells. *Adv. Energy Mater.* **6**, 1601325 (2016).
153. Elschner, C. *et al.* Determining the C60 molecular arrangement in thin films by means of X-ray diffraction. *J. Appl. Crystallogr.* **44**, 983–990 (2011).
154. 2017_United-States_Energy.pdf. *Laboratory, Lawrence Livermore National* <https://flowcharts.llnl.gov/commodities/energy> (2017).
155. He, J. & Tritt, T. M. Advances in thermoelectric materials research: Looking back and moving forward. *Science (80-.)*. **357**, eaak9997 (2017).
156. Yee, S. K., LeBlanc, S., Goodson, K. E. & Dames, C. \$ per W metrics for thermoelectric power generation: beyond ZT. *Energy Environ. Sci.* **6**, 2561–2571 (2013).
157. Snyder, G. J. & Toberer, E. S. Complex thermoelectric materials. *Nat. Mater.* **7**, 105–114 (2008).
158. Lin, S. *et al.* Tellurium as a high-performance elemental thermoelectric. *Nat. Commun.* **7**, 10287 (2016).
159. Wang, C. *et al.* Enhancement of Conductivity and Thermoelectric Property of PEDOT:PSS via Acid Doping and Single Post-Treatment for Flexible Power Generator. *Adv. Sustain. Syst.* **2**, 1800085 (2018).
160. Kim, S. J., We, J. H. & Cho, B. J. A wearable thermoelectric generator fabricated on a glass fabric. *Energy Environ. Sci.* **7**, 1959–1965 (2014).
161. Bubnova, O. & Crispin, X. Towards polymer-based organic thermoelectric generators. *Energy Environ. Sci.* **5**, 9345–9362 (2012).
162. Bharti, M., Singh, A., Samanta, S. & Aswal, D. K. K. Conductive polymers for thermoelectric power generation. *Prog. Mater. Sci.* **93**, 270–310 (2018).
163. Kiefer, D. *et al.* A Solution-Doped Polymer Semiconductor:Insulator Blend for

- Thermoelectrics. *Adv. Sci.* **4**, 1600203 (2017).
164. Angrist, S. W. *Direct energy conversion*. (Allyn and Bacon, 1977).
 165. Duda, J. C., Hopkins, P. E., Shen, Y. & Gupta, M. C. Thermal transport in organic semiconducting polymers. *Appl. Phys. Lett.* **102**, 251912 (2013).
 166. Brill, J. W. *et al.* Frequency-dependent photothermal measurement of transverse thermal diffusivity of organic semiconductors. *J. Appl. Phys.* **118**, 235501 (2015).
 167. Kroon, R. *et al.* Thermoelectric plastics: from design to synthesis, processing and structure–property relationships. *Chem. Soc. Rev.* **45**, 6147–6164 (2016).
 168. McGrail, B. T., Sehirlioglu, A. & Pentzer, E. Polymer composites for thermoelectric applications. *Angew. Chemie - Int. Ed.* **54**, 1710–1723 (2015).
 169. Zhang, Q., Sun, Y., Xu, W. & Zhu, D. Organic Thermoelectric Materials: Emerging Green Energy Materials Converting Heat to Electricity Directly and Efficiently. *Adv. Mater.* **26**, 6829–6851 (2014).
 170. Kim, G.-H., Shao, L., Zhang, K. & Pipe, K. P. Engineered doping of organic semiconductors for enhanced thermoelectric efficiency. *Nat. Mater.* **12**, 719–23 (2013).
 171. Reenen, S. Van & Kemerink, M. Correcting for contact geometry in Seebeck coefficient measurements of thin film devices. *Org. Electron.* **15**, 2250–2255 (2014).
 172. Culebras, M., Gómez, C. & Cantarero, A. Review on Polymers for Thermoelectric Applications. *Materials (Basel)*. **7**, 6701–6732 (2014).
 173. Bubnova, O. *et al.* Optimization of the thermoelectric figure of merit in the conducting polymer poly(3,4-ethylenedioxythiophene). *Nat. Mater.* **10**, 429–433 (2011).
 174. Liu, J. *et al.* N-Type Organic Thermoelectrics: Improved Power Factor by Tailoring Host-Dopant Miscibility. *Adv. Mater.* **29**, 1701641 (2017).
 175. Zhang, Q., Sun, Y., Xu, W. & Zhu, D. Thermoelectric energy from flexible P3HT films doped with a ferric salt of triflimide anions. *Energy Environ. Sci.* **5**, 9639 (2012).
 176. Hynnen, J. *et al.* Enhanced Thermoelectric Power Factor of Tensile Drawn Poly(3-hexylthiophene). *ACS Macro Lett.* **8**, 70–76 (2019).
 177. Liang, Z. *et al.* Influence of dopant size and electron affinity on the electrical conductivity and thermoelectric properties of a series of conjugated polymers. *J. Mater. Chem. A* **6**, 16495–16505 (2018).
 178. Glaudell, A. M., Cochran, J. E., Patel, S. N. & Chabynyc, M. L. Impact of the Doping Method on Conductivity and Thermopower in Semiconducting Polythiophenes. *Adv. Energy Mater.* **5**, 1401072 (2015).

179. Jacobs, I. E. *et al.* Comparison of Solution-Mixed and Sequentially Processed P3HT:F4TCNQ fFlms: Effect of Doping-Induced Aggregation on Film Morphology. *J. Mater. Chem. C* **4**, 3454–3466 (2016).
180. Shi, K. *et al.* Toward High Performance n-Type Thermoelectric Materials by Rational Modification of BDPPV Backbones. *J. Am. Chem. Soc.* **137**, 6979–6982 (2015).
181. Liu, J. *et al.* N-Type Organic Thermoelectrics of Donor-Acceptor Copolymers: Improved Power Factor by Molecular Tailoring of the Density of States. *Adv. Mater.* **30**, 1804290 (2018).
182. Sun, J. *et al.* Simultaneous Increase in Seebeck Coefficient and Conductivity in a Doped Poly(alkylthiophene) Blend with Defined Density of States. *Macromolecules* **43**, 2897–2903 (2010).
183. Zuo, G., Abdalla, H. & Kemerink, M. Conjugated Polymer Blends for Organic Thermoelectrics. *Adv. Electron. Mater.* 1800821 (2019) doi:10.1002/aelm.201800821.
184. Zuo, G., Liu, X., Fahlman, M. & Kemerink, M. Morphology Determines Conductivity and Seebeck Coefficient in Conjugated Polymer Blends. *ACS Appl. Mater. Interfaces* **10**, 9638–9644 (2018).
185. Yoo, D., Kim, J. & Kim, J. H. Direct synthesis of highly conductive poly(3,4-ethylenedioxythiophene):poly(4-styrenesulfonate) (PEDOT:PSS)/graphene composites and their applications in energy harvesting systems. *Nano Res.* **7**, 717–730 (2014).
186. Yoo, D. *et al.* Effects of one- and two-dimensional carbon hybridization of PEDOT:PSS on the power factor of polymer thermoelectric energy conversion devices. *J. Mater. Chem. A* **3**, 6526–6533 (2015).
187. Arkhipov, I. V., Heremans, P., Emelianova, E. V., Adriaenssens, G. J. & Bäessler, H. Weak-field carrier hopping in disordered organic semiconductors: The effects of deep traps and partly filled density-of-states distribution. *J. Phys. Condens. Matter* **14**, 9899–9911 (2002).
188. Austin, I. G. & Mott, N. F. Polarons in crystalline and non-crystalline materials. *Adv. Phys.* **50**, 757–812 (2001).
189. Mott, N. F. Conduction in non-crystalline systems. *Philos. Mag.* **17**, 1259–1268 (1968).
190. Fishchuk, I. I., Arkhipov, V. I., Kadashchuk, A., Heremans, P. & Bäessler, H. Analytic model of hopping mobility at large charge carrier concentrations in disordered organic semiconductors: Polarons versus bare charge carriers. *Phys. Rev. B - Condens. Matter Mater. Phys.* **76**, 1–12 (2007).
191. Bäessler, H. Charge Transport in Disordered Organic Photoconductors a Monte Carlo Simulation Study. *Phys. status solidi* **175**, 15–56 (1993).

192. Fishchuk, I. I. *et al.* Triplet energy transfer in conjugated polymers. II. A polaron theory description addressing the influence of disorder. *Phys. Rev. B - Condens. Matter Mater. Phys.* **78**, 1–8 (2008).
193. Roichman, Y. & Tessler, N. Generalized Einstein relation for disordered semiconductors - Implications for device performance. *Appl. Phys. Lett.* **80**, 1948–1950 (2002).
194. Lu, N., Li, L. & Liu, M. Universal carrier thermoelectric-transport model based on percolation theory in organic semiconductors. *Phys. Rev. B - Condens. Matter Mater. Phys.* **91**, 1–5 (2015).
195. Mendels, D. & Tessler, N. Thermoelectricity in Disordered Organic Semiconductors under the Premise of the Gaussian Disorder Model and Its Variants. *J. Phys. Chem. Lett.* **5**, 3247–3253 (2014).
196. Tessler, N., Preezant, Y., Rappaport, N. & Roichman, Y. Charge transport in disordered organic materials and its relevance to thin-film devices: A tutorial review. *Adv. Mater.* **21**, 2741–2761 (2009).
197. Xuan, Y. *et al.* Thermoelectric properties of conducting polymers: The case of poly(3-hexylthiophene). *Phys. Rev. B - Condens. Matter Mater. Phys.* **82**, 1–9 (2010).
198. Brédas, J. L., Chance, R. R. & Silbey, R. Comparative theoretical study of the doping of conjugated polymers: Polarons in polyacetylene and polyparaphenylene. *Phys. Rev. B* **26**, 5843–5854 (1982).
199. Valeev, E. F., Coropceanu, V., da Silva Filho, D. A., Salman, S. & Brédas, J.-L. Effect of Electronic Polarization on Charge-Transport Parameters in Molecular Organic Semiconductors. *J. Am. Chem. Soc.* **128**, 9882–9886 (2006).
200. Lu, N., Li, L. & Liu, M. A review of carrier thermoelectric-transport theory in organic semiconductors. *Phys. Chem. Chem. Phys.* **18**, 19503–19525 (2016).
201. Thomas, E. M., Popere, B. C., Fang, H., Chabinye, M. L. & Segalman, R. A. Role of Disorder Induced by Doping on the Thermoelectric Properties of Semiconducting Polymers. *Chem. Mater.* **30**, 2965–2972 (2018).
202. Arkhipov, V. I., Heremans, P., Emelianova, E. V. & Bäessler, H. Effect of doping on the density-of-states distribution and carrier hopping in disordered organic semiconductors. *Phys. Rev. B - Condens. Matter Mater. Phys.* **71**, 1–7 (2005).
203. Abdalla, H., Zuo, G. & Kemerink, M. Range and energetics of charge hopping in organic semiconductors. *Phys. Rev. B* **96**, 241202 (2017).
204. J. Heeger, A. Nobel Lecture : Semiconducting and metallic polymers : generation of polymeric materials *. *Rev. Mod. Phys.* **73**, 681 (2001).
205. Kang, S. D. & Snyder, G. J. Charge-transport model for conducting polymers. *Nat. Mater.* **16**, 252–257 (2017).

206. Nenashev, A. V, Oelerich, J. O. & Baranovskii, S. D. Theoretical tools for the description of charge transport in disordered organic semiconductors. *J. Phys. Condens. Matter* **27**, 093201 (2015).
207. Fishchuk, I. I. *et al.* Temperature dependence of the charge carrier mobility in disordered organic semiconductors at large carrier concentrations. *Phys. Rev. B - Condens. Matter Mater. Phys.* **81**, 1–12 (2010).
208. Arkhipov, V. I. *et al.* The effect of deep traps on carrier hopping in disordered organic materials. *Synth. Met.* **138**, 209–212 (2003).
209. Arkhipov, V. I., Emelianova, E. V., Heremans, P. & Bäessler, H. Analytic model of carrier mobility in doped disordered organic semiconductors. *Phys. Rev. B* **72**, 235202 (2005).
210. Martens, H. C. F., Blom, P. W. M. & Schoo, H. F. M. Comparative study of hole transport in poly(p-phenylene vinylene) derivatives. *Phys. Rev. B* **61**, 7489–7493 (2000).
211. Arkhipov, V. I., Heremans, P., Emelianova, E. V., Adriaenssens, G. J. & Bäessler, H. Charge carrier mobility in doped semiconducting polymers. *Appl. Phys. Lett.* **82**, 3245–3247 (2003).
212. Tietze, M. L. *et al.* Correlation of open-circuit voltage and energy levels in zincphthalocyanine: C₆₀ bulk heterojunction solar cells with varied mixing ratio. *Phys. Rev. B* **88**, 085119 (2013).
213. Sun, J. *et al.* Simultaneous Increase in Seebeck Coefficient and Conductivity in a Doped Poly(alkylthiophene) Blend with Defined Density of States. *Macromolecules* **43**, 2897–2903 (2010).
214. Reiser, P. *et al.* Dopant Diffusion in Sequentially Doped Poly(3-hexylthiophene) Studied by Infrared and Photoelectron Spectroscopy. *J. Phys. Chem. C* **122**, 14518–14527 (2018).
215. Wang, G., Swensen, J., Moses, D. & Heeger, A. J. Increased mobility from regioregular poly(3-hexylthiophene) field-effect transistors. *J. Appl. Phys.* **93**, 6137–6141 (2003).
216. Chu, P. H. *et al.* Synergistic Effect of Regioregular and Regiorandom Poly(3-hexylthiophene) Blends for High Performance Flexible Organic Field Effect Transistors. *Adv. Electron. Mater.* **2**, 1–12 (2016).
217. Zhao, Y. *et al.* Complementary Semiconducting Polymer Blends for Efficient Charge Transport. *Chem. Mater.* **27**, 7164–7170 (2015).
218. Paniagua, S. A. *et al.* Production of heavily n- and p-doped CVD graphene with solution-processed redox-active metal-organic species. *Mater. Horizons* **1**, 111–115 (2014).
219. Said, M. M. *et al.* Ultra-low p-doping of poly(3-hexylthiophene) and its impact on polymer aggregation and photovoltaic performance. *Org. Photonics Photovolt.* **4**,

- 1–16 (2016).
220. Euvrard, J. *et al.* The formation of polymer-dopant aggregates as a possible origin of limited doping efficiency at high dopant concentration. *Org. Electron. physics, Mater. Appl.* **53**, 135–140 (2018).
 221. Kim, G. & Pipe, K. P. Thermoelectric model to characterize carrier transport in organic semiconductors. *Phys. Rev. B* **86**, 085208 (2012).
 222. Fishchuk, I. I., Bäessler, H., Köhler, A., Genoe, J. & Kadashchuk, A. Unraveling the Role of Multiphonon Excitations and Disorder Concerning the Meyer-Neldel Type Compensation Effect in Organic Semiconductors. *Phys. Rev. Appl.* **10**, 054063 (2018).
 223. Jacobs, I. E. *et al.* Direct-Write Optical Patterning of P3HT Films Beyond the Diffraction Limit. *Adv. Mater.* **29**, 1603221 (2017).
 224. Kroon, R. *et al.* Thermoelectric plastics: from design to synthesis, processing and structure–property relationships. *Chem. Soc. Rev.* **45**, 6147–6164 (2016).
 225. Bubnova, O. & Crispin, X. Towards polymer-based organic thermoelectric generators. *Energy Environ. Sci.* **5**, 9345 (2012).
 226. Li, H. *et al.* Dopant-Dependent Increase in Seebeck Coefficient and Electrical Conductivity in Blended Polymers with Offset Carrier Energies. *Adv. Electron. Mater.* **5**, 1800618 (2019).
 227. Snyder, G. J. & Snyder, A. H. Figure of merit ZT of a thermoelectric device defined from materials properties. *Energy Environ. Sci.* **10**, 2280–2283 (2017).
 228. Lu, N. *et al.* Thermoelectric Seebeck Effect of Disordered Organic Semiconductors. in *Advanced Thermoelectric Materials* 79–111 (John Wiley & Sons, Inc., 2019). doi:10.1002/9781119407348.ch3.
 229. Jiang, X. *et al.* Doping-induced change of carrier mobilities in poly(3-hexylthiophene) films with different stacking structures. *Chem. Phys. Lett.* **364**, 616–620 (2002).
 230. Lu, G. *et al.* Moderate doping leads to high performance of semiconductor/insulator polymer blend transistors. *Nat. Commun.* **4**, 1588 (2013).
 231. Yurash, B. *et al.* Towards understanding the doping mechanism of organic semiconductors by Lewis acids. *Nat. Mater.* **18**, 1327–1334 (2019).
 232. Kiefer, D. *et al.* Double doping of conjugated polymers with monomer molecular dopants. *Nat. Mater.* **18**, 149–155 (2019).
 233. Boyle, C. J. *et al.* Tuning charge transport dynamics via clustering of doping in organic semiconductor thin films. *Nat. Commun.* **10**, 2827 (2019).
 234. Yamashita, Y. *et al.* Efficient molecular doping of polymeric semiconductors driven by anion exchange. *Nature* **572**, 634–638 (2019).

235. Cendra, C. *et al.* Role of the Anion on the Transport and Structure of Organic Mixed Conductors. *Adv. Funct. Mater.* **29**, 1807034 (2019).
236. Heimel, G. The Optical Signature of Charges in Conjugated Polymers. *ACS Cent. Sci.* **2**, 309–315 (2016).
237. Paula, F. L. de O. *et al.* Dynamical Mechanism of Polarons and Bipolarons in Poly(p-Phenylene Vinylene). *Sci. Rep.* **9**, 18131 (2019).
238. Steyrlleuthner, R. *et al.* Impact of morphology on polaron delocalization in a semicrystalline conjugated polymer. *Phys. Chem. Chem. Phys.* **19**, 3627–3639 (2017).
239. Chew, A. R. *et al.* Unraveling the Effect of Conformational and Electronic Disorder in the Charge Transport Processes of Semiconducting Polymers. *Adv. Funct. Mater.* **28**, 1804142 (2018).
240. Ghosh, R. *et al.* Anisotropic Polaron Delocalization in Conjugated Homopolymers and Donor–Acceptor Copolymers. *Chem. Mater.* **31**, 7033–7045 (2019).
241. Bombile, J. H., Janik, M. J. & Milner, S. T. Energetics of exciton binding and dissociation in polythiophenes: a tight binding approach. *Phys. Chem. Chem. Phys.* **21**, 11999–12011 (2019).
242. Bombile, J. H., Shetty, S., Janik, M. J. & Milner, S. T. Polaron hopping barriers and rates in semiconducting polymers. *Phys. Chem. Chem. Phys.* **22**, 4032–4042 (2020).
243. Ghosh, R., Pochas, C. M. & Spano, F. C. Polaron Delocalization in Conjugated Polymer Films. *J. Phys. Chem. C* **120**, 11394–11406 (2016).
244. Chew, A. R., Ghosh, R., Shang, Z., Spano, F. C. & Salleo, A. Sequential Doping Reveals the Importance of Amorphous Chain Rigidity in Charge Transport of Semi-Crystalline Polymers. *J. Phys. Chem. Lett.* **8**, 4974–4980 (2017).
245. Bombile, J. H., Janik, M. J. & Milner, S. T. Tight binding model of conformational disorder effects on the optical absorption spectrum of polythiophenes. *Phys. Chem. Chem. Phys.* **18**, 12521–12533 (2016).
246. Duong, D. T. *et al.* Mechanism of Crystallization and Implications for Charge Transport in Poly(3-ethylhexylthiophene) Thin Films. *Adv. Funct. Mater.* **24**, 4515–4521 (2014).
247. Noriega, R. *et al.* A general relationship between disorder, aggregation and charge transport in conjugated polymers. *Nat. Mater.* **12**, 1038–1044 (2013).
248. Kline, R. J. *et al.* Dependence of Regioregular Poly(3-hexylthiophene) Film Morphology and Field-Effect Mobility on Molecular Weight. *Macromolecules* **38**, 3312–3319 (2005).
249. Aubry, T. J. *et al.* Dodecaborane-Based Dopants Designed to Shield Anion Electrostatics Lead to Increased Carrier Mobility in a Doped Conjugated Polymer.

- Adv. Mater.* **31**, 1805647 (2019).
250. Flagg, L. Q., Giridharagopal, R., Guo, J. & Ginger, D. S. Anion-Dependent Doping and Charge Transport in Organic Electrochemical Transistors. *Chem. Mater.* **30**, 5380–5389 (2018).
 251. Scholes, D. T. *et al.* The Effects of Crystallinity on Charge Transport and the Structure of Sequentially Processed F4TCNQ-Doped Conjugated Polymer Films. *Adv. Funct. Mater.* **27**, 1–13 (2017).
 252. Bubnova, O., Berggren, M. & Crispin, X. Tuning the Thermoelectric Properties of Conducting Polymers in an Electrochemical Transistor. *J. Am. Chem. Soc.* **134**, 16456–16459 (2012).
 253. Tanaka, H. *et al.* Thermoelectric properties of a semicrystalline polymer doped beyond the insulator-to-metal transition by electrolyte gating. *Sci. Adv.* **6**, eaay8065 (2020).
 254. Chew, A. R. *et al.* Unraveling the Effect of Conformational and Electronic Disorder in the Charge Transport Processes of Semiconducting Polymers. *Adv. Funct. Mater.* **28**, 1804142 (2018).
 255. Lim, E., Glauddell, A. M., Miller, R. & Chabynyc, M. L. The Role of Ordering on the Thermoelectric Properties of Blends of Regioregular and Regiorandom Poly(3-hexylthiophene). *Adv. Electron. Mater.* **5**, 1800915 (2019).
 256. Tsoi, W. C. *et al.* The Nature of In-Plane Skeleton Raman Modes of P3HT and Their Correlation to the Degree of Molecular Order in P3HT:PCBM Blend Thin Films. *J. Am. Chem. Soc.* **133**, 9834–9843 (2011).
 257. Li, M. *et al.* Impact of polymorphism on the optoelectronic properties of a low-bandgap semiconducting polymer. *Nat. Commun.* **10**, 2867 (2019).
 258. Yang, Y. *et al.* A Facile Approach to Improve Interchain Packing Order and Charge Mobilities by Self-Assembly of Conjugated Polymers on Water. *Adv. Sci.* **5**, 1801497 (2018).
 259. Thiburce, Q., Porcarelli, L., Mecerreyes, D. & Campbell, A. J. High performance photolithographically-patterned polymer thin-film transistors gated with an ionic liquid/poly(ionic liquid) blend ion gel. *Appl. Phys. Lett.* **110**, 233302 (2017).
 260. Allen, F. H., Kennard, O., Watson, D. G., Brammer, L. & Orpen, A. G. Tables of Bond Lengths determined by X-Ray and Neutron Diffraction. Part. 1–19 (1987).
 261. Hofmann, S. *Auger- and X-Ray Photoelectron Spectroscopy in Materials Science*. vol. 49 (Springer Berlin Heidelberg, 2013).
 262. Ebel, M. F. SCHICHTEN MITTELS XPS DICKE D / x DuNNER Eme der Jungeren Anwendungen der Rontgenphotoelektronenspektro- metne beschafflgt such mlt der Bestlmmung der reduzlerten Dlcke D / X (D mlttlere frele Weglange der Elektronen) dunner Schlichten Schlchtdlcke , X D. *J. Electron Spectros. Relat. Phenomena* **14**, 287 (1978).

263. D. Briggs, M. P. S. *Practical Surface Analysis by Auger and X-Ray Photoelectron Spectroscopy*. (1983).
264. John F. Moulder, William F. Stickle, Peter E. Sobol, K. D. B. *Handbook of X-ray Photoelectron Spectroscopy*. (1992).
265. Gao, W., Zielinski, K., Drury, B. N., Carl, A. D. & Grimm, R. L. Elucidation of Chemical Species and Reactivity at Methylammonium Lead Iodide and Cesium Tin Bromide Perovskite Surfaces via Orthogonal Reaction Chemistry. *J. Phys. Chem. C* **122**, 17882–17894 (2018).
266. Cumpson, P. J. & Seah, M. P. Elastic Scattering Corrections in AES and XPS. II. Estimating Attenuation Lengths and Conditions Required for their Valid Use in Overlay/Substrate Experiments. *Surf. Interface Anal.* **25**, 430–446 (1997).
267. Feddes, B., Vredenberg, A. M., Wolke, J. G. C. & Jansen, J. A. Determination of photoelectron attenuation lengths in calcium phosphate ceramic films using XPS and RBS. *Surf. Interface Anal.* **35**, 287–293 (2003).

VITA

Ashkan Abtahi

Education

Doctor of philosophy in Physics and Astronomy Expected Fall of 2020
University of Kentucky **Cumulative GPA: 3.83**
Dissertation title: “A Theoretical and Experimental Study of Charge Transport in Organic Thermoelectric Materials and Charge Transfer States of Organic Photovoltaics”
Advisor: Professor K. R. Graham and Professor J. W. Brill

Master of science Physics and Astronomy May of 2017
University of Kentucky
Project title: “Effect of Halogenation on Energetics and Aggregation in Model Organic Photovoltaic System”
Advisor: Professor K. R. Graham and Professor J. W. Brill

Bachelor of science Physics and Astronomy May of 2013
University of Tehran
Project title: “Analyzing received data from ionosphere in Very Low Frequency (VLF) range and detection of solar flare in VLF range” Advisor: Dr. A. Abasi

Publications

- One work in process:
 - Anion size effect on TE properties of polymers via electrochemical transistors (first author)
- Liang, Z.; Choi, H. H.; Luo, X.; Liu, T.; **Abtahi, A.**; Ramasamy, U. S.; Hitron, J. A.; Hempel J. L.; Boehm, A. M.; Ansary, A.; Strachan, D. R.; Mei, J.; Risko, C.; Podzorov, V.; Graham, K. R.; “n-Type Charge Transport in Heavily p-Doped Polymers”, **Nat. Mater.**, 2020, Under Revision
- Park, S. M.; **Abtahi, A.**; Boehm, A. M.; Graham, K. R.; “Surface Ligands for Methylammonium Lead Iodide Films: Surface Coverage, Energetics, and Photovoltaic Performance”, **ACS Energy Lett.**, 2020, 5, 799-806
- Boehm, A. M.; Liu, T.; Park, S. M.; **Abtahi, A.**; Graham, K.R.; “Influence of Surface Ligands on Energetics at FASnI₃/C₆₀ Interfaces and Their Impact on Photovoltaic Performance”, **ACS Appl. Mater. Interfaces**, 2020, 12, 5209-5218
- **Abtahi, A.**; Johnson, S.; Park, S. M.; Luo, X.; Liang, Z; Mei, J.; Graham, K. R.; “Designing π -Conjugated Polymer Blends with Improved Thermoelectric Power Factors” **J. Mater. Chem. A**, 2019, 7, 19774–19785.

- Wang, F.; Ye, Z.; Sarvari, H.; Park, S. M.; **Abtahi, A.**; Graham, K.; Zhao, Y.; Wang, Y.; Chen, Z. D.; Li, S.; “Humidity-Insensitive Fabrication of Efficient Perovskite Solar Cells in Ambient Air.” *J. Power Sources*, **2019**, 412, 359–365.
- Park, S. M.; Mazza, S. M.; Liang, Z.; **Abtahi, A.**; Boehm, A. M.; Parkin, S. R.; Anthony, J. E.; Graham, K. R.; “Processing Dependent Influence of the Hole Transport Layer Ionization Energy on Methylammonium Lead Iodide Perovskite Photovoltaics.” *ACS Appl. Mater. Interfaces*, **2018**, 10, 15548–15557.
- **Abtahi, A.**; Mazza, S. M.; Ryno, S. M.; Loya, E. K.; Li, R.; Parkin, S. R.; Risko, C.; Anthony, J. E.; Graham, K. R.; “Effect of Halogenation on the Energetics of Pure and Mixed Phases in Model Organic Semiconductors Comprised of Anthradithiophene Derivatives and C₆₀” *J. Phys. Chem. C*, **2018**, 122, 4757–4767
- Fursule, I. A.; **Abtahi, A.**; Watkins, C. B.; Graham, K. R.; Berron, B. J.; “*In situ* crosslinking of surface-initiated ring opening metathesis polymerization of polynorbornene for improved stability” *J. Colloid Interface Sci.*, **2018**, 510, 86–94.